Bioinspired Dinuclear Copper Complexes for Oxygen Activation

Dissertation

zur Erlangung des mathematisch-naturwissenschaftlichen Doktorgrades

„Doctor rerum naturalium“

der Georg-August-Universität Göttingen

im Promotionsprogramm Chemie

der Georg-August University School of Science (GAUSS)

vorgelegt von

Martin Alfred Dzemski

aus Frankfurt am Main

Göttingen, 2022

Betreuungsausschuss

Prof. Dr. Franc Meyer, Institut für Anorganische Chemie, Georg-August-Universität Göttingen

Prof. Dr. Inke Siewert, Institut für Anorganische Chemie, Georg-August-Universität Göttingen

Mitglieder der Prüfungskommission

Referent: Prof. Dr. Franc Meyer, Institut für Anorganische Chemie, Georg-August-Universität Göttingen

Korreferentin: Prof. Dr. Inke Siewert, Institut für Anorganische Chemie, Georg-August-Universität Göttingen

Weitere Mitglieder der Prüfungskommission:

Dr. Matthias Otte, Institut für Anorganische Chemie, Georg-August-Universität Göttingen

Prof. Dr. Konrad Koszinowski, Institut für Organische und Biomolekulare Chemie, Georg-August-Universität Göttingen

Prof. Dr. Ricardo Mata, Institut für Physikalische Chemie, Georg-August-Universität Göttingen

Prof. Dr. Burkhard Geil, Institut für Physikalische Chemie, Georg-August-Universität Göttingen

Tag der mündlichen Prüfung: 29.09.2022

Table of contents

1 Introduction

1.1 General introduction

The production of indispensable basic chemicals requires often enormous amounts of resources and energy. Improving or even replacing existing chemical processes is essential for successfully facing the challenges of the climate crisis, resource scarcity and rising energy demand.[1]

The synthesis of methanol can require huge amounts of energy. This molecule is an important starting material as a C_1 building block in the chemical industry and it is used as a fuel additive.[2,3] For example, the direct partial oxidation of methane to methanol requires reaction temperatures of up to 800 °C and pressures of up to 40 bar due to the necessary activation of the strong C–H-bond of methane (105 kcal/mol).[4–9]

In contrast, nature uses metalloenzymes to catalyze these conversions efficiently without employing harsh reaction condition.[10] For example, the particulate methane monooxygenase (pMMO), which is found in methanotrophs, catalyzes the selective oxidation of methane to methanol at ambient temperatures.[11,12] This remarkable reactivity is achieved by a copper center at the active site of the pMMO.[13–15] Additionally, these enzymes stand out due to their high substrate specificity, low toxicity and high efficiency even at low educt concentrations.[16]

Bioinorganic chemistry is the study of these metalloproteins and their active site to gain insight into their reaction mechanism and to elucidate the underlying principles. If these principles are properly understood, it may be possible to design new biomimetic and environmentally benign catalysts that reproduce these exceptional reactivities and that may contribute towards reducing the global carbon footprint.[17]

Besides transition metals such as iron and zinc, many metalloenzymes are based on copper.[18] The easily accessible Cu^{I}/Cu^{II} redox couple is capable of mediating a variety of processes such as dioxygen (O_2) transport, electron transfer, reduction of O_2 to water or catalytic oxidations of substrates.[19–22] Since this work is inspired by copper proteins, the following chapter will focus on the introduction of a few copper sites in nature.

1.2 Copper proteins in nature

Nowadays, copper proteins are divided into seven classes. An earlier classification into only three classes based on spectroscopic properties was abandoned after the discovery of copper proteins that could not be assigned to any of these three classes.[23] The current classification scheme recognizes the classes Type I, Type II and Type III copper proteins from the old classification scheme. The fourth class is the class of multicopper proteins such as laccase.[24] The fifth class consists of mixed-valent copper proteins that are classified as Cu_A sites.[25,26] The sixth class is the class of heteronuclear Cu_B sites.[27,28] The seventh class consist of the Cu_Z centers of the N_2O-reductases.[29,30]

In this section, Type I, Type II and Type III copper proteins will be introduced as examples for copper proteins. Figure 1 shows a relevant copper enzyme example for each of these three classes.

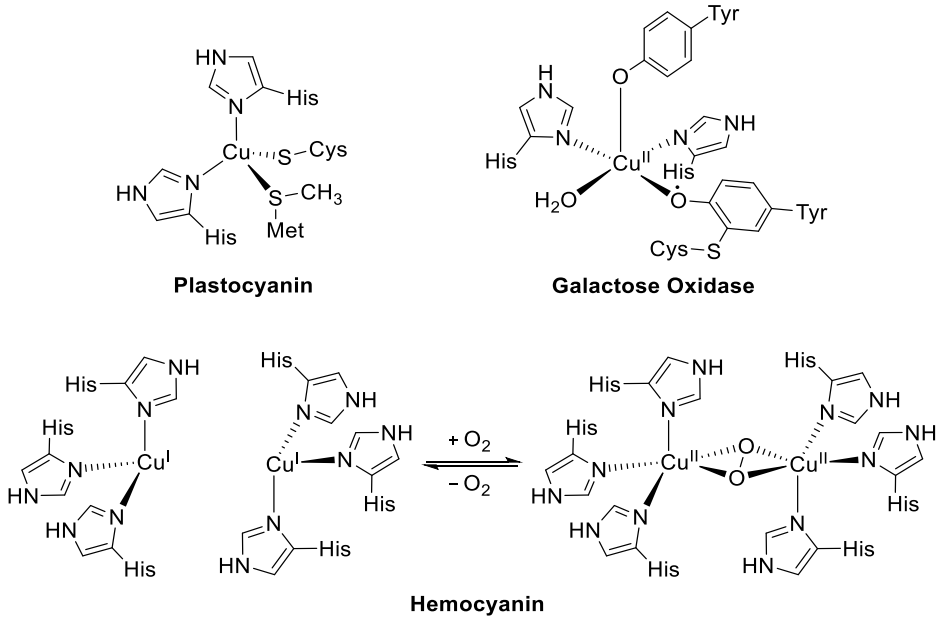

Figure 1: Overview of the active sites of the copper proteins: Plastocyanin, oxidized galactose oxidase at pH = 7 and hemocyanin (Hc) which is shown as deoxygenated hemocyanin (deoxyHc) and oxygenated hemocyanin (oxyHc).[23,31–33]

1.2.1 Type I copper proteins

Type I copper proteins are also called blue copper proteins. In nature, they enable and participate in fast electron transfer (ET) process.[23,34] The characteristic blue color originates from a ligand to metal charge transfer (LMCT) from a sulphur atom of cysteine to the Cu^{II} ion.[35] Example of the copper proteins in this class are amicyanin, azurin and plastocyanin.[23,36,37] The mononuclear copper sites are coordinated by two histidine, one cysteine residue and an additional ligand that varies for each type I copper protein. The molecular structure of the active site of plastocyanin is depicted in Figure 1. The shuttling of electrons requires a fast change of the oxidation state of the copper ion at the active center. These ET reactions are accompanied by a change of the coordination sphere. This is because the preferred coordination geometries differ for Cu^{I} (tetrahedral or trigonal geometry) and Cu^{II} (square planar). However, a complete reorganization of the coordination sphere would greatly slow down the ET process. Therefore,

type I copper proteins such as plastocyanin exhibit a highly distorted tetrahedron structure.[38] This so-called entatic state lies between the two preferred geometries of the respective oxidation states, thus lowering the reorganization energy and making fast electron transfers possible.[39–41]

1.2.2 Type II copper proteins

Type II copper proteins are involved in reactions such as the hydroxylation of aromatic substrates, disproportionation of superoxide anions and oxidation of primary alcohols.[23] There are commonly known as "normal" copper enzymes since their electron paramagnetic resonances (EPR) signals are similar to normal tetragonal copper(II) complexes.[24] Important representatives of this class are the copper-zinc superoxide dismutase, phenylalanine hydroxylase and galactose oxidase. [42–46] The latter is shown in Figure 1.

The galactose oxidase catalyze the oxidation of primary alcohols to aldehydes and in a second step reduces dioxygen to hydrogen peroxide to regenerate the active site.[47,48] Figure 1 shows the coordination sphere of the metal ion in the active site. This coordination sphere consists of two histidine residues, a tyrosine residue, a water molecule and a tyrosyl radical modified by a cysteine.[23,33,46] Together with the metal ion, the tyrosyl radical enables the two-electron reductions.[48,49]

1.2.3 Type III copper proteins

Type III copper proteins are characterized by the dinuclear copper center in their active site.[23] The most studied copper proteins in this class are the catechol oxidase and tyrosinase.[50–52] The catechol oxidase catalyze the oxidation of diphenols such as catechol to the corresponding *ortho*-quinones.[53] The same reaction is facilitated by tyrosinase. An advantage of the tyrosinase is that it also catalyzes the *ortho*-hydroxylation of phenols.[24,31,52]

The oxygen transporter protein hemocyanin (Hc) is another example of a type III copper protein. Hc is one of three oxygen transporters in nature.[54,55] It is the only oxygen transporter that is based on copper ions. Haemoglobin which is used by mammals and birds as well as hemerythrin are iron-based complexes.[23,56,57] Hc serves as an oxygen transport protein in molluscs and arthropods, especially in arachnids.[31,58]

Despite very different roles, the type III copper enzymes exhibit a very similar coordinated active site. Each copper ion of the dinuclear active site is coordinated by three histidine residues of the protein scaffold.[24,31] Figure 1 shows the active site of Hc and the reversible oxygen uptake. The deoxygenated form of Hc (deoxyHc) consists of two cuprous ions and is colorless. The binding of dioxygen to Hc (oxyHc) is accompanied by a change in the oxidation state from Cu^{I} to Cu^{II} and by a change of the coordination geometry from distorted trigonal planar to square pyramidal. The dioxygen molecule is coordinated as a side-on bridging peroxide in a μ-η^2:η^2 coordination mode.[59,60] Due to a charge transfer transition ($O_2^{2-} \rightarrow Cu^{II}$) the oxyHc exhibits an intense blue color.[20,61]

The binding of the dioxygen requires a two-electron reduction. This reaction of the diamagnetic core of deoxyHc with oxygen is spin forbidden since oxygen has a triplet ground state.[20] METZ and SOLOMON investigated the mechanism of the activation of dioxygen at deoxyHc by spectroscopically calibrated density functional theory (DFT).[59] It was found that if oxygen approaches the binuclear active site that the perpendicular π^*-orbitals interact with each copper(I) ion.[62] The resulting reduction of the energy difference between the two ground states allows the transfer of two electrons from the copper(I) ions to the approaching dioxygen molecule. As a result, a so-called butterfly structure is formed (Figure 2). This distorted structure consists of the μ-η^2:η^2-O_2 molecule coordinated to ferromagnetically coupled Cu^{II} ions (S = 1). The resulting reduction of the energy difference between the two different ground states and the flattening of the butterfly structure lead to an intersystem crossing (ISC). This leads finally to antiferromagnetic coupled Cu^{II} ions (S = 0).[59,63]

Later studies corroborated this proposed process experimentally. KINDERMANN *et. al.* succeeded in this by using a model complex, a peroxo dicopper(II) complex based on an *i*Pr_2TACN/pyrazolate compartmental ligand scaffold, with a ground state S = 1 and ferromagnetic coupling of the two Cu^{II} ions.[64,65] This model complex can be seen as a snapshot of the initial binding of oxygen.[64]

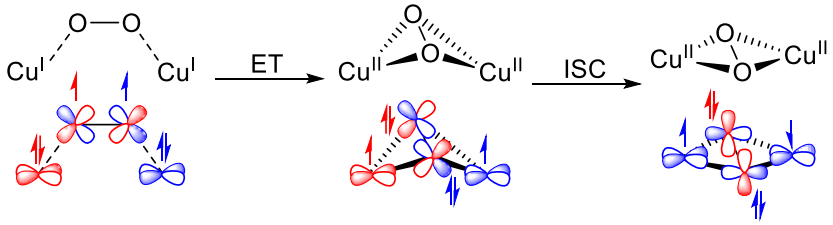

Figure 2: Mechanism of oxygen activation at the active site of Hc showing electron transfer (ET) and intersystem crossing (ISC), according to METZ and SOLOMON.[59,66]

The concept of model complexes and the modelling of a dinuclear active site of a copper enzyme will be introduced in the next chapter.

1.3 Modelling of copper proteins

In nature, a vast array of bimetallic protein structures can be found.[11,19,52,54,67–71] Many of these metalloenzymes are capable of extraordinary catalytic reactivity under mild conditions based on the cooperativity of two metal centers in close proximity at the protein binding pocket.[72] Since it is not possible to reproduce the whole protein for studying the reaction mechanism in the laboratory, only the active site is structurally modelled as a metal complex. For this purpose, a large number of ligands have been developed in the last decades that can mimic the coordination spheres of the active sites.[22] For the study of copper enzymes, many ligands based on nitrogen, sulfur and oxygen donors were established, since these are the typical donor atoms in the parent enzymes. Figure 3 shows some examples for typical N-donor ligands.

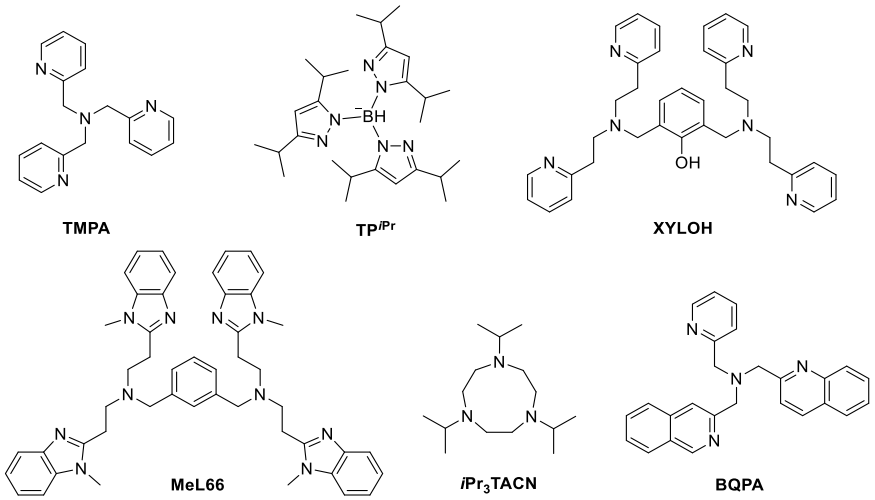

Figure 3: Overview of various ligands that can support dinuclear copper-oxygen complexes.[22,73–80] **TMPA** = tris(2-pyridylmethyl)amine[73,81], **TP^{iPr}** = hydrotris(3,5-diisopropylpyrazolyl)borate anion[74], **XYLOH** = 2,6-bis((bis[2-(2-pyridyl)ethyl]amine)methyl)phenol[79,80,82], **MeL66** = 3,5-bis{bis-[2-(1-methyl-1H-benzimidazol-2-yl)-ethyl]-amino}methylbenzene[76], ***i*Pr$_3$TACN** = 1,4,7-triisopropyl-1,4,7-triazacylcononane[77], **BQPA** = bis(2-pyridylmethyl)(2-quinolylmethyl)amine[75,83].

Different ligand scaffolds can support different oxygen binding motifs. The different coordinated Cu_2O_2 cores are shown in Figure 4 along with their abbreviations. For example, the ligands shown in Figure 3 support different oxygen binding motifs in dicopper complexes: **TP^{iPr}**, **MeL66** and **iPr$_3$TACN** support the formation of ^{S}**P** complexes, **TMPA** can stabilize a ^{T}**P** intermediate, **BQPA** is able to support a bis(μ-oxo) core **O** and **XYLOH** can help to isolate a μ-1,1-hydroperoxo binding motif.

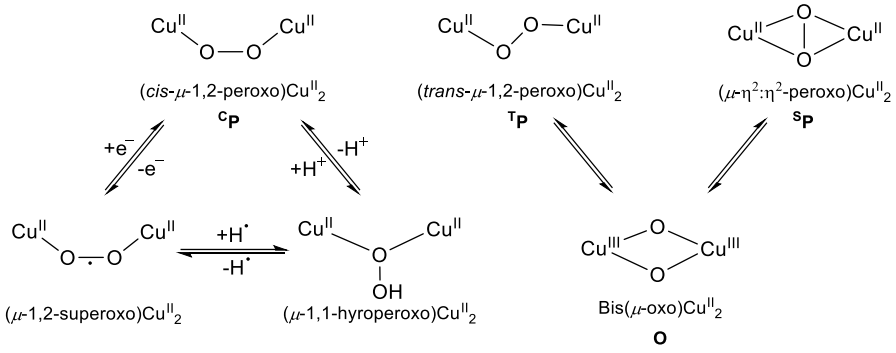

Figure 4: Typical oxygen binding motifs for dinuclear copper oxygen complexes.[9,84]

The importance of model complexes for bioinorganic chemistry can be illustrated by the example of the early investigation of the copper protein oxyHc. Before the molecular structure of the active site of oxygenated hemocyanin was elucidated by crystallography, model complexes were used to investigate the possible oxygen-binding motif. At that time, ^{S}**P**, ^{T}**P** and ^{C}**P** were considered as Cu_2O_2 binding motifs in oxyHc.[85] In particular, the synthesis and subsequent crystallization of two model complexes helped to determine the binding motif of oxyHc. On the one hand, KITAJIMA *et. al.* prepared a dinuclear copper complex based on **TP^{iPr}** which exhibits a side-on coordinated μ-η^2:η^2 motif (Figure 5).[74,85] On the other hand, KARLIN *et. al.* synthesized a trans-μ-1,2 (^{T}**P**) end-on dimer based on the ligand **TMPA**.[73,81,83,86]

Each binding mode of the peroxide is characterized by unique and characteristic spectroscopic properties.[87] The comparison of the spectroscopic properties of oxyHc with those of the model complexes led to the identification of the binding motif of oxyHc. For example, earlier studies at oxyHc showed a distinctive resonance Raman (rR) band at 749 cm^{-1} with a laser excitation at 340 nm.[74,88–90]

The dinuclear model complex of KARLIN *et. al.* shows an isotopically sensitive vibration at around 830 cm^{-1}.[73,81,87,91] In contrast, the dinuclear copper complex based on **TP^{iPr}** of KITAJIMA *et. al.* exhibits a distinctive band at 741 cm^{-1} in the rR spectrum.[85] Therefore, a **^{S}P** motif was suspected for the active site of oxyHc. In addition, the UV/vis data were also consistent. For the model complex of KITAJIMA *et. al.* absorbance features were found at 349 nm ($\varepsilon \approx 21000\ M^{-1}\ cm^{-1}$) and 551 nm ($\varepsilon \approx 800\ M^{-1}\ cm^{-1}$) in the UV/vis spectra.[85] These are similar to the UV/vis bands at 345 nm ($\varepsilon \approx 20000\ M^{-1}\ cm^{-1}$) and 570 nm ($\varepsilon \approx 1000\ M^{-1}\ cm^{-1}$) of the oxyHc.[20,85] The suspected **^{S}P** motif was later confirmed by X-ray crystallography.[92]

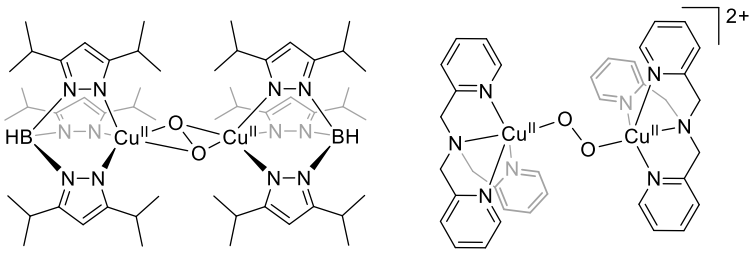

Figure 5: Left: Dinuclear copper oxygen complex based on **TP^{iPr}** with with a **^{S}P** binding motif of KITAJIMA *et. al.*.[74,85] Right: Model complex of KARLIN *et. al.* with a **^{T}P** binding motif.[81,86]

1.4 Ligand design

1.4.1 Dinucleating ligands

The modelling of dinuclear active sites with the help of synthetic analogous coordination compounds is of great interest and has received a lot of attention in recent years.[93] This section introduces an approach to form dinuclear model complexes that employs a highly preorganized and compartmental ligand structure. This structure consists typically of a bridging unit and two adjacent chelating side arms.[72]

1.4.2 Bridging units

Typically, the main function of the bridging unit is to bring two transition metal ions, such as copper ions, in close proximity to facilitate cooperative effects between theses metal ions. The resulting metal-metal separation depends mainly on the employed bridging unit. Additionally, the metal-metal separation can be tuned by the linked side arms.[72] The spatial proximity of the metal ions can lead to distinct physical properties in the resulting bimetallic complexes, such as higher catalytic activity, increased selectivity or multielectron transfer mechanism via redox cooperativity of the two centers.[72,94]

Several bridging units have been explored in the last years. One of the most popular bridging units are the phenolate and the alkoxide bridging units. These bridging units can be modified easily via the introduction of substituents, for example in the ortho-position of the phenolate. They are also relatively easy to synthesize.[72]

Another important class of bridging units are the monocyclic *N*-heterocycles like thiadiazole, oxadiazole, pyridazine, pyrazolate and triazolate. These are shown in Figure 6. The latter can also be used to form trinuclear complexes.[95–97]

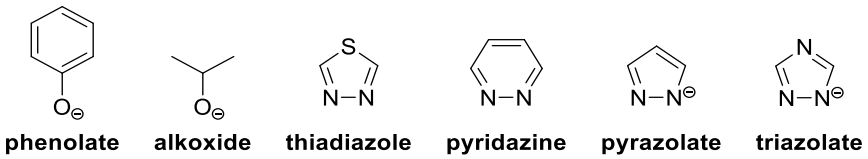

Figure 6: Overview of important bridging units that can coordinate two transition metal ions.[72]

The monoanionic pyrazolate is especially well suited for the formation of binuclear model complexes, due to its ability to serve as an exo-bidentate ligand and to form strong bridging structures with high stability.[72,98,99] In the resulting binuclear complexes, the pyrazolate, the two metal ions and one or even two additional bridging atoms form five or six membered rings.[72] These ring structures have a low ring strain energy and are therefore the preferred geometries.[100]

Additionally, the deprotonated pyrazole bridging unit can support metal ions distances between 2.8 Å and 4.5 Å.[93,101] Since many metal-metal distances in the parent bimetallic metalloenzyme are precisely in this range, pyrazolates are ideal bridging units for biomimetic model complexes. It is possible to fine-tune the metal-metal separation by varying the length of chelating side-arms in the 3- and 5-position of the pyrazolate.[65,93] Moreover, the pyrazolate can be functionalized in the 4-postion which allows to anchor the molecule to another moiety.

Another reason for using pyrazole based ligands in model complex is their structural similarity to the heteroaromatic imidazole in the histidine residue of proteins which often coordinates the metal ions in the active site of the parent enzymes. For example, the metal ions in urease, metallo-β-lactamase or catechol oxidase are mainly coordinated by histidine residues.[51,102–104] Lastly, the pyrazolate can mimic carboxylate bridges which are a very common bridging ligands in metalloenzymes.[65,105–107]

A drawback of using polydentate binucleating ligands containing pyrazolate is that their synthesis is rather challenging and more elaborated than the synthesis of, for example, phenoxide ligands.[72]

1.4.3 Side arms

The two metal ions that are brought into proximity by the bridging unit are further coordinated by multidentate and chelating side arms. These are often covalently linked to the bridging unit by an aliphatic spacer. Firstly, the covalent bond suppresses the dissociation of the complex into two mononuclear species.[108] Secondly, the length of the spacer can be tuned to obtain a stable complex and influences the

metal-metal separation in the resulting binuclear model complex.[64,109–112] Longer spacers can lead to shorter metal ions distances and vice versa.[98] The type and size of the chelating side arms themselves also have an influence on the metal-metal distance by changing the geometry of the resulting complex.[113] Thirdly, two different spacer in a molecule can introduce asymmetry into the ligand scaffold.[93] This way, it is possible to form heterobimetallic complexes by altering the coordination sphere. Furthermore, heteronuclear complexes can be obtained by introducing two different side arms that prefer to coordinate different metal ions.[114]

Depending on the requirements of the well-defined bimetallic core, a vast range of chelating moieties can be used as side arms in a dinucleating ligand scaffold.[65] These side arms are varying by the nature of the donor atoms, the size of resulting chelating rings or the denticity for example.[72,93]

In the present work, 1,4,7-triazacyclononane (TACN) derivates are used as the chelating side arms. This saturated macrocycle is a tripodal tridentate ligand which prefers a facial coordination geometry that allows it to effectively block three adjacent sites at a coordination center.[115,116] A tripodal tetradentate subunit per metal ion can be formed in combination with the donor atoms of the bridging unit. [101] In this work, monoanionic pyrazolate is used as a bridging unit.

Macrocyclic side arms form transition metal complexes with higher stability than simple chelating side arms due to the macrocyclic effect.[117] This predominantly enthalpic effect originates mainly from an increase of ligand preorganisation and a higher degree of alkylation. This leads to donor atoms with a higher intrinsic basicity in comparison to the donor atoms of similar open chain chelate ligand.[118] Additionally, increased alkylation reduces steric strain energy in the ligand.[119]

The steric bulk of the TACN side arms can be varied in the 1- and 4-postion. Steric hindrance can be used to encapsulate or open the bimetallic cavity in the resulting complexes.[65] Alternatively, these binding sites can be used to introduce pendent arms which allow to mimic secondary coordination sphere interactions at the active site of metalloenzymes.[93,116] These additional groups in the direct periphery of the bimetallic core can help stabilize substrates by hydrogen bonding or increase reactivity.[120]

1.4.4 TACN/pyrazolate ligand scaffolds

In recent years, several TACN/pyrazolate ligands for the formation of copper-oxygen complexes have been established by MEYER and co-authors.[38,64,65,104,105,110–112,121–125] These ligand frameworks vary in two positions. First, the length of the spacer between the bridging unit and the steric demand at the side arm can be changed. This has a significant effect on the copper ions distances in the corresponding dicopper complexes. As discussed above, short spacers lead to large distances and long spacers lead to shorter distances. Second, the steric hindrance at the TACN side arms can be reduced from *iso*-propyl to methyl groups. Figure 7 shows the established TACN/pyrazolate ligands.[38,65,104,121,123] The variations of the spacer lengths are shown in red and the steric bulk is depicted in blue.

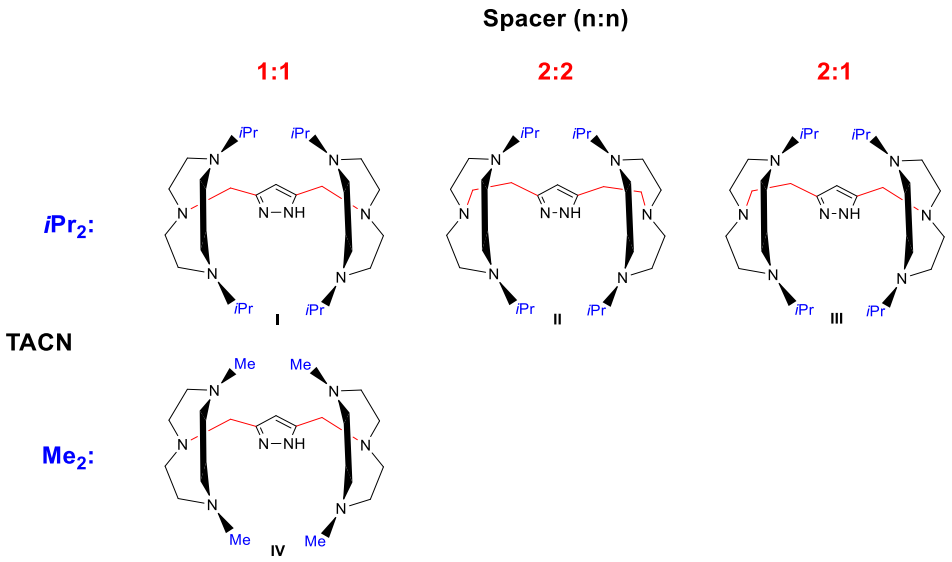

Figure 7: Overview of established TACN/pyrazolate ligand scaffolds.[38,65,104,121,123]

1.5 Previous studies of copper oxygen adducts based on TACN/pyrazolate ligands

The TACN/pyrazolate ligand scaffolds allow to form various reactive copper oxygen adducts. An overview of all established copper oxygen adducts based on various TACN/pyrazolate ligands which are relevant for this work can be found in Chapter 12.[38,65,104,121,123]

Earlier studies have shown that it is possible to isolate the μ-1,2-peroxo dicopper(II) complexes **Ib**, **IIb** and **IIIb** by addition of dry oxygen to the corresponding dicopper(I) complex **Ia**, **IIa** and **IIIa**.[38,64,65,121] Figure 8 shows their molecular structures.

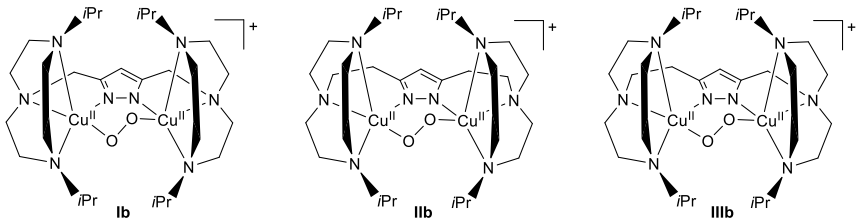

Figure 8: Isolated μ-η^1:η^1-peroxo dicopper(II) complexes based on the ligand scaffolds **I**, **II** and **III**.[38,64,65,121]

These cupric peroxides differ only in their length of the spacer in the ligand backbone. Based on this series, the effects of lengthening the spacer have been described. Longer spacers do not only decrease the copper-copper ion distance. They also change the properties of the complex.[38,65,121] For example, the magnetic properties change due to increasing Cu–O–O–Cu angles with longer spacers. **Ib** has a torsion angle of 55 ° and exhibits antiferromagnetic coupling with a singlet ground state.[121] In contrast, **IIb** is ferromagnetic coupled and exhibits a triplet ground state (S = 1).[65] It has a torsion angle of 104 °. **IIb** was the first copper oxygen complex which exhibits a triplet ground state.[64] **IIIb** can be considered as a mixture of **Ib** and **IIb** due to the non-symmetric geometry.[38] The non-symmetric complex **IIIb** has an torsion angle of 86°, is weak ferromagnetically coupled and has a triplet ground state.[112]

Recent studies show that the length of the spacer can lead to a more exposed active site of the cupric peroxides.[38,121] Short methylene spacer in the ligand backbone allow interactions of Lewis acid with the Cu_2O_2 core.[110] BRINKMEIER *et. al.* show that the peroxo dicopper(II) complex **Ib** can interact with alkali metal ions, such as Li^+ (Scheme 1).[104,111,121]

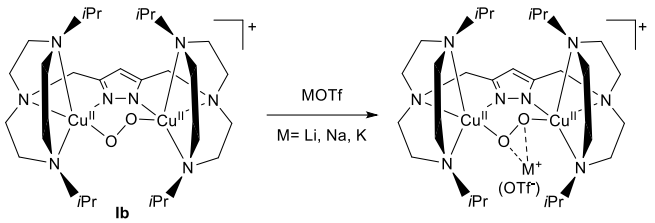

Scheme 1: Synthesis of the alkali metal ion adducts of the peroxo dicopper(II) complex **Ib**.[110,111,121]

It has been found that the interacting alkali metals influence the molecular and electronic structure of **Ib**.[121] For example, the alkali metal ions influence the Cu–O–O–Cu torsion angles. The lithium adduct has the largest deviation from the original angle with an angle of 71°. This influences the antiferromagnetic coupling. The crystallized alkali metal ion adducts have also been examined by UV/vis spectroscopy. A shift of the characteristic bands to shorter wavelengths has been observed for the alkali metal adducts. The smaller the ionic radius of the interacting alkali metal ion the larger is the observed shift of the distinctive absorbance features. [111,121]

Similar results were found for the peroxo dicopper(II) complex **IIIb**.[38,112] In addition, **IIIb** is interacting with hydrogen bond donor substrates like phenol, methanol and 2,2,2-trifluoroethanol (TFE).[38] The resulting UV/vis spectra show a blueshift after adding the of the substrates. The TFE adduct exhibits a temperature dependent equilibrium which is shown in Scheme 2. UV/vis experiments show that at lower temperatures a μ-1,1-hydroperoxo binding motif is preferred whereas at higher temperatures a μ-1,2-peroxo core is preferred in presence of TFE.[38]

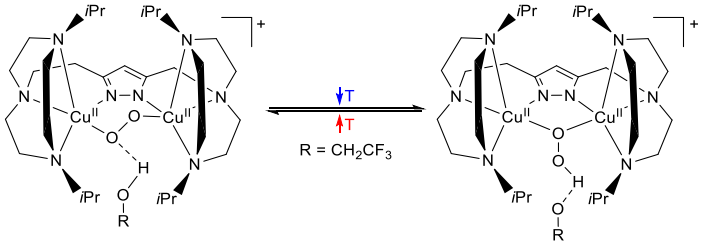

Scheme 2: Equilibrium between the μ-1,2-peroxo and the μ-1,1-hydroperoxo oxygen binding motif. The equilibrium is temperature dependent.[38]

Other reactive oxygen adducts like the hydroperoxo copper(II) complexes have been isolated.[38,65,121] The molecular structures of the crystallized hydroperoxo copper(II) complexes **Ic**, **IIc** and **IIIc** are depicted in Figure 9. The corresponding pK_a values have been determined by UV/vis back titration experiments with adequate bases.[38,65,121,124]

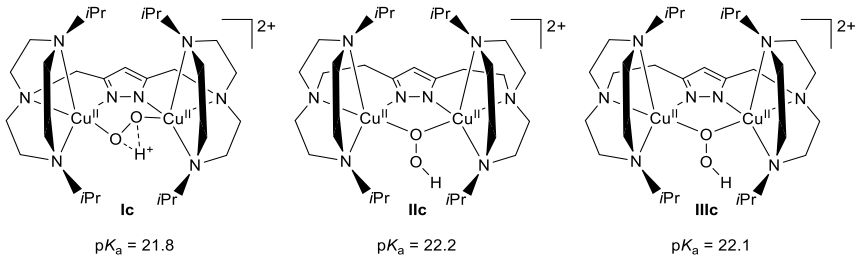

Figure 9: Crystallized hydroperoxo dicopper(II) complexes **Ic**, **IIc** and **IIIc** based on the *i*Pr$_2$TACN/pyrazolate ligands **I**, **II** and **III**.[38,65,121,124]

Despite the high reactivity of the cupric superoxides, Brinkmeier *et. al.* succeed in crystalizing this important bimetallic reactive oxygen adduct **Id** (Figure 10).[121,122] X-Band EPR studies confirm the expected spin ground state of the superoxo dicopper(II) complex **Id** of S = ½.[122] The complex has been synthesized from the *cis*-μ-1,2-peroxo dicopper(II) complex **Ib** by addition of 1 eq. of silver triflate.

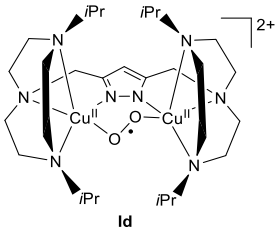

Figure 10: Molecular structure of the superoxo dicopper(II) complex **Id** based on the *i*Pr$_2$TACN/pyrazolate ligand **I**.[121,122]

In contrast to the copper oxygen adducts based on the *i*Pr$_2$TACN/pyrazolate ligand scaffolds **I**, **II** and **III**, the copper oxygen complexes based on the Me$_2$TACN/pyrazolate ligand **IV** are clearly less stable and it has not been possible to crystallize their reactive oxygen intermediates [121,123] However, it has been possible to isolate a novel dicopper(II) complex with a bridging acetate **IVc**. The reduction of **IVc** leads to an unseen mixed-valent intermediate and to the dicopper(I) complex **IVa** (Scheme 3).

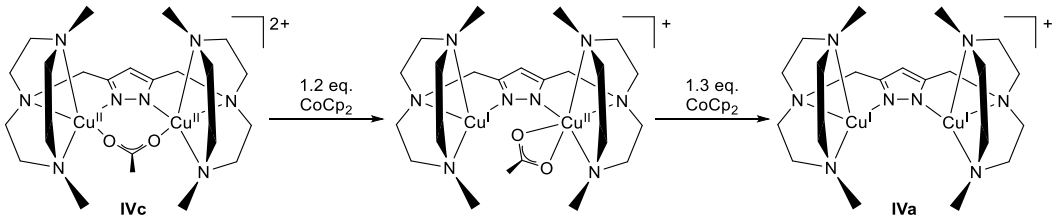

Scheme 3: Reduction of **IVc** to the dicopper(I) complex **IVa** via a mixed-valent copper complex in MeCN.[123]

The existence of the mixed-valent species has been confirmed by the addition of dry oxygen since the corresponding superoxo complex has been observed in a UV/Vis stopped flow experiment.[123]

2 Thesis Objective

In previous studies, it was shown that dinuclear copper complexes based on TACN/pyrazolate compartmental ligands can mimic the Type III copper proteins and can lead to new insights into their reaction mechanism.[38,64,65,104,105,110–112,121–125] The ligand scaffolds shown in grey in Figure 11 were synthesized to investigate the corresponding copper oxygen complexes in earlier works.[38,65,104,121,123] These ligands were mainly varied in their aliphatic spacer. Additionally, attempts were made to reduce the steric bulk at the TACN side arms.

Completing the existing ligand series and extending the range of TACN/pyrazolate ligands requires synthesizing the two methyl substituted ligands **HL$_{sym}$** and **HL$_{asym}$**. The molecular structures of these new ligands are shown in black in Figure 11. The successful synthesis and isolation of **HL$_{sym}$** and **HL$_{asym}$** is one of the objectives of the presented work.

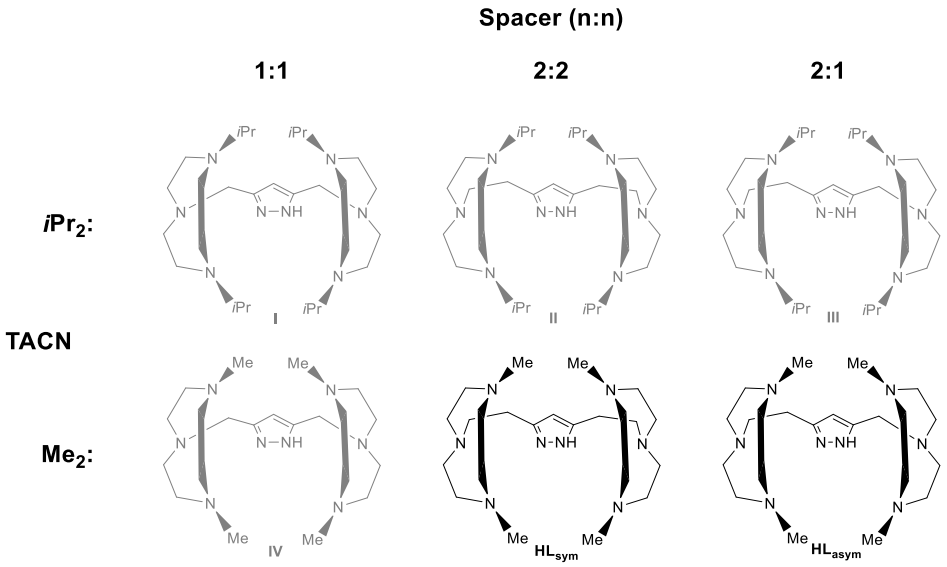

Figure 11: Overview of TACN/pyraazolate hybrid ligands. The existing ligand scaffolds shown in grey. The ligands **HL$_{sym}$** and **HL$_{asym}$** are shown in black.[38,65,104,121,123]

In addition, the aim is to synthesize and characterize the corresponding peroxo dicopper(II) complexes. Since the spacer is not changed in comparison to the ligand **II** and **III** it is expected that the molecular and electronic structure is similar to their peroxo dicopper(II) complexes. The influence of the methyl groups of the TACN side arms on the core of the copper complexes is of particular interest. It is expected that a deshielding of the Cu_2O_2 core can occur due to the reduced steric demand. This may result in increased reactivity.

In addition, a more expose bimetallic cavity may also lead to unknown interactions with new substrates and Lewis acids such as alkali metal ions. To explore this, the present thesis will test whether Lewis acid like Ca^{2+}-ions can interact with the cupric peroxides.

Furthermore, the investigation and isolation of the other occurring reactive intermediates (hydroperoxo and superoxo) is of great interest. The final goal is to test these systems in the oxygen reduction reaction.

3 Novel TACN/pyrazolate ligand scaffolds

3.1 Syntheses of novel TACN/pyrazolate ligands

In previous works, several strategies have been developed to synthesize the dinucleating TACN/pyrazolate ligand scaffolds.[38,65,104,109,121] Normally, the target molecule is obtained by the reaction of a 3,5-substituted pyrazole synthon and two functionalized TACN synthons. From the perspective of retrosynthetic analysis, this approach makes sense because it must be taken into account that the synthesis of both building blocks are already complex multistep syntheses with low yields. The coupling of the two synthons can be achieved by the reaction of a pyrazole acyl chloride or a chlorinated pyrazole with the unprotected secondary amine moiety of the TACN unit. Unfortunately, the more reactive pyrazole acyl chloride building block could not be synthesized as the pyrazole synthon.[32,126] Therefore, the syntheses via the chlorinated pyrazole units are preferred in this work. In this chapter the syntheses of the HMe_2TACN moiety, the symmetric and non-symmetric pyrazole building blocks and the subsequent coupling of both units are described and discussed.

3.1.1 The TACN unit

The simple preparation of aza-crown ethers like 1,4,7-triazacyclononane (TACN) in the laboratory is of high interest. In general, a major challenge in syntheses of all types of macrocycles is to control the formation of large macrocycles with a well-defined ring size. Typically, an uncontrolled ring-closing macrocyclization leads to the formation of a mixture of polymers and macrocycles with relatively small ring sizes. Even if the desired macrocycle was formed by chance during the reaction, the low yields and the complex purification process means that the synthetic effort is not worthwhile.

This problem can be solved mainly by two different classic synthetic strategies. Firstly, a high dilution synthesis approach can be used which favors the intramolecular end-to-end condensation of an open-chain compound instead of the competing concentration dependent bimolecular reaction leading to the formation of oligomers or polymers.[127] Secondly, a widely used strategy is the usage of templates that lead to a favorable preorganization of the reagents prior to the actual ring forming reaction and thereby enabling the efficient syntheses of the correct ring size macrocycle.[128] For example, the template effect was exploited by GREENE in the synthesis of the crown ether 18-crown-6 from the diol triethylene glycol and ditosylated triethylene glycol in the presence of potassium *tert*-butoxide in tetrahydrofuran (THF).[129,130] In this case, the potassium cation preorganized the two reagents prior to ring closure and thus enabled a high yield of the product. This has been described as a cation-template effect which was also observed in the synthesis of the nitrogen analogues of the crown ethers the aza-crown ethers.[128,129] The latter can be produced in moderate yields by using the previous mentioned high dilution technique, as STETTER and ROOS reported.[131] For the cyclization, a terminal dihalide was reacted with the disodium salts of an *N*-tosylated diamine in a highly diluted dimethylformamide/methanol reaction mixture. RICHMAN and ATKINS expanded on that knowledge and developed this reaction further.[132] Instead of

the dihalide, a ditosylated diol with a deprotonated *N*,*N*′,*N*″-tritosyldiethylenetriamine was used to produce a *N*,*N*′,*N*″-tritosyl-1,4,7-triazacyclononane (Scheme 4). The product of this macrocyclization was obtained in a high yield of 71 %.[132]

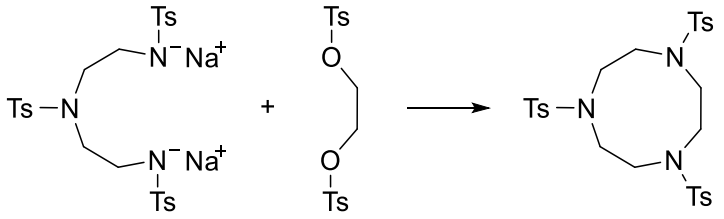

Scheme 4: Ring-closing reaction in the RICHMAN-ATKINS synthesis of the polyaza crown compound *N*,*N*′,*N*″-tritosyl-1,4,7-triazacyclononane.[132]

Surprisingly, this small modification made it possible to do the reaction without using high dilution condition. In addition, this allows to produce these polyazamacrocycles in large scale in the laboratory. Also remarkable is the finding that a sodium cation-template effect is not the dominating factor in the RICHMAN-ATKINS approach. In the original publication RICHMAN and ATKINS described that even if the sodium cations were exchanged against tetramethylammonium cations, the yields were still relatively high.[132] Based on these findings, it was later shown that even the isolated disodium salt was not needed. An *in-situ* deprotonation of the pertosylated polyamine with potassium carbonate or even better a caesium carbonate in the polar aprotic solvent DMF was a more efficient synthesis of these pertosylated polyazamacrocycles. Also in this case, a template effect is not responsible for the efficient synthesis but rather the efficient *in-situ* formation of the tosylamide salt with the metal carbonates.[128,133,134] Eventually, the high yields of the widely used RICHMAN-ATKINS route can be traced back to an entropy effect induced by the *p*-toluenesulfonyl groups. These bulky side groups preorganize the polyaza-compound and reduce the internal entropy by reducing the rotational freedom of the pertosylated open-chain.[128] Large rings are formed if their reaction entropy is higher in comparison to the open-chain reaction.[135] To sum up, the RICHMAN and ATKINS synthesis gives easy access to the *N*,*N*′,*N*″-tritosyl-1,4,7-triazacyclononane in high yields and allows for easy scalability of the synthesis. As large amounts of the resulting 1,4-dimethyl-1,4,7-triazacyclononane are needed to balance out the low yields of the actual ligand synthesis from the two units, a modified and refined synthesis of this synthetic route was chosen for this work (Scheme 5).

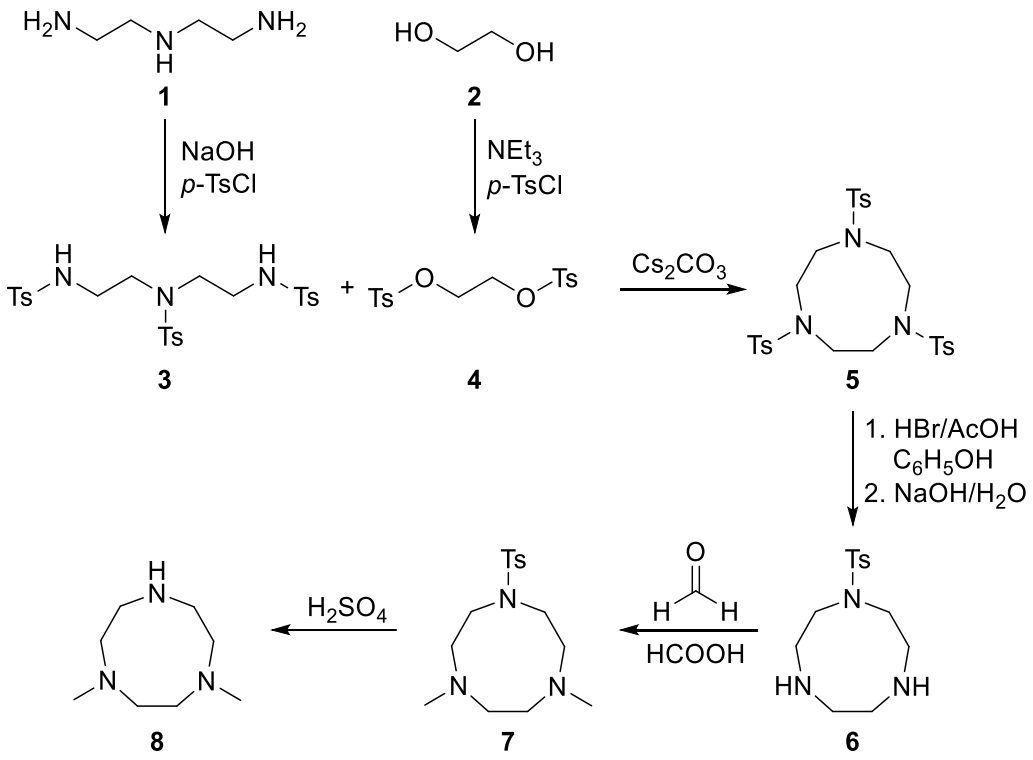

Scheme 5: Synthesis of the TACN unit 1,4-dimethyl-1,4,7-triazacyclononane by using a modified and refined RICHMAN and ATKINS approach.[132,136]

For this synthesis diethylenetriamine and ethylene glycol were commercially acquired. Tosyl protecting groups were introduced by sulfonylation of both reagents under basic conditions leading to the compounds **3** and **4**. Macrocyclization was accomplished with caesium carbonate in dry DMF, as described in the prior section. The subsequent selective deprotection was achieved by the addition of a mixture of 33 % hydrobromic acid in acetic acid and phenol which can act as a bromine scavenger.[116] In a second step the obtained intermediate 1-(*p*-tosyl)-1,4,7-triazacyclononane dihydrobromide can be reacted to compound **6**.[137] This molecule shows the desired $R_a/2R_b$ TACN substitution pattern and can be converted to 4,7-dimethyl-1-(*p*-tosyl)-1,4,7-triazacyclononane **7** under ESCHWEILER-CLARKE methylation reaction conditions. Under harsh conditions the last protection group was removed and after purification by distillation at reduced pressure the desired product **8** was obtained as a colorless oil.[132,136–138] The overall yield of this synthesis of 1,4-dimethyl-1,4,7-triazacyclononane was 23.5 %.

This low yield underlines the fact that scalability of this synthesis is very important for producing large amounts of **8**. Furthermore, the intermediates **3**, **4**, **5** and **7** are very stable and can easily be stored. This fact allowed to accumulating large amount of these intermediates and optimizing in this way the following reaction step of the synthesis. Obviously, the batch sizes where significantly increased in comparison to the described procedures in literature.[136] Since with bigger batches the safety risks and health risks in case of an accident are exponentially higher, this optimizing strategy has its limits in the standard chemical laboratory. Risks and benefits had to be accessed and weighed carefully against each other. This is especially true for the reaction of **5** to **6** where phenol and hydrobromic acid in acetic acid are

used in excess. Additionally, large amounts of gaseous HBr are evolving during the reaction and must be managed. In addition to that, the commonly known problems of scale up, as for instance particle formation or liquid/liquid separation, had to be considered.[139]

Since compound **8** is relatively unstable, it was used directly in the ligand synthesis. It was possible to store **8** at −26 °C under argon atmosphere for two days. Longer storage periods led to partial decomposition which was visible as a color change of the oil from colorless to pale yellow. A bulb-to-bulb distillation made it possible to separate clean compound **8** again, but this procedure reduced the low yield of the synthesis even further and therefore storage was avoided whenever possible. As mentioned in the last paragraph, the precursor 4,7-dimethyl-1-(*p*-tosyl)-1,4,7-triazacyclononane **7** was very stable and thus the deprotection to form compound **8** was only done when the coupling reaction with the pyrazole unit was planned.

All intermediates of the synthesis of 1,4-dimethyl-1,4,7-triazacyclononane **8** were characterized by ^{1}H- and ^{13}C-NMR spectroscopy and the obtained data was consistent with literature.[136] In addition, characterisation by ESI mass spectrometry was done for the product and confirmed the successful synthesis. Figure 12 shows the ^{1}H-NMR spectrum of the end-product **8**.

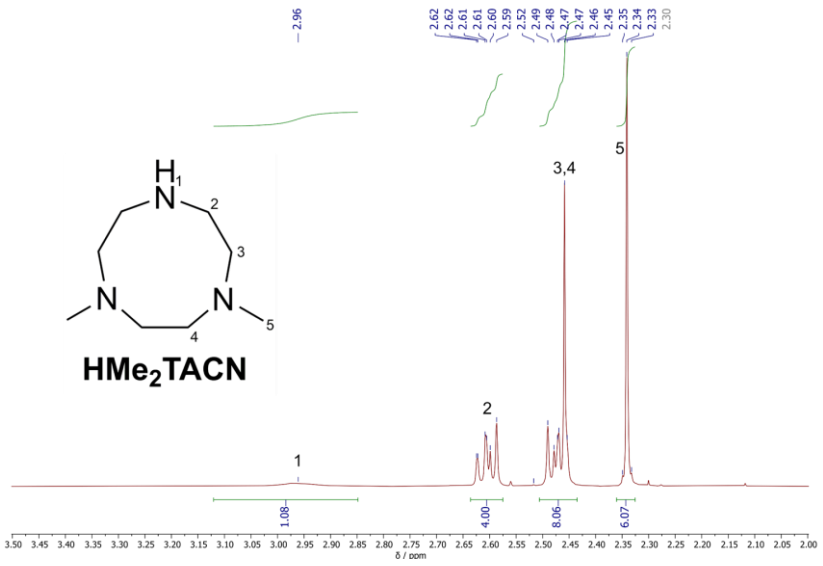

Figure 12: ^{1}H-NMR spectrum (300 MHz) of 1,4-dimethyl-1,4,7-triazacyclononane (HMe_2TACN) **8** measure in deuterated chloroform at room temperature.

Regarding the synthesis of the TACN unit, it must be mentioned that also newer TACN-synthesis concepts are available like the synthesis route of DENAT *et al.*, which was refined by GROS and HASSERODT, or the TACN synthesis according to SCARBOROUGH *et al.*.[140–142] These syntheses were developed to avoid the drawbacks of the classical RICHMAN-ATKINS route. These disadvantages are long reaction times, the need for tosyl protection groups for preorganisation which are not atom-economic and the harsh reaction conditions to get rid of these residues.[140] Considering the concept of green chemistry these newer synthetic procedures should be preferred, but those also have disadvantages.[143]

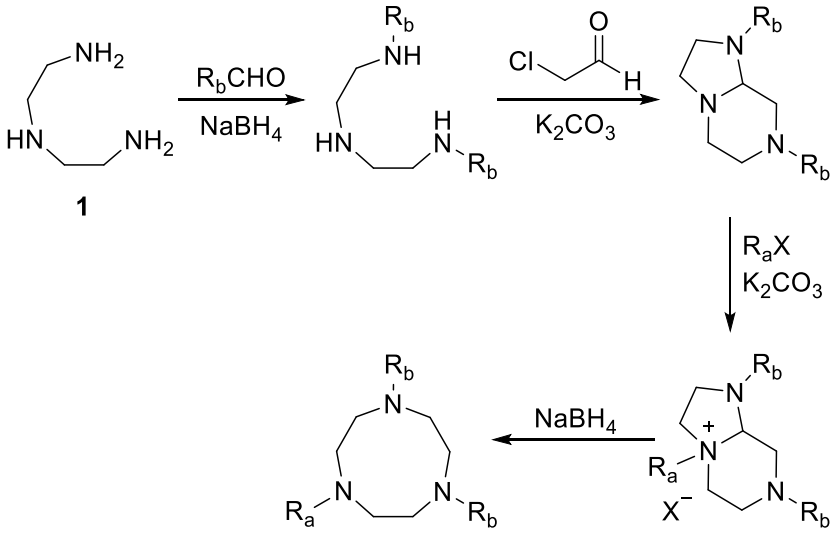

Scheme 6: Synthesis of a $2R_b/R_a$ N-functionalised TACN according to GROS and HASSERODT.[140,141]

Normally, these alternative syntheses introduce the two R_b side groups of the $R_a/2R_b$-substituted TACN in the first step of the synthesis, as shown in Scheme 6.[141] Therefore, the protection and deprotection procedure of the nitrogen atoms can be avoided. Unfortunately, high yields of the TACN product are only achieved for bulky substituents in the R_b positions.[141] Also, high amounts of dry solvents are needed for theses reactions. The reasons given above and the fact that these syntheses are not easily scalable lead to the conclusion that in this case the synthesis of 1,4-dimethyl-1,4,7-triazacyclononane **8** the RICHMAN-ATKINS synthesis should be preferred.

3.1.2 The pyrazole units

Depending on the length of the spacer between the pyrazole bridging unit and the side arms different synthetic approaches are needed. This chapter covers the syntheses of a symmetric and a non-symmetric pyrazole unit. Several suitable and also more complex pyrazole building blocks and their advantages and disadvantages for the synthesis of the corresponding ligand scaffold have been discussed in previous works.[32,38,65,126]

3.1.2.1 Symmetric pyrazole units

The synthesis of the symmetrical pyrazole is inspired by the published synthetic procedure of AKITA *et al.* and LANGER *et al.*.[144,145] Both symmetrical pyrazole units are based on the same key precursor 3,5-Bis(2-hydroxyethyl)-1*H*-pyrazole. This molecule **13** was synthesized and provided by the MEYER working group (Scheme 7).

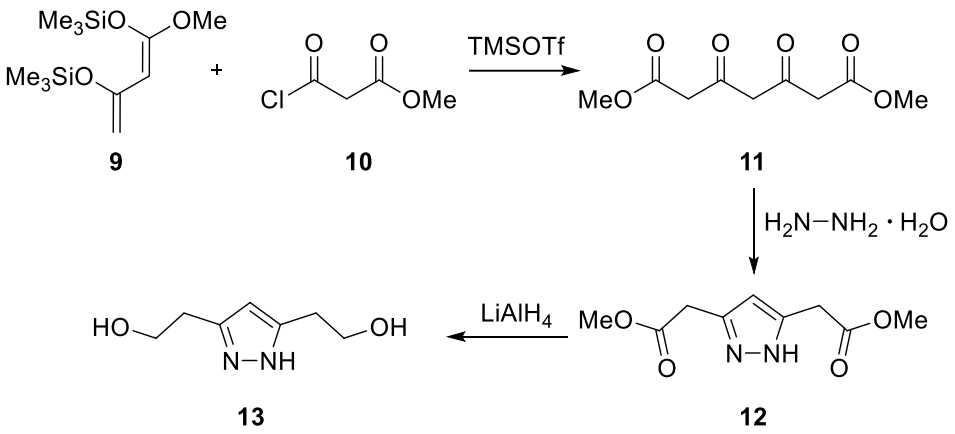

Scheme 7: Synthetic protocol for the formation of the precursor 3,5-Bis(2-hydroxylethyl)-1*H*-pyrazole **13** from 1-methoxy-1,3-bis(trimethylsilyloxy)-1,3-butadiene **9** and methyl malonyl chloride **10**.[144–146]

As in Scheme 7 depicted, 1-methoxy-1,3-bis(trimethylsilyloxy)-1,3-butadiene **9** and methyl malonyl chloride **10** were reacted with help of trimethylsilyl triflate which acts as a catalyst. To the resulting dimethyl dioxopimelate **11**, hydrazine hydrate was added to obtain 3,5-di(methoxycarbonylmethyl)pyrazole **12** via a cyclocondensation at the electrophilic keto groups. Subsequently, reduction with lithium aluminium hydride led to the required key precursor **13**.[144–146]

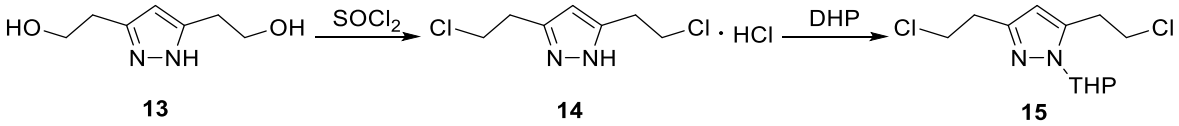

Scheme 8: Synthesis of the pyrazole bridging units 3,5-bis(2-chloroethyl)-1*H*-pyrazole hydrochloride **14** and 3,5-bis(2-chloroethyl)-1-(tetrahydro-2*H*-pyran-2-yl)-pyrazole **15** from the precursor **13**.[32,65,144,147]

In a second synthetic procedure the final two symmetrical pyrazole bridging units **14** and **15** were obtained (Scheme 8). The first unit **14** was synthesized with the chlorinating reagent thionyl chloride ($SOCl_2$). To avoid potential oligomerization of the free NH unit at the pyrazole, 3,4-dihydro-2*H*-pyran (DHP) was used as a protection group.[64] The resulting 2-tetrahydropyranyl group can be cleaved off with an ethanolic hydrochloric acid solution and allows to regain the unprotected pyrazole unit. The product 3,5-Bis(2-chloroethyl)-1-(tetrahydro-2*H*-pyran-2-yl)-pyrazole **15** as well as compound **14** are stable molecules and can therefore be stored easily under standard conditions. The products were successfully isolated and characterized by ^{1}H-, ^{13}C-NMR spectroscopy and ESI-mass spectrometry (for further information see chapter 8.2).

3.1.2.2 A non-symmetric pyrazole unit

The last chapter showed that the synthesis of the symmetric pyrazole unit via a 1,3-dicarbonyl compound is a multistep reaction which required special starting materials[148]. These two factors mean that this pyrazole synthesis is very time consuming, gives low yields and many different chemicals are required. This is a common disadvantage of pyrazole syntheses. Often harsh reaction conditions and transition-

metal catalysts are needed.[148,149] These drawbacks can be avoided if the structural pyrazole motif is synthesized via a Cope-type hydroamination of 1,3-dialkynes with hydrazine.[148]

The formation of 3,5-disubstituted pyrazoles from different substituted 1,3-butadiynes and hydrazine was studied by PAUDLER and ZEILER.[150] They found that it is possible to obtain 5-(2-hydroxyethyl)-3-(hydroxymethyl)-1*H*-pyrazole from 2,4-hexadiyne-1,6-diol and an aqueous hydrazine solution. Furthermore, BUCHLER used this [3 + 2] cycloaddition to gain access to an non-symmetric pyrazole bridging unit (Scheme 9).[151] This progress made it possible to synthesize the first non-symmetric *i*Pr$_2$TACN/pyrazolate ligand which allowed the tuning of the metal-metal-separation in the corresponding bimetallic complexes in comparison to the related symmetric complexes.[109] Later ACKERMANN used this non-symmetric ligand scaffold to produce the first non-symmetric dicopper-complex.[152] This work was later revived, extended and refined by SPYRA.[38]

The main advantages of this pyrazole synthesis are the instant access to the desired pyrazole unit via a metal catalyst free synthesis, high yields and mild reaction conditions. Additionally, the cycloaddition of diynes is a very atom-efficient transformation.[153]

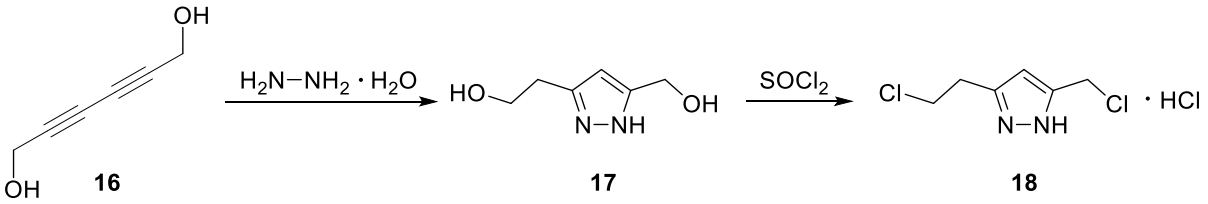

Scheme 9: Synthesis of the non-symmetrical pyrazole unit 5-(2-chloroethyl)-3-(chloromethyl)-1*H*-pyrazole hydrochloride **18**.[109,150,151]

The reagent 2,4-hexadiyne-1,6-diol **16** was purchased commercially. In general, these 1,3-butadiynes derivates can also be synthesized by a copper catalyzed oxidative homo-coupling of terminal alkynes.[148,154] 2,4-Hexadiyne-1,6-diol was reacted with hydrazine monohydrate in ethanol overnight, as shown in Scheme 9. Purification led to the isolation of 5-(2-hydroxyethyl)-3-(hydroxymethyl)-1*H*-pyrazole **17** as a brown oil. It must be mentioned that the successful synthesis and the yield of **17** depend highly on the degree of purity of the educt **16**.[38] The product **18** was obtained as a colorless solid by chlorination with thionyl chlorid. 5-(2-chloroethyl)-3-(chloromethyl)-1*H*-pyrazole hydrochloride **18** was stored under inert conditions at −26 °C and was characterized by ^{1}H-, ^{13}C-NMR spectroscopy and ESI-mass spectrometry (for further information see chapter 8.2.2.4). To avoid decomposition and due to the hygroscopic nature of compound **18** the non-symmetrical pyrazole unit was used directly for the synthesis of the ligand scaffold.

BUCHLER *et al.* also described that the pyrazole unit **18** can be protected with 3,4-dihydro-2*H*-pyran.[109] This protection procedure could not be reproduced in this work, but it turned out that this additional step was not necessary for the successful synthesis of the non-symmetrical Me$_2$TACN/pyrazolate compartmental ligand which will be discussed in chapter 3.2.2.

3.2 Ligand synthesis

3.2.1 A novel symmetric Me_2TACN/pyrazolate ligand scaffold

In previous studies the synthesis of pure and clean symmetrical methylated TACN/pyrazolate hybrid ligands with an ethyl-spacer was not successful. However, these works provided important insights into the coupling reaction.[32,126] The standard procedure of KINDERMANN was used and adapted to synthesize the new ligand scaffold, as depicted in Scheme 10.[65]

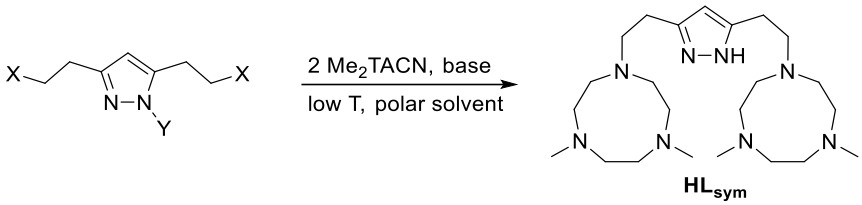

Scheme 10: Adapted synthetic procedure for the formation of the symmetric Me_2TACN/pyrazolate hybrid ligand **HL_{sym}** according to KINDERMANN.[32,65]

First and foremost, it is important to realize that even though the molecular structure of the Me_2TACN/pyrazolate ligands **HL_{sym}** is almost similar to the related *i*Pr_2TACN/pyrazolate ligand, the synthesis is more complicated and challenging. Firstly, it was shown that more and higher amounts of side products are formed and therefore the yields are much lower. Typically, elimination products, monosubstituted side products and even dimerization products were found. The most common side products are depicted in Figure 13. Secondly, the optimization of the leaving group in this nucleophilic substitution and the protection of the pyrazole led to higher yields.[32] The synthetic effort to obtain this specialized pyrazole unit, like 3,5-Bis(2-*p*-tosylethyl)-1-(methoxymethyl)-pyrazole, is very high and the yield of the synthesis of this substituted pyrazole is low. These two factors meant that a larger scale synthesis of this molecule was not reasonable. Thirdly, higher basicity of the used base resulted in higher amounts of elimination products without higher yields of the target molecule. Fourthly, higher reaction temperature led also to higher percentage of the elimination vinyl products.[65] In contrast, lower temperature during the reaction led to higher amounts of monosubstituted side products. Fifthly, protection of the NH-unit of the pyrazole building unit prevented dimerization via the nucleophilic attacks of another pyrazole.[65,155]

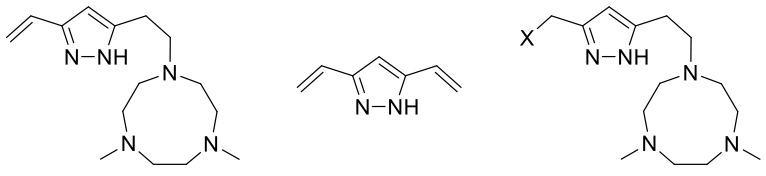

Figure 13: Overview of the common side products in this coupling reaction.

Considering these preliminary results, an optimized synthesis was needed to form the ligand scaffold in substantial amounts. Therefore, 3,5-Bis(2-chloroethyl)-1-(tetrahydro-2*H*-pyran-2-yl)-pyrazole **15** was

reacted with two equivalents of 1,4-dimethyl-1,4,7-triazacyclononane **8** under basic conditions in acetonitrile, as depicted in Scheme 11.

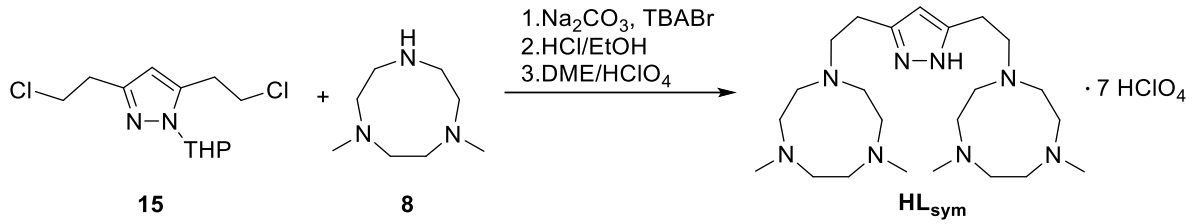

Scheme 11: Synthesis of the new symmetric Me_2TACN/pyrazolate hybrid ligand with 3,5-Bis(2-chloroethyl)-1-(tetrahydro-2*H*-pyran-2-yl)-pyrazole **15**.

Sodium carbonate (Na_2CO_3) was used as a base and tetrabutylammonium bromide (TBABr) was added in catalytic amounts to enable the *in-situ* exchange to the bromide which is a better leaving group in comparison to the chloride residue. In a second step, the protection group was removed under acidic conditions. Subsequently, the resulting product was precipitated with perchloric acid in 1,2-dimethoxyethan (DME). This procedure will be explained and discussed later in this chapter. This synthesis strategy was chosen because of the expected favorable product to side product ratio and reasonable yields of the desired $\mathbf{HL_{sym}}$.

As mentioned, previous studies suggested to avoid high temperatures during the reaction and recommended to keep the temperature lower than 40 °C.[65] Despite this, different reaction temperatures from 30 °C to 60 °C were tested to find the optimal temperature for this conversion. Furthermore, the reaction time was varied from four to nine days. These extraordinary long reaction durations were chosen to compensate for the lower reaction temperatures and to reduce the formation of monosubstituted side products. It must also be taken into account that longer reaction times at low temperatures can lead to higher yields of the elimination products. Two different strategies were tested to prevent this problem. On the one hand, the stoichiometric ratio of 1,4-dimethyl-1,4,7-triazacyclononane **8** was raised stepwise from 2.0 to 2.3 equivalents to counteract the excessive formation of monosubstituted side products. On the other hand, it was tested to add the pyrazole building block dropwise during the reaction to an excess of **8** to avoid the formation of elimination products. Unfortunately, in both cases significant quantities of side products were still found after the reactions. Additionally, the stoichiometric excess of **8** could not be fully regained by vacuum distillation after the reaction. The easy decomposition of **8** under theses reaction condition explains this finding. Since reagent **8** is a valuable asset, because of its time consuming and expensive synthesis, this synthesis strategy of $\mathbf{HL_{sym}}$ was avoided eventually.

For the experiments concerning the optimal reaction temperature, it was found that higher reaction temperatures gave a better product to side products ratio and increased the overall yield. Interestingly, higher reaction temperatures did not lead to higher amounts of elimination products, as reported previously.[65] This observation coincides with recent and similar experiments concerning the synthesis of the related *i*Pr_2TACN/pyrazolate ligand scaffold.[38]

The set of experiments regarding the optimization of the reaction duration showed that even at very long reaction times still significant amounts of side products, especially monosubstituted side product, were found in the ^{1}H-NMR spectra after purification and were also detected by ESI-MS spectroscopy. Therefore, it can be reasonably concluded that long reaction times just prolong the already long synthesis procedure without solving the underlining problems of this synthesis.

Another factor to consider is the role of NH-protection at the pyrazole unit in this reaction. The tetrahydropyranylation was performed because previous studies had observed dimerization of unprotected pyrazole units.[65] Scheme 12 shows the dimerization of two pyrazole units with a methyl spacer in the backbone, such as 3,5-bis(chlormethyl)-1*H*-pyrazole. Furthermore, it was reported that protection of the NH-group could make a purification of the protected ligand via column chromatography possible.[156]

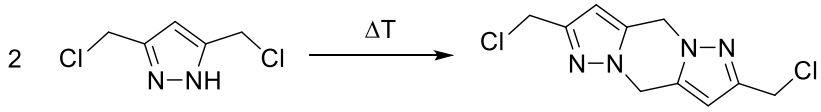

Scheme 12: Dimerization of the pyrazole unit 3,5-bis(chlormethyl)-1*H*-pyrazole.[156]

This result could not be replicated for the protected TACN/pyrazolate hybrid ligands with the longer ethyl bridge in the backbone. Unfortunately, the screening of different absorbents and eluents combination for column chromatography were also not successful. Moreover, the dimerization was never observed if instead of the protected pyrazole unit **15** the unprotected reagent 3,5-bis(2-chloroethyl)-1*H*-pyrazole hydrochloride **14** was used in the ligand synthesis. This can be explained by two effects. First, if the pyrazole unit **14** nucleophilic attacks another pyrazole molecule **14** the resulting dimer will feature an eight-membered ring. The ring strain energy of this eight-membered heterocycle would be much higher in comparison to the ring strain of the six-membered ring formed in case of the mentioned dimerization of two molecules of 3,5-bis(chlormethyl)-1*H*-pyrazole. Higher ring strain energies should adversely affect the formation of the dimer. Second, the pyrazole unit **14** is less reactive in comparison to 3,5-bis(chlormethyl)-1*H*-pyrazole since the chloride atoms are not in the allylic position of the heterocycle. Consequently, the dimerization of **14** is not favored and therefore the proposed advantages of the protection groups are not relevant in this case.

Taken all these results and insights into account, several conclusions can be made. On the one hand, longer reaction times at moderate temperatures are not the most efficient way to synthesize the new ligand scaffolds. On the other hand, higher temperature during the reaction led to better yields of the target molecule $\mathbf{HL_{sym}}$ without higher amounts of elimination side products. In addition, dimerization of the pyrazole unit seems to be not a problem and therefore as already implied in the last paragraph a simpler synthesis was used and optimized. 3,5-Bis(2-chloroethyl)-1*H*-pyrazole hydrochloride **14** was reacted under basic conditions with two equivalents of 1,4-dimethyl-1,4,7-triazacyclononane **8** in acetonitrile at 100 °C, as shown in Scheme 13. Additionally, tetrabutylammonium bromide was added in catalytic amounts.

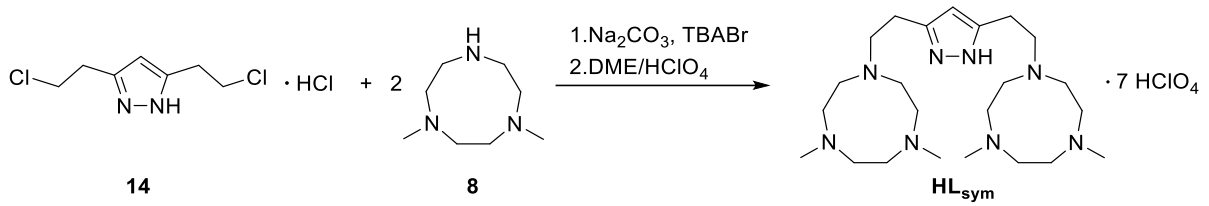

Scheme 13: Synthesis of the new symmetric Me_2TACN/pyrazolate hybrid ligand with 3,5-Bis(2-chloroethyl)-1*H*-pyrazole hydrochloride **14**.

The high reaction temperature was chosen to avoid the excessive formation of the monosubstituted side product and to reduce the prolonged reaction durations of the first synthesis. Interestingly, analytics of the obtained product mixture showed that the amount of elimination products did not rise in comparison to the experiments at lower temperatures, such as 40 °C or 60 °C. Additionally, it was observed that still traces of the monosubstituted side product can be found in the sample. These two findings are in good agreement with the product analysis of the parent symmetric *i*Pr_2TACN/pyrazolate ligand synthesis. Here, the ligand scaffold was also never obtained in analytically pure form and all attempts to purify the reaction mixtures by column chromatography failed.[38]

Purification of the reaction mixture is a major challenge for nearly all the TACN/pyrazolate hybrid ligand syntheses. The exception are syntheses where a pyrazole acyl chloride building block is available. In these cases, the higher reactivity of the acyl chloride led to a more favorable product to side product ratio and higher purity. It was even shown that it is possible to crystallize the resulting amide intermediate.[104,121]

Since column chromatography of **HL_{sym}** is not an option, different strategies to purify the ligand were tested. Normally, the best purification strategy is the crystallization of the ligand. Therefore, the ligand was deprotonated with sodium *tert*-butoxide (NaO^tBu) in propionitrile to afford the corresponding sodium salt NaL_{sym}, following the reported procedure of DALLE.[104] Different solvents combinations (acetone, acetonitrile or propionitrile with diethyl ether) and crystallization techniques (slow vapour evaporation and diffusion layering) were tested at room temperature. Crystalline material was not obtained in theses attempts. Probably, the purity of the starting material was not sufficient to form crystals. It is well-known from literature that various TACN/pyrazolate hybrid ligands and even the corresponding copper complexes only crystallize if the purity of the starting material is very high.[38,65,104,121]

Consequently, precipitation was tested as a purification method for the ligand **HL_{sym}**.[38,65] Therefore, the crude product **HL_{sym}** was dissolved in 1,2-dimethoxyethane and concentrated perchloric acid was added dropwise as an aqueous solution to the mixture until the forming colorless precipitate started to dissolve again. Subsequently, a 1:1 mixture of ethanol and diethyl ether was added to the flask and the reaction mixture was stirred for an hour. The formed solid was separated and the solvent mixture was discarded. The addition of ethanol to the solid and stirring of the mixture for two days led to an orange solid and an off-white powder. The solvent was carefully decanted, substituted by fresh ethanol and the reaction mixture was stirred again for one day. This process was repeated until the orange solid was

completely dissolved. Finally, the product was obtained as an off-white powder. For further and more detailed information about this procedure see chapter 8.2.3.1.

This purification procedure led to a high purity of the product **HL$_{sym}$**. However, the following points should be noted: If too much or too little perchloric acid was added the resulting yields would be significantly lower and even more important the purity of the product would be compromised. Furthermore, at least four cycles of stirring the product in fresh ethanol are required to obtain the product in good quality. Additional purification cycles with ethanol did not lead to significantly higher purity of **HL$_{sym}$**. The product quality was improved by stirring the off-white powder in diethyl ether for one day after the purification cycles with ethanol. Lastly, the use of larger volumes of concentrated perchloric acid should be avoided, because of the hazardous properties of concentrated perchloric acid. Especially, the formation of unstable perchlorates which are shock sensitive, can be a major concern.[157]

Employing the discussed methods led to the successful synthesis and subsequent isolation of **HL$_{sym}$**.

3.2.2 A novel non-symmetric Me$_2$TACN/pyrazolate ligand scaffold

The synthesis of the non-symmetric ligand scaffold **HL$_{asym}$** is based on the work of BUCHLER *et al.*. Combining their insights with the synthetic procedures established by KINDERMANN led to a new synthesis approach for non-symmetric TACN/pyrazolate ligands.

The non-symmetric Me$_2$TACN/pyrazolate compartmental ligand was synthesized as depicted in Scheme 14. Therefore, 5-(2-chloroethyl)-3-(chloromethyl)-1*H*-pyrazole hydrochloride **18** was reacted with 2.2 equivalents of 1,4-dimethyl-1,4,7-triazacyclononane **8** in acetonitrile under basic conditions at 100 °C. Tetrabutylammonium bromide was added in catalytic amounts to facilitate the nucleophilic substitution. This synthesis was implemented and refined in a close cooperation with SPYRA, who used a similar synthetic procedure to gain access to an non-symmetric *i*Pr$_2$TACN/pyrazolate ligand.[38]

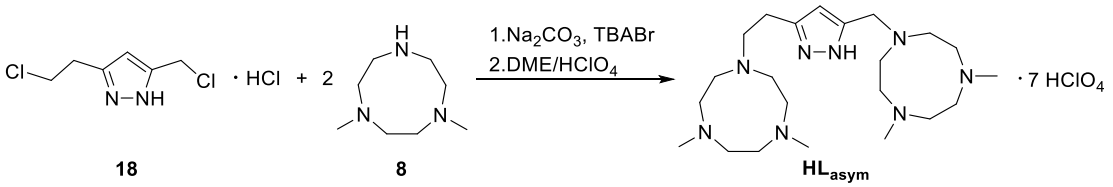

Scheme 14: Synthesis of the new non-symmetric Me$_2$TACN/pyrazolate hybrid ligand with 5-(2-chloroethyl)-3-(chloromethyl)-1*H*-pyrazole hydrochloride **18**.

In comparison to the previously discussed syntheses, the formation of side products is reduced by the fact that in the non-symmetric pyrazole unit **18** has only one ethyl chloride residue instead of two. Also, the nucleophilic substitution at the methyl chloride side is much faster and more efficient in the allylic position to the heterocycle and therefore higher yields of the desired product were expected. Initial ^{1}H-NMR analysis of the reaction mixture showed that the possible dimerization product, as shown in Scheme 15, did not form. The dimerization product can only form if the methyl chloride residue is

available However, due to the high reaction temperature of 100 °C, the stoichiometric excess of 1,4-dimethyl-1,4,7-triazacyclononane **8** and the fast nucleophilic substitution the methyl chloride site reacts immediately with the TACN unit. The resulting monosubstituted pyrazole intermediate cannot form the dimerization product because it only features the ethyl chloride residue which can react in the next step with another equivalent of HMe_2TACN.

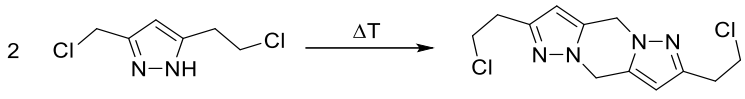

Scheme 15: Dimerization of the pyrazole unit 5-(2-chloroethyl)-3-(chloromethyl)-1*H*-pyrazole **18**.

Even though, the typical side products like the monosubstituted or the monosubstituted elimination product can still be found in the reaction mixture, the quantity of theses impurities are much lower in contrast with the amounts found in the syntheses discussed in chapter 3.2.1..

As a result of all these factors the product to side product ratio is more favorable and therefore the desired non-symmetric Me_2TACN/pyrazolate ligand can be obtained in higher yields and purity. Especially the latter enables an easier and shortened workup of the reaction. The purification process developed for $\mathbf{HL_{sym}}$ was adapted and used for $\mathbf{HL_{asym}}$. The points made in the last chapter concerning the purification of $\mathbf{HL_{sym}}$ apply also for the ligand scaffold $\mathbf{HL_{asym}}$. However, it needs to be emphasized that the precise precipitation with concentrated perchloric acid is the crucial step for achieving a pure product. For further and detailed information see Chapter 8.2.3.3. The product was obtained as a colorless powder.

Previous works showed that higher purity of the TACN/pyrazolate compartmental ligands helped to successfully form and crystallize the corresponding dicopper complexes.[38,64,65,111,124] Based on this observation, additionally great efforts were put into the crystallization of the ligand scaffold $\mathbf{HL_{asym}}$ to further improve the purity of the products, even though ^{1}H-NMR and ESI-MS analysis showed that the precipitated ligand was already of high and sufficient purity. Therefore, a previously reported procedure by DALLE was adjusted and used.[104] The ligand was dissolved in methanol, one equivalent of ammonium tetrafluoroborate was added and the reaction mixture was stirred for an hour. After workup, the protonated ligand was dissolved in acetonitrile and slow vapour crystallization was carried out with diethyl ether as precipitant.[105] Similar experiments were conducted for the symmetric ligand scaffold $\mathbf{HL_{sym}}$. Unfortunately, crystalline material of the expected protonated ligand scaffold $\mathbf{[H_3L_{asym}](BF_4)_2}$ or even $\mathbf{[H_3L_{sym}](BF_4)_2}$ could not be isolated.

3.3 Summary and conclusion

A new series of TACN/pyrazolate ligands with lower steric hindrance were introduced and successfully isolated despite a wide array of possible side products. This was achieved by employing a scaled up multistep HMe_2TACN synthesis, which is based on the RICHMAN-ATKINS route, and a coupling via a nucleophilic substitution of the TACN and pyrazole subunits. The synthesized molecules were mainly characterized by ^{1}H-NMR. An overview and summary of all involved reaction is depicted in Scheme 16.

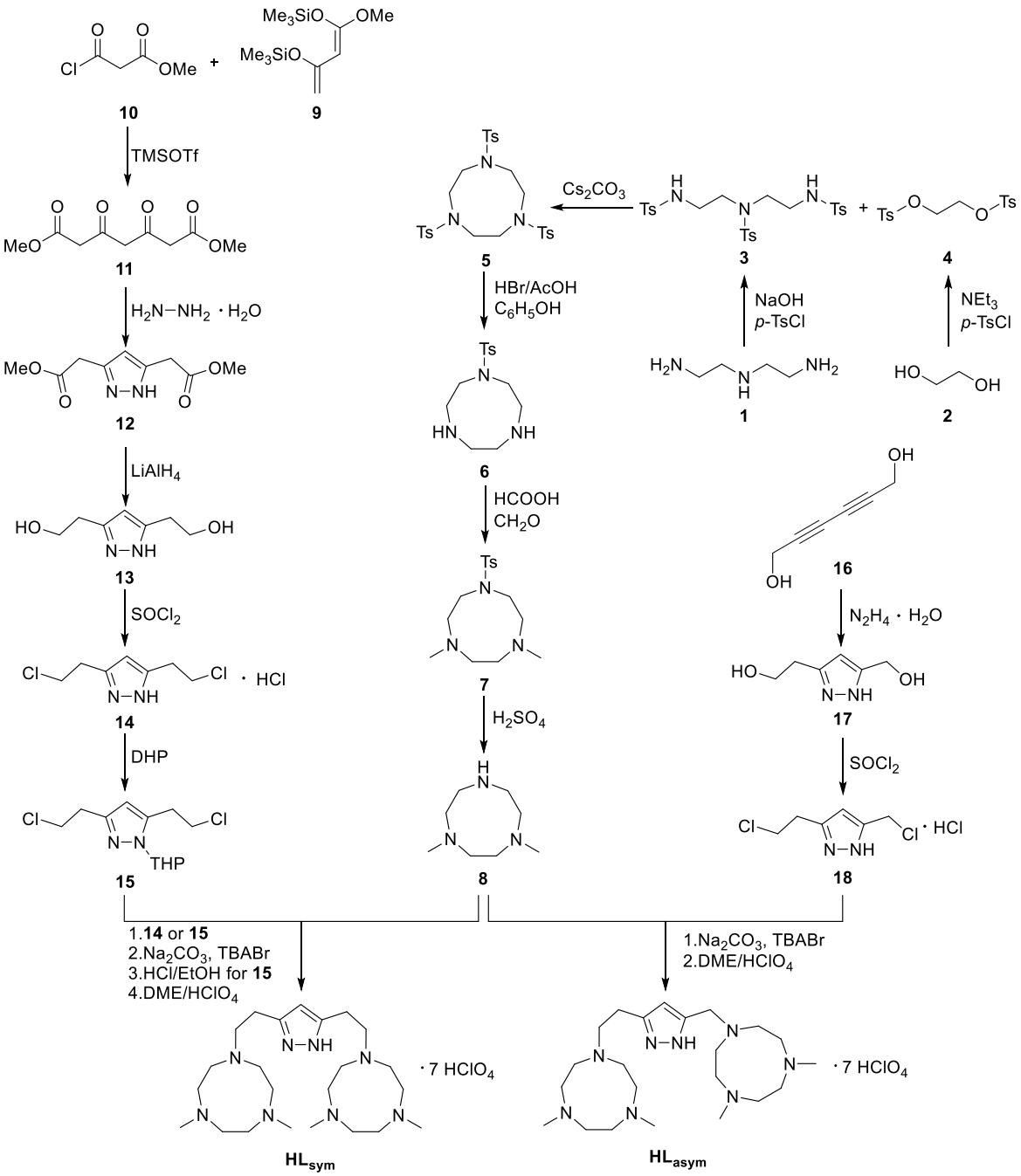

Scheme 16: Overview of the syntheses of the novel Me_2TACN/pyrazolate hybrid ligands.

The previously reported finding that higher reaction temperatures lead to higher amounts of elimination products in the coupling reaction, could not be confirmed and reproduced.[65] Instead, higher reaction temperatures led to increased yields of the target molecules, reduced the amount of side products and helped to achieve faster reaction times. These findings are in good agreement with recently published results of SPYRA.[38] These data suggest that this trend is independent of the functionalization of the TACN subunit. In summary, it can be stated that optimization of the reaction conditions to higher reaction temperatures and an excess of HMe_2TACN lead to a more favorable product distribution.

Additionally, a refined purification procedure for this class of ligand scaffolds was developed to reduce the occurring impurities. The purification by precipitation with perchloric acid in DME is the key step for the successful isolation of $\mathbf{HL_{sym}}$ and $\mathbf{HL_{asym}}$.

In comparison to the related and well-investigated symmetric and non-symmetric *i*Pr_2TACN/pyrazolate ligand scaffolds the syntheses of the ligands presented in this work are more challenging. The major reasons are the higher amounts of side products, complicated purification and isolation of the target molecules. Consequently, the applied reaction condition had to be set and monitored carefully.

The here presented syntheses are impressive examples that even slight modification of a well-known ligand scaffold can change the whole approach of synthesizing and purification of a ligand.

In conclusion the exiting series of TACN/pyrazolate compartment ligands could be extended by $\mathbf{HL_{sym}}$ and $\mathbf{HL_{asym}}$. This achievement allows to study the steric influences of the functionalized TACN in the resulting copper complexes which will be presented in the next chapters.

4 Copper Complexes and reactive dioxygen adducts

4.1 Formation of a symmetric peroxo dicopper(II) complex

4.1.1 A symmetric dicopper(I) complex

In previous works on TACN/pyrazolate compartmental ligands the formation of the corresponding peroxo dicopper(II) complexes are achieved by a two-step synthesis.[38,65,104,121] It is also reported, that the successful isolation and crystallization of the subsequent copper-dioxygen adducts is highly dependent on the success of the initial dicopper(I) complex synthesis and crystallization.[64,111,112,122,124,125] The procedures described in these reports are adapted for **HL$_{sym}$** and the reactions are formulated and proposed, as depicted in Scheme 17. This reaction scheme is plausible because of the structural similarities of the ligand scaffold to the already established *i*Pr$_2$TACN/pyrazolate ligands of KINDERMANN and SPYRA.[38,65]

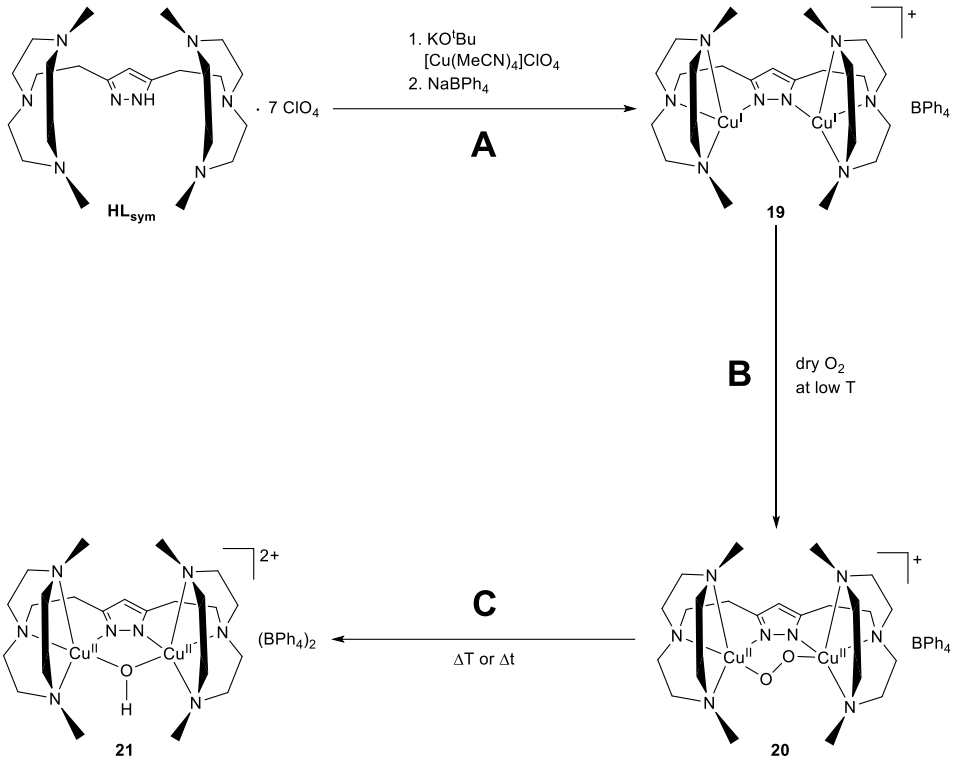

Scheme 17: Proposed two-step synthesis of the peroxo dicopper(II) complexes **20** (**A**+**B**) and subsequent decomposition to the μ-hydroxo dicopper(II) complexes **21** (**C**).[38,65,104,121]

The proposed process consists of three reactions **A**-**C**. First, the dicopper(I) complex is formed under inert conditions. In a subsequent reaction **B**, dried oxygen is added to the copper(I) complex to obtain the expected μ-1,2-peroxo dicopper(II) complex. If this intermediate is not used for further reactions, such as the synthesis of a superoxo or hydroperoxo dicopper(II) complex, the peroxo dicopper(II) complex will decompose in a third step **C** to the μ-hydroxo dicopper(II) complex.

Based on this assumed reaction scheme, the synthesis and the crystallization of the dicopper(I) complex **19** were targeted, as shown in step **A** in Scheme 17. Therefore, **HL$_{sym}$** was deprotonated with an excess

of the strong and non-nucleophilic base potassium *tert*-butoxide in dry methanol. Additionally, two equivalents of tetrakis(acetonitrile)copper(I) perchlorate were added, as a Cu^{I}-source under inert conditions. The precipitate potassium perchlorate was filtered out, discarded and a pale-yellow solution was obtained. Then, the precipitation of the reaction mixture with sodium tetraphenylborate yielded a colorless solid which is the crude dicopper(I) complex **19**. The product was redissolved in dry acetone and crystallization was attempted by slow vapor diffusion of dry diethyl ether into the solution at low temperatures under inert condition.

Unfortunately, no crystalline material could be obtained but interestingly blue-colored oil droplets formed in most cases after few days under inert conditions. The color change could be traced back to the formation of the μ-hydroxo dicopper(II) complex **21** which has a blue color. This was confirmed by ESI-MS analysis of the formed oil. According to Scheme 17, the formation of the decomposition product **21** could be explained for example by traces of oxygen in the solution which led to the formation and subsequent decomposition of **20**. Since the impurities come most likely from the used solvents, the solvents were again thoroughly dried, degassed by the freeze-pump-thaw method and the water content was checked by KARL-FISCHER titration.[158] Moreover, freshly prepared tetrakis(acetonitrile)copper(I) perchlorate and a new batch of potassium *tert*-butoxide were used.[159] However, the formation of the decomposition product **21** could still be observed even though the work was conducted under strict inert conditions inside a glove box. Furthermore, the crystallization conditions were varied in terms of temperature, solvents (acetonitrile, propionitrile and acetone) and especially the amount of the precipitant. In addition, different copper(I) salts were screened, such as $[Cu(MeCN)_4][PF_6]$, $[Cu(MeCN)_4][BF_4]$ or $[Cu(MeCN)_4][OTf]$. Even though, the dicopper(I) complexes could not be successfully isolated and purified by crystallization. The reaction mechanism for the formation of the hydroxo dicopper(II) complex **21** remains unclear. It seems likely that impurities such as traces of water or oxygen are involved in the degradation process.

Previous works on the related *i*Pr_2TACN/pyrazolate ligand scaffolds never encountered such problems. This suggest that the dicopper(I) species of the Me_2TACN/pyrazolate ligand may be more reactive.[38,65] Since reactivity and stability are often at odds with each other, these preliminary findings point in the direction of higher reactivity and possibly a more open core structure with low steric hinderance in comparison to the related dicopper(I) species.

Moreover, these empirical results imply that the desired synthetic access to the important peroxo dicopper(II)-complex **20**, as shown in Scheme 17, is completely blocked. A clean synthesis of **20** is the key intermediate for the synthesis of other copper oxygen adducts and therefore essential for this work. In order to avoid the synthetic impasse, it was attempted to synthesize the peroxo dicopper(II)-complex **20** from the crude dicopper(I) complex **19**. However, the crude dicopper(I) complex was not sufficient for producing clean **20** after the addition of dry dioxygen. In general, this synthetic route should be avoided, since it could introduce a variety of potential impurities that would lead to a system that is difficult to

analyze in reactivity studies. An alternative synthesis that does not involve the formation of the **19** is required to gain access to the important key product **20**.

These new results are consistent with findings from previous works on the closely related Me_2TACN/pyrazolate system with methylene spacers in the backbone **IV**.[121,123] For that system, previous work has not succeed in isolating the dicopper(I) complex directly. Instead, a hexanuclear hydride copper(I) complex with an dimeric ligand structure can formed by chemical reduction of a formate-bridged dicopper(II) complex **IVd**.[78] For the discussed proligand $\mathbf{HL_{sym}}$, this type of formation of a Cu^I-species is unlikely to succeed. This is because the ethylene spacer in the ligand backbone prevents the formation of a dimer.

4.1.2 The recycling of the decomposition product

Since the crystallization of the dicopper(I) complex **19** was not achieved, an alternative synthesis route of the required peroxo dicopper(II) complex **20** was explored. This unconventional approach revolves around the decomposition product **21**. The remainder of this section motivates this approach from the existing literature.

Normally, the known decomposition products of the dicopper(II)-TACN/pyrazolate complexes, which are shown in Figure 14, are treated as a typical degradation product with limited use and are therefore discarded.[65] From the perspective of green chemistry, this represents a serious loss. The ligand itself as well as the corresponding copper complexes are produced at considerable cost, both in terms of resources and labor.[38,121]

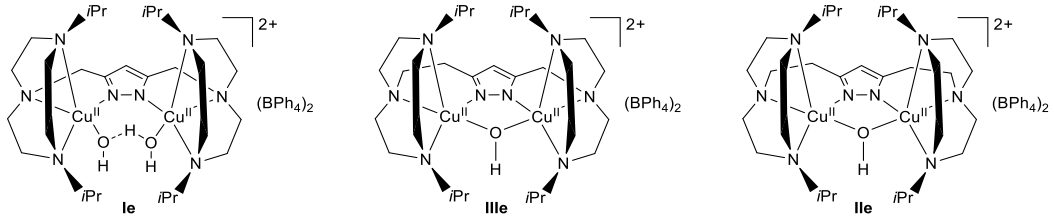

Figure 14: Structures of the known decomposition products of the corresponding peroxo dicopper(II)-TACN/pyrazolate complexes with different spacer length in the 3,5- position of the pyrazolate.[38,65,121]

In his work, BRINKMEIER describes an initial attempt to selectively recycle the decomposition product **Ie** which is depicted in Scheme 18.[121] First, cyclovoltammetry experiments of **Ie** showed a reductive wave at E = –1.1 V which corresponds to the reduction to the dicopper(I) complex **Ia**. This finding was directly confirmed in a subsequent UV/vis experiment. In this experiment, the decomposition product was chemically reduced with cobaltocene which has a reduction potential of E = –1.33 V vs. Fc/Fc^+.[160] The bleaching of the typical features of the decomposition product **Ie** were detected in the UV/vis spectrum.[121]

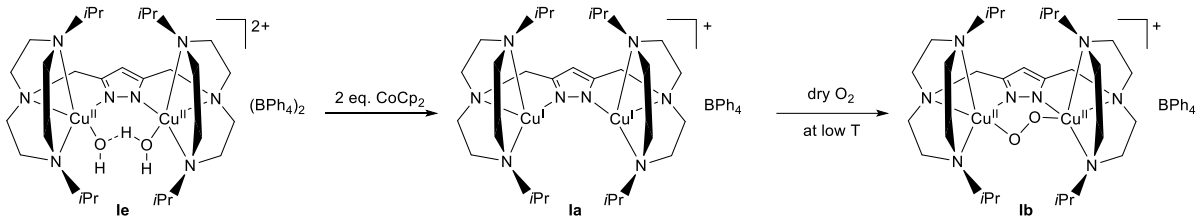

Scheme 18: Presumed reaction sequence of the reduction of the decomposition product of BRINKMEIER with subsequent reaction with dry oxygen at low temperatures to form the desired peroxo dicopper(II) complex **Ib**.[121]

In a second step, it was confirmed that the dicopper(I) complex **Ia** had formed and that the peroxo dicopper(II)complex **Ib** really could be partly regained. Therefore, dry oxygen was added to the presumed dicopper(I) complex **Ia** and the typical spectrum of the peroxo dicopper(II) complex **Ib** was observed.[121]

These promising results could not be transferred to the related hydroxo dicopper(II) complex **IIe** with elongated spacer in the backbone.[65] This was attributed to the fact that the binding pocket of **IIe** is much smaller and sterically hindered due to the ethylene spacers in the ligand backbone and the resulting shortened spacing of the copper ions.[65] Later, SPYRA *et. al.* was able to demonstrate in a similar experiment that the recycling of hydroxo dicopper(II) complex **IIIe** is possible.[38,161] In spite of this progress, only a *pseudo*-isosbestic point was observed. In addition, in both successful reduction cycles the expected concentrations of the peroxo dicopper(II) complex **Ib** and **IIIb** were lower than expected.[38,121,161] This could point into the direction of an unexpected formation of a side product or an initially incomplete reduction of the educt.

Based on these findings, a new synthesis strategy for the peroxo dicopper(II) complex **20** is proposed, as shown in Scheme 19.[38,65,121,161] Even though $\mathbf{HL_{sym}}$ has also ethylene spacers in the ligand backbone like **II**, it was assumed that the steric hinderance would be reduced and a reduction could be possible.

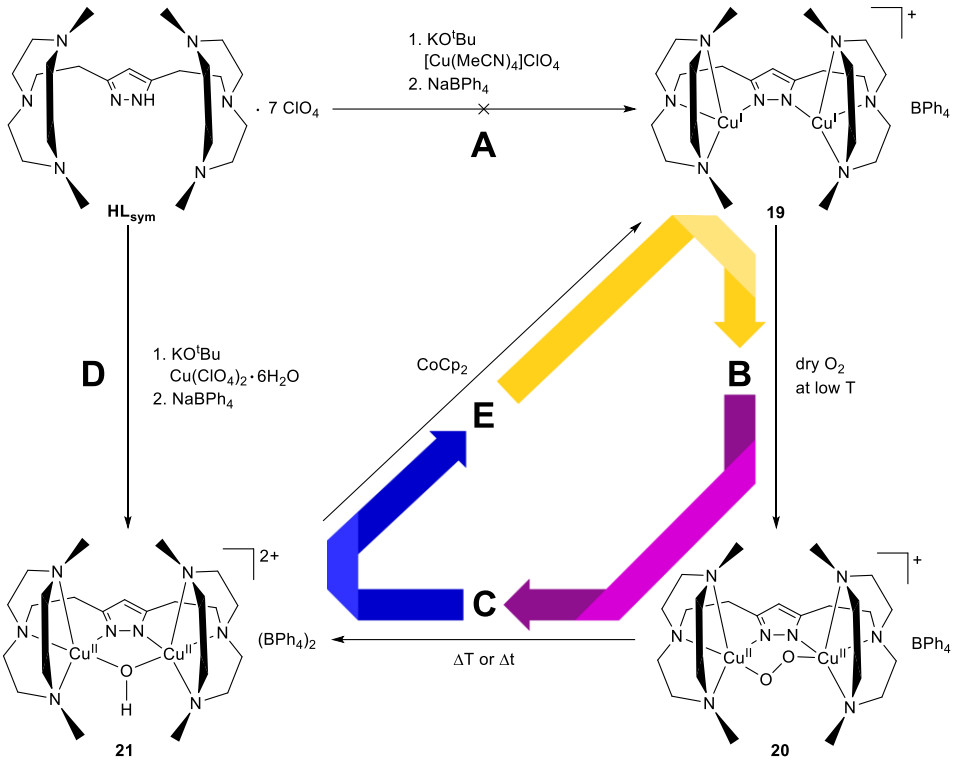

Scheme 19: Revised synthesis strategy for the peroxo dicopper(II) complex **20** which includes the recycling procedure of the former decomposition product, the hydroxo dicopper(II) complex **21**, by chemical reduction. The colors of the depicted arrows represent the expected color chances of the involved copper complexes. The most likely counterion were added for the sake of completeness for **19** and **20**.

This approach requires the successful isolation of μ-hydroxo dicopper complex **21** which then could be used to generate the corresponding dicopper(I) complex **19** *in-situ* (**E**). The reactive oxygen adduct **20** can be formed after addition of dry oxygen at low temperatures (**B**). Decomposition **C** to the hydroxo dicopper(II) complex **21** would close the recycling cycle. Initial UV/vis experiments with crude hydroxo dicopper(II) complex **21** demonstrated the feasibility of this route, but also showed that a clean educt is essential.

4.1.3 The symmetric μ-hydroxo dicopper(II) complex

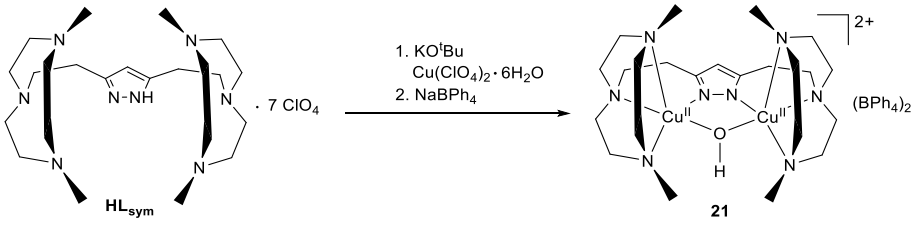

Scheme 20: Synthesis of the hydroxo dicopper(II) complex **21** of **HL$_{sym}$**.

For the synthesis of the μ-hydroxo dicopper(II) complex **21**, the proligand **HL$_{sym}$** was deprotonated with an excess of potassium *tert*-butoxide in methanol and two equivalents of copper(II) perchlorate hexahydrate were added under air. Precipitation with sodium tetraphenylborate gave the crude product **21**, as a

blue colored solid. Slow vapor diffusion of diethyl ether into a solution of **21** in propionitrile or acetonitrile resulted in an amorphous blue solid. Initial MS-ESI analyzes revealed that the collected solid contains many side products and by-products in addition to the desired product. The corresponding ESI mass spectrum in positive mode is depicted in Figure 15. The peak at *m*/*z* = 288.1 can be assigned to the doubly charged product, identified as $[L_{sym}Cu_2OH]^{2+}$. The corresponding isotopic pattern with simulation can be found in the appendix. The peak at *m*/*z* = 895.4 can be attributed to the product as $[L_{sym}Cu_2OH + BPh_4]^+$. It is probably because of the large number of side products that direct crystallization of **21** cannot be achieved.

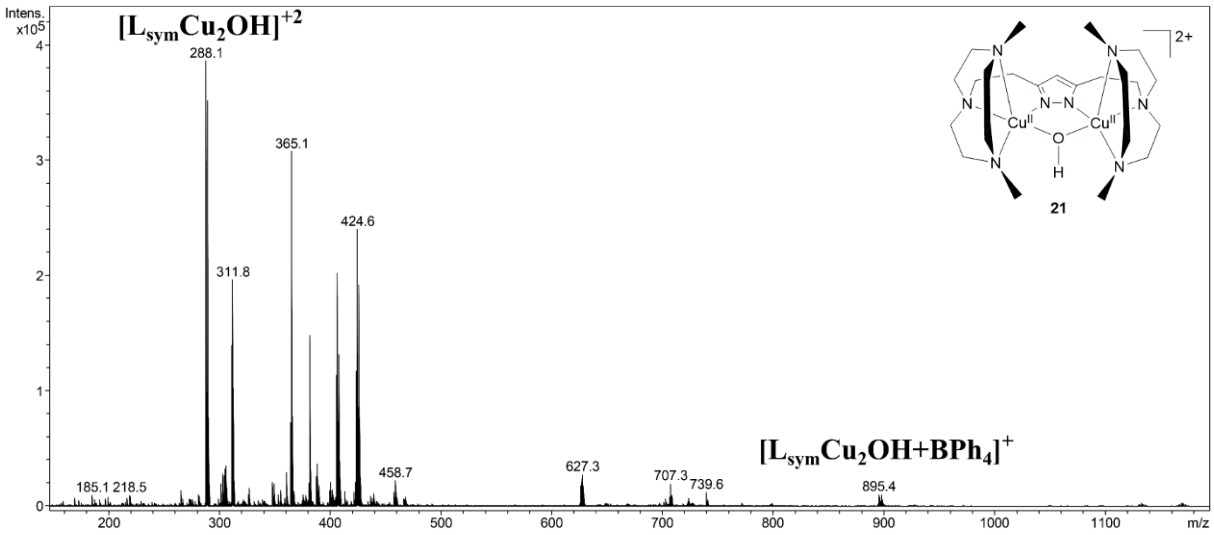

Figure 15: Initial MS-ESI spectra of the product mixture of the μ-hydroxo dicopper(II) complex **21** synthesis in MeCN. The measurement was performed by the central analytics department (IOBC, Georg-August-Universität Göttingen).

Therefore, an extended purification process by slow vapor diffusion crystallization was carried out that, with each iteration yielded a cleaner product. Scheme 21 shows the purification procedure. The conditions for the crystallization attempts were different for different steps. After each iteration, only the obtained amorphous blue solid was redissolved and used in the succeeding crystallization attempt. In general, three cycles of slow vapor diffusion were necessary to gain access to a cleaned product.

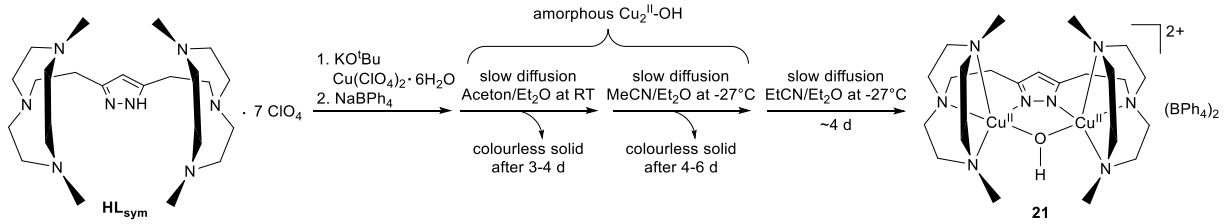

Scheme 21: Synthesis route of **21** and the subsequent purification process by slow vapor diffusion crystallization.

The ESI mass spectrum after the last cycle is shown in Figure 16. Compared to previous measurements, almost all peaks can be assigned to the target molecule **21** and essentially none of the previous impurities are present in the cleaned sample anymore. In addition to the peak at *m*/*z* = 288.1 ($[L_{sym}Cu_2OH]^{2+}$), also

the peak at *m*/*z* = 689.2 can be assigned to the hydroxo dicopper(II) complex **21**. In this case, it is a species that is formed in the mass spectrometer from the desired complex **21** and an impurity of trifluoroacetate in the device. Comparison of the recorded isotope pattern at *m*/*z* = 689.2 with the simulated isotope pattern confirms that the formed species can be denoted as $[L_{sym}Cu_2OH + CF_3CO_2]^+$. The peak labelled *m*/*z* = 897.4 belongs to the complex. In particular, this peak is part of the isotopic pattern of the peak at *m*/*z* = 895.4 and can be assigned to the complex with one additional counterion $[L_{sym}Cu_2OH + BPh_4]^+$. The corresponding isotopic patterns can be found in the appendix.

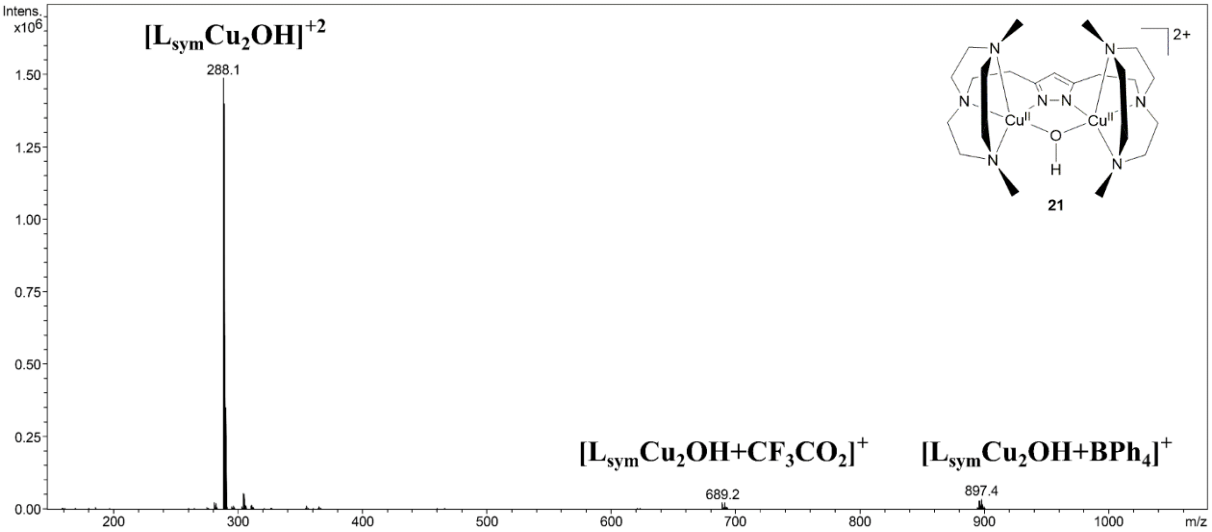

Figure 16: MS-ESI spectra of the μ-hydroxo dicopper(II) complex **21** after the cleaning procedure. The measurement was performed by the central analytics department (IOBC, Georg-August-Universität Göttingen).

A more detailed account of the cleaning procedures is given in chapter 8.3.2.1. The product that is obtained after the final iteration of the cleaning procedure can be crystalized by slow vapour diffusion crystallization. The fact that the successful crystallization depends on a thorough cleaning shows once again that the purity of the starting material for this class of molecules must be very high for them to crystallize at all. The collected single crystals of the hydroxo dicopper(II) complex **21** were suitable for an XRD experiment. The cationic part of the molecular structure is depicted in Figure 17.

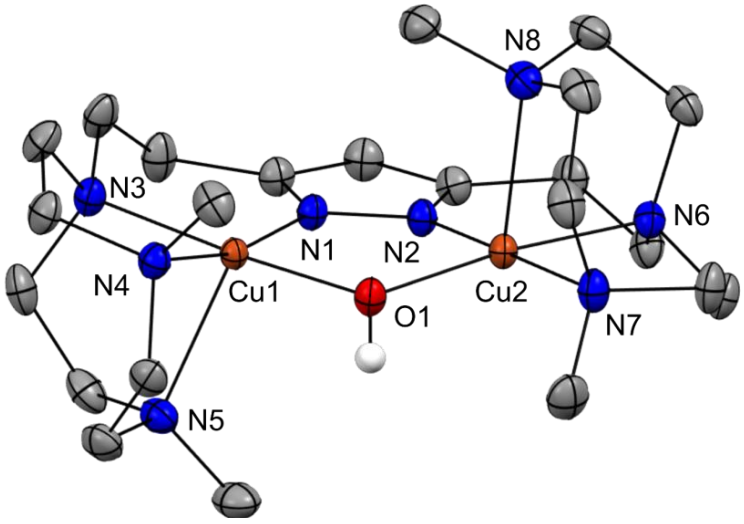

Figure 17: Molecular structure of the μ-hydroxo dicopper(II) complex **21** (thermal displacement ellipsoids given at 50 % probability). The two tetraphenylborate anions, propionitrile and the unnecessary hydrogen atoms are omitted for clarity. Selected bond length, distances and bond angles can be found in 8.1.10 and Table 1. Sample preparation and measurement was done by Dr. Sebastian Dechert (IAC, Georg-August-Universität Göttingen).

As expected, the solid state structure is similar to the closely related μ-hydroxo dicopper(II) complex **IIe** which is based on a *i*Pr$_2$TACN/pyrazolate ligand scaffold with ethylene spacer in the ligand backbone. There are also some significant differences due to the changed sterics. For example, the copper-to-copper ion distance of **21**, at 3.340 Å, is the shortest of any of the hydroxo dicopper complexes based on TACN/pyrazolate ligands. The Cu–O–Cu angle was determined to be 118.0 ° and is a less obtuse angle compared to **IIe**. The Cu–N bonds are longer to the TACN nitrogen donor atoms (2.05-2.27 Å) than to the pyrazolate nitrogen atoms (1.94-1.95 Å). One of the Cu–N$_{TACN}$ bonds is elongated (2.23-2.27 Å) due to the JAHN-TELLER effect.[162] In addition, the Cu–O bonds are elongated compared to **IIe**. This finding and the Cu–O–Cu angle have a great influence on the magnetic properties of **21**. Important bond length and distances are summarized in Table 1.

Table 1: Selected bond length and distances for **21** and **IIe**.[65]

bond/distance	21	IIe
Cu1-O1	1.947 Å	1.933 Å
Cu2-O2	1.951 Å	1.933 Å
Cu1-N1	1.952 Å	1.949 Å
Cu1-N3	2.054 Å	2.039 Å
Cu1-N4	2.087 Å	2.094 Å
Cu1-N5	2.233 Å	2.330 Å
Cu···Cu	3.340 Å	3.405 Å

The coordination environment of the copper(II) cations of **21** can be described with the τ_5-parameter.[163,164] Both copper ions exhibited a slightly distorted square pyramidal geometry, since the calculated values are τ_5(Cu1) = 0.129 and τ_5(Cu2) = 0.063.

A comparison of the space-filling models of the molecular structures of **21** and **IIe** reveals the influences of the steric bulk attached to the TACN sidearms.

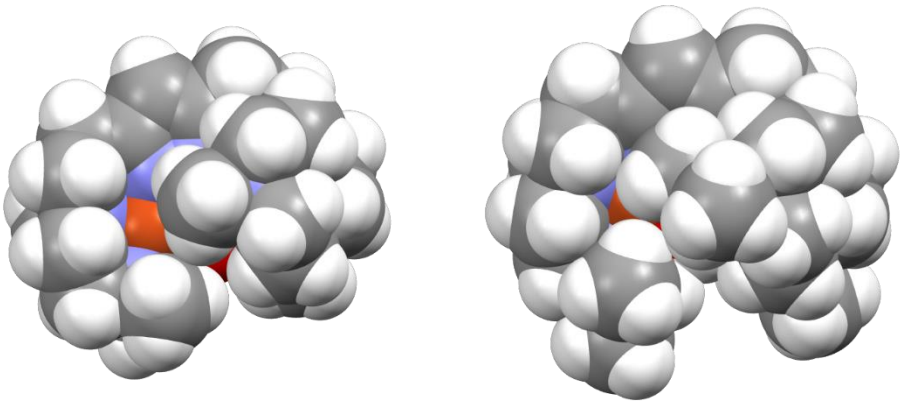

21 **IIe**

Figure 18: Top view of the space-filling models of the solid-state structures of the μ-hydroxo dicopper(II) complexes **21** and **IIe**. The atoms are color coded: white: hydrogen, grey: carbon, blue: nitrogen, red: oxygen and orange: copper.[65]

As depicted in Figure 18, the top view on the two molecules shows that the bimetallic cleft is deshielded for the μ-hydroxo dicopper(II) complex **21** compared to **IIe**. The Me_2TACN/pyrazolate ligand is not big enough to completely encapsulate the dicopper(II) core. This could be a clue as to why the corresponding dicopper(I) complex could not be isolated. If the dicopper(I) complex has a similar structure to **21** the reactive dicopper(I) core would be unprotected and a potential decomposition reaction could occur easily. In particular, the bottom view of the molecules in Figure 19 reveals the naked dimetallic core of **21**. A drawback of these models is that they are based on the molecular structure of the solid and admit only very limited conclusions about the spatial structure in solution and even the structure of other oxidation states.

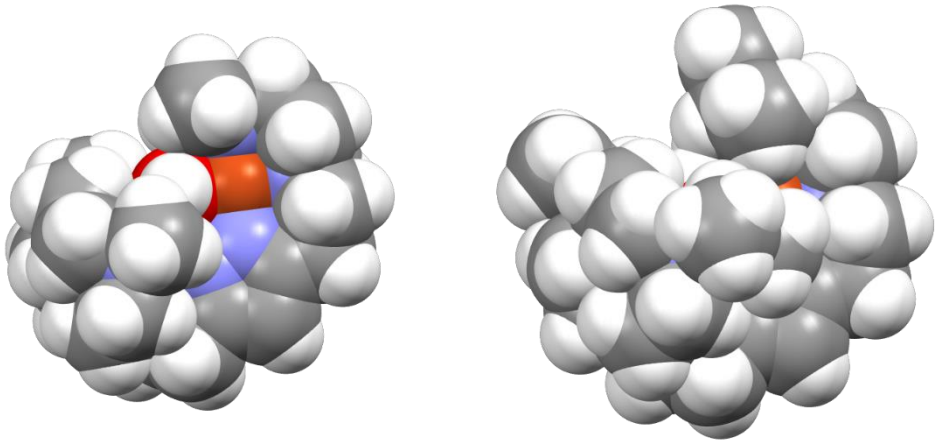

21 **IIe**

Figure 19: Bottom view of the space-filling models of the solid state structures of the μ-hydroxo dicopper(II) complexes **21** and **IIe**. The atoms are color coded: white: hydrogen, grey: carbon, blue: nitrogen, red: oxygen and orange: copper.[65]

In conclusion, the goal of opening the bimetallic center by employing the Me_2TACN/pyrazolate ligand was achieved. However, the molecular structure of the reactive oxygen adducts such as **20** would be more crucial for discussing the influence of the deshielding.

UV/vis absorbance spectroscopy of complex **21** (see Figure 20) shows two absorbances features at 353 nm ($\varepsilon \approx 3300$ M^{-1} cm^{-1}) and at 596 nm ($\varepsilon \approx 280$ M^{-1} cm^{-1}). The latter band can be assigned to a parity-forbidden d-d transition which explains the weak band.[65]

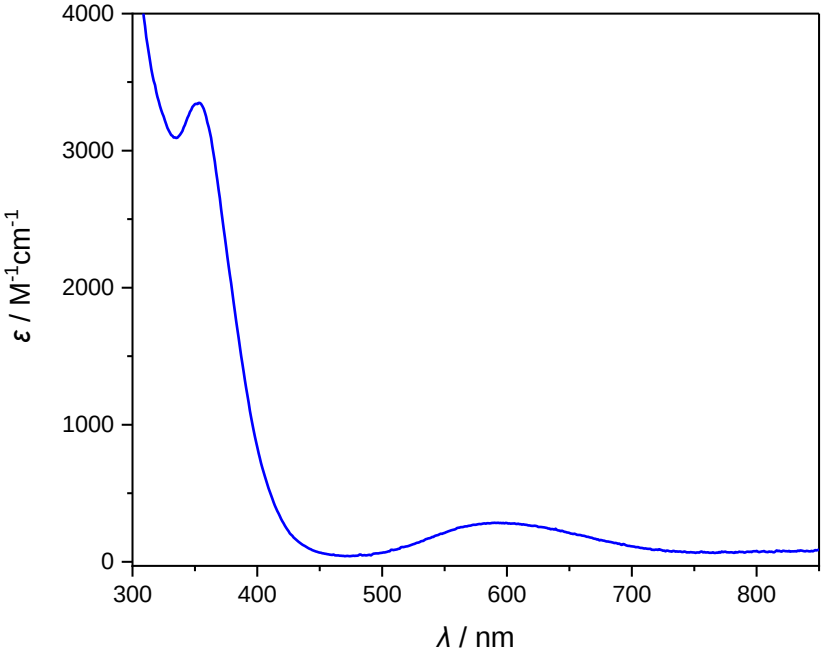

Figure 20: UV/vis spectrum of the μ-hydroxo dicopper(II) complex **21** in dry MeCN at 25 °C.

Similar absorbance features and extinction coefficients have been reported for the other μ-hydroxo dicopper(II) complexes.[38,65] As shown in Table 2, the comparison of the absorption bands reveals that the obtained UV/vis spectrum is similar to the data sets of the closely related derivatives.

Table 2: Comparison of the typical absorbance features of μ-hydroxo dicopper(II) complexes based on different TACN/pyrazolate ligand scaffolds.[38,65]

Complex	λ_1 / nm (ε / M^{-1} cm^{-1})	λ_2 / nm (ε / M^{-1} cm^{-1})
IIIe	374 (4500)	626 (240)
IIe	356 (3700)	613 (200)
21	353 (3300)	595 (280)

The magnetic properties of μ-hydroxo dicopper(II) complex **21** were investigated using a SQUID magnetometer. The measurement was performed with a microcrystalline powder sample of **21** at a magnetic field of $B = 0.5$ T and in the temperature range from 2 K to 300 K. In Figure 21 the obtained experimental data and the corresponding simulation using a HEISENBERG-DIRAC-VANVLECK Hamiltonian is depicted.

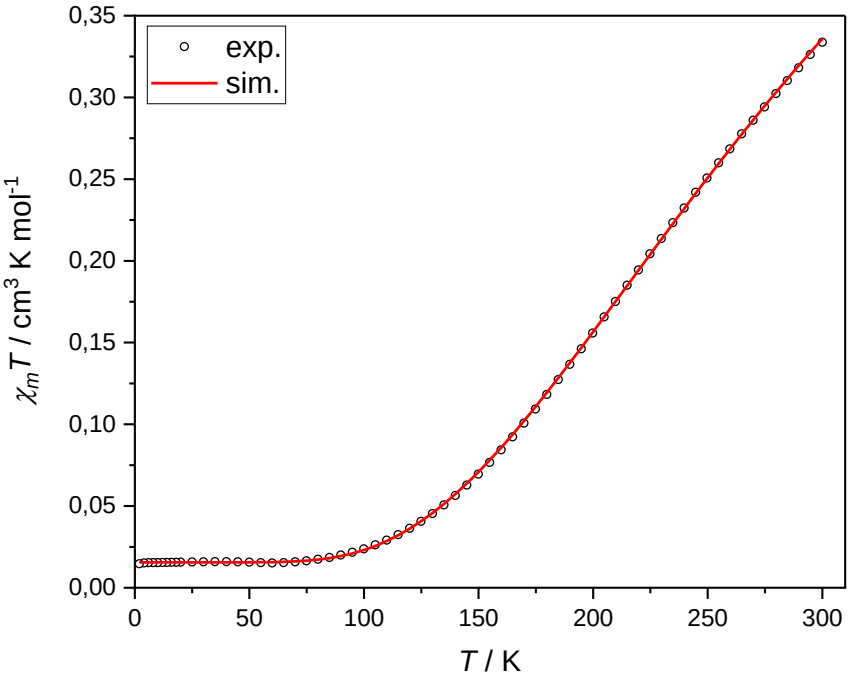

Figure 21: Magnetic susceptibility data of the μ-hydroxo dicopper(II) complex **21** from 2 K to 300 K at a magnetic field of 0.5 T (black) and the corresponding simulation (red). The following three parameters could be determined: J = –212.3 cm^{-1}, g = 2.179, PI = 4.1 %. Sample preparation and measurement was done by Dr. Serhiy Demeshko (IAC, Georg-August-Universität Göttingen).

The spectrum shows that the two copper(II) ions are strongly antiferromagnetically coupled and a coupling constant of J = –212.3 cm^{-1} was derived. Antiferromagnetic coupling is well-known and described for μ-hydroxo dicopper(II) complexes that features a pyrazolate bridging unit.[38,65,165] Typically, the coupling term for these compounds is influenced by three structural factors.[165] Firstly, the Cu–O–Cu angle has the largest influence. For Cu–O–Cu angles above 97.5° the antiferromagnetic coupling term dominates and increases further angles that are even larger.[65,165,166] Secondly, longer Cu–O distances lead to a larger antiferromagnetic term.[167] Thirdly, a larger displacement of the H-Atom out of the Cu_2OH plane results in a smaller coupling constant.[65,168] Since the Cu–O–Cu angle of **21** was determined as 118.0° the antiferromagnetic coupling was expected. In comparison to the closely related μ-hydroxo dicopper(II) complex **IIe**, the value of the coupling constants J is significantly higher.[65] This strong deviation was not expected, since these two compounds are structurally very similar and differ only slightly in the steric demand at the TACN side arms. However, the lower steric demand leads to changes in the geometry of the structure. In addition, μ-hydroxo dicopper(II) complex **21** features an out-of-plane displacement of the hydrogen atom of the hydroxide. This is expected to lead to a small J value. This result can also be explained by the elongated Cu–O bond compared to **IIe**.

Table 3: Comparison of the coupling constants and structural parameter of μ-hydroxo dicopper(II) complexes based on TACN/pyrazolate ligand scaffolds.[38,65]

Complex	J / cm^{-1}	Cu–O–Cu angle / °	Cu–O bond length / Å
IIIe	–293.9	121.8	1.97
IIe	–184	123.3	1.93
21	–212.3	118.0	1.95

In addition to the resource-intensive synthesis described above, another route was established to crystallize the μ-hydroxo dicopper(II) complex **21** in good yields. Previous works of BRINKMEIER and LÜCKEN demonstrates that the decomposition product based on a Me_2TACN/pyrazolate proligand with methylene spacers in the backbone can feature a bridging acetate **IVc** or formate **IVd**, as shown in Figure 22.[121,123]

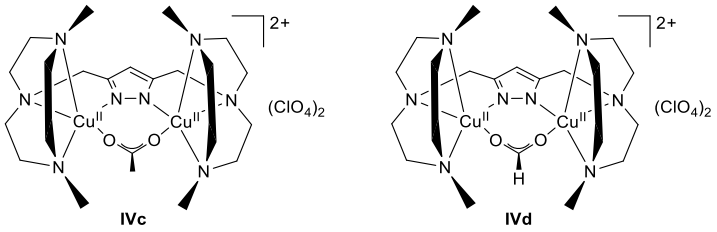

Figure 22: Dicopper(II) complexes based on a Me_2TACN/pyrazolate ligand featuring a acetate (**IVc**) or formate (**IVd**) molecule in the bimetallic cleft.[78,121,123]

Because of the congeneric molecular structure of **IV** and $\mathbf{HL_{sym}}$, it is reasonable to assume that a similar coordination pattern may also exists for a dicopper(II) complex based on $\mathbf{HL_{sym}}$. Consequently, the syntheses routes of LÜCKEN for **IVc** and **IVd** were adapted. They are partly depicted in Scheme 22.[123] The proligand $\mathbf{HL_{sym}}$ was first deprotonated with potassium *tert*-butoxide in methanol . Then, sodium acetate or sodium formate was added. Subsequent addition of copper(II) perchlorate hexahydrate led to blue colored reaction mixture. Complete dissolution was achieved by the addition of a few drops of distilled water. Crystalline material was gained by slow vapour diffusion of diethylether into the solution. XRD analysis revealed that, instead of the proposed acetate or formate adduct, the μ-hydroxo dicopper(II) complex was obtained as the perchlorate salt **21b** and **21c**. Slightly different crystal structures were obtained depending on the used additive. This is summarised in Scheme 22. Presumably, the small differences occur during crystal growth, are more solvent dependent and are not directly related to the additive. The additives sodium acetate and sodium formate promote the crystallization of the μ-hydroxo dicopper(II) complex and reduce the synthetic effort compared to the previously shown purification and crystallization cycle (Scheme 21).

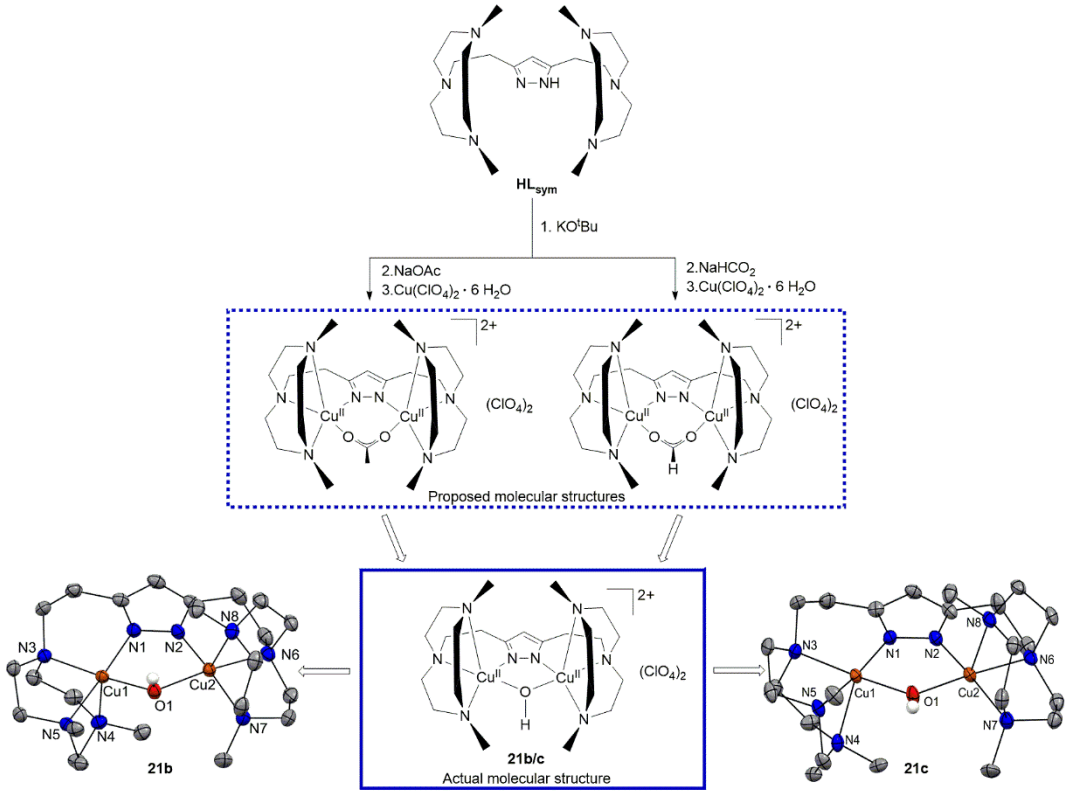

Scheme 22: Synthesis of μ-hydroxo dicopper(II) complex **21b** and **21c**. Selected bond length and bond angles of the molecular structures **21b** and **21c** can be found in 8.1.10. Sample preparations and XRD-measurements were performed by Dr. Sebastian Dechert (IAC, Georg-August-Universität Göttingen).

Since the isolation of the proposed adducts was not possible, these experiments demonstrate that a larger copper-to-copper ion distance is of primary importance rather than a more favorable steric demand on the TACN side arms for the isolation of the formate or acetate species. Considering the various related TACN/pyrazolate hybrid ligands, it is probably only possible to obtain the formates, acetates, or adducts with even larger space requirements, provided that the ligand backbone consists of methylene units, as in the case of **IV**. This raises the question of whether this assertion also holds for the non-symmetric proligand **HL$_{asym}$** which has at least one methylene unit. In Chapter 4.2.3 this claim will be further discussed and put to the test with **HL$_{asym}$**.

4.1.4 *In-situ* formation of a dicopper(I) complex

After the successful isolation and characterization of the dicopper(II) complex **21** and the corresponding perchlorate salts **21b/c** were achieved, it was possible to proceed with the first step of the revised synthetic strategy presented in Scheme 15. To this end, it was tested if it is possible to prepare the dicopper(I) complex **19** *in-situ* by chemical reduction of **21** with cobaltocene which was established as the ideal reductant in previous works.[38,121,123,161] Scheme 23 shows the reaction equation. Since the reaction features a significant color change, it was tracked with temperature-controlled UV/vis spectrometry.

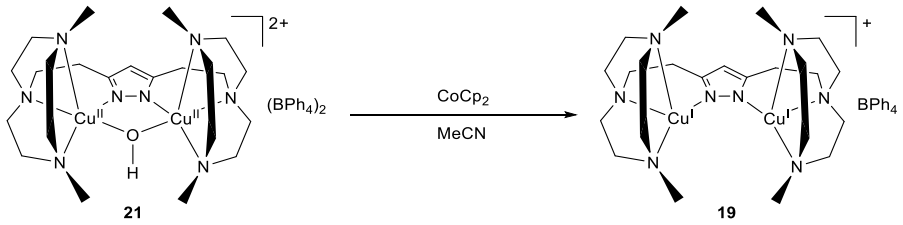

Scheme 23: Chemical reduction of the μ-hydroxo dicopper(II) complex **21** to the dicopper(I) complex **19** with $CoCp_2$ as the reductant in dry MeCN under UV/vis conditions. Since the specific counterion of **19** is not known, the most probable counterion was added to **19** for the sake of completeness and to maintain the charge neutrality of the reaction.

Initial investigations of this reaction revealed only minor and irrelevant changes in the UV/vis absorption spectrum. After gradual optimisation of the reaction conditions, the desired reaction was achieved. In particular, the quality of the dried solvent, the use of freshly sublimed cobaltocene and a reaction temperature of 25 °C were crucial for the successful conversion.

The UV/vis titration spectrum shows that the stepwise addition of the reductant leads to an incremental bleaching of the band at 596 nm (Figure 23). The vanishing of this d-d transition band is an important marker for the formation of the desired Cu^{I}-species. As shown in the bottom of Figure 23, the reduction is complete after the addition 2.2 eq. of cobaltocene. The deviation from the ideal value of 2.0 eq. is probably due to minor impurities in the sample and small experimental deviations. Depending on the experiment, this value was subject to slight fluctuations from 1.9 to 2.2 eq. Furthermore, the appearance of two isosbestic points at 538 nm and 384 nm is a clear indication that the reduction occurs without an intermediate. The corresponding absorbance traces run horizontally until the over titration at 2.4 eq. occurs. The appearance of the isosbestic points is also a good indicator of the quality of the used starting material.

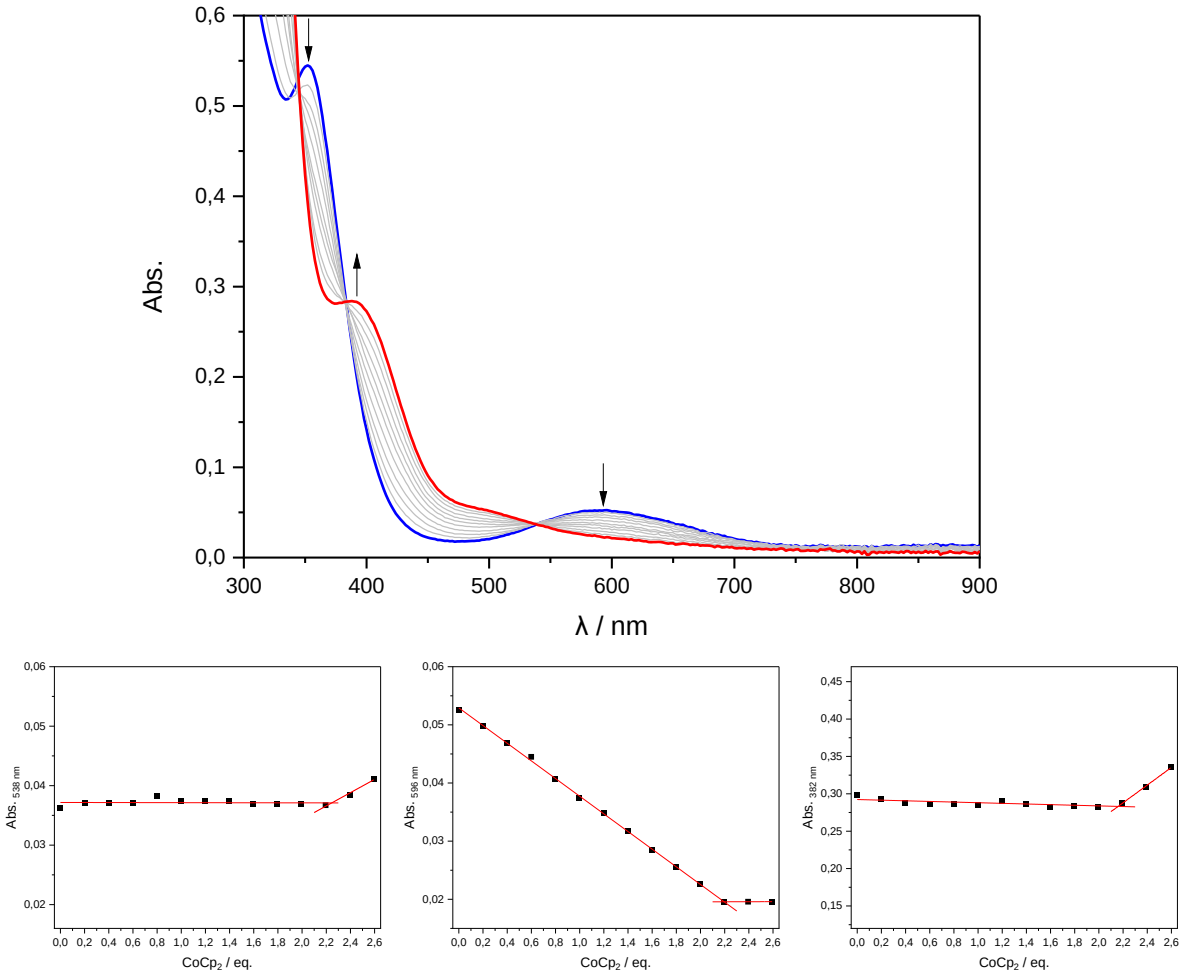

Figure 23: Top: UV/vis spectrum of the titration of the μ-hydroxo dicopper(II) complex **21** (blue) with 2.2 eq. $CoCp_2$ in dry MeCN at 25 °C under inert conditions. The recorded spectra form a *pseudo*-isosbestic point at 344 nm and two isosbestic points at 384 nm and 538 nm. Bottom: Traces of the above shown UV/vis titration with 2.6 eq. of cobaltocene in 0.2 eq. steps. Besides the traces of the two isosbestic points on the left and right side, the trace of the bleaching of the crucial d-d transition at 596 nm is shown in the middle.

The reaction of cobaltocene to cobaltocenium is also visible in the titration spectrum. The gradually rising band at 409 nm can be assigned to the cobaltocenium ion in the solution.[123,160] Since only aprotic polar solvents were used in these experiments, the typical precipitation of cobaltocenium salts in non-polar solvents did not occur. Furthermore, the removal of the resulting cobaltocenium from the solution under inert conditions via evaporation und subsequent extraction was unsuccessful.[160] This means that it cannot be completely ruled out that the $CoCp_2/CoCp_2^+$ redox couple influences the subsequent reactions.[169] However, no influences could be detected in the subsequent experiments. This was confirmed by comparative experiments with the already established TACN/pyrazolate systems **II** and **III**. Additionally, cobaltocenium is known to usually be an innocent reagent. In the literature only a few cases of interaction are reported.[160,170]

As discussed in Chapter 4.1.1, the dicopper(I) complex is very unstable and decomposes easily. In order to improve the lifetime of the reduced complex and to enable easier handling of the compound, the effects of adding an excess of cobaltocene to the complex were investigated under UV/vis conditions.

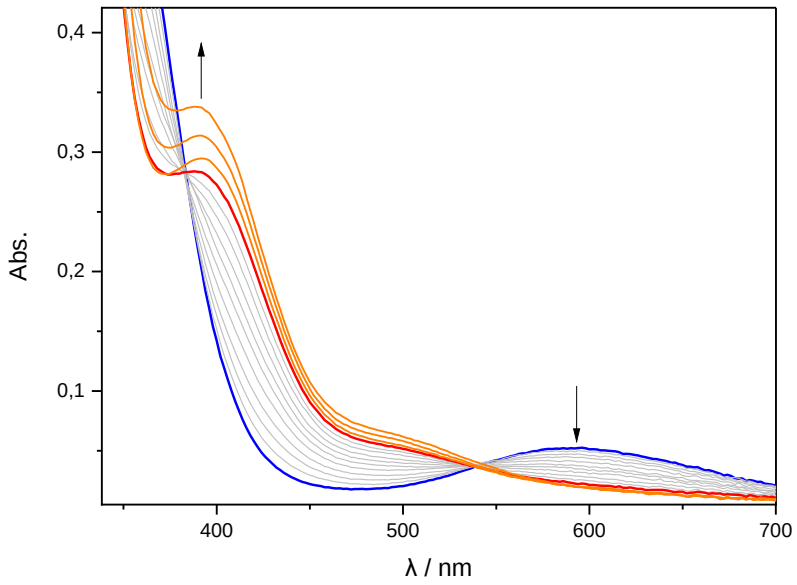

Figure 24: UV/vis spectrum of the overtitration of μ-hydroxo dicopper(II) complex **21** (blue) via the dicopper(I) complex **19** (red) with 2.8 eq. $CoCp_2$ in dry MeCN at 25 °C under inert conditions. $CoCp_2$ was added in 0.2 eq. increments. The spectra caused by the excess of $CoCp_2$ (2.4 eq, 2.6 eq. and 2.8 eq.) are shown in orange.

The resulting UV/vis absorption spectra shows that the isosbestic points are lost and the bands caused by the redox couple have accordingly a higher intensity. The excess of reducing agent ensures that the dicopper(I) complex is more stable. For example, if the compound reacted with traces of dioxygen in the solution, the dicopper(I) complex would be immediately formed again due to the excess of reductant. It turns out that even a small excess of cobaltocene (0.2 eq.) was sufficient for achieving a stable dicopper(I) complex **19** for extended time periods. Based on these results, several attempts were made to crystallize the copper(I) complex by adding 2.2 eq. of cobaltocene to **21** at room temperature. Excess cobaltocenium salts crystalized on top of the solution, but no crystalline material of **19** was isolated by slow vapour diffusion crystallization.^{1}H-NMR spectroscopy of the reduced species was inconclusive.

In general, the results reported here for the reductive formation of the dicopper(I) complex are in line with previous work.[38,121,161] The comparison of the UV/vis titration spectra shows that the spectra presented above - are characterized by their high quality. This is particularly evident in the appearance of the clear isosbestic points and underlines the importance of the purification cycle of the crystalline starting material. Without the cleaning procedures, the formation and stabilization of this reactive species would not be possible. This is how the problems with the reductive formation discussed in 4.1.2 were avoided.

Compared to the acetato dicopper(II) complex of the closely related Me_2TACN/pyrazolate system with methylene spacers in the backbone **IV**, a two-step reduction via a Cu^ICu^{II} species was not observed.[123] The hydroxo dicopper(II) complex **21** does not have the ability to stabilize the mixed-valent state upon reduction in the same manner as the dicopper(II) complex with an bridging acetate in the bimetallic cleft.

4.1.5 *In-situ* formation of a peroxo dicopper(II) complex

The successful reduction and temporary stabilization of the presumptive dicopper(I) complex **19** with a small excess of cobaltocene made it possible to test the reactivity towards dry oxygen at low temperatures. The copper(I) complex was generated from the hydroxo dicopper(II) complex **21** *in-situ* in dry acetonitrile at 25 °C under inert conditions and was immediately cooled to –40 °C. A pale yellow solution formed. Subsequently, dry oxygen was added in excess to the stirring solution. Simultaneously, the color of the reaction mixture changed to purple. The reaction was tracked with help of a temperature-controlled UV/vis absorption spectrometer.

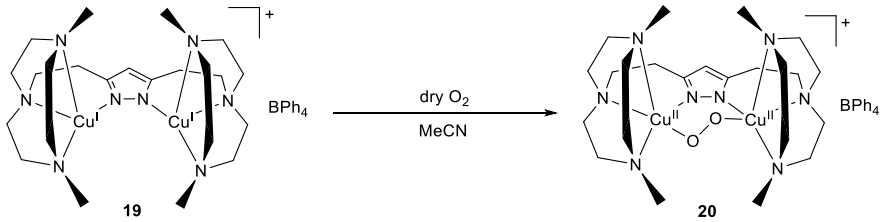

Scheme 24: Synthesis of the peroxo dicopper(II) complex **20** by addition of an excess of dry dioxygen to the dicopper(I) complex **19** at low temperatures in MeCN.

As depicted in Figure 25, exposure of the dicopper(I) complex solution (blue spectrum) to an atmosphere of molecular dioxygen immediately changes the spectrum (red spectrum).

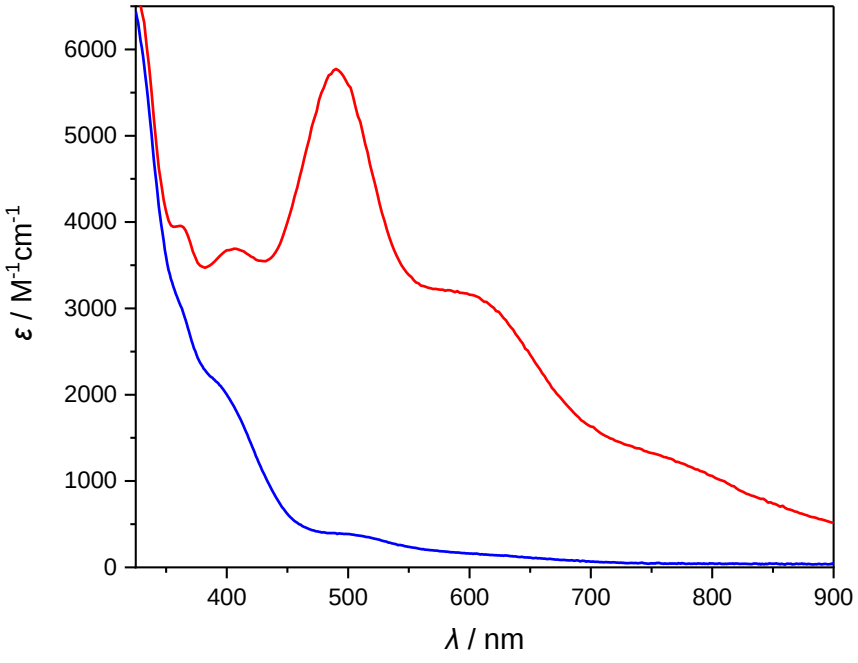

Figure 25: UV/vis spectrum of the *in-situ* produced dicopper(I) complex **19** (blue) in acetonitrile at 25 °C and the resulting peroxo dicopper(II) complex **20** of $\mathbf{L_{sym}}$ (red) after addition of dry oxygen gas at –40 °C.

A distinct new absorbance band forms at 490 nm ($\varepsilon \approx 5800$ M^{-1} cm^{-1}) and a pronounced shoulder at 595 nm ($\varepsilon \approx 3200$ M^{-1} cm^{-1}). These bands can be assigned to LMCT transitions ($O_2^{2-} \rightarrow Cu^{II}$). Similar absorbance features have been reported for all known peroxo dicopper(II) complexes of the TACN/pyrazolate series and are typical for μ-1,2-peroxo dicopper(II) complexes.[38,64,66,104,121] A comparison of

these typical absorbance bands shows that the obtained data fit well into the existing picture (Table 4). The collected data suggests that there is a shift to smaller wavelengths as the spacer length of the bridging unit increases and the steric demand of the side arms decreases.

Table 4: Comparison of the typical absorbance features of peroxo dicopper(II) complexes based on different TACN/pyrazolate ligand scaffolds.[38,65,121,123]

Complex	λ_1 / nm (ε / M^{-1} cm^{-1})	λ_2 / nm (ε / M^{-1} cm^{-1})
Ib	527 (5000)	648 (3900)
IVb	510	630
IIIb	520 (5500)	617 (3300)
IIb	506 (4800)	600 (2800)
20	490 (5800)	595 (3200)

Besides these distinctive bands, a broad shoulder formed at 755 nm ($\varepsilon \approx 1300$ M^{-1} cm^{-1}). This absorbance band has been observed in previous works only for μ-1,2-peroxo dicopper(II) complexes that have at least one ethylene spacer in the TACN/pyrazolate ligand scaffold.[38,65] For example, KINDERMANN reported a similar band at 807 nm ($\varepsilon \approx 1500$ M^{-1} cm^{-1}) for **IIb**.[64,65] Thus, the shift of the band is also evident here.

The other absorbance features at around 407 nm and 360 nm can be assigned to the reducing agent which was used to form the starting material **19** *in-situ*. However, it cannot be excluded completely that there are overlaps with absorbance bands of the product or impurities within that wavelength range.

The temperature change from 25 °C to –40 °C during the UV/vis experiment is essential. The low temperature not only ensures that the presumed dicopper(I) complex **19** is decomposing more slowly. It also ensures that the actual oxygen adduct formation can be observed and studied. If it is not possible to achieve a sufficiently rapid temperature change, the discussed slight overtitration with the metallocene can help stabilize the dicopper(I) species for this time. Since an excess of molecular dioxygen is added to the gas phase of the UV/vis cuvette, the additional amount of reducing agent does not influence the reaction and is consumed immediately. It is likely that during this process, the peroxo dicopper(II) complex forms initially due to the excess of oxygen but is then immediately reduced again by the small excess of cobaltocene. As soon as the excess of reducing agent is consumed, the peroxo dicopper(II) complex can form. This process is so fast that it is barely visible in the time resolved UV/vis spectrum. However, this assumption was confirmed by addition of cobaltocene in excess to the established μ-1,2-peroxo dicopper(II) complex **IIb** and **IIIb** which allowed to regain the corresponding dicopper(I) species.

In conclusion, the μ-1,2-peroxo dicopper(II) complex **20** was successfully synthesized. This conclusion is backed up by the very similar spectroscopical features of the complex, the resulting characteristic purple color of the solution, as well as the reaction behavior of the peroxo dicopper(II) complex **20** in follow-up reactions. These reactions are described and discussed in chapter 4.3.

Further evidence for the successful synthesis of the μ-1,2-peroxo dicopper(II) complex **20** was obtained by Raman spectroscopy. The resonance Raman spectrum of **20** was recorded with laser excitation of 633 nm. This is the wavelength at which intensive absorption occurs. In preparation for this experiment, concentrated solutions of the dicopper(I) complex **19** in acetonitrile were prepared in YOUNG NMR tubes and exposed to either $^{16}O_2$ or the heaviest stable isotope of oxygen $^{18}O_2$ at –40 °C. The freshly prepared solutions were immediately frozen in liquid nitrogen and the resonance Raman spectrum was recorded. Additionally, a frozen solution of the solvent was measured to determine the solvent signals.

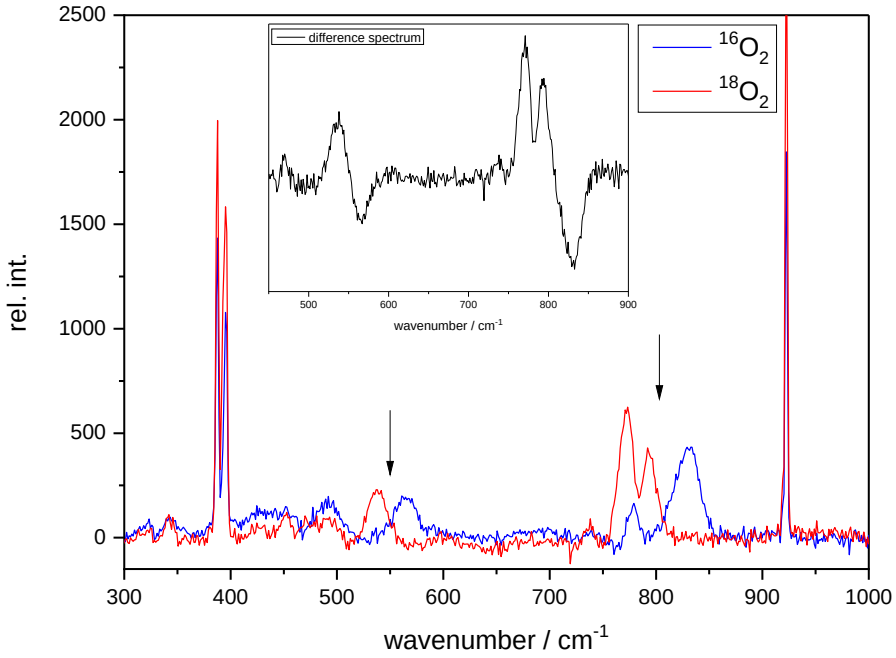

Figure 26: rR spectra for $^{16}O_2$ and $^{18}O_2$ labelled peroxo dicopper(II) complexes in frozen MeCN solution (λ_{ex} = 633 nm). The inset shows the difference spectrum. The measurement was done by Dr. Sebastian Dechert (IAC, Georg-August-Universität Göttingen).

As shown in Figure 26, two features at 829 cm^{-1} and 564 cm^{-1} shift to lower wavenumbers due to the isotopic labelling. The first can be assigned to the peroxide O-O stretch. The $^{16}O_2$ as well as the $^{18}O_2$ labelled spectrum show unexpected bands in this region which are most likely the result of FERMI resonances.[38] The peroxide O–O stretching band shifts from 829 cm^{-1} to 773 cm^{-1} ($\Delta^{16}O_2$–$^{18}O_2$ = 56 cm^{-1}). Therefore, $\tilde{\nu}(^{16}O–^{16}O)/\tilde{\nu}(^{18}O–^{18}O)$ is 1.072 and fits to the corresponding calculated value of 1.061 for the isolated harmonic dioxygen oscillator.[20,112] A very similar multiplet pattern has be observed in the resonance Raman spectrum for the congener **IIb** in propionitrile.[64,65] Furthermore, in this case the closely spaced peaks corresponding to the O–O stretch were attributed to the occurrence of FERMI resonances which have been reported for several μ-1,2-peroxo dicopper(II) complexes.[84,110,121,171] The oxygen isotope sensitive feature at 564 cm^{-1} shifts to 538 cm^{-1} ($\Delta^{16}O_2$–$^{18}O_2$ = 26 cm^{-1}) and probably originates from the Cu–O stretches. The spectroscopic features at 922 cm^{-1}, 396 cm^{-1} and 388 cm^{-1} can be assigned to the used solvent acetonitrile. These results are typical for a μ-1,2-peroxo dicopper(II) complexes and indicate that complex **20** was formed. A molecular structure would further support this claim but could not be obtained. This is because the *in-situ* formed peroxo dicopper(II) complex **20** decays rapidly.

4.1.6 Decomposition of the peroxo dicopper(II) complex

Most of the related μ-1,2-peroxo dicopper(II) complexes based on the TACN/pyrazolate compartmental ligands were stable in solution at lower temperatures and could even be crystallized at –27 °C.[38,65,104,121] Furthermore, the obtained crystalline materials were stable at room temperature and could be stored easily.[38] This is not the case for the peroxo dicopper(II) complexes of the Me_2TACN/pyrazolate type.[123] After the *in-situ* formation of the μ-1,2-peroxo dicopper(II) complex **20** in solution, a rapid decay of that species can be observed. The reaction leads to a color change of the solution from purple to blue. ESI mass spectrometry and UV/vis absorbance spectroscopy showed that the product of the decomposition is the μ-hydroxo dicopper(II) complex **21**, as depicted in Scheme 25.

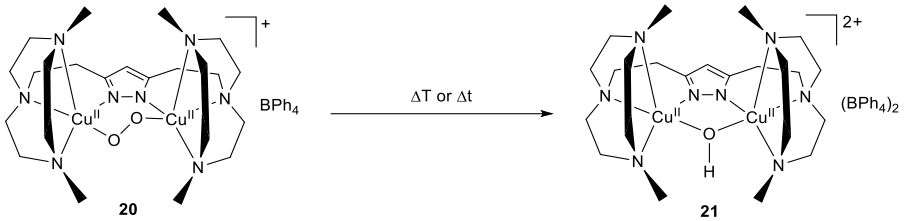

Scheme 25: Decomposition of the peroxo dicopper(II) complex **20** in MeCN yields the hydroxo dicopper(II) complex **21**.

A typical UV/vis absorbance spectrum for the decomposition was recorded to demonstrate the rapid decay at elevated temperature. As depicted in Figure 27, the characteristic absorbance features of the *in-situ* formed peroxo dicopper(II) complex **20** start to bleach immediately and the distinctive bands of the hydroxo dicopper(II) complex **21** are regained.

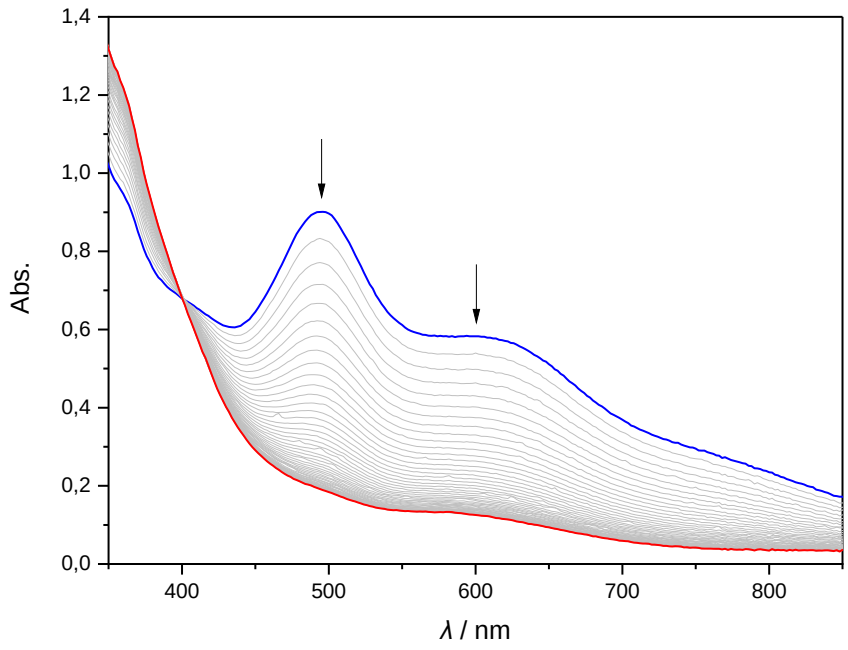

Figure 27: UV/vis absorbance spectra of the decomposition of the μ-1,2-peroxo dicopper(II) complex **20** (red) to the μ-hydroxo dicopper(II) complex **21** (blue) in dry MeCN at 20 °C. The spectrum features an isosbestic point at 400 nm.

Since this spectrum also features absorbance bands of cobaltocenium which was used to synthesize the dicopper(I) complex **19**, the final spectrum of the decomposition process is not identical to the UV/vis absorbance spectrum of the pure μ-hydroxo dicopper(II) complex **21** in acetonitrile. However, the characteristic absorption features of **21** are clearly recognizable as a weak band at 595 nm and a shoulder at 353 nm. The formation of an isosbestic point at 400 nm shows that the conversion proceeds without the occurrence of an intermediate.

Under theses reaction condition the decomposition is already completed after approximately 600 s. Assuming an exponential decay of a first-order reaction, the half-life time would be $t_{1/2}$ = 124 s. Further analysis of the bleaching of the absorbance feature at 490 nm reveals that the decomposition is a second-order chemical reaction since a plot of $1/A_{490\ nm}$ vs. t can be fitted linearly (Figure 28). According to the integrated rate equation for second-order reactions (Equation 1), the rate constant k can be calculated with help of the slope coefficient of the linear fit.[172] The derived value of the rate constant is $k = 9.94 \cdot 10^{-3}$ L·mmol^{-1}·s^{-1}.

$$\frac{1}{[A_0]} - kt = \frac{1}{[A]} \qquad \text{Equation 1}$$

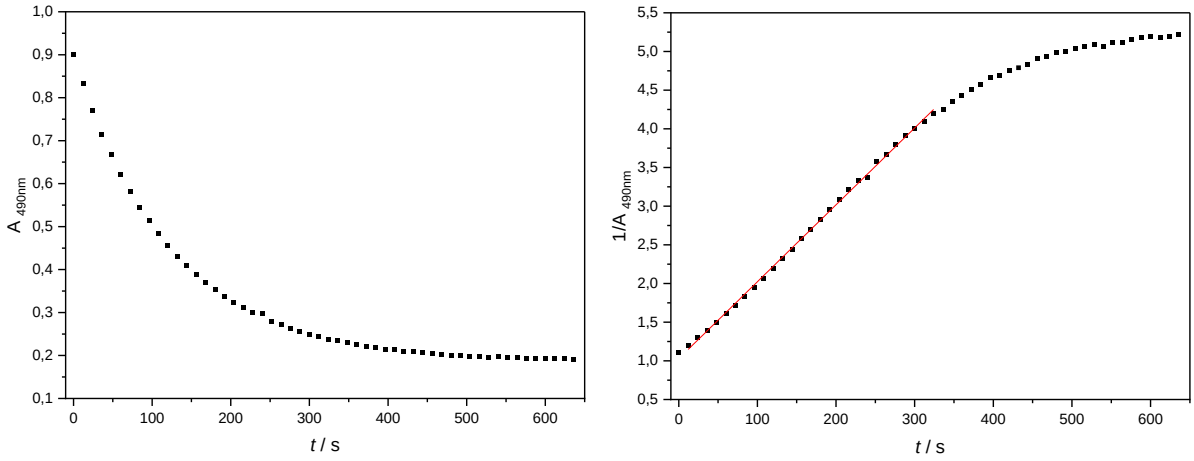

Figure 28: Left: Bleaching of the absorbance band at λ = 490 nm over time. Right: Plot of $1/A_{490\ nm}$ vs t displays the typical linear behavior of a second-order reaction. The derived rate constant is $k = 9.94 \cdot 10^{-3}$ L·mmol^{-1}·s^{-1}.

The half-life for second order reaction is not constant, since it depends on the concentration A of the species, as indicated in Equation 2.

$$t_{1/2} = \frac{1}{(k \cdot [A])} \qquad \text{Equation 2}$$

Based on Equation 3 below, a value that admits a comparison with similar data sets can be derived. This equation uses the initial concentration A_0 to calculate the half-life $t_{1/2,0}$. This equation yields a value of $t_{1/2,0}$ = 112 s.

$$t_{1/2,0} = \frac{1}{(k \cdot [A_0])}$$ Equation 3

In this experiment it was shown that the starting material **21** could be regained. This means that the whole recycling process was completed successfully (see Scheme 19). Before the obtained μ-hydroxo dicopper(II) complex **21** can be used again, it has to be recrystallized to remove the impurities.

This experiment shows also that the instability of the μ-1,2-peroxo dicopper(II) complex **20** poses a major problem for further studies of the other reactive dioxygen adducts and their reactivity. The fast decay makes the interpretation of the results difficult and in some cases impossible. Moreover, the decay makes titrations often impossible. Even though the decomposition process of the μ-1,2-peroxo dicopper(II) complex **20** can be slowed by lowering the temperature. Solutions of **20** in propionitrile or acetone at –80 °C show significant decay in the UV/vis absorbance spectrum.

A series of experiments was performed to gain more insights into the decomposition mechanism and to collect correction data at different temperatures. In previous works different reaction orders were proposed for the decay and the rate constant could often not be derived because several repetitions of the same experiment gave inconsistent data.[38,104,123] Furthermore, there is a lack of data for different reaction temperatures. Therefore, the decomposition of the μ-1,2-peroxo dicopper(II) complex **20** was investigated for a temperature range from 20 °C to –40°C in increments of 10 °C. The reactions were tracked by UV/vis spectroscopy. The recorded data were checked for inconsistencies and normalized. A stock solution of **21** and the reductant cobaltocene was used to ensure that the starting concentration of **20** was the same in all experiments. Overtitration with cobaltocene was avoided. All solutions were prepared under inert conditions and the same batch of solvent was used. A UV/vis spectrometer with a fitted cryostat and integrated stirring plate was used for the temperature-controlled measurements. Liquid nitrogen was used as coolant. Even though the cryostat was fully automated, a major challenge was to keep the temperature consistent over long time periods and to avoid the gradual formation of ice crystals inside the cooling systems. Freezing of the nitrogen inlet can lead to significant deviations in the spectrum. This problem is more likely to occur the longer the measurement duration and the lower the temperature is. This may be one of the main reasons why the decay of the peroxo dicopper(II) complexes has mostly been studied at room temperature and deviations occurred when repeating experiments at lower temperatures in previous work.[38,65,121,123] For this reason, all the experiments were done at low humidity conditions and formed ice crystals were immediately removed. In addition, all equipment and glassware were dried thoroughly prior to use and no measurements under –40 °C were performed.

A representative collection of the recorded UV/vis data which was used in subsequent analysis can be found in the Appendix. In this series of experiments, the bleaching of the characteristic absorption feature of the peroxo dicopper(II) complex **20** at 490 nm was of particular interest and was tracked. The normalized data for the different temperatures are presented in Figure 29.

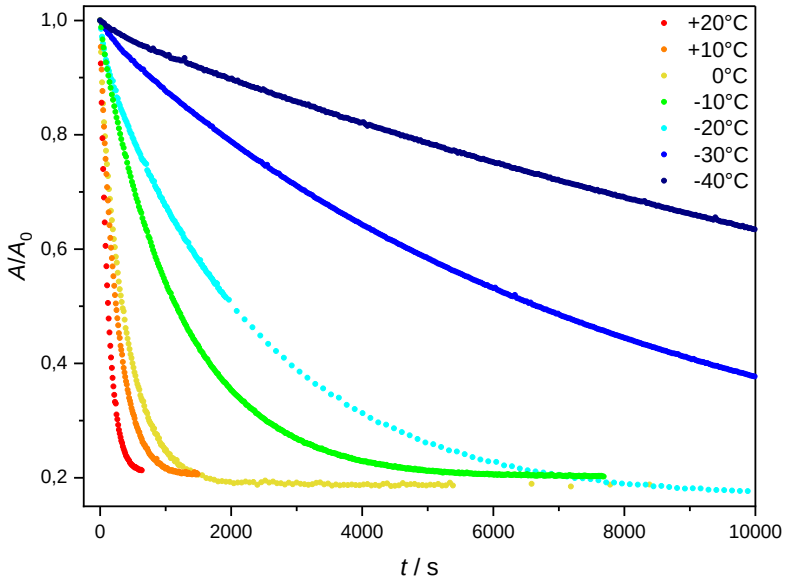

Figure 29: Bleaching of the characteristic absorption feature at 490 nm of the peroxo dicopper(II) complex **20** during the decay to the μ-hydroxo dicopper(II) complex **21** in a temperature range of 20 °C to –40 °C in dry MeCN.

The resulting plot of A/A_0 vs. t shows that lower temperatures have a huge influence on the stability of the peroxo dicopper(II) complex **20**. The plot can be used to estimate the lifetime of the reactive species at different temperatures. The traces of the bleaching for 0 °C and –20 °C show a small deviation of the expected A/A_0 end values. This deviation is expected to be the same for all traces. For the 0 °C and –20 °C trace, the end value is lower than expected. This is probably a result of the experimental setup, during the experiments two baseline corrections must be performed which can lead to a slight discrepancy of the absorbance. In the further analysis only the values for the start of the actual decay are considered and measurement errors at the end point do not influence the calculated results.

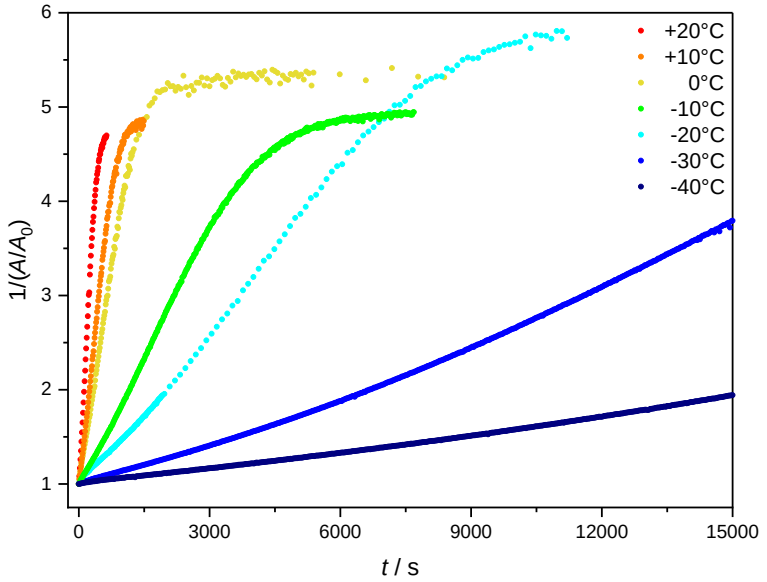

Figure 30: Plot of $1/(A/A_0)$ vs. t displays the typical linear behavior of a second-order reaction at the beginning of the decay of the peroxo dicopper(II) complex **20** in dry MeCN at various temperatures.

For the calculation of the rate constants k and the half-life times $t_{1/2,0}$, Figure 30 plots $1/(A/A_0)$ against time. A linear progression can be identified at the beginning of the decay which confirms that it is a second-order chemical reaction. The values for k and $t_{1/2,0}$ were calculated based on Equation 1 and Equation 3. The calculated values are given in Table 5.

Table 5: Overview of the calculated kinetic data for the decay of the μ-1,2-peroxo dicopper(II) complex **20** to the μ-hydroxo dicopper(II) complex **21** at different temperatures in dry MeCN.

T / °C	k / L·mmol^{-1}·s^{-1}	$t_{1/2,0}$ / s
20	$9.94 \cdot 10^{-3}$	112
10	$5.81 \cdot 10^{-3}$	225
0	$4.04 \cdot 10^{-3}$	326
–10	$1.18 \cdot 10^{-3}$	1082
–20	$6.01 \cdot 10^{-4}$	1736
–30	$1.49 \cdot 10^{-4}$	4825
–40	$4.53 \cdot 10^{-5}$	13591

The assignment to a second-order chemical reaction is very clear for temperatures down to –20 °C. The two lower temperatures –30 °C and –40 °C, seem to display almost linear curves in the plot $\ln(A/A_0)$. This is depicted in Figure 31 for comparison. This evidence may suggest a first-order reaction. However, it is more likely that the impression of linearity results from the fact that the measurement times were too short for these low temperatures. Analysis at these low temperatures is particularly challenging since it is not feasible to keep the measurement conditions constant for longer time periods. Therefore, a second-order reaction seems more likely and is assumed going forward. Nevertheless, it cannot be excluded completely that the reaction order changes at lower temperatures.

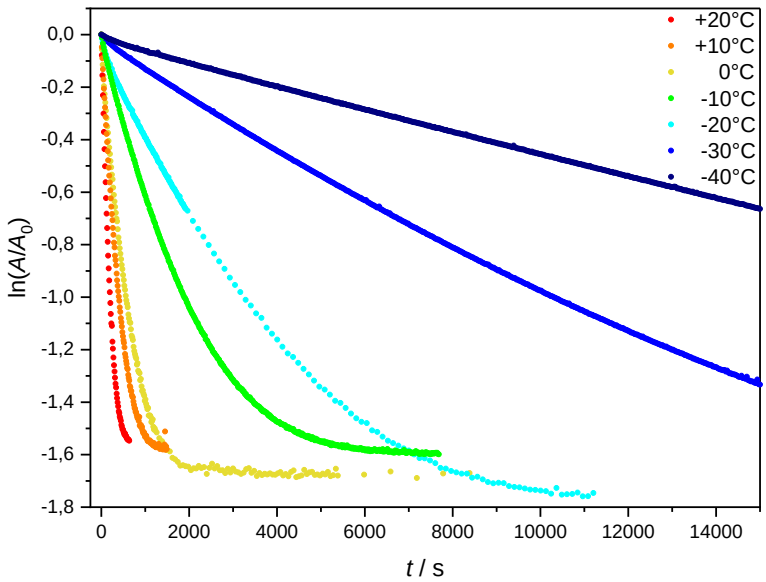

Figure 31: Plot of $\ln(A/A_0)$ vs. t of the decay of the peroxo dicopper(II) complex **20** in dry MeCN at different temperatures.

The calculated rate constants k can be used to determine the activation energy E_A for the decomposition process. The ARRHENIUS equation was used for this purpose (Equation 4).[172] The calculated values for an ARRHENIUS plot can be found in Table 6.

$$\ln(k) = \ln(A) - \frac{E_A}{R} \cdot \frac{1}{T} \qquad \text{Equation 4}$$

Table 6: Overview of the calculated values for the ARRHENIUS plot of the decomposition of μ-1,2-peroxo dicopper(II) complex **20** to the μ-hydroxo dicopper(II) complex **21** in dry MeCN.

T / °C	$1/T$ / K^{-1}	k / $L \cdot mmol^{-1} \cdot s^{-1}$	$\ln k$ / $L \cdot mmol^{-1} \cdot s^{-1}$
20	$3.41 \cdot 10^{-3}$	$9.94 \cdot 10^{-3}$	–4.61
10	$3.53 \cdot 10^{-3}$	$5.81 \cdot 10^{-3}$	–5.15
0	$3.66 \cdot 10^{-3}$	$4.04 \cdot 10^{-3}$	–5.51
–10	$3.80 \cdot 10^{-3}$	$1.18 \cdot 10^{-3}$	–6.74
–20	$3.95 \cdot 10^{-3}$	$6.01 \cdot 10^{-4}$	–7.42
–30	$4.11 \cdot 10^{-3}$	$1.49 \cdot 10^{-4}$	–8.81
–40	$4.29 \cdot 10^{-3}$	$4.53 \cdot 10^{-5}$	–10.00

To identify the ARRHENIUS parameters Figure 32 plots ln(k) against $1/T$ and a linear curve is fitted to the plot. The activation energy of decomposition of the peroxo dicopper(II) complex **20** to the hydroxo dicopper(II) complex **21** is determined as E_A = 52.6 kJ·mol^{-1} ± 3.0 kJ·mol^{-1}. The value of the pre-exponential factor is $A = 3.17 \cdot 10^{10}$ dm^3·mol^{-1}·s^{-1}, according to intercept of the linear fit.

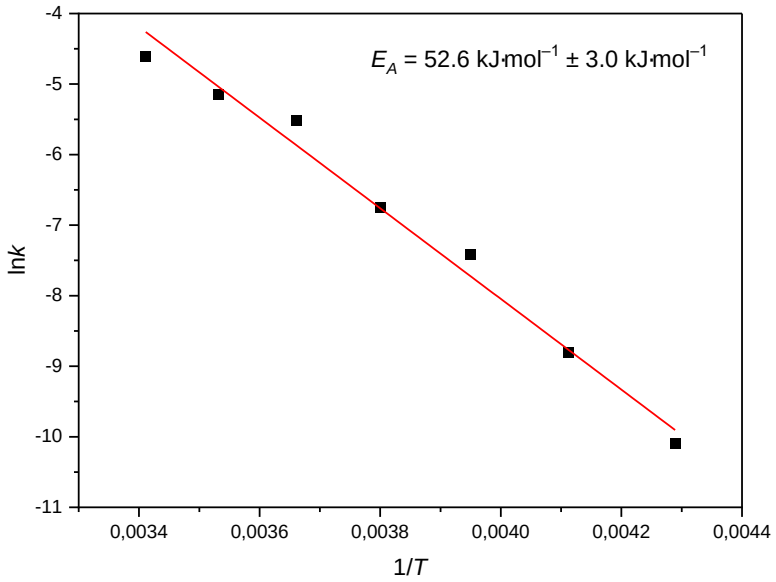

Figure 32: ARRHENIUS plot for the decomposition of the μ-1,2-peroxo dicopper(II) complex **20** to the μ-hydroxo dicopper(II) complex **21** in dry MeCN.

The determined values for the activation energy E_A and the pre-exponential factor A are in the typical range for reactions which take place in solution.[172] The value of the activation energy is further discussed in Chapter 4.2.6.

4.1.7 Summary and conclusion

In the previous chapters, it was shown that although it was not possible to obtain the desired symmetric dicopper(I) complex **19** by direct synthesis, an alternative synthetic route exists. The molecule was successfully synthesized *in-situ* by a chemical reduction of the decomposition product **21**. The reaction was investigated by UV/vis spectroscopy and showed a direct conversion to **19** without the formation of any intermediates.

The crystallization of the starting material, *i.e.*, the symmetric μ-hydroxo dicopper(II) complex **21,** was a major challenge. An extended purification process was developed that lead to the successful isolation of **21** as crystalline material. The molecule was investigated by ESI mass spectrometry, UV/vis and IR spectroscopy. The magnetic properties were studied and revealed a strong antiferromagnetic coupling. Additionally, a molecular structure was gained from a XRD experiment. A comparison of the recorded data with the reported results of the related hydroxo dicopper(II) complexes revealed that the spectroscopic data fit the patterns identified in existing work.[38,65,104,121] Particularly remarkable were the insights gained into the solid-state structure, since an easily accessible active site is recognizable. This is the result of the lower steric demand of the methyl residues. This is one of the first examples that show that it is possible to reduce shielding of the cavity in the dicopper complexes based on TACN/pyrazolate compartmental ligands.

The symmetric peroxo dicopper(II) complex **20** was synthesized successfully and was characterized by UV/vis spectroscopy. The distinctive features were found and suggest that a μ-1,2-peroxo dicopper(II) complex was formed. Resonance Raman spectroscopy with labelled oxygen confirmed the formation of **20**. In contrast to the related peroxo dicopper(II) complexes, **20** showed a rapid decay to **21**. In a series of experiments, the half-life and reaction constants for this second-order reaction were determined at various temperatures. Further analysis resulted in the determination of the activation energy of this decomposition (E_A = 52.6 kJ·mol^{-1} ± 3.0 kJ·mol^{-1}). Through decomposition of **20** the starting material **21** can be recovered and reused to regain the reactive oxygen adduct. Since the syntheses of the proligand $\mathbf{HL_{sym}}$ and the corresponding copper complexes are very resource- and time- intensive this recycling process is a particularly valuable result.

4.2 Formation of a non-symmetric peroxo dicopper(II) complex

4.2.1 A non-symmetric dicopper(I) complex

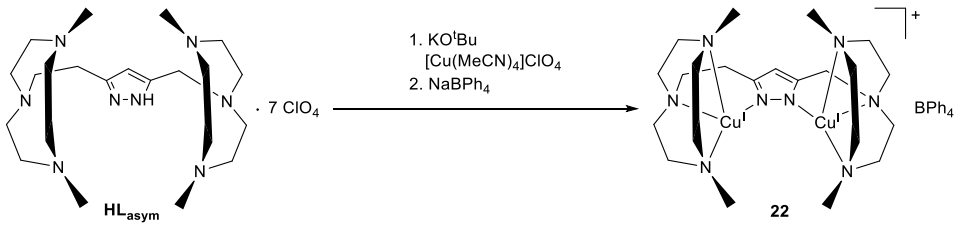

Scheme 26: Synthesis of the non-symmetric dicopper(I) complexes **22** with tetrakis(acetonitrile)copper(I) perchlorate in dry MeOH under inert conditions.

For the synthesis of the non-symmetric dicopper(I) complex **22**, **HL$_{asym}$** and potassium *tert*-butoxide were dissolved in dry methanol and a solution of tetrakis(acetonitrile)copper(I) perchlorate in dry methanol was added dropwise under inert conditions. Precipitation with a solution of sodium tetraphenylborate in dry methanol yielded the dicopper(I) complex **22** as a colorless solid. Redissolving of the product in dry acetone and slow vapor diffusion crystallization with dry diethylether under inert conditions resulted in a dark green colored solution. Analysis of the obtained reaction mixture led to the conclusion that the corresponding decomposition product, a hydroxo dicopper(II) complex, had formed. Similar to the synthesis of the symmetric dicopper(I) complex **19** (see chapter 4.1.1) variation of the used copper(I) salt, solvents and crystallization conditions did not lead to the successful isolation of crystalline material of **22**. In comparison to the synthesis attempts of **19**, it was found that the decomposition of the non-symmetric dicopper(I) complex **22** was slower. The color change associated with the formation of the decomposition product occurred later (2-3 days). This led to the conclusion that the dicopper(I) complex **22** is less sensitive towards traces of oxygen or other impurities than the symmetric equivalent **19**. The crude product of **22** was gained by the precipitation but was insufficient for producing a clean UV/vis absorbance spectrum in acetonitrile under inert conditions. Therefore, it was attempted to obtain the thermodynamically stable hydroxo dicopper(II) complex by *in-situ* formation of **22**.

4.2.2 The recycling of the decomposition product

In-situ synthesis of the dicopper(I) complex **19** is discussed in Chapter 4.1.2. This chapter adapts this synthesis strategy to the formation of the non-symmetric derivate. An overview of the modified synthesis strategy is shown in Scheme 27. The crux of this synthesis path is the successful synthesis, isolation and subsequent crystallization of the hydroxo dicopper(II) complex **24**. Without crystalline material of **24** in good yields the access to the reactive oxygen adducts is blocked. The hydroxo dicopper(II) complex can be used to synthesize the desired dicopper(I) complex by chemical reduction (**E**). It is expected that addition of dry oxygen results in the formation of a non-symmetric peroxo dicopper(II) complex **23** (**B**). Then, decomposition of this species regenerates the starting material **24** (**C**), closing the recycling cycle.

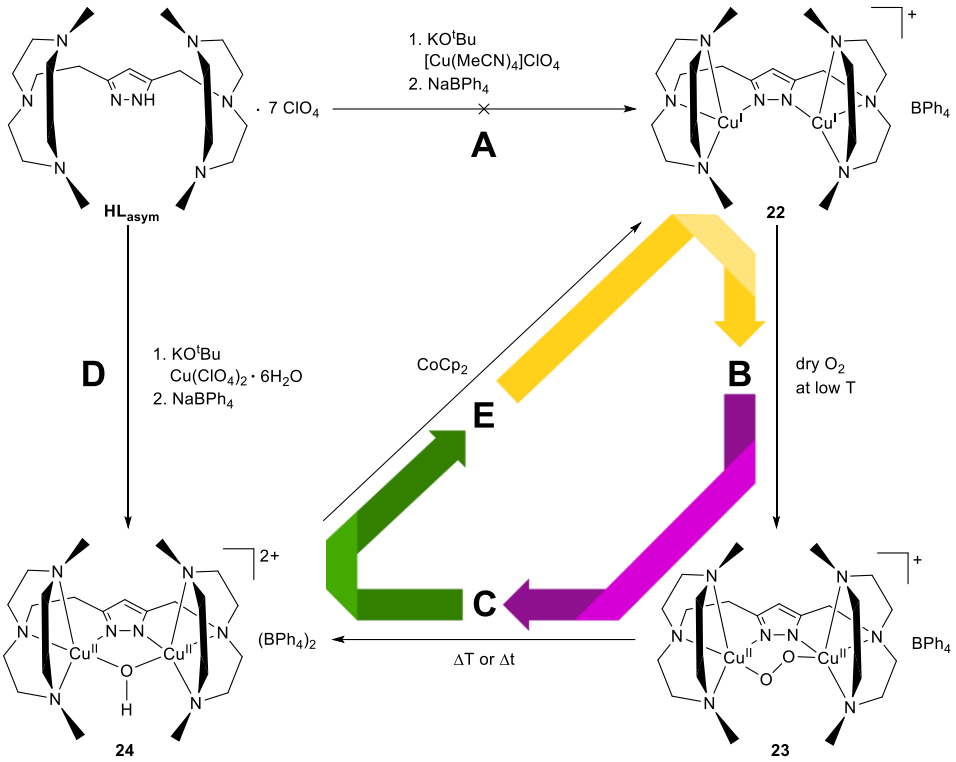

Scheme 27: Synthesis strategy for the non-symmetric peroxo dicopper(II) complex **23** via the chemical reduction of the hydroxo dicopper(II) complex **24** to the corresponding dicopper(I) complex **22**. The colors of the depicted arrows represent the expected color chances of the involved copper complexes. The most likely counter-ion for compounds **22** and **23** were added for the sake of completeness and charge neutrality.

4.2.3 The non-symmetric μ-hydroxo dicopper(II) complex

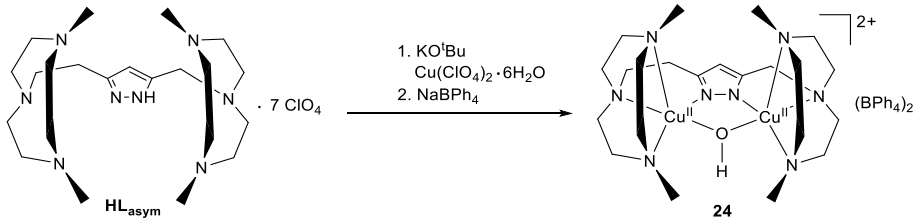

Scheme 28: Synthesis of the non-symmetric μ-hydroxo dicopper(II) complex **24**.

The hydroxo dicopper(II) complex **24** was synthesized by deprotonation of the proligand **HL$_{asym}$** and addition of a copper(II) salt, as shown in Scheme 28. The green colored complex was precipitated with sodium tetraphenylborate and the crystallization of **24** by slow vapor diffusion was started. Similar to the early crystallization of the symmetric congener **21**, only an amorphous green solid was isolated. Different copper(II) salts, solvents, crystallization temperatures and techniques were tested, but no crystalline material was obtained. The desired single crystal material of **24** was isolated by adapting the crystallization procedure for the symmetric equivalent **21** (see Chapter 4.1.3). The modified procedure is depicted in Scheme 29.

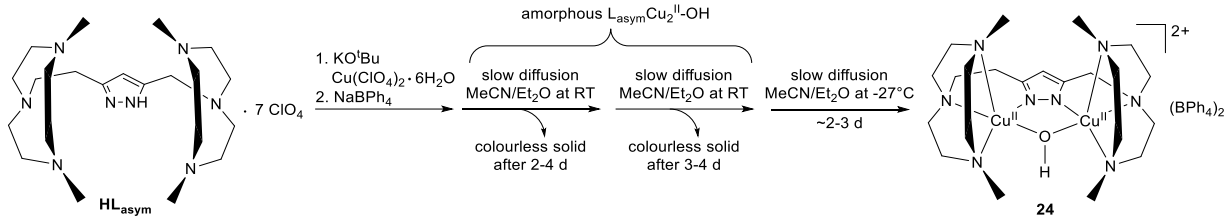

Scheme 29: Synthesis route of **24** and the subsequent purification process by slow vapor diffusion crystallization.

The success of the extended purification process was proven by ESI mass spectroscopy. The mass spectrum is shown in Figure 33. The peak at *m*/*z* = 281.1 can be assigned to the hydroxo dicopper(II) complex **24** ($[L_{asym}Cu_2OH]^{2+}$) on the basis of the expected mass-to-charge ratio and isotope pattern. Furthermore, the peak *m*/*z* = 883.4 can also be attributed to the target molecule. The isotope pattern suggests that this is the complex **24** with one tetraphenylborate anion($[L_{asym}Cu_2OH+BPh_4]^+$). The comparison of the isotopic patterns with simulated isotopic pattern can be found in the appendix.

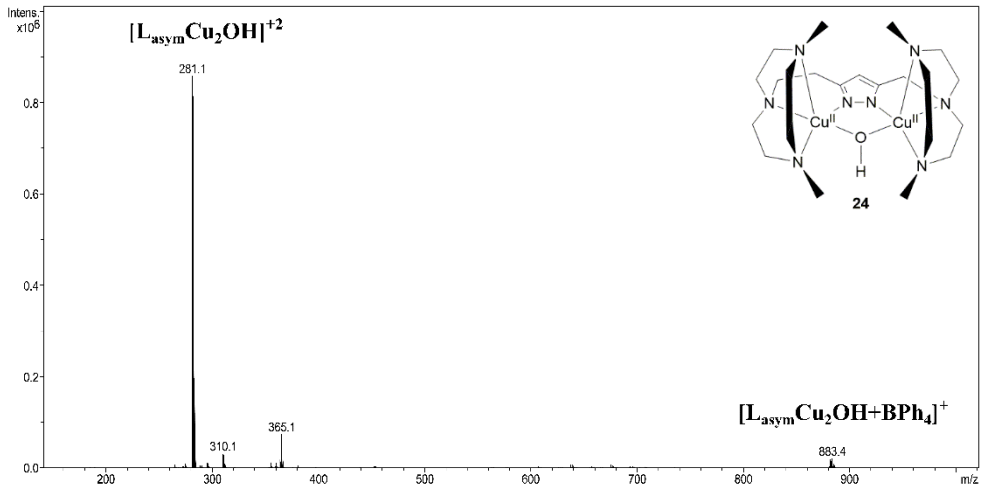

Figure 33: MS-ESI spectrum of the non-symmetric μ-hydroxo dicopper(II) complex **24** in MeCN after the extended purification process. The measurement was performed by the central analytics department (IOBC, Georg-August-Universität Göttingen).

Moreover, the obtained single crystals of **24** were suitable for a XRD experiment which confirmed the hypothesized molecular structure. The molecular structure of the cationic part is shown in Figure 34.

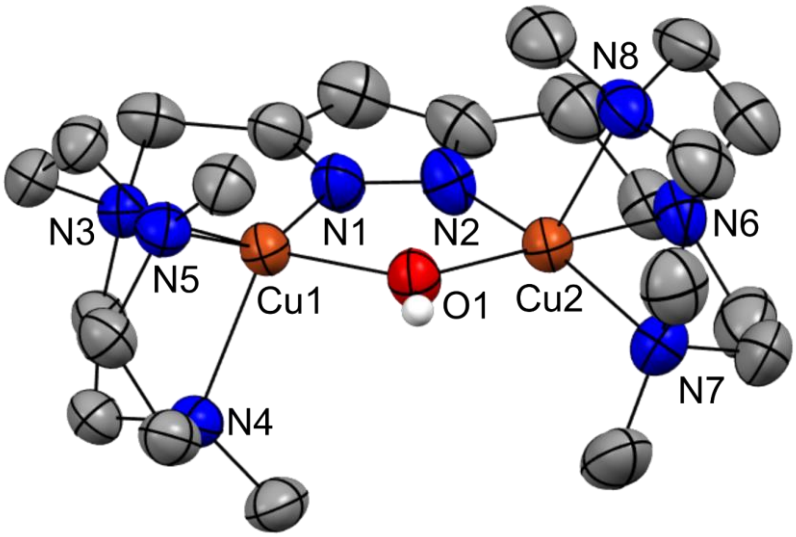

Figure 34: Molecular structure of the μ-hydroxo dicopper(II) complex **24** (thermal displacement ellipsoids given at 50 % probability). The two tetraphenylborate anions, acetonitrile, diethylether and the unnecessary hydrogen atoms are omitted for clarity. Selected Bond length [Å] and bond angles Selected bond length, distances and bond angles can be found in 8.1.10 and Table 7. Sample preparation and measurement was performed by Dr. Sebastian Dechert (IAC, Georg-August-Universität Göttingen).

According to the determined τ_5-parameter, the coordination geometry of the two copper(II) ions is slightly distorted square pyramidal. The coordination sphere of the Cu1 is more distorted since the calculated values are τ_5(Cu1) = 0.329 and τ_5(Cu2) = 0.168.[163,164] Similar to the solid state structure of **21**, one Cu–N_{TACN} bond is elongated (2.223 Å and 2.308 Å), because it lies on the JAHN-TELLER axis of the copper(II) ion.[162] With a length of 2.059-2.083 Å the other two Cu–N_{TACN} bonds are longer than the Cu–$N_{pyrazolate}$ bond (1.878 Å and 1,943 Å). The copper-to-copper ion distance of **23** is with 3.390 Å similar to **21** (3.340 Å). This is surprising because **23** features an ethylene and a methylene spacer in the ligand backbone, a longer Cu···Cu distance was expected. Important bond length and distances of **24** and the closely related complex **IIIe** are summarized in Table 7.[38]

Table 7: Selected bond length and distances for **24** and **IIIe**.[38]

bond/distance	24	IIIe
Cu1-O1	1.939 Å	1.961 Å
Cu2-O2	1.955 Å	1.968 Å
Cu1-N1	1.878 Å	1.893 Å
Cu1-N3	2.083 Å	2.093 Å
Cu1-N4	2.216 Å	2.308 Å
Cu1-N5	2.059 Å	2.057 Å
Cu···Cu	3.390 Å	3.432 Å

The Cu–O–Cu angle was determined as 121.0 ° which is very similar to the corresponding angle in the closely related non-symmetric μ-hydroxo dicopper(II) complex **IIIe** (121.8 °).[38] Since **IIIe** is based on a non-symmetric *i*Pr$_2$TACN/pyrazolate ligand scaffold the increased steric demand affects the spatial

structure. A comparison of the space-filling models of **24** and **IIIe** illustrates this perfectly, as shown in Figure 35.

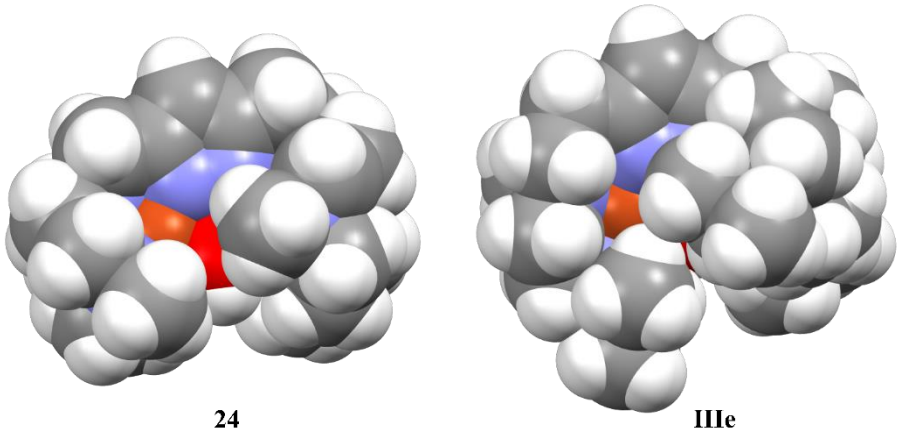

Figure 35: Top view of the space-filling models of the solid state structures of the closely related μ-hydroxo di-copper(II) complexes **24** and **IIIb**. The atoms are color coded: white: hydrogen, grey: carbon, blue: nitrogen, red: oxygen and orange: copper.

In contrast to **IIIb**, the bimetallic center of **24** is deshielded and the steric demand is significantly reduced. This may lead to higher reactivity of the corresponding reactive oxygen adducts, since reactants can interact mor easily with the reactive dicopper core. A definite conclusion cannot be obtained from these space-filling models. This is because the models are based on the solid-state structures and allow only limited inference on the spatial structure of the molecule in solution.

UV/vis absorbance spectroscopy of the non-symmetric hydroxo dicopper(II) complex **24** revealed a feature at 354 nm ($\varepsilon \approx 3500$ M^{-1} cm^{-1}) which is probably due to a LMCT transition.[38] A second feature from a spin-forbidden d-d transition can be found at 616 nm ($\varepsilon \approx 210$ M^{-1} cm^{-1}).[65] The recorded UV/vis spectra is typical and indicative for hydroxo dicopper(II) complexes based on a TACN/pyrazolate compartmental ligand scaffolds.[38,65]

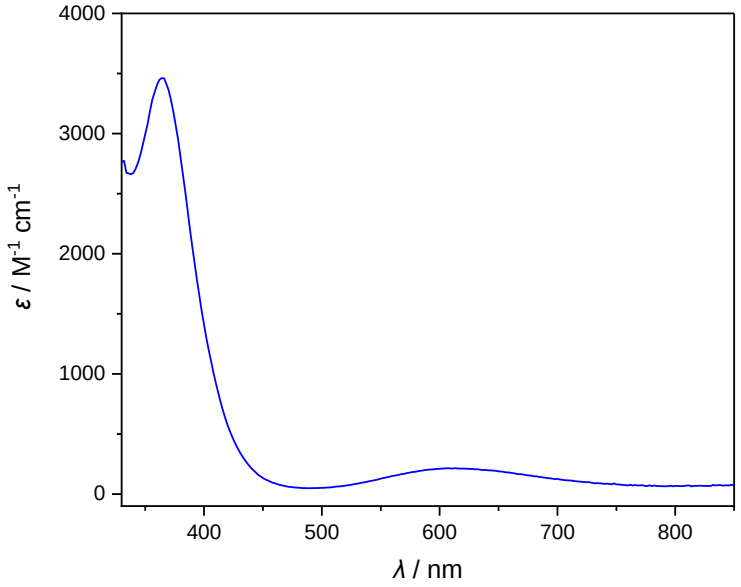

Figure 36: UV/vis absorbance spectrum of the non-symmetric μ-hydroxo dicopper(II) complex **24** in dry acetone at 25 °C.

Table 8 shows that the new data agrees with the results in the existing literature.[38,65] Furthermore, two trends can be identified. Firstly, shorter methylene spacers in the ligand backbone seem to result in a shift of the spectrum to longer wavelength. Secondly, reduction of the steric demand at the TACN moiety of the ligand leads to a shift to shorter wavelength.

Table 8: Comparison of the characteristic absorbance features of μ-hydroxo dicopper(II) complexes based on different TACN/pyrazolate ligand scaffolds.[38,65]

Complex	λ_1 / nm (ε / M^{-1} cm^{-1})	λ_2 / nm (ε / M^{-1} cm^{-1})
IIIe	374 (4500)	626 (240)
24	364 (3500)	616 (210)
IIe	356 (3700)	613 (200)
21	353 (3300)	595 (280)

Magnetic susceptibility data were obtained from freshly crushed crystalline material of the μ-hydroxo dicopper(II) complex **24** in the temperature range from 2 K to 300 K at a magnetic field of 0.5 T. The gathered data revealed a strong antiferromagnetic coupling (J = –319.6 cm^{-1}) which is the result of an extensive σ in-plane overlap of the coplanar $d_{x^2-y^2}$ magnetic orbitals and the pyrazolate bridging unit (Figure 37).[165] Remarkably, this is the highest determined value for the antiferromagnetic coupling of all known hydroxo dicopper(II) complexes which are based on TACN/pyrazolate ligand frameworks.[38,65]

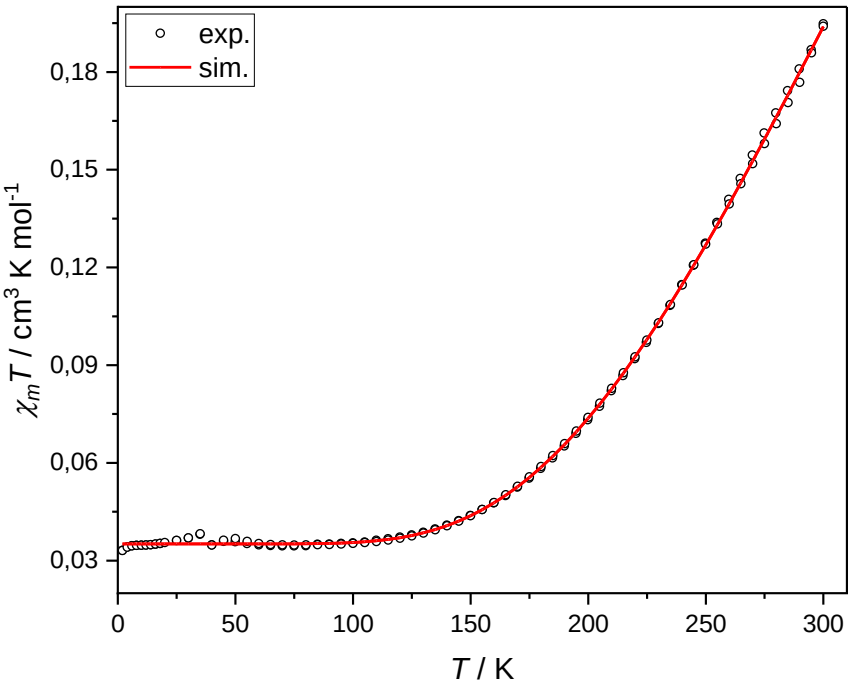

Figure 37: Magnetic susceptibility data of the non-symmetric μ-hydroxo dicopper(II) complex **24** between 2 K to 300 K at a magnetic field of 0.5 T (black) and the corresponding simulation (red). The following parameters could be determined: J = –316.6 cm^{-1}, g = 2.360, PI = 9.3 %. Sample preparation and measurement was done by Dr. Serhiy Demeshko (IAC, Georg-August-Universität Göttingen).

The magnitude of the antiferromagnetic coupling is influenced by Cu–O–Cu angle, Cu–O bond length and the out-of-plane displacement of the H-Atom in the Cu_2OH plane.[165–168] Table 9 shows a comparison of the coupling constants, Cu–O–Cu angles and Cu–O bond lengths of the characterized non-symmetric and symmetric μ-hydroxo dicopper(II) complexes.[38,65] The higher antiferromagnetic coupling of **24** in comparison to the other non-symmetric complex **IIIe** can be explained by the altered geometry of the complex due to the lower steric hindrance of the Me_2TACN/pyrazolate ligand. A similar trend can be identified for the symmetric derivates **21** and **IIe**. In addition, a smaller displacement of the H-Atom out of the Cu_2OH plane results in a bigger coupling constant for **24** compared to **IIIe**. The Cu–O–Cu angle with 121.0 ° and the Cu–O bond are in a similar range for **24** and **IIIe**. However, the Cu–O bonds are of different lengths for **24**.

Table 9: Comparison of the coupling constants and structural parameter of μ-hydroxo dicopper(II) complexes based on TACN/pyrazolate ligand scaffolds.[38,65]

Complex	J / cm^{-1}	Cu–O–Cu angle / °	Cu–O bond length / Å
IIIe	–293.9	121.8	1.97
24	–316.6	121.0	1.94/1.96
IIe	–184	123.3	1.93
21	–212.3	118.0	1.95

In summary, the obtained data align with to the existing data and known trends for the μ-hydroxo dicopper(II) complexes based on different TACN/pyrazolate compartmental ligands.

In addition, another synthesis route for the non-symmetric hydroxo dicopper(II) complex was established. This route is based on previous works by BRINKMEIER and LÜCKEN.[121,123] The unique feature of this synthesis is the addition of sodium acetate and sodium formate to the reaction mixture to gain access to dicopper(II) complexes that features an acetate or formate molecule in the bimetallic cleft. Since similar efforts have already been discussed for the symmetric hydroxo-dicopper(II) complex **21** in chapter 4.1.3, this part will focus on the differences and similarities of this synthesis approach.

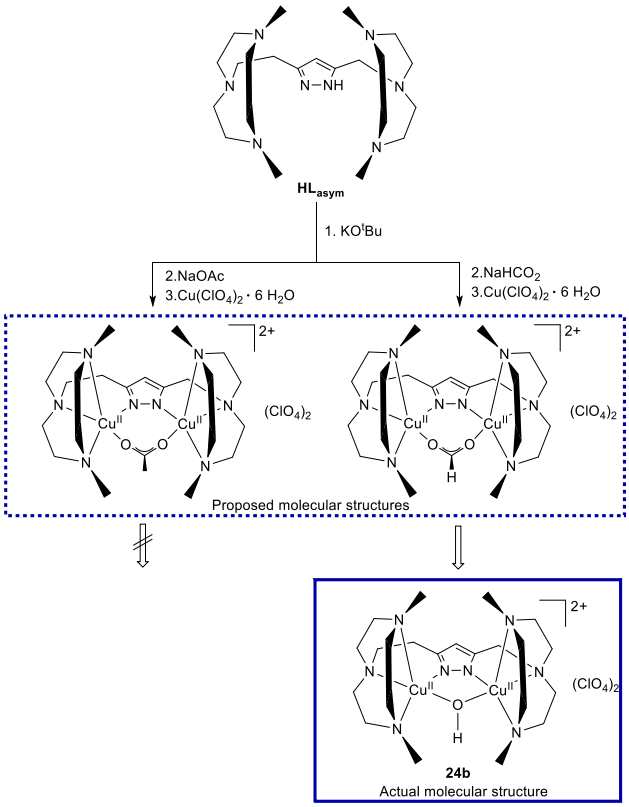

Scheme 30: Synthesis of μ-hydroxo dicopper(II) complex **24b**

Similar to the symmetric case, it was not possible to isolate the purposed complexes for the non-symmetric case. This is depicted in Scheme 30, However, the addition of sodium formate to the reaction mixture produced the non-symmetric hydroxo dicopper(II) complex as the perchlorate salt **24b** in good yields. This result implies that the bimetallic gap is not large enough to accommodate a formate or even an acetate molecule although the change of the symmetric ligand to the non-symmetric ligand is expected to result in a longer copper–copper ion distance.

However, the addition of sodium formate promotes crystallization of the µ-hydroxo-dicopper(II) complex and reduces the synthesis effort compared to the long purification and crystallization cycle of **24**. Therefore, this synthetic route is particularly suitable for preparing larger amounts of the non-symmetric μ-hydroxo dicopper(II) complex.

4.2.4 *In-situ* formation of a non-symmetric dicopper(I) complex

The successful crystallization and characterization of the μ hydroxo dicopper complexes **24** and **24b** allowed the investigation of the synthesis of the corresponding dicopper(I) by chemical reduction. This reduction is depicted in Scheme 31. Initial experiments provided proof of concept: they showed that the addition of cobaltocene to a solution of **24** in acetonitrile under inert conditions results in an immediate color change from green to yellow. Similar to the *in-situ* generation of the symmetric congener, it was found that for a successful reaction dry and thoroughly degassed solvents and a reaction temperature of 25 °C are essential.

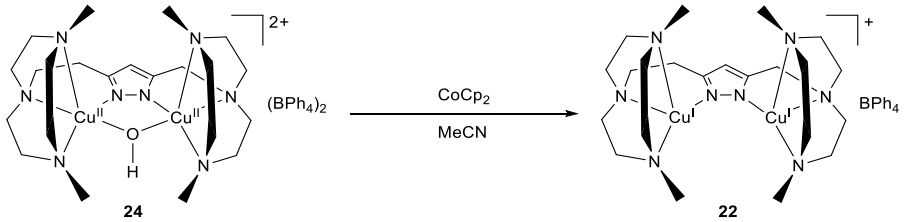

Scheme 31: Chemical reduction of the μ-hydroxo dicopper(II) complex **24** to the non-symmetric dicopper(I) complex **22** with $CoCp_2$ as the reductant in dry MeCN under UV/vis conditions. Since the specific counterion of **22** is not known, the most probable counterion was added for the sake of completeness and to maintain the charge neutrality of the reaction equation.

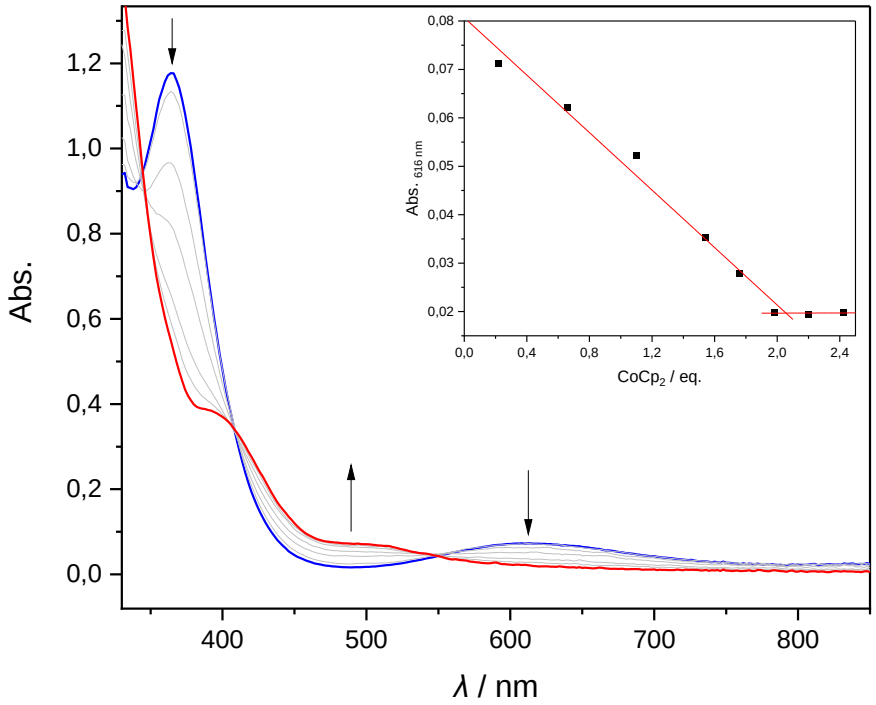

Figure 38: UV/vis spectrum of the titration of the non-symmetric μ-hydroxo dicopper(II) complex **24** (blue) to dicopper(I) complex **22** with 2.06 eq. $CoCp_2$ in dry acetone at 25 °C under inert conditions. The recorded spectrum features *pseudo*-isosbestic points at 346 nm, 409 nm and 546 nm. The inset shows the trace of the bleaching of the d-d transition at 616 nm with 2.42 eq. of cobaltocene.

The reduction of the non-symmetric hydroxo dicopper complex **24** was tracked by a UV/vis spectrophotometer and the resulting titration absorbance spectrum is depicted in Figure 38. The UV/vis measurement showed the bleaching of the typical absorbance features of the hydroxo dicopper complex **24** at 364 nm and 616 nm. In particular, the gradual disappearance of the d-d transition at 616 nm was

followed, as this reliably indicates the formation of the desired dicopper(I) complex. The corresponding trace indicates that the chemical reduction was finished after the addition of 2.06 eq. of cobaltocene. Slight variations in theses value (1.9 – 2.1 eq.) were observed in various measurements. These deviations from the expected value of 2.00 eq. are caused by intrinsic physical uncertainties and inaccuracies of the used spectrophotometer.[173] Therefore, these deviations are expected and within the error of the measurement. It can also not be ruled out completely that traces of minor impurities could cause these deviations, even though crystalline material of **24** was used as the starting material.

The vanishing of the characteristic hydroxo dicopper(II) complex features was accompanied by the rise of two bands at 400 nm and 504 nm. These can be assigned to the redox couple $CoCp_2/CoCp_2^+$. As shown in Figure 39, this assignment becomes particularly clear if the reducing agent is added in excess, since these bands rise significantly. These bands were used as a sensitive maker for the overtitration with cobaltocene.

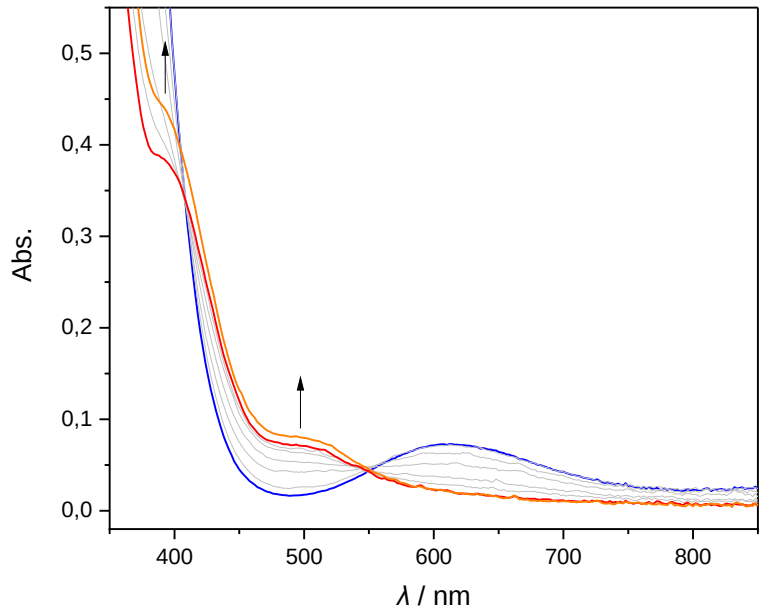

Figure 39: UV/vis absorbance spectrum of the titration of the μ-hydroxo dicopper(II) complex **24** (blue) to the dicopper(I) complex **22** with 2.06 eq. $CoCp_2$ in dry acetone at 25 °C under inert conditions. The spectra caused by excess of $CoCp_2$ (2.2 eq.) is shown in orange.

Similar to the symmetric dicopper(I) complex **19**, the addition of a slight excess of reducing agent can help to ensure that the *in-situ* formed species is immediately regenerated if decomposition does occur. This kind of stabilization of the dicopper(I) complex **22** by intentional overtitration was in most cases not necessary since **22** does not appear to be as sensitive to traces of oxygen or water as its symmetric equivalent **19**.

The UV/vis titration spectrum in Figure 38 seems to feature three isosbestic points at 346 nm, 409 nm and 546 nm which would indicate that the reaction proceeds without any intermediate or potential side reaction. However, the close-up of the spectrum (see Figure 39) clarifies that these are *pseudo*-isosbestic points. Nevertheless, it can be assumed that this is a direct conversion by reduction since deviation from

the ideal isosbestic points were minimal. The appearance of the *pseudo*-isosbestic points indicates a high quality of the starting material since even minor impurities prevent the formation of the *pseudo*-isosbestic points.

Since the dicopper(I) complex **22** produced by chemical reduction is more stable than the symmetric derivative, crystallization experiments based on this synthetic route were carried out. Several crystallization attempts with various solvents at different temperatures were made. Crystalline material was only isolated for the resulting cobaltocenium salt.

4.2.5 *In-situ* formation of a non-symmetric peroxo dicopper(II) complex

The successful synthesis of the non-symmetric dicopper(I) complex **22** allowed proceeding with the activation by oxygen. To this end, a freshly prepared solution of **22** was exposed to an excess of dry oxygen. Immediately, a color change from pale yellow to purple occurred.

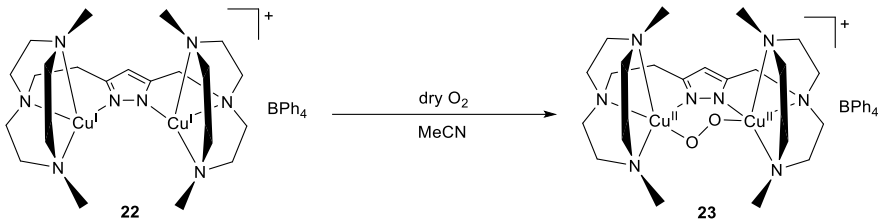

22 23

Scheme 32: Synthesis of the non-symmetric peroxo dicopper(II) complex **23** by addition of an excess of dry dioxygen to the dicopper(I) complex **22** in MeCN.

Two new bands are observed in the corresponding UV/vis absorbance spectrum (Figure 40). A distinctive band formed at 497 nm ($\varepsilon \approx 4400$ M^{-1} cm^{-1}) and a shoulder at 608 nm ($\varepsilon \approx 2800$ M^{-1} cm^{-1}). Both absorbance features are responsible for the purple color and are indicative of the formation of a peroxide adduct.[64,65,84] This pattern of bands is typical and characteristic for a μ-η^1:η^1-peroxo dicopper(II) complex.[20,64–66,81,174–177]

The distinctive absorbance features can be assigned to LMCT-transitions ($O_2^{2-} \rightarrow Cu^{II}$).[38,65,66,121] According to literature, the transition at the shorter wavelength arises from a σ-interaction of the Cu-centered orbitals with the π_σ^* orbital of the peroxide and the transition at the longer wavelength arises from the interactions of the π_v^* orbital of the peroxide.[38,87,121] The energy of the peroxide valence orbitals is split into π_σ^* and π_v^*. This occurs due to bonding interactions with the $d_{x^2-y^2}$-orbital of the copper(II) ions when the peroxide binds end-on to the copper(II) ions.[87]

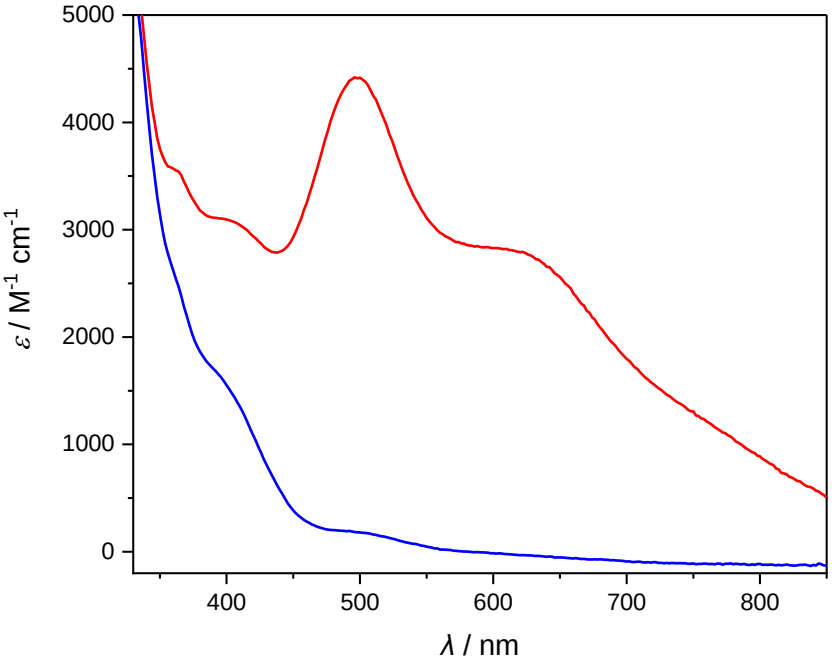

Figure 40: UV/vis spectrum of the *in-situ* produced non-symmetric dicopper(I) complex **22** (blue) in acetonitrile and the resulting non-symmetric peroxo dicopper(II) complex **23** (red) after addition of dry oxygen gas in excess at 25 °C.

In addition to these two distinctive bands, two minor shoulders are observed at around 360 nm and 409 nm. These features were already visible in the spectrum of the precursor of the dicopper(I) complex **22** and originate from the reduction agent used in the synthesis.

The data obtained for the non-symmetric peroxo dicopper(II) complex **23** fit the absorbance features of known peroxo dicopper(II) complexes based on different TACN/pyrazolate ligands perfectly. This is obvious from the comparison of the cupric peroxides in Table 10.[38,64,121–123]

Table 10: Comparison of the typical absorbance features of peroxo dicopper(II) complexes based on different TACN/pyrazolate ligand scaffolds.[38,65,121,123]

Complex	λ_1 / nm (ε / M^{-1} cm^{-1})	λ_2 / nm (ε / M^{-1} cm^{-1})
Ib	527 (5000)	648 (3900)
IVb	510	630
IIIb	520 (5500)	617 (3300)
23	497 (4400)	608 (2800)
IIb	506 (4800)	600 (2800)
20	490 (5800)	595 (3200)

The data on the typical absorbance features suggests that elongated spacers and/or lower steric demand in the ligand scaffold tend to result in a shift to shorter wavelength of the characteristic bands at λ_1 and λ_2 in the corresponding peroxo dicopper(II) complexes. Earlier works assigned this shift to the fact that the Cu-O-O-Cu torsion angles changes with the structure of the ligand.[38] The various design motifs of TACN/pyrazolate ligands impose different coordination geometries on to the copper ions.[38,64,65,121,123] Different torsion angles lead to different mixing of the involved orbitals, shifting the bands.[38] The

UV/vis spectra recorded for this work complement and extend this trend to the peroxo dicopper(II) complexes based on Me_2TACN/pyrazolate ligands. In this case, the characteristic bands are shifted to shorter wavelengths compared to the corresponding *i*Pr_2TACN/pyrazolate derivatives by an average of 19 nm for λ_1 and by an average of 14 nm for λ_2. Based on the data presented here, the non-symmetric peroxo dicopper(II) complex **23** was successfully synthesized.

To collect further evidence, resonance Raman spectroscopy experiments with labelled oxygen in frozen solution were performed. As it is typical for such peroxides, the spectrum showed a very broad peak at around 809 nm. Even though, no peaks could be assigned unambiguously and the results of the measurements were inconclusive. An example spectrum for one of the performed resonance Raman measurements can be found in the appendix. In general, this type of measurement has a higher chance of success if the sample can be measured as a solid. Due to the rapid decay of the peroxo dicopper(II) complex **23** in solution it was not possible to crystallize this species.

It is also important to note, that the formation of the non-symmetric peroxo dicopper(II) complex **23** was difficult to achieve at very low temperatures (–60 °C to –90 °C). Typically, dry oxygen was added in excess to the gas phase above the solution. At these low temperatures, this was insufficient and dry oxygen gas had to be injected directly into the stirring reaction solution over extended time periods.

4.2.6 Decomposition of the non-symmetric peroxo dicopper(II) complex

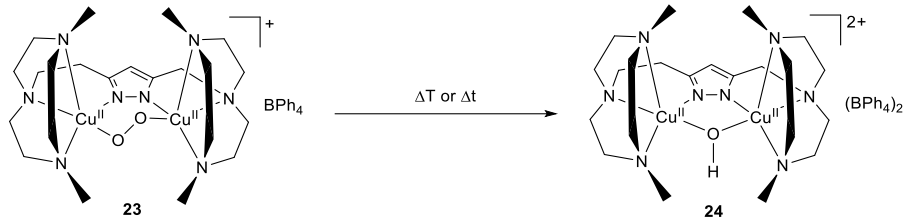

Scheme 33: Decomposition of the non-symmetric peroxo dicopper(II) complex **23** in MeCN to the non-symmetric hydroxo dicopper(II) complex **24**.

All known μ-1,2-peroxo dicopper(II) complexes based on Me_2TACN/pyrazolate ligands decompose rapidly to the corresponding μ-hydroxo dicopper(II) complexes. The non-symmetric peroxo dicopper(II) complex **23** also follows this trend, but it exhibits increased stability compared to the symmetric derivate **20** (Scheme 33). This is particularly evident in the formation and decomposition of **23** at elevated temperatures up to 35 °C which is not achievable for **20**. The decomposition is accompanied by a color change of the solution from purple to green. Figure 41 shows the UV/vis spectrum of such a decomposition at 25 °C.

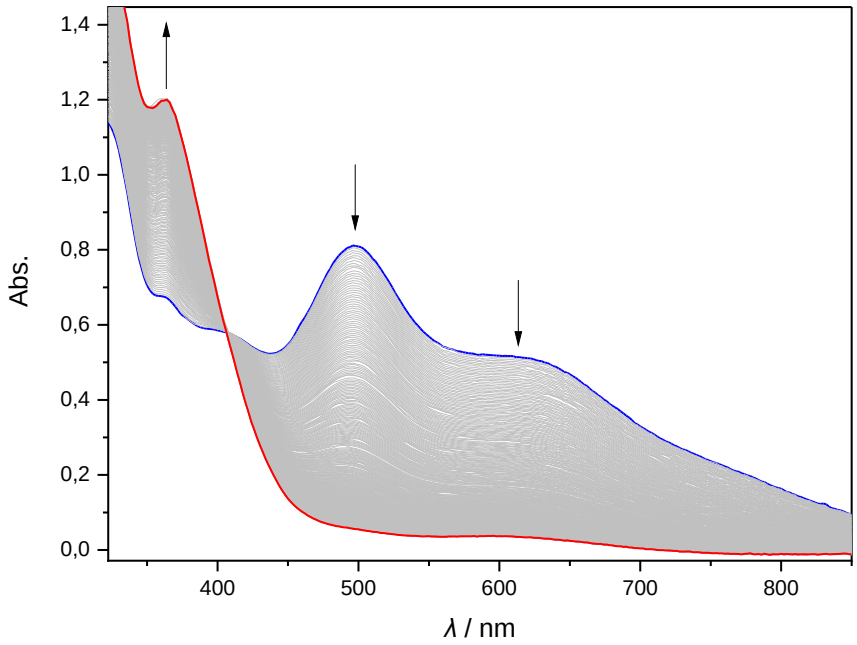

Figure 41: UV/vis absorbance spectra of the decomposition of the non-symmetric μ-1,2-peroxo dicopper(II) complex **23** (blue) to the μ-hydroxo dicopper(II) complex **24** (red) in dry MeCN at 25 °C. The spectrum features an isosbestic point at 407 nm.

The UV/vis absorbance spectrum shows the bleaching of the characteristic features of the peroxo dicopper(II) complex at 497 nm and 608 nm over time. The formation of two bands at 364 nm and 616 nm is observed. These are the distinctive features of the μ-hydroxo dicopper(II) complex **24**. Additionally, the formation of the decomposition product **24** was confirmed by ESI mass spectrometry. The reaction takes place without the formation of an intermediate. This conclusion can be drawn from the occurrence of the isosbestic point at 407 nm. Since the starting material **23** of this decomposition was synthesized by

chemical reduction artifacts of the used reductant can also be found in the recorded spectrum. Examples of such artefacts are the two bands around 360 nm and 409 nm. This evidence demonstrates that the starting material **24** can be regained and proves that the suggested recycling process (Scheme 27) works.

The bleaching of the absorbance feature at 497 nm was further analyzed. The trace of the bleaching shows an exponential decay, as depicted in Figure 42. A plot of ln*A* against time *t* reveals a linear relationship and a negative slope. This indicates that this decay is a first-order reaction. In contrast, decomposition of the symmetric peroxo dicopper(II) complex **20** was found to be a second-order reaction. Here, the rate of the decomposition of **23** depends only on the concentration of one reactant. This suggests that the two decompositions are based on different reaction mechanisms. Given the close structural relationship between the two molecules **20** and **23**, this result is unexpected and particularly noteworthy. Small variations in the ligand backbone, such as adding a methylene unit, seem to have a big influence on the reaction kinetics.

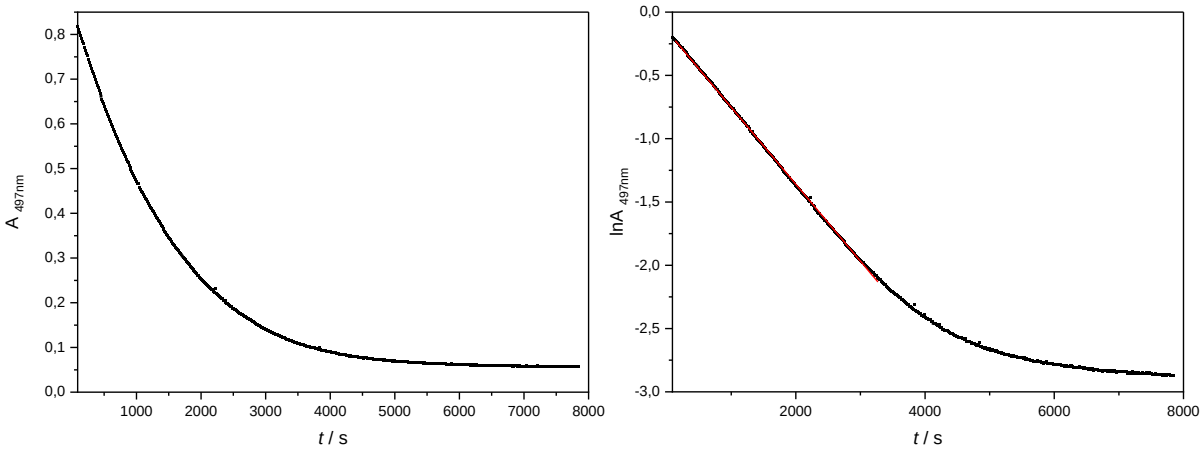

Figure 42: Left: Bleaching of the absorbance band at λ = 497 nm over time. Right: Plot of ln$A_{497\ nm}$ against time *t* displays the typical linear behavior of a first-order reaction. The calculated rate constant for this reaction is $k = 1.53 \cdot 10^{-3}\ s^{-1}$.

The rate constant of the decomposition of **23** can be calculated from the slope of a plot of lnA/A_0 against time *t* according to the integrated first-order rate equation (Equation 5).[172] The derived value for the rate constant is $k = 1.53 \cdot 10^{-3}\ s^{-1}$ at 25 °C.

$$\ln\left(\frac{[A]}{[A_0]}\right) = -kt \qquad \text{Equation 5}$$

The half-life for a first-order reaction can be determined according to Equation 6. The half-life time for the decomposition is $t_{1/2}$ = 456 s.

$$t_{1/2} = \frac{\ln(2)}{k} \qquad \text{Equation 6}$$

These results lead to the conclusion that the decomposition of the non-symmetric peroxo dicopper complex **23** is about four times slower than the decomposition of the symmetric derivative **20** at the same reaction temperature. Compared with the half-lives determined for the peroxo dicopper(II) complex

based on *i*Pr$_2$TACN/pyrazolate ligands this is still a relatively rapid decay of the reactive oxygen adduct. For **IIb** a value of around 10 h was determined for $t_{1/2}$ in propionitrile at room temperature.[65] The half-life of **IIIb** is 32 h in acetonitrile at 25 °C.[38] Thus, the half-life of **IIIb** is about 253 times as long as the half-life of the presented peroxo dicopper complex **23**. This direct comparison illustrates once again why it is difficult to handle the peroxo dicopper(II) complex based on Me$_2$TACN/pyrazolate ligand scaffolds. Moreover, this illustrates the large influence of the TACN substituents on the stability of the complexes.

Similar to Chapter 4.1.6, the decomposition of **23** was investigated for different temperatures. Also in this case, the reaction was monitored with UV/vis spectroscopy. Deviating from the previous protocol, the decay was investigated at higher temperatures. This was done in order to avoid very long measurement times. Long measurement durations increase the probability of large deviations in the recorded data due to freezing of the cryostat.

A selection of the recorded UV/vis spectra can be found in the appendix. For these experiments, the bleaching of the characteristic absorption feature of the peroxo dicopper(II) complex **23** at 497 nm in acetonitrile is of particular interest. The normalized data for the temperatures from 35 °C to –15 °C are shown in Figure 43.

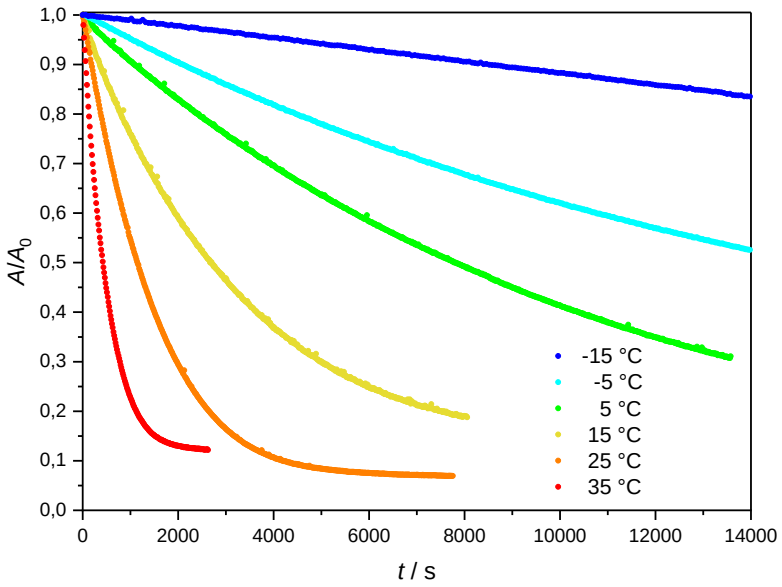

Figure 43: Bleaching of the characteristic absorption feature at 497 nm of the non-symmetric peroxo dicopper(II) complex **23** at 497 nm to the non-symmetric μ-hydroxo dicopper(II) complex **24** in a temperature range of 35 °C to –15 °C in dry MeCN.

The plot shows the bleaching of the characteristic band at 497 nm at various temperatures. Similar to the corresponding plot for the symmetric peroxo dicopper(II) complex **20** (Figure 29), it is clearly visible that lowering the temperature by 50 °C leads to a significant slowdown of the decay. The trace of the bleaching for 25 °C shows a small deviation from the expected A/A_0 end value. This can be the result of a small discrepancy that occurs during the baseline correction. Since a stock solution was used for all measurements, it can be excluded that a UV/Vis solution with a different concentration of the starting

material causes this deviation. For further analysis, only the values at the beginning of the decay are of interest. Therefore, the small difference in the end value does not affect the following results.

In order to determine the reaction order, $\ln(A/A_0)$ vs. time t was plotted, as shown in Figure 44. A linear progression was found for all temperatures. Since a plot of $1/(A/A_0)$ against time t did not show any signs of linearity, all reactions can be classified as first-order reactions.

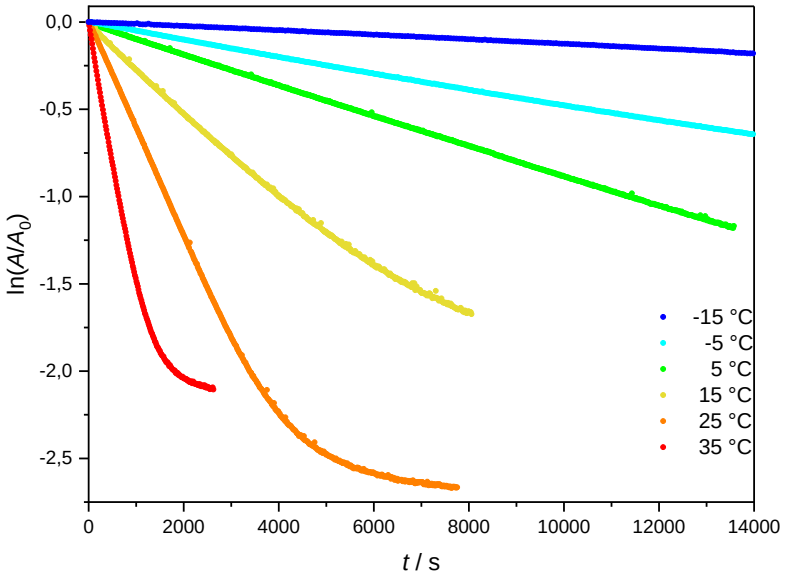

Figure 44: Plot of $\ln(A/A_0)$ against time t of the decay of the non-symmetric peroxo dicopper(II) complex **23** in dry MeCN at different temperatures.

The rate constants were calculated with help of the corresponding slopes according to Equation 5. The half-life times were calculated with Equation 6. The results are summarized in Table 11.

Table 11: Overview of the calculated kinetic data for the decay of the non-symmetric μ-1,2-peroxo dicopper(II) complex **23** to the μ-hydroxo dicopper(II) complex **24** at different temperatures in dry MeCN.

T / °C	k / s^{-1}	$t_{1/2}$ / s
35	$1.52 \cdot 10^{-3}$	456
25	$6.08 \cdot 10^{-4}$	1140
15	$2.37 \cdot 10^{-4}$	2926
5	$8.68 \cdot 10^{-5}$	7987
-5	$4.46 \cdot 10^{-5}$	15554
-15	$1.29 \cdot 10^{-5}$	53528

The rate constants k can be used to determine the activation energy E_A and the pre-exponential factor A (Equation 4). All values for an ARRHENIUS plot were calculated and are shown in Table 12.

Table 12: Overview of the calculated values for the ARRHENIUS Plot of the decomposition of non-symmetric μ-1,2-peroxo dicopper(II) complex **23** to the non-symmetric μ-hydroxo dicopper(II) complex **24** in dry MeCN.

T / °C	$1/T$ / K^{-1}	k / s^{-1}	ln$k$ / s^{-1}
35	$3.25 \cdot 10^{-3}$	$1.52 \cdot 10^{-3}$	–6.49
25	$3.35 \cdot 10^{-3}$	$6.08 \cdot 10^{-4}$	–7.41
15	$3.47 \cdot 10^{-3}$	$2.37 \cdot 10^{-4}$	–8.35
5	$3.60 \cdot 10^{-3}$	$8.68 \cdot 10^{-5}$	–9.35
-5	$3.73 \cdot 10^{-3}$	$4.46 \cdot 10^{-5}$	–10.02
-15	$3.87 \cdot 10^{-3}$	$1.29 \cdot 10^{-5}$	–11.25

Figure 45 shows the corresponding ARRHENIUS plot. As previously described, a linear fit was used to determine the slope. Form this slope an activation energy of E_A = 61.7 kJ·mol^{-1} ± 2.1 kJ·mol^{-1} was obtained. The value of the pre-exponential factor is A = 3.98 ·10^7 s^{-1}.

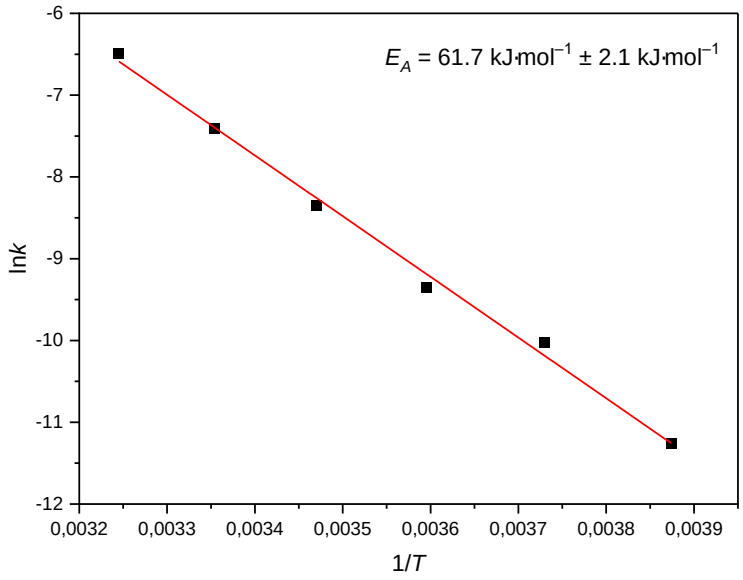

Figure 45: ARRHENIUS plot for the decomposition of the non-symmetric μ-1,2-peroxo dicopper(II) complex **23** to the non-symmetric μ-hydroxo dicopper(II) complex **24** in dry MeCN.

For the decomposition of the symmetric μ-1,2-peroxo dicopper(II) complex **20** an activation energy of E_A = 52.6 kJ·mol^{-1} ± 3.0 kJ·mol^{-1} was determined. This means that the energy barrier is lower for the symmetric complex **20** than for the non-symmetric complex **23**. Therefore, more energy is necessary for the decomposition of **23**. Both values are in the range of typical reaction in solution.[172]

These conclusion from the experimental data are not expected and remain counterintuitive. The non-symmetric peroxo dicopper(II) complex **23** is expected to have a lower activation energy and to decompose faster. This expectation is based on the expected molecular structure. In particular, it is expected that **23** displays a reduced shielding of the active site as a result of a shorter spacer in the backbone. Additionally, the methylene spacer is expected to lead to a larger bimetallic cleft which allows easier access to active site. The experimental results suggest that easy access to the active site is not that as crucial as previously assumed. It seems that the geometry of the Cu–O–O–Cu core is more important.

The molecular structure of the two peroxo dicopper(II) complexes **20** and **23** and the exact reaction mechanism of the decomposition are unknown. Therefore, it can only be speculated what factors lead to the higher activation energy for **23**.

In general, it can be stated that the higher the activation energy is the slower the reaction proceeds. To conclude, the decomposition of the non-symmetric complex **23** is slower than the decomposition of the symmetric complex **20**.

4.2.7 Summary and conclusion

The proligand $\mathbf{HL_{asym}}$ was used to gain access to the non-symmetric μ-hydroxo dicopper(II) complex **24**. Therefore, an extensive purification process was developed to produce crystalline material of **24**. Subsequent ESI mass spectrometry, UV/vis and IR spectroscopy confirmed the successful synthesis. A temperature dependent magnetic susceptibility measurement with a SQUID magnetometer revealed the strongest antiferromagnetic coupling of all known μ-hydroxo dicopper(II) complex based on TACN/pyrazolate compartmental ligands. In addition, the molecular structure in the solid-state was determined by an X-ray diffraction experiment. The Cu–Cu distance was observed to be elongated compared to the symmetric equivalents. This is expected to favor the formation of an accessible active center. Furthermore, the low steric demand of the methyl residues at the TACN do not block the access to the bimetallic cleft. The widened dicopper core may explain the instability of the corresponding reactive oxygen adducts.

Since the direct synthesis of the dicopper(I) complex **22** was not successful, the chemical reduction of μ-hydroxo dicopper(II) complex **24** was explored. UV/vis spectroscopy showed the successful conversion to **22** under reductive conditions. The formation of any intermediates was not observed. The *in-situ* formed dicopper(I) complex **22** was used to successfully synthesize the non-symmetric peroxo dicopper(II) complex **23**. In the UV/vis spectrum the characteristic features of a μ-1,2-peroxo dicopper(II) complex were found. The obtained data for **23** fitted to the absorbance features of the known peroxo dicopper(II) complexes perfectly.[38,64,110,122,123]

Similar to all peroxo dicopper(II) complexes which are based on a Me_2TACN/pyrazolate ligand scaffold, **22** showed a rapid decay.[123] The decomposition is around four times slower than the decay of the symmetric equivalent **20**. Further experiments revealed that the decomposition is a first-order reaction. Rate constants and half-lives were determined for various temperatures. The activation energy of the decomposition (E_A = 61.7 kJ·mol^{-1} ± 2.1 kJ·mol^{-1}) was determined with an ARRHENIUS plot. The activation energy is around 9.1 kJ·mol^{-1} higher than the E_A of the decomposition of symmetric derivative **20** to **21**.

4.3 Symmetric and non-symmetric hydroperoxo and superoxo dicopper(II) complexes

The successful synthesis of the novel μ-1,2-peroxo dicopper(II) complexes **20** and **23** makes it possible to explore the other reactive oxygen adducts such as the hydroperoxido or superoxido intermediates. Investigating these species in model complexes is of great interest since they are key species in catalytic substrate oxygenation and oxidation reactions in nature.[20,22] For example, the multicopper oxidase laccase can catalyze the four electron reduction of oxygen to water.[178] Thereby the formation of a cupric hydroperoxo species by protonation of the bridging peroxide intermediate is likely to be a crucial step in the oxygen reduction to water.[63,179–181]

4.3.1 Earlier studies on hydroperoxo dicopper(II) complex based on TACN/pyrazolate ligands

In previous studies the hydroperoxo dicopper(II) complexes **Ic**, **IIc** and **IIIc** based on different *i*Pr$_2$TACN/pyrazolate ligand scaffolds have been investigated (Figure 46).[38,65,121,124] Typically, these complexes are synthesized by protonation of the respective crystallized peroxo dicopper(II) complexes. For all conversions 2,6-lutidinium triflate (HLutOTf) is used as the proton source. Due to their high stability and consequently long half-lives at low temperatures, it has been possible to investigate the reversible deprotonation reaction to the cupric peroxide by addition of adequate bases. Existing studies have been able to derive the pK_a value of the hydroperoxide species by UV/vis titration experiments.[38,121,124] Additionally, the molecular structure of the μ-1,1-hydroperoxo dicopper complexes **IIc** and **IIIc** by X-ray crystallography has been determined.[38,65] Knowledge of this structure allows for further characterization by ^{1}H-NMR experiments, magnetic measurements and resonance Raman spectroscopy.[124]

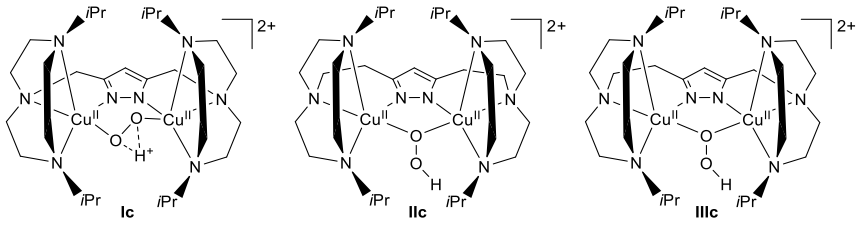

Figure 46: Established hydroperoxo dicopper(II) complexes **Ic**, **IIc** and **IIIc** based on various *i*Pr$_2$TACN/pyrazolate ligands. [38,65,121,124]

In contrast, evidence is lacking completely for hydroperoxo dicopper complexes with Me$_2$TACN/pyrazolate ligand scaffold. Recent studies have considered the peroxo dicopper(II) complex **IVb** which is based on a Me$_2$TACN/pyrazolate ligand with methylene spacers in the backbone. These recent studies show that it is not possible to convert **IVb** to the corresponding hydroperoxo dicopper complex.[123] This is probably due to the very rapid decomposition reaction of **IVb** at low temperatures.

This chapter contributes to the literature by gathering the first evidence for hydroperoxo dicopper(II) complexes based on a Me$_2$TACN/pyrazolate ligand scaffold.

4.3.2 Formation of a symmetric hydroperoxo dicopper(II) complex 25

The synthesis of a novel symmetric hydroperoxo dicopper(II) complex based on $\mathbf{HL_{sym}}$ is a multistep synthesis. This is because the crystalline material of the dicopper(I) complex **19** or the peroxo dicopper(II) complex **20** could not be isolated. Instead, the precursor **20** needs to be produced *in-situ*. This approach leads to a complex system with multiple influencing factors.

For the synthesis of **25**, crystalline compound **21** was dissolved in MeCN and reduced by cobaltocene at room temperature, as shown in Scheme 34. After cooling the reaction mixture to –40 °C, dry oxygen was added in excess. Subsequently, 1.2 eq. of 2,6-lutidinium triflate were added. Several attempts were necessary to fine tune the reaction condition and to obtain results.

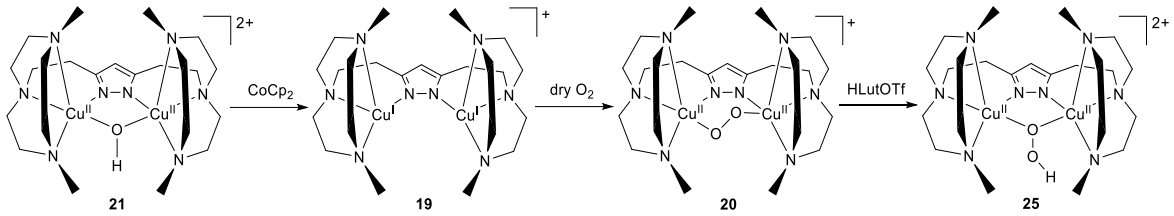

Scheme 34: Synthesis of the μ-hydroperoxo dicopper complex **25** from the μ-hydroxo dicopper complex **21**.

Eventually, a drastic change of the UV/vis spectrum occurred immediately after the addition of 2,6-lutidinium triflate, as shown in Figure 47.

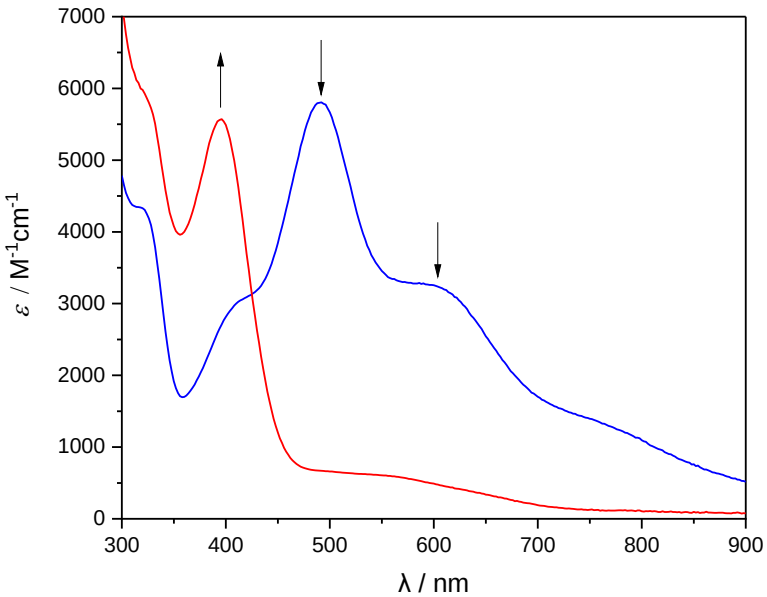

Figure 47: UV/vis spectrum of the addition of 2,6-lutidinium triflate to an in-situ generated μ-1,2-peroxo dicopper(II) complexes **20** (blue) leads to the formation of the μ-hydroperoxo dicopper complex **25** (red) in dry MeCN at –40 °C under inert conditions.

Bleaching of the characteristic absorbance features of the symmetric μ-1,2-peroxo dicopper(II) complexes **20** at 490 nm and 595 nm was observed and a new distinctive band emerged at 396 nm ($\varepsilon \approx 5600\ M^{-1}\ cm^{-1}$). Additionally, a weak band formed at 555 nm ($\varepsilon \approx 600\ M^{-1}\ cm^{-1}$). The resulting UV/vis absorbance spectrum is reminiscent of the other μ-hydroperoxo dicopper complexes based on *i*Pr$_2$TACN/pyrazolate ligand scaffolds.[38,65,121] A comparison of the characteristic bands is shown in

Table 13. The compiled and recorded data shows that the longer spacer in the ligand backbone and reduced steric demand results in a shift of λ_1 to shorter wavelength. Therefore, the new set of UV/vis data complements and extends the underlining trend. The experimental data shows that a hydroperoxo dicopper(II) complex based on a Me_2TACN/pyrazolate ligand was successfully synthesized. It seems that this is the first time this synthesis has been achieved.

Table 13: Comparison of the typical absorbance features of the hydroperoxo dicopper(II) complexes based on different TACN/pyrazolate ligand scaffolds.[38,65,121,124]

Complex	λ_1 / nm (ε / M^{-1} cm^{-1})	λ_2 / nm (ε / M^{-1} cm^{-1})
Ic	435 (6000)	620 (600)
IIIc	424 (6500)	605 (300)
IIc	416 (5700)	614 (700)
25	396 (5600)	555 (600)

An attempt was made to determine the necessary equivalents of 2,6-lutidinium triflate for the conversion by UV/vis titration. This attempt proved to be difficult because of the rapid decomposition of **20** Normally, the addition of 1.2 eq 2,6-lutidinium triflate were sufficient for producing **25**.

Earlier studies show that the μ-1,1-hydroperoxo dicopper complexes **IIc** and **IIIc** are stable over weeks at –27 °C and thus can be crystallized.[38,124] At room temperature, half-lifes of 9 h for **IIc** and 12 h for **IIIc** have been determined.[38,65] In contrast, the new hydroperoxo dicopper complex **25** is decomposing very quickly. Figure 49 shows a snapshot of the beginning rapid decay of **25** after formation. Assuming a first-order decay, a half-life of 2718 s was determined. This demonstrates again that all the dicopper complexes of the Me_2TACN/pyrazolate ligands are not stable. This is why a crystallization of this new species was impossible. However, the decomposition product is the corresponding μ-hydroxo dicopper complex.

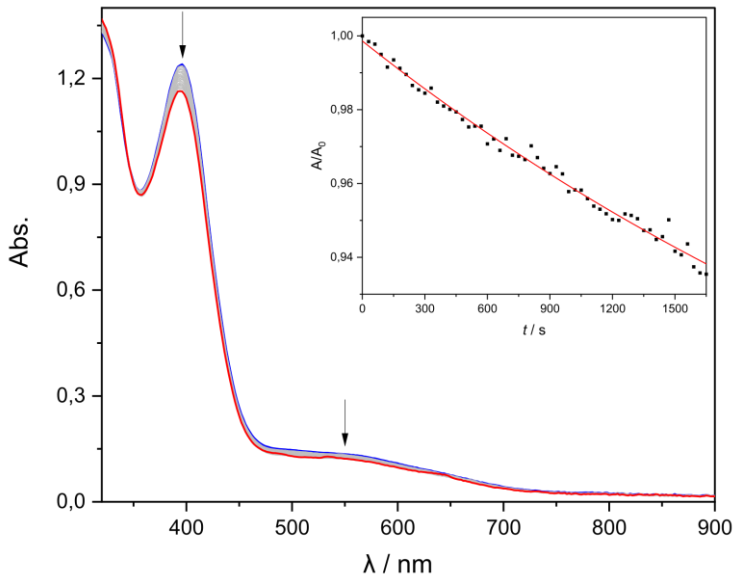

Figure 48: UV/vis spectrum of the starting decomposition of the μ-hydroperoxo dicopper(II) complex **25** (blue) to the hydroxo dicopper(I) complex **21** in dry MeCN at –40 °C under inert conditions.

Resonance Raman measurements of the frozen solution of the μ-hydroperoxo dicopper(II) were attempted. Unfortunately, the results were inconclusive even at a laser excitation wavelength of 457 nm. In particular, a poor signal-to-noise ratio and a broad signal at around 850 cm^{-1} prevented the conclusive assignment. Similar problems were encountered in previous studies of **IIc** and **IIIc**.[38,65,124] In these cases, the signal assignment was difficult and partially unambiguous, even for measurements of the crystallized compounds.

4.3.3 Formation of a non-symmetric hydroperoxo dicopper(II) complex 27

The synthesis of the non-symmetric μ-hydroxo dicopper complex **27** was based on the synthesis approach of the symmetric derivate **25**. Scheme 35 shows the adjusted synthesis route.

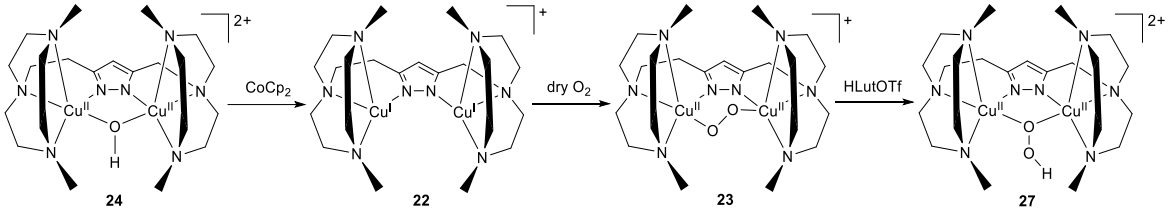

Scheme 35: Synthesis of the μ-hydroperoxo dicopper complex **27** from the non-symmetric μ-hydroxo dicopper complex **24**.

Upon addition of 2,6-lutidinium triflate a drastic change can be observed in the UV/vis spectrum which is depicted in Figure 49. A new distinctive band forms at 398 nm ($\varepsilon \approx 6100$ M^{-1} cm^{-1}) while the characteristic features of the cupric peroxide **23** bleach. Simultaneously, a weak band emerges at 591 nm ($\varepsilon \approx 600$ M^{-1} cm^{-1}). The appearance of an isosbestic point at 437 nm is a clear indication that a direct conversion is taking place.

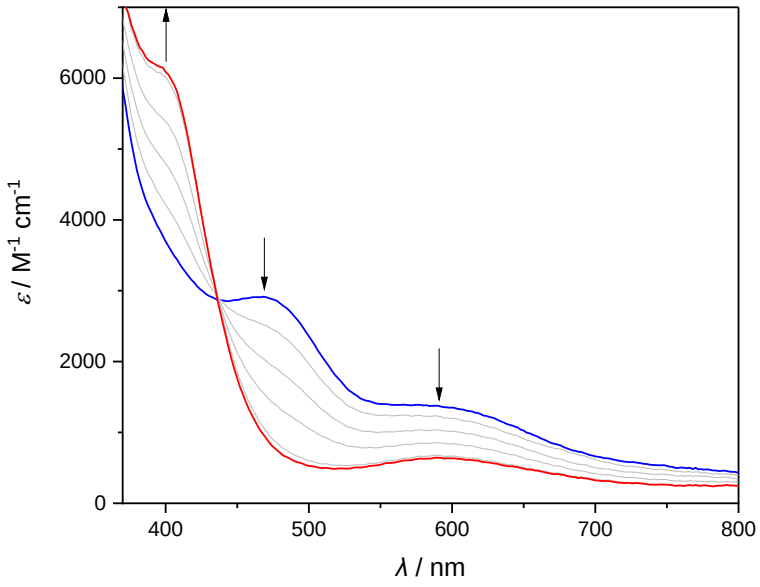

Figure 49: UV/vis spectrum of the addition 1.5 eq. of HLutOTf to the non-symmetric μ-1,2-peroxo dicopper(II) complex **23** (blue) to form the non-symmetric hydroperoxo dicopper(II) complex **27** (red) in dry EtCN at –80 °C under inert conditions.

A comparison with the previously studied hydroperoxo dicopper(II) complexes (Table 14) shows that the recorded data fits to the general trend.[38,121,124] Therefore, it can be assumed that the non-symmetric hydroperoxo dicopper(II) complex **27** was synthesized for the first time.

Table 14: Comparison of the typical absorbance features of the hydroperoxo dicopper(II) complexes based on different TACN/pyrazolate ligand scaffolds.[38,65,121,124]

Complex	λ_1 / nm (ε / M^{-1} cm^{-1})	λ_2 / nm (ε / M^{-1} cm^{-1})
Ic	435 (6000)	620 (600)
IIIc	424 (6500)	605 (300)
27	398 (6100)	591 (600)
IIc	416 (5700)	614 (700)
25	396 (5600)	555 (600)

Further experiments were attempted but were not successful. For instance, the raid decay of **27** prevented the measurement of a resonance Raman spectrum, since it was not possible to produce a frozen solution of the μ-hydroperoxo dicopper(II) without the formation of the hydroxo dicopper(II) complex **24**. Additionally, UV/vis titration experiments to determine the exact amount of needed acid were inconclusive due to the rapid decomposition.

4.3.4 Earlier studies on superoxo dicopper(II) complex based on TACN/pyrazolate ligands

Figure 50 shows the established superoxo dicopper(II) complexes of the different *i*Pr$_2$TACN/pyrazolate ligands of previous studies.[38,122,125] All of these cupric superoxides complexes are synthesized from the respective crystallized dicopper(I) complex. This is the preferred approach since a high purity of the starting materials is essential for a successful synthesis. The desired complexes have been observed after the addition of dry oxygen and an one-electron oxidant such as silver tetrafluoroborate ($AgBF_4$) or ferrocenium hexafluorophosphate ($FcPF_6$) to the reaction mixture.[38,121,160,182]

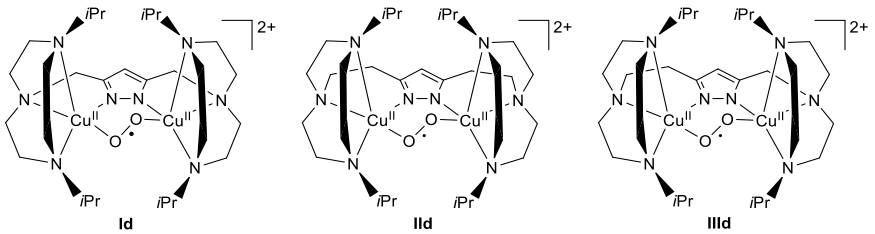

Figure 50: Established superoxo dicopper(II) complexes **Id**, **IId** and **IIId** based on different *i*Pr$_2$TACN/pyrazolate ligands.[38,122,125]

Typically, these reactive oxygen intermediates are relatively unstable and decay over time to the corresponding hydroxo dicopper(II) complexes.[38] Interestingly, it has been possible to crystallize the superoxo dicopper(II) complex **Id**, resulting in the first molecular structure of a cis-μ-1,2-superoxo dicopper(II) complex.[121,122]

In contrast, initial attempts to directly synthesize a cupric superoxide from the peroxodicopper(II) complex **IVb** based on a Me_2TACN/pyrazolate ligand scaffold have been unsuccessful.[123] This is probably due to the fact that it has not been possible to start the synthesis from the pure and crystalline dicopper(I) complex **IVa**. Moreover, it can be assumed that the target complex decomposes very rapidly. Only a stopped-flow UV/Vis experiment showed briefly the expected absorbance feature at 430 nm of a superoxo dicopper(II) complex after the addition of a saturated oxygen solution to the unique Cu^ICu^{II} complex of **IV**.[123]

In this chapter the formation of the superoxo dicopper(II) complexes of the novel Me_2TACN/pyrazolate proligands $\mathbf{HL_{sym}}$ and $\mathbf{HL_{asym}}$ are presented and discussed. Since the new hydroxo dicopper(II) complexes **21** and **24** do not form a Cu^ICu^{II} complex after one-electron reduction, a multistep synthesis approach was chosen.

4.3.5 Formation of a symmetric superoxo dicopper(II) complex 26

For the synthesis of a symmetric superoxo dicopper(II) complex **26**, the recycling of the μ-hydroxo dicopper complex **24** was used to gain access to the *in-situ* formed cupric peroxide complex **20** in MeCN at –40 °C. Subsequently, the one-electron oxidizing agent $FcPF_6$ was added to the reaction mixture, as shown in Scheme 36.

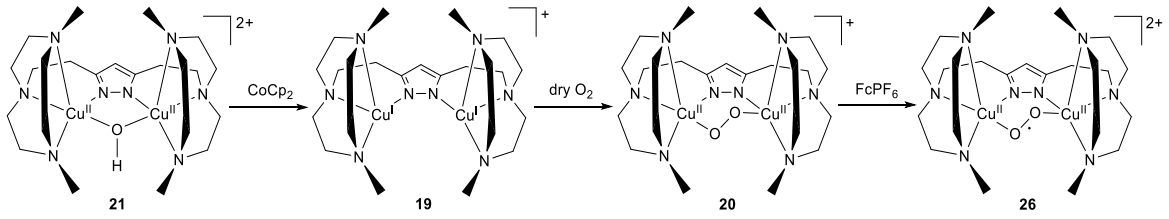

Scheme 36: Synthesis of the superoxo dicopper complex **26** from the symmetric μ-hydroxo dicopper complex **21** in MeCN.

Initial experiments showed the formation of a new band at 409 nm ($\varepsilon \approx 6500$ M^{-1} cm^{-1}) in the UV/vis spectrum (see Figure 51). Additionally, a very broad shoulder formed at 614 nm ($\varepsilon \approx 1500$ M^{-1} cm^{-1}). The originally absorbance features of the precursor **20** vanished after the addition of the oxidant.

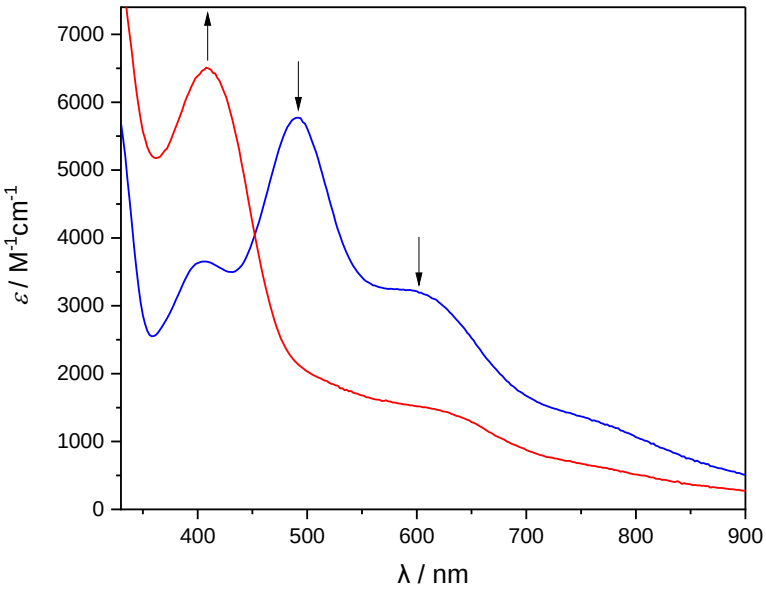

Figure 51: UV/vis spectrum of the presumed superoxo dicopper(II) complex **26** (red) synthesized from the symmetric μ-1,2-peroxo dicopper(II) complex **20** (blue) in MeCN at –40 °C.

A comparison with the established cupric superoxide complexes reveals that the obtained data does not follow the trend that is familiar from existing work, as shown in Table 15.[65,122,125] Although the methyl congener of the superoxo dicopper(II) complex **Id** showed a blueshift of a 14 nm compared to **Id**, the observed shift of 31 nm compared to the closely related **IId** is much larger.[121,123,125] Moreover, the prominent band at 409 nm is reminiscent of the hydroperoxo dicopper(II) complex **25** which is characterized by a distinctive band at 396 nm and a shoulder at 555 nm. The direct comparison also shows that it cannot be a pure hydroperoxo dicopper(II) complex. In particular, the comparison of the bands at longer wavelengths confirms this suspicion.

Table 15: Comparison of the typical absorbance features of the superoxo dicopper(II) complexes based on different TACN/pyrazolate ligand scaffolds.[38,121,122,125]

Complex	λ_1 / nm (ε / M^{-1} cm^{-1})	λ_2 / nm (ε / M^{-1} cm^{-1})
Id	444 (10000)	570 (1500)
IIId	444 (11500)	545 (2100)
IId	440 (10300)	545 (2100)

Further analysis of the UV/Vis experiment provides more information about the possible product of the reaction. As shown in Figure 52, the UV/vis spectra of the presumed superoxo dicopper(II) complex **26** (blue) starts to shift immediately after formation to the red spectrum. This spectrum with absorbance features at 391 nm and 553 nm is even more reminiscent of the hydroperoxo complex **25**. In addition, the occurring shift with an *pseudo*-isosbestic point at 375 nm is reminiscent of the typical UV/vis spectra resulting from the addition of TEMPO-H (1-hydroxy-2,2,6,6-tetramethylpiperidine) to the previously established superoxo dicopper(II) complexes.[38,122,125] Therefore a possible explanation for the recorded data is that the produced superoxo dicopper(II) complex is able to abstract H-atoms from a weak R-H

bond. This would explain the formation of a hydroperoxo dicopper(II) complex **25**. The source of the H-atom in this proposed H-atom abstraction remains unknown.

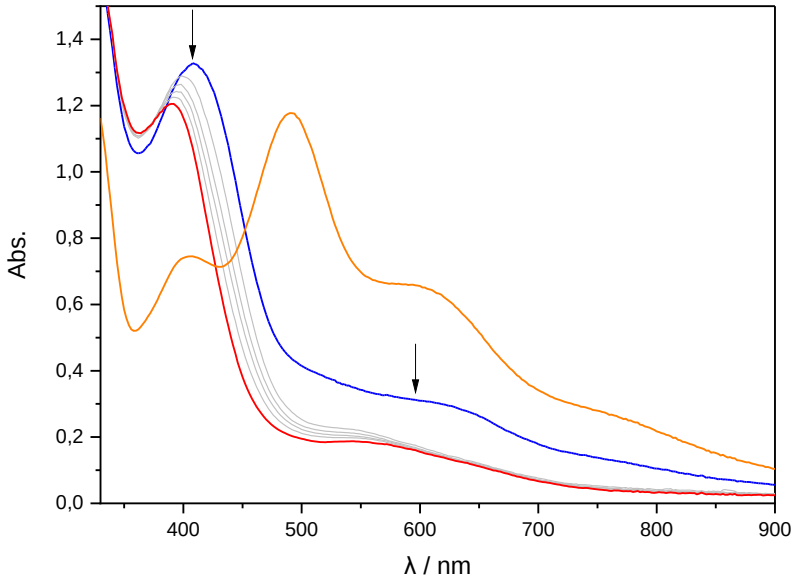

Figure 52: UV/vis spectrum of the presumed superoxo dicopper(II) complex **26** (blue) in MeCN at –40 °C. Directly after the formation occurs a fast shift of the bands to a presumed hydroperoxo dicopper(II) complex **25** (red). The initial spectrum of the symmetric μ-1,2-peroxo dicopper(II) complex **20** is shown in orange for comparison.

Since all previous hypotheses are only based on the comparison of characteristic UV/vis absorbance features, it was tested if it is possible to regain the peroxo dicopper(II) complex **20** after the formation of the presumed superoxo dicopper(II) complex **26**. To this end, cobaltocene was added as a reductant to the reaction mixture after formation of **26**. The resulting UV/vis spectrum is shown in Figure 53 and shows the reversibility of the one-electron oxidation.

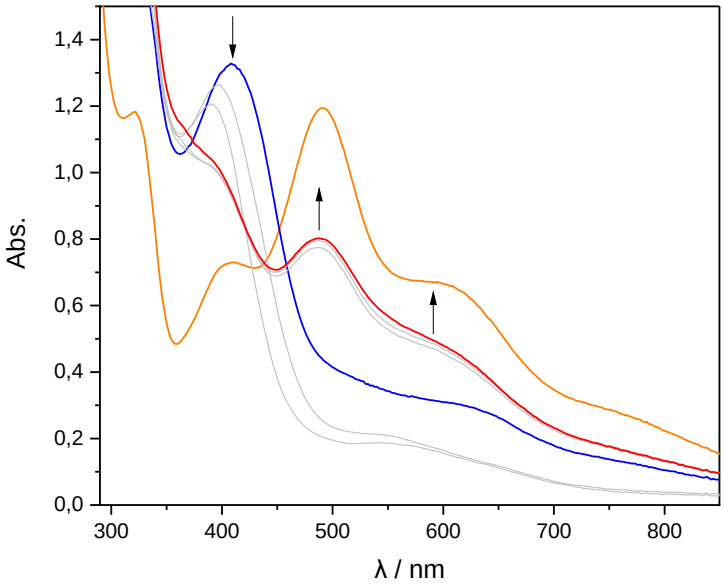

Figure 53: UV/vis spectrum of the addition of cobaltocene (1.10 eq.) to the presumed superoxo dicopper(II) complex **26** (blue) in MeCN at –40 °C. The resulting peroxo dicopper(II) complex is shown in red. For comparison is the original peroxo dicopper(II) complex **20** shown in orange.

After addition of $FcPF_6$ to **20** and formation of the presumed superoxo dicopper(II) complex (blue spectrum), the reducing agent $CoCp_2$ was added immediately and the typical bands of the cupric peroxide **20** formed. Comparing the resulting spectrum (red spectrum) with the original spectrum of **20** (orange spectrum), shows that a quantitative recovery of **20** was not achieved. This can be explained by the rapid decay of all involved species.

Since the discussed shift of the distinctive band is fast and occurs immediately after the addition of the oxidizing agent, **26** was synthesized at even lower temperatures to identify the initial UV/vis spectrum of **26**. Therefore, the synthesis of **26** was performed in propionitrile (EtCN) at –80 °C. The resulting UV/vis spectrum is shown in Figure 54.

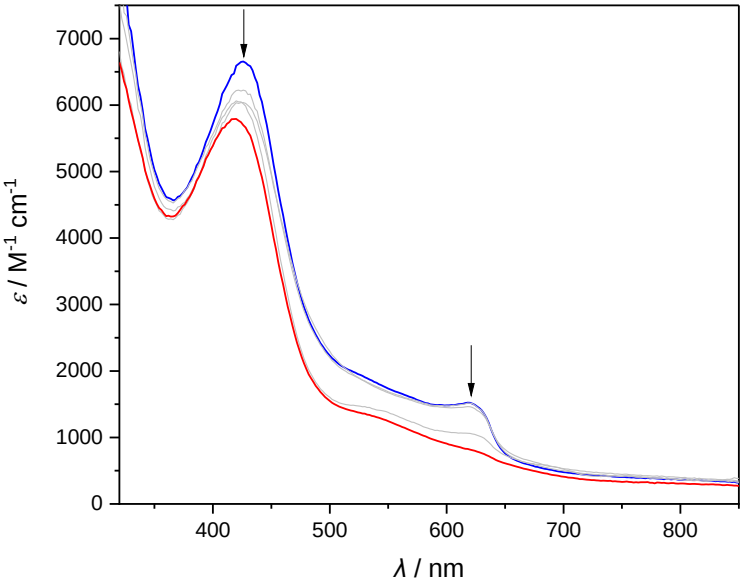

Figure 54: UV/vis spectrum of the presumed superoxo dicopper(II) complex **26** (blue) in EtCN at –80 °C. Directly after the formation of **26** occurs a shift to the red spectrum.

A distinctive band at 426 nm ($\varepsilon \approx 6700\ M^{-1}\ cm^{-1}$) formed due to the oxidation of the peroxo dicopper(II) complex **20**. This absorbance feature is more similar to the known bands of a superoxo dicopper(II) complex based on a Me_2TACN/pyrazolate ligand.[123] It is noted that the molar attenuation coefficient deviates strongly from the previous reported values.[38,122,125] The main reason for this is that this value is influenced by the ongoing decomposition. This probably applies to all the novel reactive oxygen adducts but the decay has the greatest effect on the superoxo dicopper(II) complex **26**. This results in a smaller coefficient. Additionally, even the solvent, pH value and the temperature can influence the molar attenuation coefficient.

The initial spectra show an additional band at 619 nm which can be assigned to the ferrocenium.[183] Since the oxidant $FcPF_6$ was added in a slight excess (1.2 eq.) and the reaction was slower, theses spectra are probably a snapshot in time of the initial formation of the superoxo dicopper(II) complex. Another explanation may be that the superoxo dicopper(II) complex is still being formed and therefore unconsumed ferrocenium is still visible. Simultaneously, the presumed reaction to hydroperoxo complex **25**

is already taking place. This implies that the recorded UV/vis spectrum may results from a product mixture of **25** and **26**.

More evidence is needed to support or disprove these explanations. Unfortunately, it was not possible to perform electron paramagnetic resonance (EPR) or resonance Raman spectroscopy (rR). The procedure of freezing the reaction mixture in liquid nitrogen results in a blue colored solution which clearly indicates the formation of the decomposition product **21**.

4.3.6 Formation of a non-symmetric superoxo dicopper(II) complex 28

The non-symmetric superoxo dicopper(II) complex **28** was synthesized like the symmetric derivative **26** (Scheme 37). In particular, the peroxo dicopper complex **23** was produced *in-situ*, as described in chapter 4.2. Subsequent oxidation of **23** with ferrocenium hexafluorophosphate gave the superoxo dicopper(II) complex **28**.

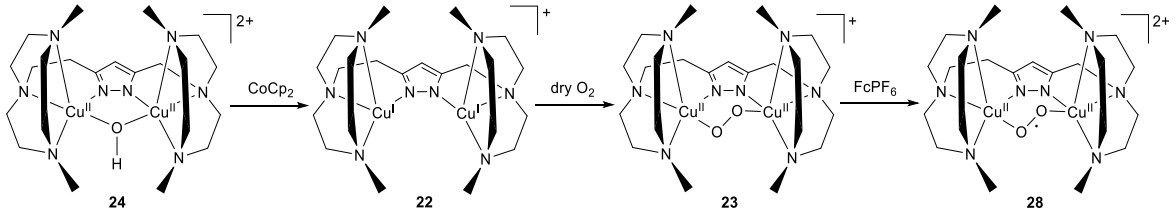

Scheme 37: Synthesis route for the non-symmetric superoxo dicopper(II) complex starting from the non-symmetric μ-hydroxo dicopper complex **24**.

Based on the findings for the synthesis of the symmetric superoxo dicopper(II) complex **26**, the synthesis of the non-symmetric derivative **28** was also carried out in propionitrile at lower temperatures. In this case a temperature of –60 °C proved to be sufficient because the non-symmetric reactive oxygen intermediates typically do not decompose as rapidly and are more stable in solution. The entire synthesis was monitored by UV/vis spectroscopy and the crucial reaction of the μ-1,2-peroxo dicopper complex **23** with the oxidant is shown in Figure 55.

Addition of the oxidizing agent leads to a bleaching of the characteristic absorbance features of **23**. At the same time, a new distinctive band rises at 412 nm ($\varepsilon \approx 9500\ M^{-1}\ cm^{-1}$) and a weak band forms at 562 nm ($\varepsilon \approx 1700\ M^{-1}\ cm^{-1}$). A *pseudo*-isosbestic points emerges at 464 nm during the formation of the presumed non-symmetric superoxo dicopper(II) complex **28**. Since only minimal deviations from the ideal isosbestic point were observed, it was assumed that a direct conversion had occurred. Even though the distinctive band was expected to be at around 425 nm, the molar attenuation coefficient is still in the typical range of previously studied superoxo dicopper(II) complexes (see Table 15 for comparison).

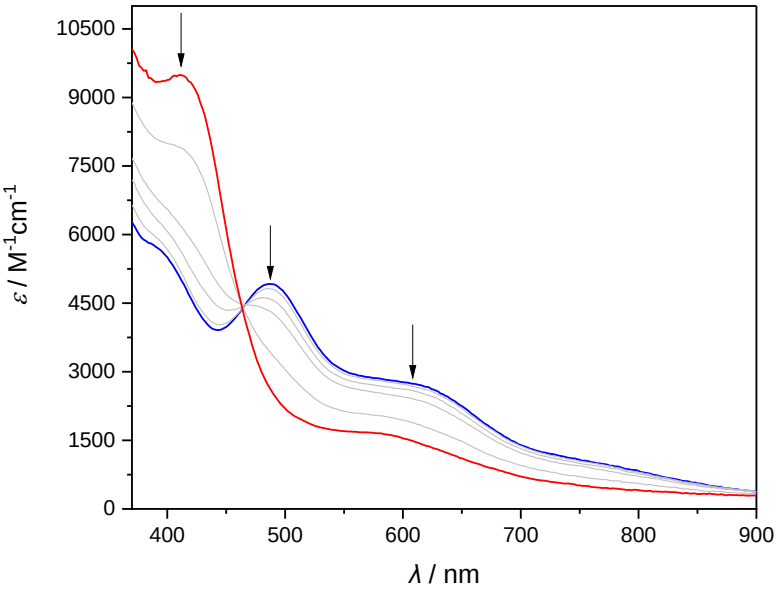

Figure 55: UV/vis spectrum of the addition of $FcPF_6$ (1.2 eq.) to the non-symmetric peroxo dicopper(II) complex **23** (blue) in dry EtCN at –60 °C. The spectrum features a *pseudo*-isosbestic point at 464 nm.

In contrast to the symmetric congener, a band of the oxidant was not observed in the recorded UV/vis data. Additionally, there are no signs of a subsequent shift of the distinctive band and formation of the respective hydroperoxo dicopper(II) complexes **27**.

It can be concluded, that the presumed non-symmetric superoxo dicopper(II) complex **28** is more stable than the symmetric derivate **26**. Nonetheless, further investigation by EPR or rR spectroscopy were hampered by the rapid thermal decay of the species of interest. All attempts of producing a frozen solution of **28** for further experiments ended in the instant formation of **23** which is the decomposition product.

4.3.7 Summary and conclusion

In this chapter, the attempts to synthesize the other reactive oxygen adducts based on the reductive recycling of the corresponding hydroxo dicopper(II) complex were described and discussed. Since these species must be synthesized *in-situ* by sequential reactions, the analysis and interpretation of the recorded UV/vis data were complicated due to a variety of possible side products and byproducts. Additionally, the rapid decay of the involved dicopper complexes made it difficult to carry out further experiments. For instance, conclusive titration experiments or resonance Raman measurements were not possible.

Despite these challenges, the hydroperoxo dicopper(II) complexes of the novel Me_2TACN/pyrazolate ligands were synthesized for the first time. UV/vis data shows the expected characteristic absorbance features of cupric hydroperoxides complexes. The distinctive bands for the novel hydroperoxo dicopper(II) complexes **25** and **27** are shifted slightly to a shorter wavelength compared to the established

species.[38,65,121,124] Furthermore, the cupric hydroperoxides **25** and **27** decompose rapidly to the respective hydroxo dicopper(II) complexes.

The syntheses of the superoxo dicopper(II) complexes **26** and **28** were successful at –40 °C. The assignment of the absorbance features in the resulting UV/vis spectrum of the symmetric derivate **26** were influenced by a subsequent reaction. The recorded UV/vis data shows that the formed superoxo dicopper(II) compley **26** is probably converted rapidly into the hydroperoxo dicopper(II) complex **25**. This consecutive reaction can be explained by a hydrogen abstraction reaction, but the origin of the needed hydrogen atoms remains inconclusive. Measurements at even lower temperatures (–80 °C) showed the initial UV/vis spectrum of **26**. Additionally, reformation of the precursor peroxo dicopper(II) complex **20** was established by the addition of cobaltocene to **26**.

5 Interaction of the peroxo dicopper(II) complexes with lithium and calcium cations

5.1 Earlier studies on interactions of the Cu_2O_2 core with Lewis acids

Previous works have revealed that the Lewis basic peroxo moiety of the peroxo dicopper(II) complexes based on TACN/pyrazolate ligands can interact with Lewis acids such as the alkali metal ions Li^+, Na^+ and K^+.[38,65,110,111] In particular, the work of BRINKMEIER *et. al.* has demonstrated impressively the influences of alkali metal ions on the electronic structure of the peroxo dicopper(II) complex **Ib**.[121] The synthesis of the alkali metal ion adducts is shown in Scheme 38. The formation of these adducts have not only been investigated in resonance Raman and electrochemical studies. It has also been possible to crystallize these adducts.[111]

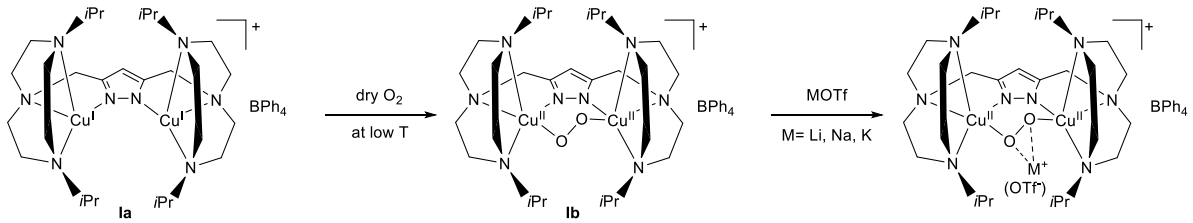

Scheme 38: Synthesis of the alkali metal ion adducts of the peroxo dicopper(II) complex.[110,111,121]

Furthermore, titrations of the peroxo dicopper(II) complex **Ib** with alkali metal triflate salts reveal dramatic changes in the UV/vis spectrum.[111,121] It has been found that the characteristic features of the peroxo dicopper(II) complex at λ_1 and λ_2 shift to a shorter wavelength and that in particular the intensity of the CT band at λ_2 ($\pi_\nu^* \rightarrow Cu^{II}$) was decreases upon addition of the cations.[111] The observed blueshift is most pronounced for Li^+ and decreased to K^+.[121]

KINDERMANN has demonstrated that the peroxo dicopper(II) complex **IIb** is able to interact with Lewis acid in solution, such as Sc^{3+}, Zn^{2+} and Li^+.[65] Later SPYRA has extended the studies of the alkali metal ions interactions to the non-symmetric cupric peroxide **IIIb** and was able to isolate the Na^+-adduct in solid state.[38] UV/vis monitored experiments verify the prior observations made by BRINKMEIER *et. al.*, such as the blue shift and intensity changes of the CT-bands.[38,121]

5.2 Interaction of the peroxo dicopper(II) complexes 20 and 23 with lithium ions

In contrast to the previously studied cupric peroxides, the symmetric and non-symmetric μ-1,2-peroxo dicopper(II) complexes **20** and **23** are based on Me_2TACN/pyrazolate ligands. Since this reduces their steric demand, the potential formation of adducts with Lewis acids is expected to be easier. Furthermore, the formation of adducts with larger ions may be possible, if the Cu_2O_2 core is less shielded. On the other hand, **20** and **23** can only be prepared *in-situ*. In an UV/vis monitored experiments, this may lead to new bands with bands overlapping bands from prior reactions (e.g. the chemical reduction with

$CoCp_2$). In addition, the decomposition reactions of **20** and **23** discussed above must be taken into account.

5.2.1 A novel lithium ion adduct

For the synthesis of the symmetric lithium ion adduct **29**, the symmetric dicopper(I) complex **19** was generated *in-situ* under inert conditions in acetonitrile at 25 °C. Addition of dry oxygen led to the formation of the symmetric peroxo dicopper(II) complex **20** at –40 °C. Finally, the addition of 10 eq. of lithium triflate gave **29**, as depicted in Scheme 39. The whole reaction was monitored by UV/vis spectroscopy. The most relevant spectra are shown in Figure 56.

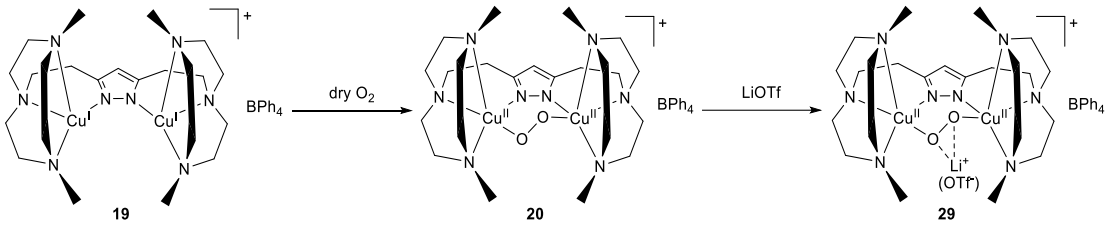

Scheme 39: Synthesis route of the symmetric lithium ion adduct **29** by addition of 10 eq. LiOTf to the symmetric μ-1,2-peroxo dicopper(II) complex **20** at –40 °C in MeCN.

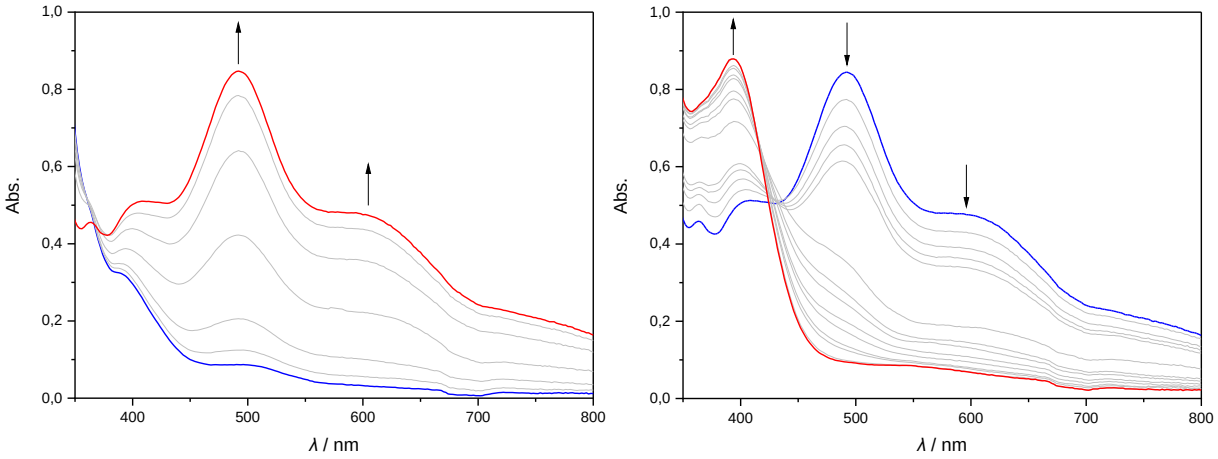

Figure 56: Left: UV/vis spectrum of the formation of the symmetric μ-1,2-peroxo dicopper(II) complex **20** (red) by addition of an excess of dry oxygen to the dicopper(I) complex **19** (blue) at –40 °C in MeCN. Right: UV/vis spectrum of the synthesis of the presumed symmetric lithium ion adduct **29** (red) by addition of 10 eq. LiOTf to the symmetric μ-1,2-peroxo dicopper(II) complex **20** (blue) at –40 °C in MeCN. The spectrum features two isosbestic points at 416 nm and 429 nm.

The recorded UV/vis spectra confirmed the successful synthesis of **20**. In particular, the characteristic bands of a μ-η^1:η^1-peroxo dicopper(II) complex were observed at 490 nm and 595 nm. The addition of 10 eq. lithium triflate led to a color change of the solution from purple to green. In the UV/vis spectrum, this can be detected as a distinctive new band at 394 nm and a weak and broader band at 552 nm. Interestingly, two isosbestic points at 416 nm and 429 nm formed at the same time. In a first step, the isosbestic point at 429 nm formed. In a consecutive step, the isosbestic point at 416 nm occurred. This result suggests that an intermediate species is involved in the reaction. It is noted that the distinct features of

29 are very similar to the characteristic bands of the symmetric hydroperoxo dicopper(II) complex **25** which has distinctive bands at 394 nm and 555 nm.

The last observation was also made in earlier studies of KINDERMANN.[65] In her study, adding 410 eq. lithium triflate to the peroxo dicopper(II) complex **IIb** results in the observation of the typical bands of the corresponding hydroperoxo dicopper(II) complex **IIc** in the UV/vis spectrum. KINDERMANN hypothesizes that traces of water in the reaction mixture may have been hydrolyzed with the Lewis acid acting as a catalyst. These protons may then react with the peroxide-unit to form the hydroperoxo dicopper(II) complex. Since no isosbestic points are observed, KINDERMANN concluded that intermediates are formed during the reaction.[65]

Taking these prior reported results and the hypotheses into account, a new reaction pathway is proposed. It is shown in Scheme 40.[65] The addition of the lithium triflate leads to a side-on or end-on coordinate lithium peroxo adduct (**29** and **29b**) in the bimetallic cleft. In a consecutive step, protons are hypothesized to react with the intermediates to the hydroperoxo dicopper(II) complex **25**. This reaction pathway explains the occurrence of the consecutive isosbestic points and the characteristic bands of **25**.

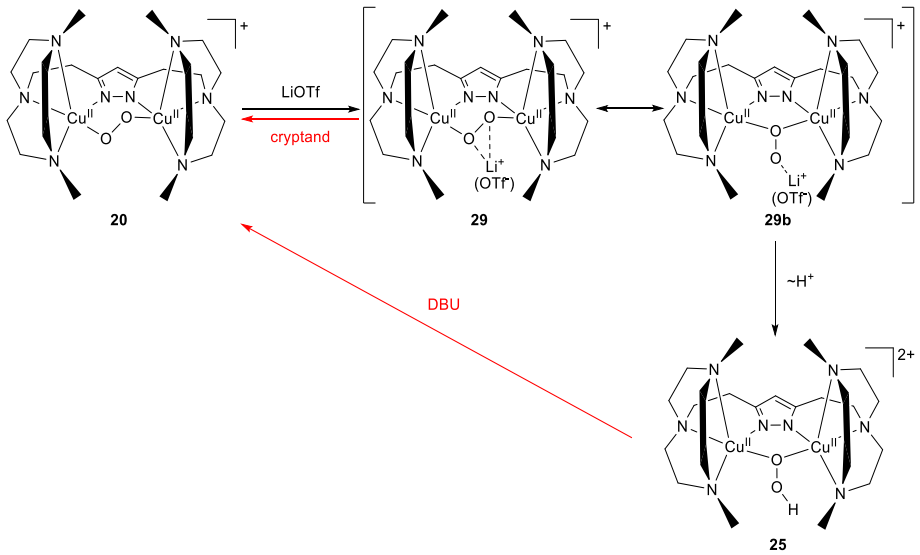

Scheme 40: Proposed reaction pathway for the synthesis to the hydroperoxo dicopper(II) complex **25** by protonation of the lithium ion adduct intermediate **29** or **29b**. In red are the reverse reactions denoted which were used to verify the proposed chemical reaction path.

Even though this theory fits the recorded data, the presence of water as a proton source in the reaction mixture is very unlikely. The *in-situ* formed symmetric dicopper(I) complex **19** and also the corresponding peroxo dicopper(II) complex **20** are known to be very sensitive to impurities. In the presence of water, they are expected to decompose immediately to the hydroxo dicopper(II) complex **21**. In order to verify whether the reaction proceeds as hypothesized, further experiments were carried out. For this purpose, two possible reverse reactions of the proposed reaction scheme were selected. The first reverse reaction is based on the following reasoning: if a hydroperoxo dicopper(II) complex is present it should be possible to regain the peroxo dicopper(II) complex **20** by adding a base. Typically, a hydroperoxo

dicopper(II) complex based on the TACN/pyrazolate scaffold can be deprotonated by 1,8-Diazabicyclo[5.4.0]undec-7-ene (DBU).[38,65,121,124] The second reverse reaction is based on the following reasoning: if the lithium peroxo adducts **29** or **29b** are the end product of the reaction the addition of a cryptand should also yield the peroxo dicopper(II) complex **20**. The cryptand 4,7,13,16,21,24-Hexaoxa-1,10-diazabicyclo[8.8.8]hexacosane is particularly suitable for removing lithium ions from the reaction mixture. These two reverse reactions are shown in red in Scheme 40.

First the addition of the [2.2.2] cryptand was tested. Therefore, the presumed lithium peroxo adduct **29** was synthesized again by the addition of 10 eq. of LiOTf to the *in-situ* generated peroxo dicopper(II) complex **20**. Subsequently, 12 eq. of the cryptand in acetonitrile were added at –40 °C. The corresponding UV/vis spectra are shown in Figure 57. Apart from a minor contamination at 360 nm which comes from the chemical reduction, the recorded data are consistent with the previous measurement. However, the addition of 12 eq. of the cryptand in acetonitrile at –40 °C, resulted in an immediate change of the UV/vis spectrum. The distinctive features of the lithium peroxo adduct started to bleach and the characteristic features of the former μ-1,2-peroxo dicopper(II) complex **20** were regained. Especially, interesting is the fact that an isosbestic point at 431 nm was observed. An identical isosbestic point at similar wavelength was found for the addition of lithium triflate to the cupric peroxide **20**. The expected second isosbestic point at 416 nm could not be observed. Since the reaction was very fast, it is possible that the UV/vis spectrometer could not resolve this isosbestic point. A promising approach for future research is to use a stopped-flow UV/vis experiment at low temperatures. This may lead to an improved measurement and show whether the first isosbestic point really exists in the reverse reaction.

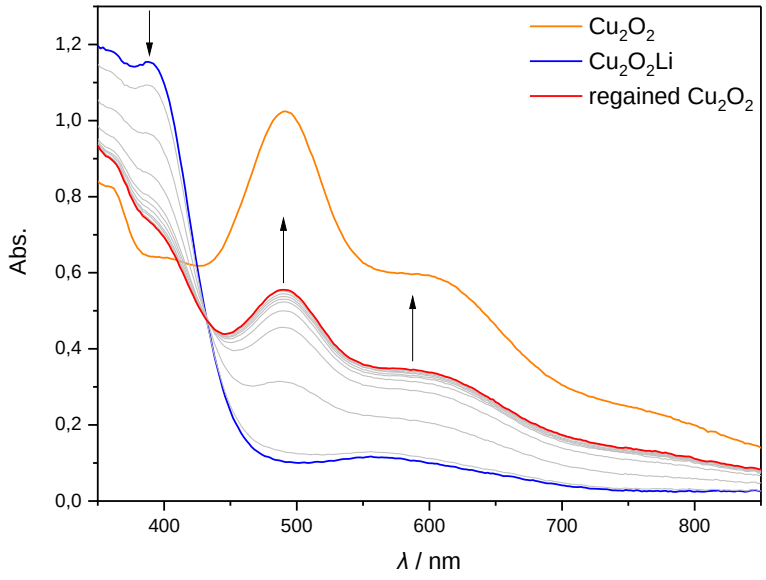

Figure 57: UV/vis spectra of the addition of 12 eq. of [2.2.2] cryptand to the presumed hydroperoxo dicopper(II) complex **25** (blue) at –40 °C in MeCN. The peroxo dicopper(II) complex **20** (red) is regained. The spectrum features an isosbestic points at 431 nm. For comparison, the spectrum of the peroxo dicopper(II) complex **20** prior to the addition of 10 eq. LiOTf is also shown (orange).

The addition of the base DBU to the presumed hydroperoxo dicopper(II) complex did not lead to any significant changes in the UV/vis spectrum. Therefore, a revised reaction pathway is needed. In conclusion, even though the distinct bands are reminiscent of the characteristic bands of the hydroperoxo dicopper(II) complex **25** a new lithium peroxide adduct was formed. Instead of the μ-1,1-OOH moiety of **25**, a structurally very similar μ-1,1-O_2 unit seems to be interacting with the lithium ion.[65] This may explain a very similar electronic structure of **25** and **29b**. Therefore, the final product of the addition of LiOTf is probably the lithium ion adduct **29b**. The appearance of consecutive isosbestic points suggests that an intermediate is involved in the reaction. Presumably, this is the molecule **29** shown in Scheme 41.

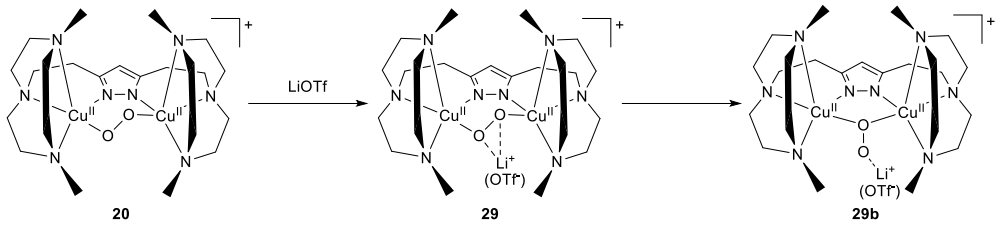

Scheme 41: Revised reaction pathway for the synthesis to of the lithium ion adduct **29b** via the lithium ion adduct intermediate **29**.

The regained characteristic bands of **20** have a lower intensity. This is caused by the typical decomposition of the dicopper complexes of the Me_2TACN/pyrazolate type. Additionally, a larger excess of the [2.2.2] cryptand may be needed. It cannot be excluded that a chemical equilibrium is present. Indeed, previous studies have shown that, for expamle, the peroxo dicopper(II) complex **Ib** is able to extract lithium cations from the corresponding crown ether due to a very high affinity for Li^+.[111,121]

In this experiment, an unprecedented lithium ion adduct was observed. This observation challenges the conclusions of earlier studies.[65] Therefore, the previous findings will be put to the test in chapter 5.2.3.

5.2.2 Interaction of the peroxo dicopper(II) complexes 23 with lithium ions

It was also tested if a non-symmetric lithium ion adduct can be synthesized. To this end, crystalline material of the non-symmetric μ-hydroxo dicopper(II) complex **24** were dissolved in acetone and chemically reduced to the corresponding dicopper(I) complex **22** at room temperature. As depicted in Scheme 42, the μ-1,2-peroxo dicopper(II) complex **23** was formed by the addition of dry oxygen to the precursor **22** at –40 °C. Subsequently, 23 eq. of lithium triflate were needed to form the potential lithium ion adduct **30**. The whole reaction was monitored by a temperature-controlled UV/vis spectrometer.

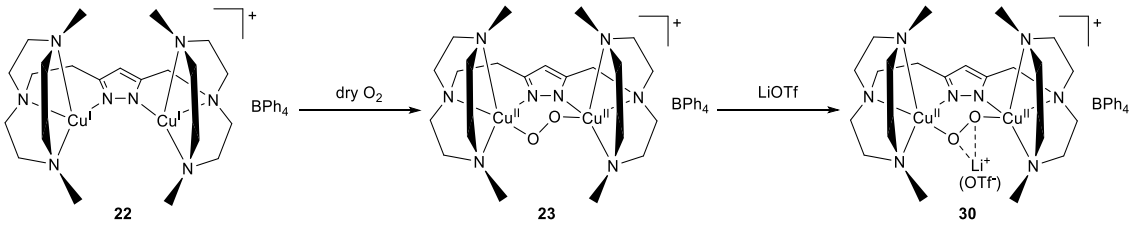

Scheme 42: Synthesis route of the non-symmetric lithium ion adduct **30** by addition of 23 eq. LiOTf to the non-symmetric μ-1,2-peroxo dicopper(II) complex **23** at –40 °C in acetone.

Figure 58 shows the UV/Vis spectrum of the crucial step of the synthesis, the addition of lithium triflate to the peroxo dicopper complex **23**. The blue colored spectrum shows the characteristic bands of the μ-1,2-peroxo dicopper(II) complex **23**. Addition of lithium triflate leads to dramatic changes in the UV/vis spectrum. The characteristic features of **23** at 494 nm and 608 nm start to bleach and a distinctive shoulder starts to form at 401 nm. An additional band forms at 590 nm as a broad shoulder. Although the displayed spectrum suggests that an isosbestic point forms at 416 nm, closer inspection revealed that no isosbestic point has formed. This observation implies the formation of intermediates and complicates the explanation of the reaction process.

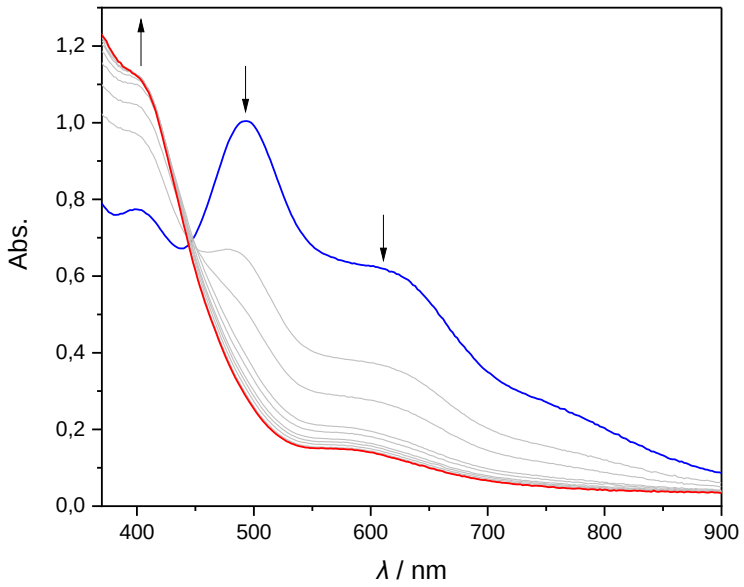

Figure 58: UV/vis spectra of the addition of 23 eq. lithium triflate to the *in-situ* generated non-symmetric peroxo dicopper(II) complex **23** (blue) at –40 °C in acetone.

The data from this experiment allows only limited conclusions about the final product. Only shoulders are formed and no isosbestic points can be observed. In particular, the shoulder at 401 nm is strongly influenced by an underlining band that is already visible in the spectrum of the peroxo dicopper complex. In order to rule out the possibility that these results were influenced by minor impurities of the used precursor, the experiment was repeated with different batches. The results were the same. At this point, the experiments were deemed inconclusive and no further investigation was conducted. The partial results still motivate further research as they show similar bands to those found for the symmetric case

and to the non-symmetric hydroperoxo dicopper(II) complex. This suggest, a similar coordinated lithium ion adduct may be present.

5.2.3 Interaction of the peroxo dicopper(II) complexes IIb with lithium ions

The investigation of the symmetric lithium ion adduct **29b** revealed that no hydroperoxo dicopper(II) complex **25** was formed. This contradicts conclusions from previous work. In order to re-evaluate earlier studies, the lithium adduct formation of the symmetric peroxo dicopper(II) complex **IIb** was investigated.[65] This complex is based on an *i*Pr$_2$TACN/pyrazolalte ligand scaffold instead of the Me$_2$TACN/pyrazolate ligand. The same experimental setup as in previous experiments was chosen to ensure that the results are comparable. In particular, the hydroxo dicopper(II) complex **IIe** was used as starting material, although the dicopper(I) complex **IIa** or even the peroxo dicopper(II) complex **IIb** were also available as crystalline starting material. Similar to the procedure described in chapter 5.2.1, the hydroxo dicopper(II) complex **IIe** was chemically reduced by the addition of cobaltocene in acetonitrile at room temperature. The *in-situ* formed dicopper(I) complex **Ia** was exposed to dry oxygen at –40 °C, as shown in Scheme 43. Subsequent addition of 400 eq. lithium triflate to **IIb** gave the presumed lithium ion adduct **IIf**.

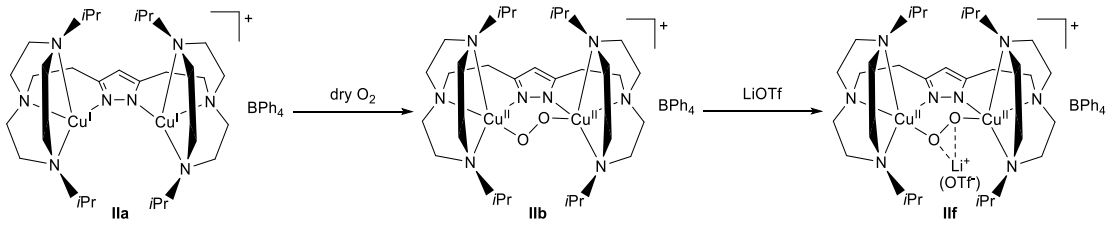

Scheme 43: Synthesis route of the presumed lithium ion adduct **IIf** by addition of 400 eq. LiOTf to the symmetric μ-1,2-peroxo dicopper(II) complex **IIb** at –40 °C in MeCN.

All reactions were monitored by UV/vis spectroscopy and the resulting spectra of the last two reactions are depicted in Figure 59. The left UV/vis spectrum shows the formation of the μ-1,2-peroxo dicopper(II) complex **IIb**. Addition of dry oxygen in excess resulted in the formation of the expected distinctive bands of **IIb** at 506 nm and 600 nm. The other UV/vis spectrum shows the addition of lithium triflate to **IIb** which led to an immediate bleaching of the characteristic features of **IIb** and the formation of a band at 416 nm and a broader and weaker band at 605 nm. Additionally, an isosbestic point at 452 nm formed. The presented results are similar to the results of the earlier studies even though the synthesis route is different.[65] This shows that the prior results are reproducible. The newly formed bands were first assigned to the lithium ion adduct **IIf**. Since the new bands are similar to the characteristic bands of the hydroperoxo dicopper(II) complex **IIc**, KINDERMANN concludes that traces of water in the reaction mixture are probably hydrolyzed with help of the Lewis acid acting as a catalyst and therefore **IIb** is just protonated.[65]

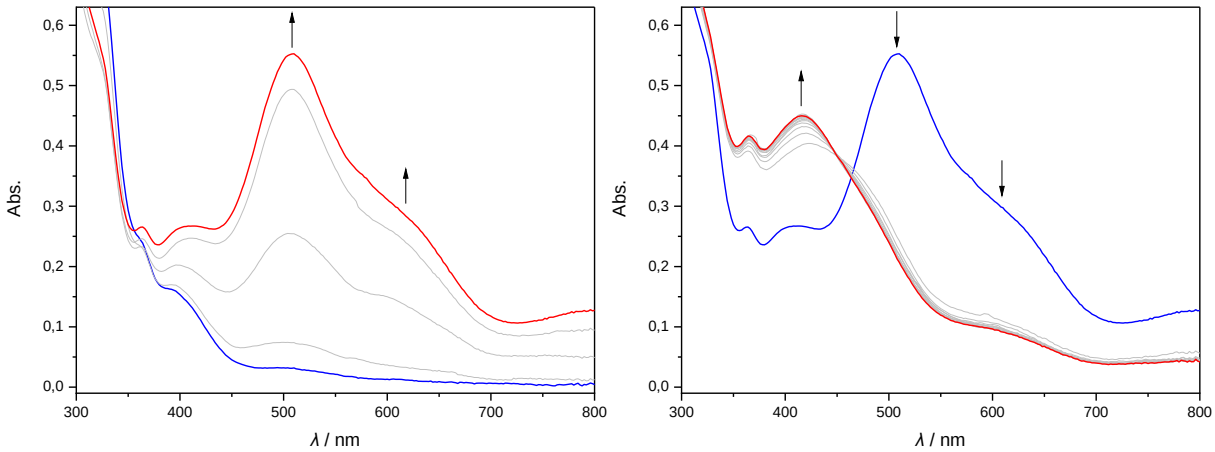

Figure 59: Left: UV/vis spectrum of the formation of the μ-1,2-peroxo dicopper(II) complex **IIb** (red) by addition of an excess of dry oxygen to the dicopper(I) complex **IIa** (blue) at –40 °C in MeCN. Right: UV/vis spectrum of the synthesis of the presumed lithium ion adduct **IIf** (red) by addition of 400 eq. LiOTf to the symmetric μ-1,2-peroxo dicopper(II) complex **IIb** (blue) at –40 °C in MeCN. The spectrum features an isosbestic points at 452 nm.

This conclusion is challenged by the experiments below (Scheme 44). The formation of the possible lithium adducts **IIf** and **IIg** or the hydroperoxo dicopper(II) complex **IIc** were tested by the reverse reactions. On the one hand, the addition of the [2.2.2] cryptand can confirm the formation of **IIf** or **IIg**. On the other hand, addition of the non-nucleophilic and strong base DBU to the reaction mixture can show if **IIc** has been formed.

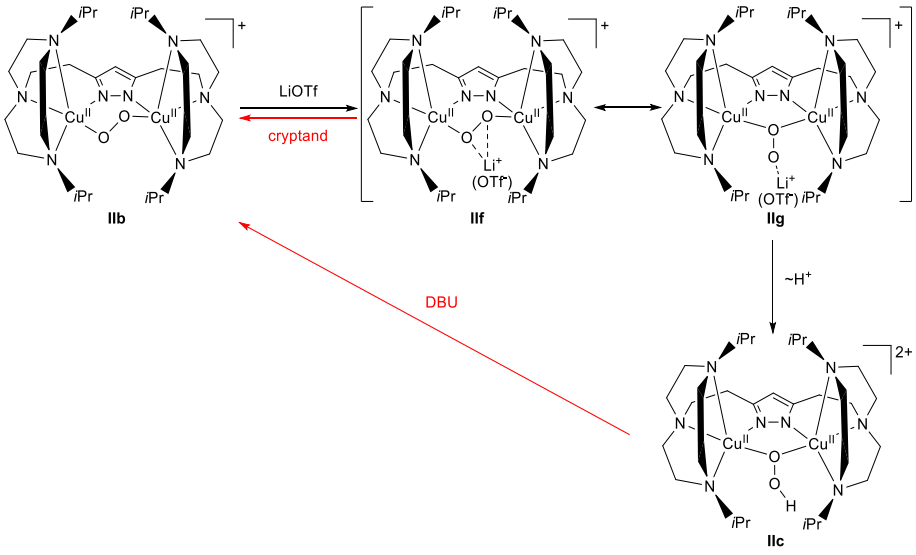

Scheme 44: Proposed reaction pathway for the synthesis to the hydroperoxo dicopper(II) complex **IIc** by protonation of the lithium ion adduct intermediate **IIf** or **IIg**. In red are the reverse reactions denoted which were used to verify the proposed chemical reaction path.[65]

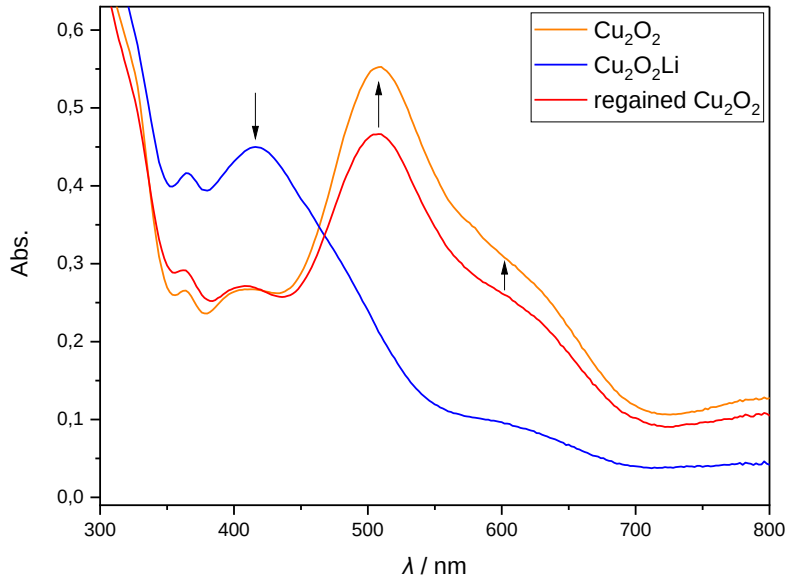

Figure 60: UV/vis spectra of the addition of 400 eq. of [2.2.2] cryptand to the presumed hydroperoxo dicopper(II) complex **IIc** (blue) at –40 °C in MeCN. The peroxo dicopper(II) complex **IIb** (red) is regained. For comparison, the spectrum of the peroxo dicopper(II) complex **IIb** prior to the addition of 400 eq. LiOTf is shown in orange.

The result of the addition of 400 eq. of the [2.2.2] cryptand 4,7,13,16,21,24-Hexaoxa-1,10-diazabicyclo[8.8.8]hexacosane to the reaction mixture is shown in Figure 60. The recorded UV/Vis spectrum shows the regeneration of the former bands of the peroxo dicopper(II) complex **IIb** (red spectrum) while the band at 416 nm vanishes (blue spectrum). For comparison the original spectrum of **IIb** is shown in orange. The comparison shows that **IIb** could not be fully regained, probably because **IIb** decomposes slowly and it cannot be excluded that an excess of the cryptand is needed to fully regain **IIb**. Direct comparison with a modification of the experiment where **20** is regained after the addition of the cryptand in chapter 5.2.1, shows that the proportion of recovered peroxo dicopper(II) complex **IIb** is significantly higher. This implies that **IIb** is significantly more stable that the closely related complex **20**.

In conclusion, this experiment provides evidence for the conjecture that in the prior reaction a lithium adduct was formed and the presumed hydroperoxo dicopper(II) complex **IIc** was not synthesized.

Further evidence for this conjecture was provided by the second experiment. The addition of the base 1,8-Diazabicyclo[5.4.0]undec-7-ene (400 eq.) to a freshly produced reaction mixture did not lead to significant changes of the spectrum, as shown in Figure 61. Moreover, the small decrease of the absorbance band at 416 nm after the addition of the base in acetonitrile (red spectrum) is due to the dilution of the reaction mixture. There are no signs that the original bands of **IIb** (orange spectrum) are regained. A return to the original bands would imply that the hydroperoxo dicopper(II) complex **IIc** is involved in the reaction. Finally, a comparison of the data recorded from this experiment with established data from a typical titration with DBU of **IIc** shows that the deprotonation did not occur.[65,124]

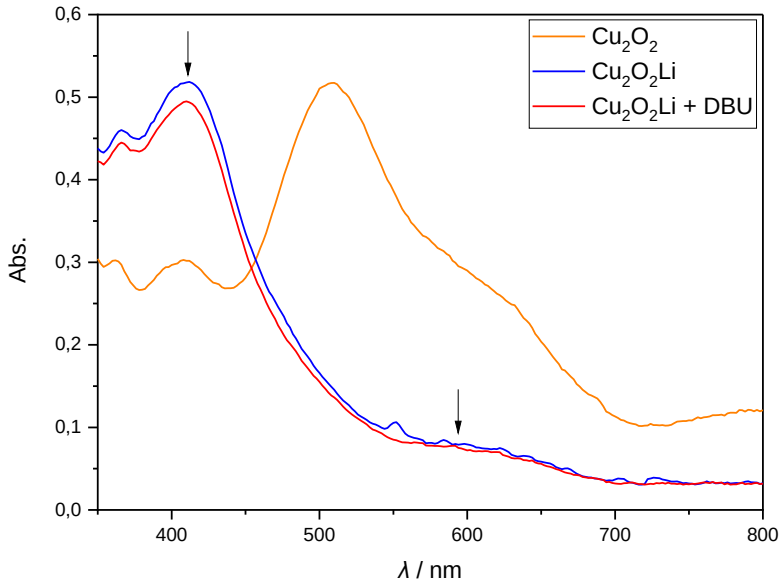

Figure 61: UV/vis spectrum of the addition of 400 eq. of DBU the presumed hydroperoxo dicopper(II) complex **IIc** (blue) at –40 °C in MeCN. For comparison, the spectrum of the peroxo dicopper(II) complex **IIb** prior to the addition of 400 eq. LiOTf is shown in orange.

In summary, all gathered evidence indicates that a lithium adduct is formed. Based on the new results a new reaction pathway is proposed. It is depicted in Scheme 45. The addition of LiOTf to **IIb** leads to the lithium ion adduct **IIf** which immediately rearranges to the final lithium ion adduct **IIg**. Since a μ-1,1-O_2 unit interacting with a lithium ion is structurally very similar to the μ-1,1-OOH moiety of **IIc**, this reaction may exhibit a similar electronic absorbance spectrum.[65] The existence of an intermediate **IIf** is concluded from the observation that no direct conversion from **IIb** to **IIg** is possible. Furthermore, an isosbestic point indicates the reaction from **IIf** to **IIg**. Another expected isosbestic point indicating the direct conversion of **IIb** to **IIf** is missing in the data and was probably not resolved due to the very fast conversion.

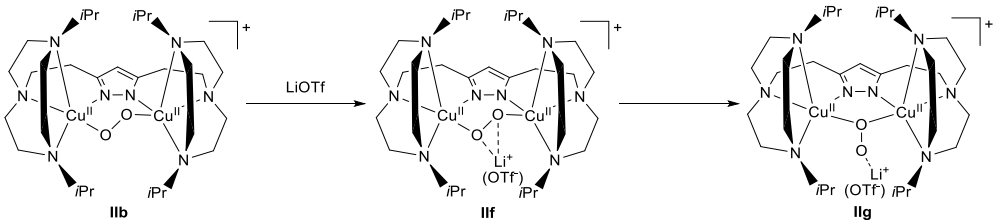

Scheme 45: Revised reaction equation for the synthesis of the lithium ion adduct **IIf** via the lithium ion adduct intermediate **IIg**.

Since **IIg** is relatively stable at low temperatures several attempts were made to crystallize this species. Although the crystallization conditions were varied, it was not possible to obtain single crystals of **IIg** to elucidate the molecular structure. Further studies are needed to prove the existence of **IIg**. For example, a stopped-flow measurement at low temperature may lead to new insights into this reaction.

5.3 Interactions of the cupric peroxides with calcium ions

In a recent publication, ROBINSON *et. al.* discuss the interaction of calcium ions with a Cu_2O_2 core.[91] In this new study, UV/vis data and resonance Raman experiments reveal that the addition of a Ca^{II} ion to the molecule $\{[Cu^{II}(TMPA)]_2(\mu\text{-}1,2\text{-}O_2^{2-})\}^{2+}$ leads to the interconversion of a μ-1,2-*trans* peroxide (**^{T}P**) to a μ-1,2-*cis* peroxide (**^{C}P**).[91,184] The proposed conversion by interaction of a calcium ion with the cupric peroxide can be reversed by the addition of the crown ether 18-crown-6, as shown in Scheme 46.[91]

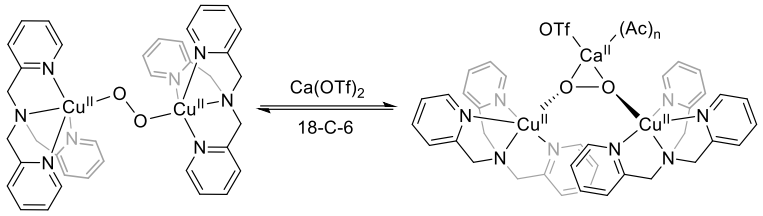

Scheme 46: Reversible interconversion of **^{T}P** and **^{C}P** motifs of $\{[Cu^{II}(TMPA)]_2(\mu\text{-}1,2\text{-}O_2^{2-})\}^{2+}$ mediated by a calcium ion at low temperatures.[91]

In nature, calcium ions play an important role as a redox-inactive metal that can modulate important intermediates.[91,111,185] For example, the calcium ion is an essential part of the Mn_4CaO_5 core of the oxygen-evolving complex in photosystem II.[91,111,185–188] Since Ca^{II}-ions participate in transition metal complexes as redox-inactive metal ions and cofactors for the activation and production of dioxygen, the investigation of interaction with the Cu_2O_2 core of the peroxo dicopper(II) complexes based on TACN/pyrazolate ligands was initiated.[91,189]

5.3.1 Interaction of the peroxo dicopper(II) complexes 20 with calcium ions

Compared to the $\{[Cu^{II}(TMPA)]_2(\mu\text{-}1,2\text{-}O_2^{2-})\}^{2+}$ complex used by ROBINSON *et. al.*, the peroxo dicopper complexes based on TACN/pyrazolate ligand scaffold are more ridged. This is because they are designed as linked compartmental ligands.[91,93] The symmetric cupric peroxide **20** was chosen for the initial experiments because it is most likely to interact with the calcium ion due to the low steric demand of the side arms. Therefore, the μ-hydroxo dicopper(II) complex **21** was reduced to the cuprous complex **19** at room temperature. Addition of dry oxygen gas at –40 °C led to a color change of the reaction mixture from yellow to dark purple. Subsequently, 1.5 eq. of calcium triflate were titrated to the obtained μ-1,2-peroxo dicopper(II) complex **20**, as depicted in Scheme 47. During the titration a color change from dark purple to green was observed.

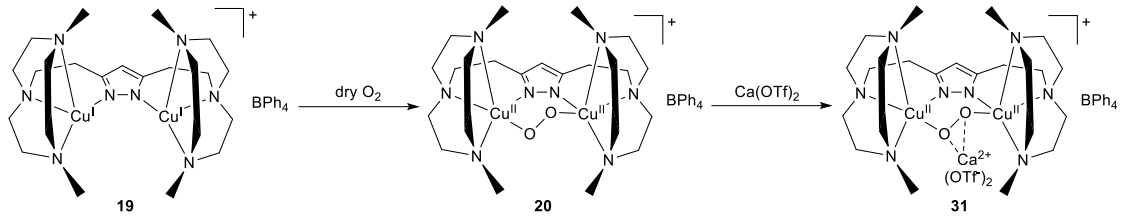

Scheme 47: Synthesis of a novel calcium adduct **31** by addition of dry oxygen to an *in-situ* generated dicopper(I) complex **19** at low temperatures and subsequent addition of a solution of calcium trifluoromethanesulfonate in MeCN.

The titration was tracked by a temperature-controlled UV/vis spectrometer. Furthermore, the titration was performed rapidly to minimize the impact of the decomposition reaction on the result of the titration. As discussed in chapter 4.1.6, the μ-1,2-peroxo dicopper(II) complex **20** decomposes even at low temperatures to the thermodynamically stable μ-hydroxo dicopper(II) complex **21**.

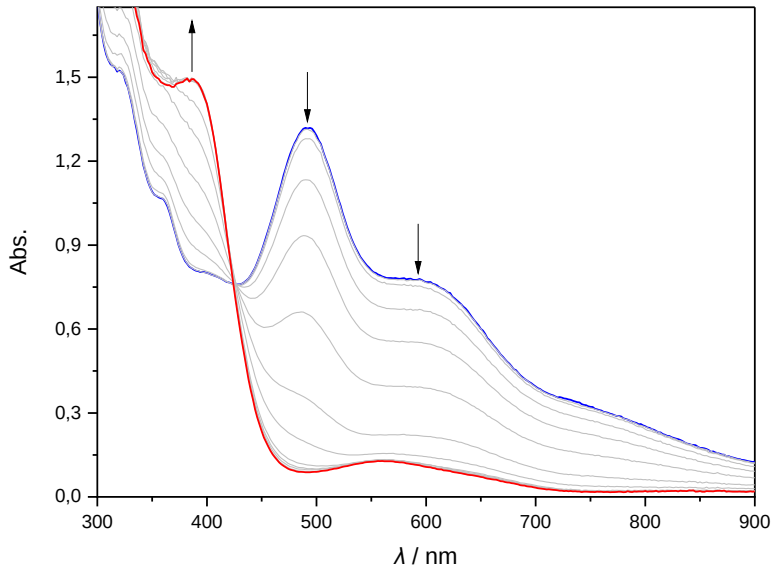

Figure 62: UV/vis absorbance spectrum of the titration of the symmetric μ-1,2-peroxo dicopper(II) complex **20** (blue) to the calcium ion adduct **31** (red) with 1.5 eq. $Ca(OTf)_2$ in dry MeCN at –40 °C under inert conditions. The spectrum features a *pseudo*-isosbestic point at around 426 nm.

The conversion from the μ-1,2-peroxo dicopper(II) complex **20** to the presumed calcium adduct **31** is shown in Figure 62. The stepwise addition of the calcium triflate solution to **20** leads to the bleaching of the characteristic bands of the cupric peroxide at 490 nm, 600 nm and 755 nm. This process is accompanied by the gradual occurrence of new bands at 386 nm and 560 nm. A *pseudo*-isosbestic point emerges at 426 nm. This indicates a potential side reaction. Since there is only one *pseudo*-isosbestic point in the spectrum and the deviation from an ideal isosbestic point is minimal, it can be assumed that this is a direct conversion of **20** to **31**.

The distinctive bands of the presumed calcium adduct **31** appear to be very similar to the previously discussed features of the hydroperoxo dicopper complex **25** (394 nm and 554 nm) and the lithium adduct **29b** (394 nm and 552 nm). The bands of **31** are slightly blue shifted to 386 nm and 560 nm. A similar coordination geometry can be assumed. This hypothesis can, however, only be confirmed by a solid

molecular structure of **31**. All attempts of obtaining a solid structure by crystallizing this novel adduct were unsuccessful because **31** decomposes easily to the μ-hydroxo dicopper(II) complex **21** at low temperatures.

For a more detailed insight into the reaction, the absorbance titration traces of the bands of interest were plotted. The two vanishing bands of the peroxo dicopper(II) complex as well as the new emerging band of the calcium ion adduct **31** were analyzed, as shown in Figure 63. All plots have in common that the first addition of 0.1 eq of calcium triflate did not lead to a significant decrease or increase of absorbance as the following additions. This may indicate that a side reaction is taking place. Only at higher calcium concentrations the desired reaction can be started. An additional linear fit at the beginning of the titration was introduced to correct for this offset. The bleaching traces at 490 nm and 600 nm indicate that the reaction is completed after the addition of 0.52 eq. and 0.51 eq., respectively. In contrast, an analysis of the trace at 386 nm shows that 0.58 eq. of calcium triflate are required to complete the reaction.

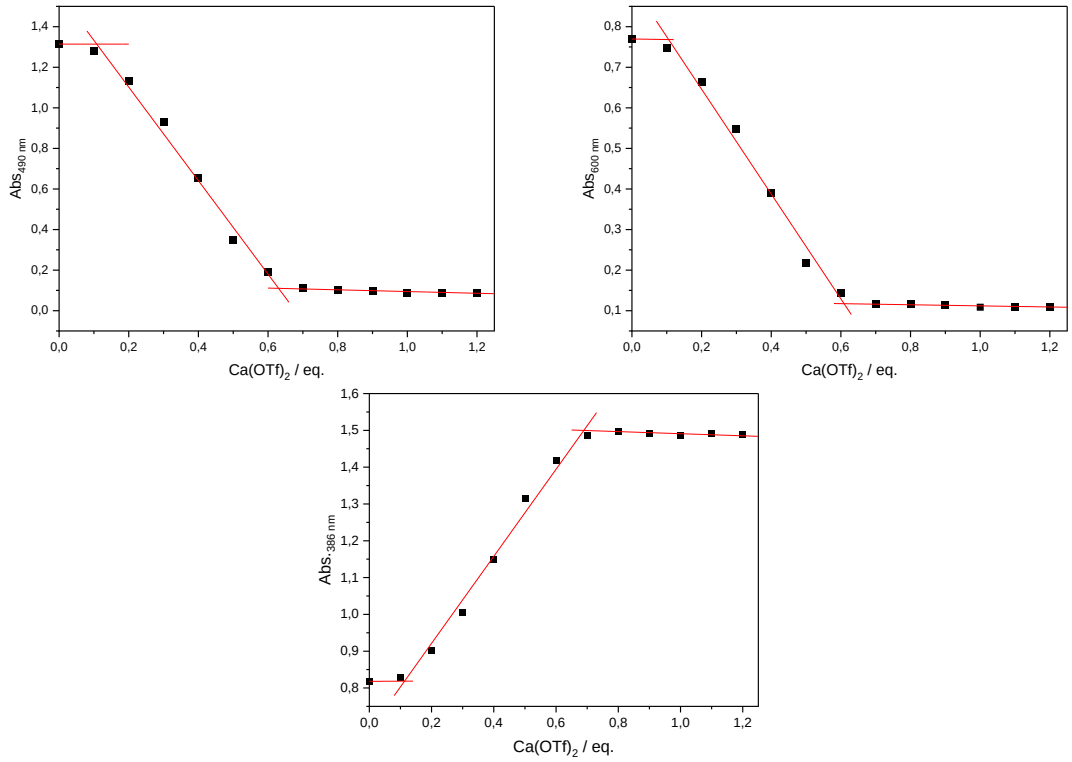

Figure 63: UV/vis absorbance traces of the titration of the symmetric μ-1,2-peroxo dicopper(II) complex **20** to the calcium ion adduct **31** with 1.5 eq. $Ca(OTf)_2$ in dry MeCN at –40 °C under inert conditions. Top: Bleaching absorbance traces of the characteristic cupric peroxide features at 490 nm (0.52 eq.) and 600 nm (0.51 eq.). Bottom: Trace of the raising band at 386 nm (0.58 eq.).

This discrepancy can be traced back to the decomposition reaction because all experiments showed that the presumed calcium adduct **31** is more stable than the precursor **20**. During the titration the cupric peroxide decays faster than the produced calcium adduct. Nevertheless, it should be noted that the decomposition reaction affects all intermediate and therefore all values obtained must be carefully evaluated. Under the assumption that the ongoing decomposition reaction is considered negligible, the determined values may indicate that a dimer was formed. Further research is needed to assess this hypothesis and gain more valuable insights into this complicated system.

The experiments recorded in this section show for the first time that it is possible to form calcium adducts with the peroxo dicopper(II) complex based on a TACN/pyrazolate compartmental ligands.

5.3.2 Interaction of the peroxo dicopper(II) complexes 23 with calcium ions

The same experimental setup as in the previous chapter was used to study the interaction of the non-symmetric μ-1,2-peroxo dicopper(II) complex **23** with calcium ions. To this end, the non-symmetric hydroxo dicopper(II) complex **24** was used as a starting material. After reduction, oxygenation and step-wise addition of calcium triflate the presumed calcium adduct was obtained, as shown in Scheme 48.

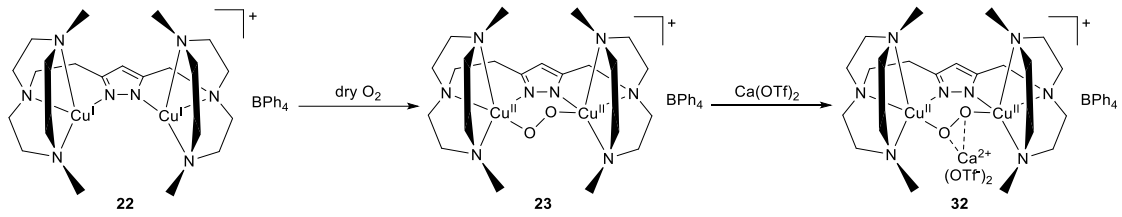

Scheme 48: Synthesis of a novel calcium adduct **32** by addition of dry oxygen to an *in-situ* generated dicopper(I) complex **22** at low temperatures and subsequent addition of a solution of calcium trifluoromethanesulfonate in MeCN.

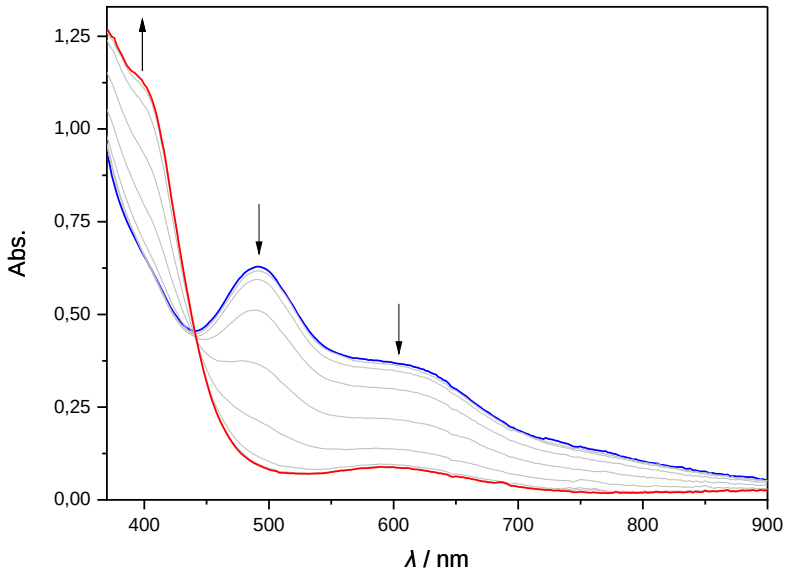

Figure 64: UV/vis absorbance spectrum of the titration of the non-symmetric μ-1,2-peroxo dicopper(II) complex **23** (blue) to the calcium ion adduct **32** (red) with 1.5 eq. $Ca(OTf)_2$ in dry MeCN at –40 °C under inert conditions. The spectrum features a *pseudo*-isosbestic point at around 441 nm.

The UV/vis spectrum for the last step of the synthesis shows the bleaching of the characteristic bands of **23** at 494 nm and at around 598 nm (Figure 64). At the same time, a new band emerges as a shoulder at 395 nm. A weak absorbances feature is formed at 594 nm and a *pseudo*-isosbestic point is formed at around 441 nm. The deviation from the expected isosbestic point is probably caused by minor impurities of the precursor **24** or the used reductant. Therefore, it was assumed in spite of the observed deviation that a direct conversion from **23** to **32** occurred. Several attempts were made to reduce the influences of impurities.

The relevant absorbance traces of the titration with 1.5 eq. calcium triflate were plotted and are shown in Figure 65. Also, in the case of the non-symmetric complex, the first additions of the calcium ion source are not used for the main reaction. This assumption was made because the corresponding bands do not show the expected decrease. The concentration of peroxo dicopper(II) complex **23** decrease significantly only after adding about 0.2 eq. of calcium triflate. Impurities of the starting material and reducing agent where already discussed above. Here it can be assumed that such impurities react with the calcium ions. An additional linear fit at the start of the titration was used to correct for this behavior. Given that the same problem occurred also during the titration of the symmetric complex **20**, it can be assumed that the chosen synthetic route for **31** and **32** is suboptimal. As shown in the next chapters 5.3.3 and 5.3.4, these problems can be avoided when the starting material of the syntheses are the crystallized dicopper(I) complexes instead of the decomposition products. This option does not exist for the dicopper complexes based on Me_2TACN/pyrazolate ligands since the corresponding dicopper(I) complexes cannot be isolated. This is discussed in Chapter 4.1.1 and 4.2.1.

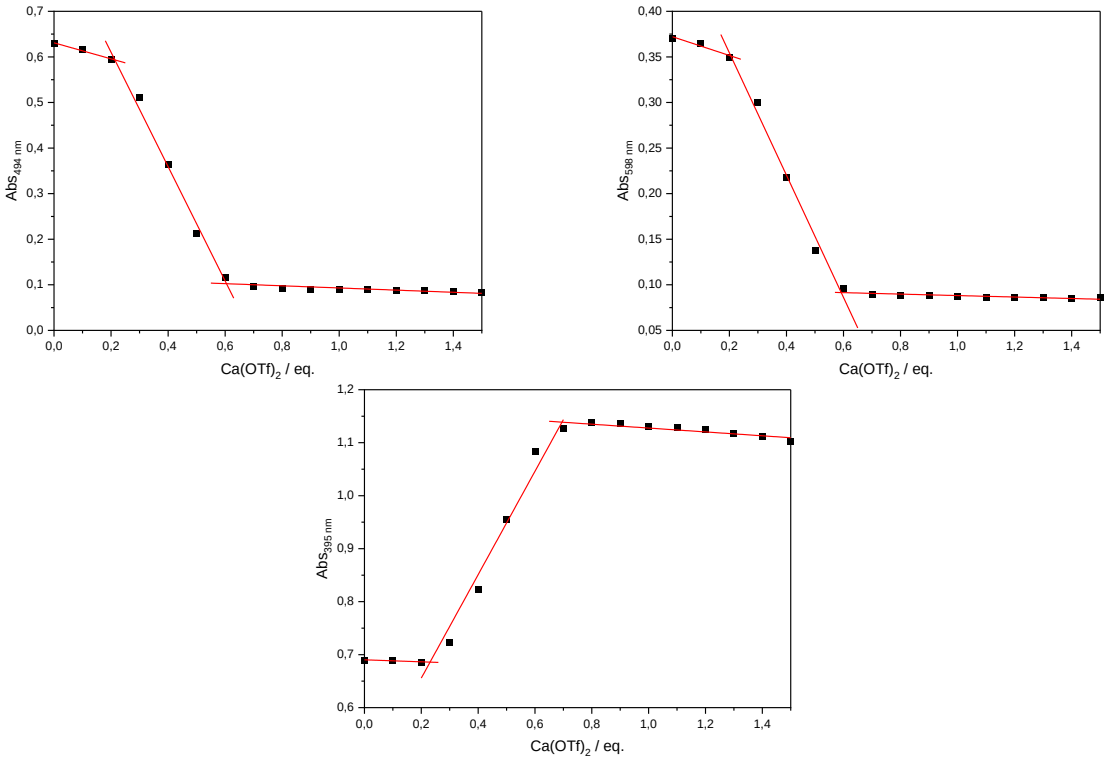

Figure 65: UV/vis absorbance traces of the titration of the non-symmetric μ-1,2-peroxo dicopper(II) complex **23** to the calcium ion adduct **33** with 1.5 eq. $Ca(OTf)_2$ in dry MeCN at –40 °C under inert conditions. Top: Bleaching absorbance traces of the characteristic cupric peroxide features at 494 nm (0.40 eq.) and 598 nm (0.39 eq.). Bottom: Trace of the raising band at 395 nm (0.46 eq.).

The overall consumption of $Ca(OTf)_2$ was determined from the absorbance traces. The traces at 484 nm and 598 nm, imply that around 0.40 eq. of calcium triflate are required for a complete conversion to **32**. A slightly higher consumption of 0.46 eq. can be derived from the absorbance trace at 395 nm. Although the non-symmetric cupric peroxide **23** does not decompose as fast as the symmetric derivate **20**, both complexes decompose significantly during the titration experiment. This suggests that the values deter-

mined here underestimate the true values. However, both complexes show a similar trend for the consumption of $Ca(OTf)_2$. A formation of a dimer may also explain the moderate consumption of $Ca(OTf)_2$. Despite the discussed problems, the recorded data shows that the calcium adduct **32** is produced for the first time.

5.3.3 Interaction of the peroxo dicopper(II) complexes IIb with calcium ions

The observation that cupric peroxides based on Me_2TACN/pyrazolate ligand scaffolds are capable of forming calcium adducts poses the question whether the sterically more demanding dicopper complexes based on *i*Pr_2TACN/pyrazolate ligands can also interact with Ca^{2+} ions. Therefore, initial experiments were conducted for the peroxo dicopper(II) complex **IIb** using the established synthesis route of the prior calcium adducts **31** and **32**. For this purpose the dicopper(I) complex **IIa** was produced by chemical reduction of the µ-hydroxo dicopper(II) complex **IIe**. Subsequent exposure to dry oxygen gas and addition of calcium triflate gave the desired calcium adduct. Since the analysis of the titration data showed similar problems as discussed for **31** and **32**, the synthesis approach was changed. Therefore, the dicopper(I) complex **IIa** was synthesized and crystallized successfully, as described in 8.3.1.3.[65] As shown in Scheme 49, the crystalline material of **IIa** was used to synthesize the peroxo dicopper(II) complex **IIb** and subsequent the calcium adduct **IIh**. This approach allows to avoid the chemical reduction of the hydroxo dicopper (II) complex which caused the discussed problems.

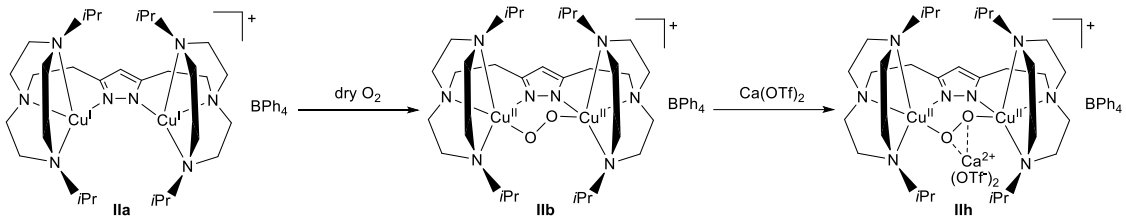

Scheme 49: Synthesis of the calcium adduct **IIh** starting from the crystalline dicopper(I) complex **IIa** via the peroxo dicopper(II) complex **IIb**.

UV/vis spectroscopy of the conversion of **IIb** to the presumed **IIh** showed a bleaching of the characteristic bands at 507 nm, 606 nm and 807 nm. Simultaneously, new bands emerged at 414 nm and 607 nm (see Figure 66). Additionally, the UV/vis spectrum features an isosbestic point at 452 nm. This indicates that intermediates are not forming and no side reactions are occurring. In contrast, the initial experiments for this reaction show *pseudo*-isosbestic points. This again shows that the synthesis route via the hydroxo dicopper(II) complex has its weaknesses and can lead to ambiguous results.

The cupric peroxides based on *i*Pr_2TACN/pyrazolate ligand scaffolds have the advantage that they do not decompose at low temperatures. This made exact titration experiments possible. An UV/vis titration of the symmetric μ-1,2-peroxo dicopper(II) complex **IIb** with 2.0 eq. $Ca(OTf)_2$ gave access to the titration absorbance traces which are plotted in Figure 67.

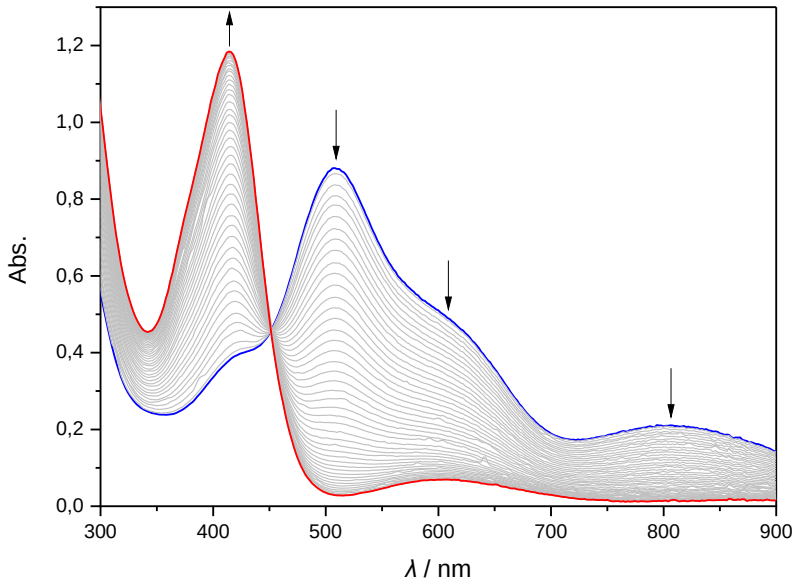

Figure 66: UV/vis absorbance spectrum of the titration of the symmetric μ-1,2-peroxo dicopper(II) complex **IIb** (blue) to the calcium ion adduct **IIh** (red) with 2.0 eq. $Ca(OTf)_2$ in dry MeCN at –40 °C under inert conditions. The spectrum features an isosbestic point at around 451 nm.

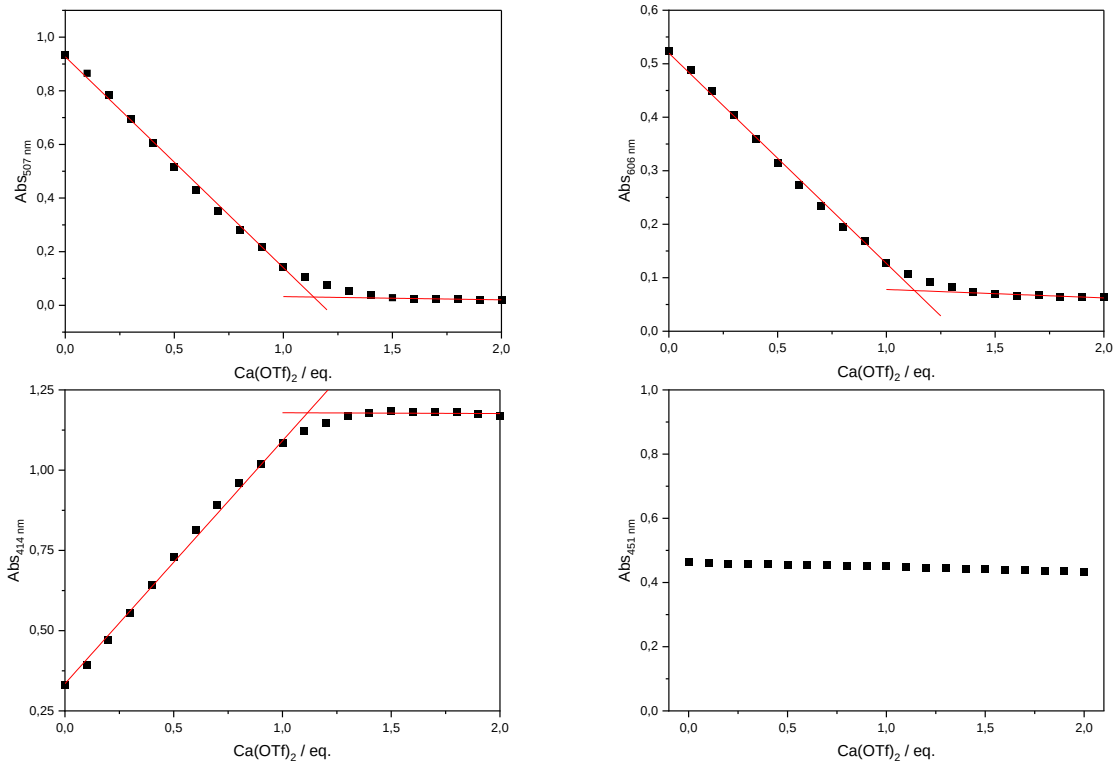

Figure 67: UV/vis absorbance traces of the titration of the symmetric μ-1,2-peroxo dicopper(II) complex **IIb** to the calcium ion adduct **IIh** with 2.0 eq. $Ca(OTf)_2$ in dry MeCN at –40 °C under inert conditions. Top: Bleaching traces of the characteristic cupric peroxide features at 507 nm (1.13 eq.) and 606 nm (1.13 eq.). Bottom: Trace of the raising band at 414 nm (1.12 eq.) and the linear trace of the isosbestic point at 451 nm.

The recorded data indicates that the reaction is completed after the addition of 1.13 eq. of calcium triflate. Moreover, the linear trace at 451 nm confirms the isosbestic point. The deviation from the expected value of 1.00 eq. can be explained by intrinsic and physical uncertainties and inaccuracies of the used spectrophotometer.[173] It is unlikely that traces of minor impurities cause these minor deviations since

crystalline starting material **IIa** was used. However, this alternative explanation cannot be ruled out completely.

The recorded UV/vis absorbance spectrum (Figure 66) is reminiscent of the respective spectrum of the protonation of the μ-1,2-peroxo dicopper(II) complex **IIb** to the μ-hydroperoxo dicopper(II) complex **IIc** which has characteristic bands at 416 nm and 615 nm.[65,124] Therefore, the recorded spectrum is also very similar to the lithium adduct, as demonstrated in chapter 5.2.3. In order to exclude the possibility that **IIc** instead of **IIh** was formed by a reaction with protons, the reverse reaction was investigated. Addition of an adequate base to **IIc** is expected to lead to a deprotonation and reformation of the cupric peroxide **IIb**.[65,124] Accordingly, the base 1,8-Diazabicyclo[5.4.0]undec-7-ene (4 × 1 eq.) was added to the presumed complex **IIh**. The resulting UV/Vis absorbance spectrum is shown in Figure 68.

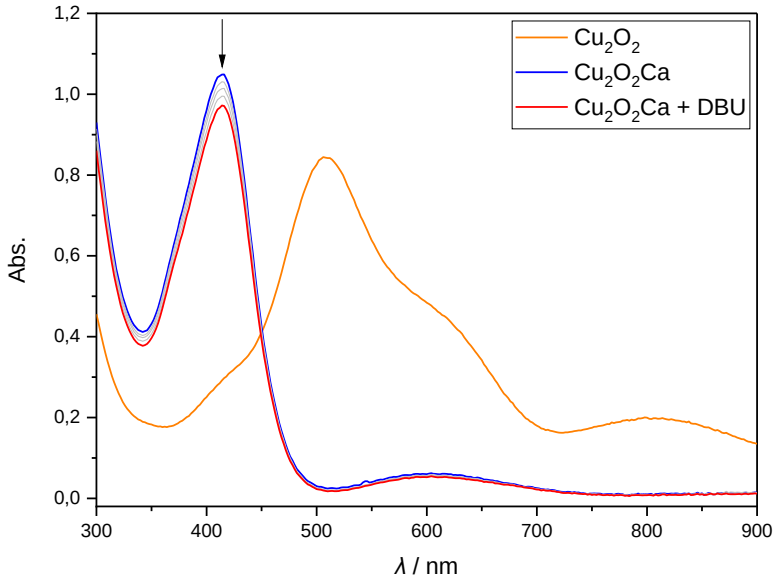

Figure 68: UV/vis absorbance spectrum of the addition of the base DBU (4 × 1.00 eq.) to the calcium ion adduct **IIh** (blue). The original spectrum of the symmetric μ-1,2-peroxo dicopper(II) complex **IIb** spectrum (orange) is shown for comparison.

Upon addition of the base DBU the distinctive band at 416 nm decreases but the typical peroxo dicopper(II) complex bands are not regained. This observation makes it seem likely that complex **IIh** is present. Still, an explanation for the slightly decreasing band is needed. In total 4.00 eq. of DBU were added in 1.00 eq. steps. Each addition reduces the absorbance of the band at 416 nm by around 2%. Since every dose of base increases also the total volume of the reaction mixture by 50 µL, the concentration of **IIh** decreases accordingly. The decrease of the absorbance feature can therefore be attributed to dilution because it can be calculated that the absorbance should decrease by approximately 2.4 % with every injection of 50 µL base solution. In addition to these experiments, several attempts were made to crystallize the novel calcium adduct **IIh**. Even though **IIh** does decomposes very slowly at low temperatures, all crystallization efforts were unsuccessful.

The presented new experimental results show that it is possible to form calcium adducts with the peroxo dicopper(II) complexes based on a *i*Pr$_2$TACN/pyrazolate ligand. This increases the range of known adducts with redox-inactive metal ions. In addition, it was demonstrated that the synthesis of **IIh** from crystalline dicopper(I) complex **IIa** leads to less ambiguous results than the previously attempted synthesis route.

5.3.4 Interaction of the peroxo dicopper(II) complexes IIIb with calcium ions

The successful synthesis of the calcium adduct **IIh** suggests that the closely related non-symmetric μ-1,2-peroxo dicopper(II) complex **IIIb** may also form a corresponding Ca^{2+} adduct. **IIIb** does not decompose easily at low temperatures. In addition, the crystalline dicopper(I) complex **IIIa** is available as a starting material for the synthesis. The results from the previous two chapters suggest that these two factors can favor a successful synthesis of reactive intermediates. Moreover, earlier works of SPYRA shows that **IIIb** forms adducts with alkali metal ions at low temperatures.[38]

The established synthesis route (Scheme 50) led to the characteristic color change of the reaction mixture from purple to green in the last step. In particular, a drastic change of the characteristic absorbance features of **IIIb** were observed in the corresponding UV/vis spectrum which is shown in Figure 69. The distinctive bands of the cupric peroxo complex bleach and a new band forms at 422 nm with a prominent shoulder at 374 nm. Additionally, a weak absorbance features emerges at 612 nm.

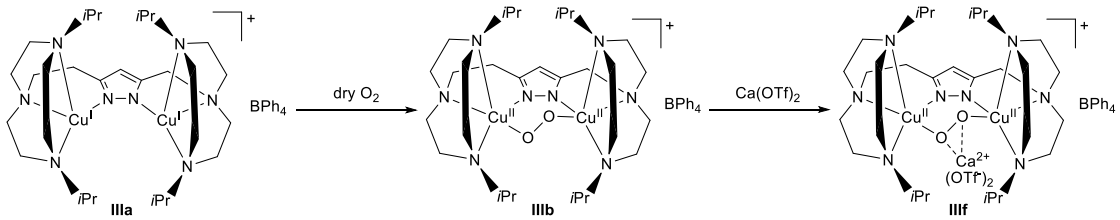

Scheme 50: Synthesis of the calcium adduct **IIIf** starting from the crystalline dicopper(I) complex **IIIa** via the non-symmetric peroxo dicopper(II) complex **IIIb**.

An isosbestic point at 464 nm indicates a clean conversion from **IIIb** to the presumed complex **IIIf**. Analysis of the absorbance traces of the corresponding titration reveals that around 1.28 eq. of $Ca(OTf)_2$ are needed to complete the reaction. All changes in absorbance of the relevant bands vs. the equivalents of calcium triflate are plotted and shown in Figure 70.

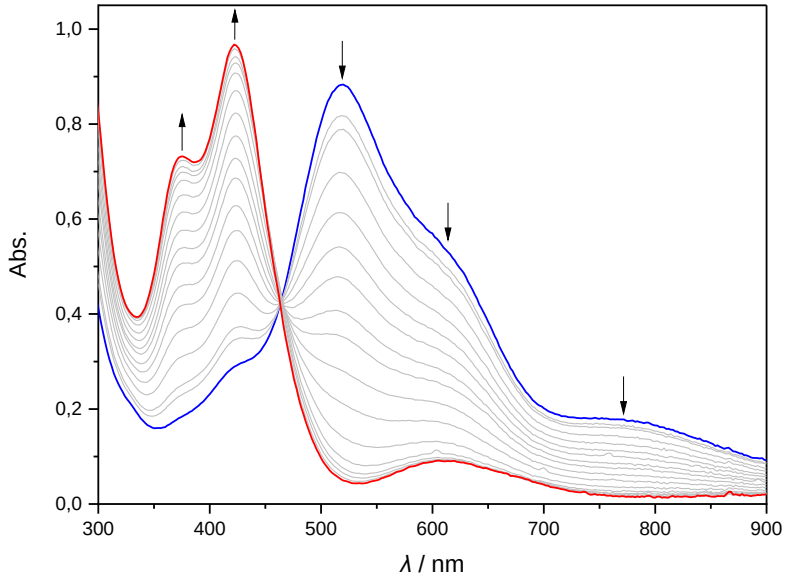

Figure 69: UV/vis absorbance spectrum of the titration of the non-symmetric μ-1,2-peroxo dicopper(II) complex **IIIb** (blue) to the calcium ion adduct **IIIf** (red) with 2.0 eq. $Ca(OTf)_2$ in dry MeCN at –40 °C under inert conditions. The spectrum features an isosbestic point at around 464 nm.

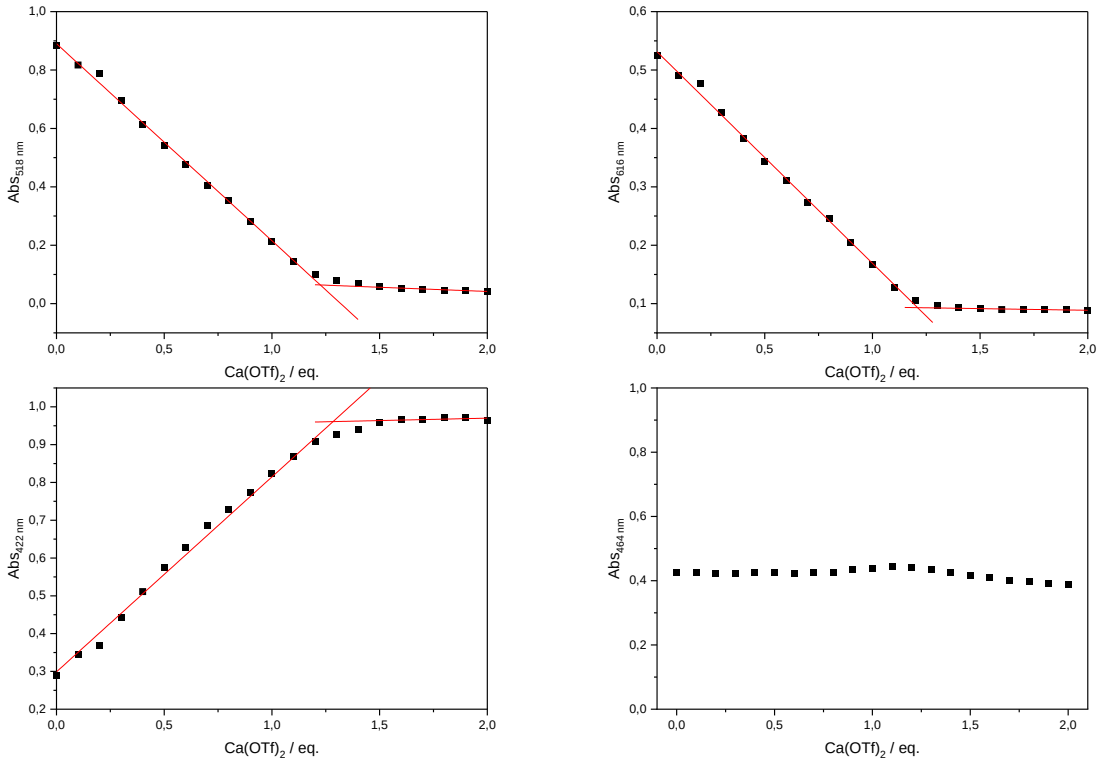

Figure 70: UV/vis absorbance traces of the titration of the non-symmetric μ-1,2-peroxo dicopper(II) complex **IIIb** to the calcium ion adduct **IIIf** with 2.0 eq. $Ca(OTf)_2$ in dry MeCN at –40 °C under inert conditions. Top: Bleaching traces of the characteristic cupric peroxide features at 518 nm (1.22 eq.) and 616 nm (1.21 eq.). Bottom: Trace of the increasing band at 422 nm (1.28 eq.) and the linear trace of the isosbestic point at 464 nm.

The recorded data represent the first efforts to characterize this presumed new adduct **IIIf**. Since crystallization of the calcium adduct was unsuccessful, further research and evidence is needed to provide further evidence for the presence of **IIIf**.

5.4 Summary and conclusion

This chapter presented and discussed the interactions of the cupric peroxides based on TACN/pyrazolate ligands with Lewis acids.

Firstly, novel lithium adducts with the symmetric and non-symmetric cupric peroxides **20** and **23** were established. UV/vis monitored experiments showed that the addition of lithium ions led to drastic changes of the characteristic bands. These were accompanied by the formation of two consecutive isosbestic points. The experimental evidence suggests that at least one intermediate is involved in the reaction. The emerging new bands are reminiscent of the distinctive bands of a hydroperoxo dicopper(II) complex. Earlier studies on a closely related derivative **IIb** hypothesized that a protonation of the peroxo dicopper(II) complex occurred. This was investigated by further experiments for the symmetric complex.[65,124] In particular, two reverse reaction were tested. The addition of a [2.2.2] cryptand provided the most compelling evidence. It showed unambiguously that the product was a novel lithium ion adduct and not the hydroperoxo dicopper(II) complex. This new evidence challenges the conclusions from previous studies. Similar experiments were conducted for **IIb**. Also in this case, the addition of the cryptand or an adequate base to the reaction mixture clearly demonstrates that the lithium ion adduct had formed. Therefore, a new reaction pathway for both of these cases was proposed. It is based on the gained insights by UV/vis spectroscopy and shown in Scheme 51.

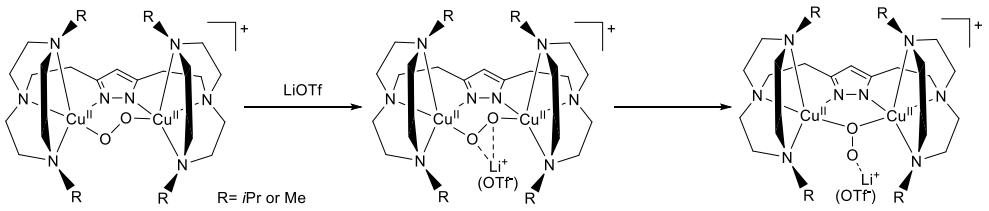

Scheme 51: Proposed reaction pathway for the formation of the lithium adducts for different TACN/pyrazolate derivatives.

Because of the close resemblance with the UV/Vis spectra of the corresponding hydroperoxo dicopper(II) complexes, it seems likely that instead of the μ-1,1-OOH moiety, a structurally related μ-1,1-O_2 unit is interacting with the lithium ion. This may lead to a similar electronic structure. Based on the observed isosbestic points and the cryptand experiments, a side-on coordinated lithium peroxo adduct is presumed as the intermediate.

Secondly, initial experiments show that is possible to form calcium ion adducts with the peroxo dicopper(II) complexes. For the cupric peroxides **20** and **23**, with reduced steric demand, it was found that unprecedented absorbance features formed after the addition of calcium triflate. Titration experiments were performed, even though the competing decomposition reaction interfered with the main reaction. The conversion was completed after approximately 0.5 eq. of calcium triflate. In general, the synthesis of these adducts from the corresponding hydroxo dicopper(II) complexes resulted in a complex system with numerous independent factors. The complexity of the system complicates the interpretation of the

recorded data. Therefore, the calcium ion adducts of the cupric peroxides with increased steric hindrance **IIb** and **IIIb** were synthesized from the corresponding crystallized dicopper(I) complexes **IIa** and **IIIa**.[38,65] This resulted in unambiguous UV/vis titration data. For example, for the formation of the calcium ion adduct **IIh** 1.13 eq. of calcium triflate were needed to complete the reaction. Since the absorbance features of **IIh** are similar to the bands of the corresponding μ-hydroperoxo dicopper(II) complex **IIc**, a control experiment was performed. Addition of the base DBU showed that the product was not **II**.

The adducts studied here extend the range of known adducts with redox-inactive metal ions. In case of the initial calcium ion adducts experiments, further research is needed. Especially, the molecular structures of crystalline material of **IIh** and **IIIf** could provide interesting insights into these new adducts. As another avenue for future research, prospective experiments of the reverse reaction with crown ether 18-crown-6 may help to further establish these adducts.

6 Reactivity studies

Organic substrates were tested for their reactivity with the reactive oxygen adducts. Most of the results were negative and additional inconclusive. This problem arises mainly from the fact that the copper-oxygen complexes based on Me_2TACN/pyrazolate ligands cannot be isolated as crystalline materials. Therefore, peroxo, superoxo and hydroperoxo dicopper(II) complexes must always be prepared *in-situ* from the hydroxo dicopper(II) complex. This means that in addition to the species under study, other chemicals are present which could affect the reaction. Furthermore, the constant decomposition of the copper oxygen adducts affects the results. This chapter will focus on two reactivities studies that have not been tested for other copper oxygen complexes based on TACN/pyrazolate ligands before.

6.1 Oxygen reduction reaction

In nature several enzymes can reduce efficiently dioxygen to water.[178,190,191] Typically, the oxygen reduction reaction (ORR) requires not only the activation of oxygen, but also metal centers that can provide four electrons.[80,192,193] In addition, four protons are needed for this reaction at the active site. For instance, cyctochrome *c* oxidases which is an essential part of in the respiratory chain uses a heteronuclear center to catalyzes this four-electron and four-proton ($4e^-/4H^+$) reduction of oxygen.[190,191,194] Homonuclear centers that catalyzes the ORR can also be found in nature.[80] For example, the multicopper oxidase laccase is based on four copper ions which are a type 1, a type 2, and a binuclear type 3 copper center.[178]

The $4e^-/4H^+$ reduction of oxygen has attracted a lot of attention in the recent years since this reaction plays an important role in fuel cells which uses a carbon impregnated platin cathode.[192,195,196] Since large quantities of precious metals are normally required, new efficient metal catalysts based on non-precious metals are being sought.[192]

Furthermore, an efficient $2e^-/2H^+$ reduction of oxygen to hydrogen peroxide is of interest. Hydrogen peroxide can be used as an environmentally benign oxidant and is often used in synthesis.[197,198]

$$\begin{aligned} O_2 + 2\,e^- + 2\,H^+ &\longrightarrow H_2O_2 \\ H_2O_2 + 2\,e^- + 2\,H^+ &\longrightarrow 2\,H_2O \\ \hline O_2 + 4\,e^- + 4\,H^+ &\longrightarrow 2\,H_2O \end{aligned}$$

Scheme 52: Reaction equation of the $2e^-/2H^+$ reduction of oxygen to hydrogen peroxide and the subsequent $2e^-/2H^+$ reduction to water.

In recent years homonuclear complexes based on iron, cobalt and copper ions have been developed for the catalytic $4e^-/4H^+$ reduction of oxygen.[79,80,192,199,200] Figure 71 shows two example of homonuclear complexes that are able to catalyzes the ORR.[192]

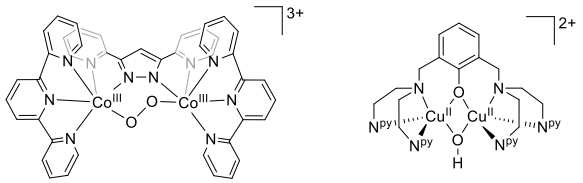

Figure 71: Examples of dinuclear metal complexes that catalyze the reduction of oxygen. Left: $[Co^{III}_2(trpy)_2(\mu\text{-bpp})(\mu\text{-}1,2\text{-}O_2)]^{3+}$.[192] Right: $[Cu^{II}_2(XYLO)(OH)]^{2+}$ with N^{py} = pyridine.[82,192,201]

The μ-1,2-peroxo dicobalt(III) complex is based on a bridging bis(pyridyl)pyrazolate (bpp) ligand and two terpyridine (trpy) ligands.[192] The $[Co^{III}_2(trpy)_2(\mu\text{-bpp})(\mu\text{-}1,2\text{-}O_2)]^{3+}$ complex can catalyze efficiently the $4e^-$-reduction of oxygen by octamethylferrocene (Me_8Fc) in the presence of trifluoroacetic acid as the proton source in MeCN at room temperature.[192,201] It was found that the rate determining step in the catalytic cycle is a proton-coupled electron transfer (PCET) reduction of $[Co^{III}_2(trpy)_2(\mu\text{-bpp})(\mu\text{-}1,2\text{-}O_2)]^{3+}$.[192] Furthermore, a dicopper complex was introduced by KARLIN *et. al*. (Figure 71).[82] The $[Cu^{II}_2(XYLO)(OH)]^{2+}$ complex is based on a *m*-xylenolate bridging unit equipped with two chelating bis(2-{2-pyridyl}ethyl)amine sidearms (XYLO).[202] Later it was reported that the complex catalyzes the reduction of dioxygen.[79,80,201] In the presents of perchloric acid and 1,1'-dimethylferrocene or ferrocene as a reductant the $2e^-/2H^+$ reduction of oxygen to hydrogen peroxide is preferred.[79] Interestingly, the $4e^-/4H^+$ reduction of oxygen to water is favored if the weaker acid trifluoroacetic acid is used instead of perchloric acid.[80,202]

In the next sections the results of the oxygen reduction reaction using the dicopper complexes based on TACN/pyrazolate ligand scaffolds will be presented and discussed.

6.1.1 Oxygen reduction reaction of the novel copper oxygen complexes

Initial experiments were performed starting from the non-symmetric μ-hydroxo dicopper(II) complex **24**. Firstly, the dicopper(I) complex **22** was synthesized by chemical reduction with cobaltocene in MeCN at room temperature. Secondly, 150 eq. of 2,6-lutidinium triflate (HLutOTf) were added as a proton source. Thirdly, 20 eq. of the reductant decamethylferrocene ($Me_{10}Fc$) were added to the reaction mixture. Subsequently, the reaction mixture was exposed to dry oxygen in excess at room temperature. The whole reaction was monitored with a temperature-controlled UV/vis spectrometer and the corresponding spectra are shown in Figure 72.

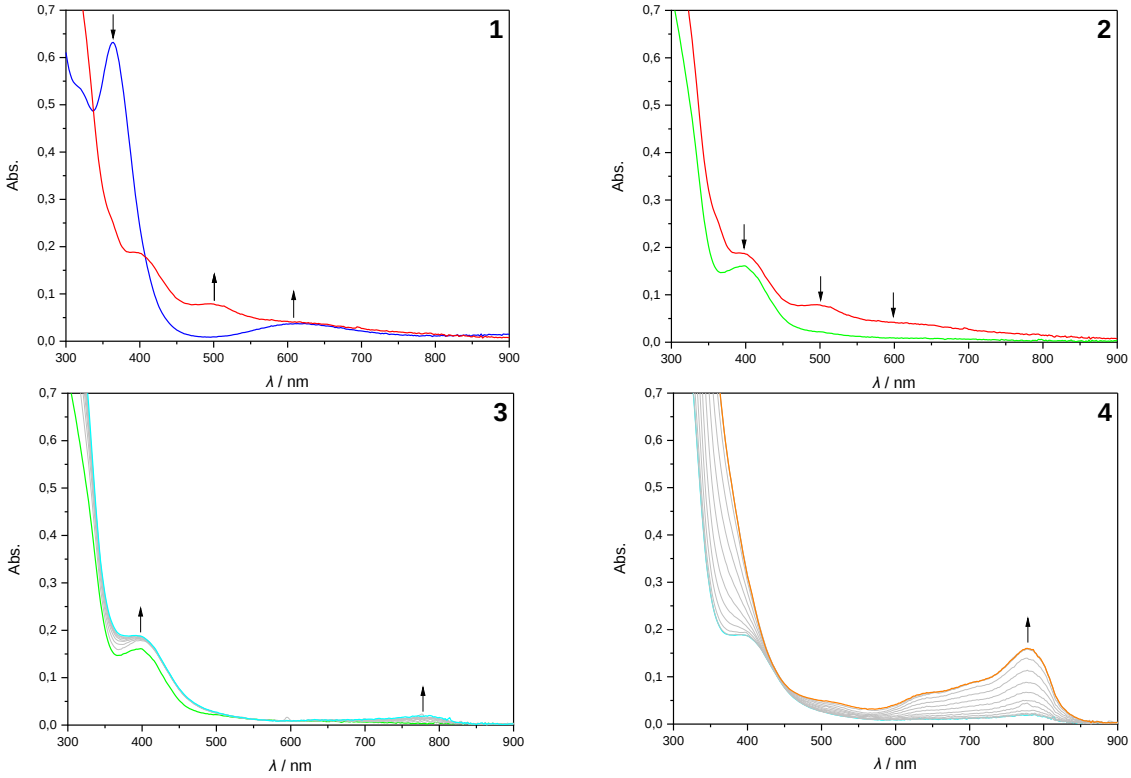

Figure 72: UV/vis spectra of the initial experiment of the oxygen reduction reaction starting from the μ-hydroxo dicopper(II) complex **24** (blue) in dry MeCN at 25 °C under inert conditions. 1: Chemical reduction with 2.0 eq. $CoCp_2$ led to the copper(I) complex **22** (red). 2: Addition of HLutOTf lead to the green spectrum. 3: The turquoise spectrum formed after the $Me_{10}Fc$ was added. 4: Exposure to dry oxygen led to the orange spectrum.

The resulting spectra show that an oxygen leak must have occurred during this experiment. This can already be seen in the first spectrum of Figure 72, because the characteristic bands of a peroxo dicopper(II) complex **23** were observed. Therefore, the addition of 2,6-lutidinium triflate led to a formation of the hydroperoxo dicopper(II) complex **27** in spectrum 2. Normally, an experiment with an oxygen leak would be conducted again, but in this case the experiment was successful as it led to a significant observation. As shown in spectrum 3, the addition of 10 eq. of $Me_{10}Fc$ leads to the formation of a weak band at 778 nm. This band can be assigned to decamethylferrocenium ($Me_{10}Fc^{+}$) which is probably formed due to the reduction of O_2.[183,203] Interestingly, the reaction stops as soon as the oxygen originating from the leak is depleted. The remaining $Me_{10}Fc$ is not consumed until the dry oxygen gas is added which is show in spectrum 4. Therefore, it can be concluded that the consumption of the reducing

agent depends only on the oxygen supply. This conclusion can be confirmed by analyzing the formation of the band at 778 nm over time, as depicted in Figure 73.

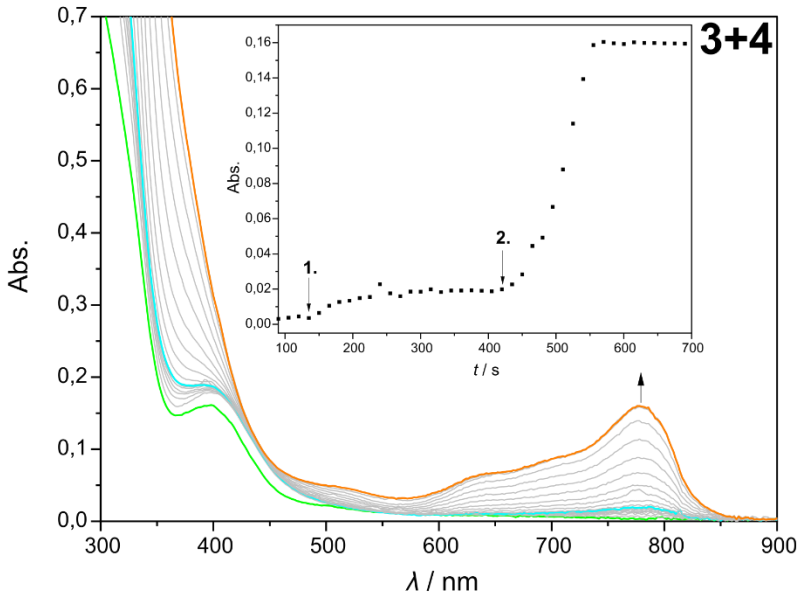

Figure 73: Summary of the crucial UV/vis spectra 3 and 4 of Figure 72. The inset shows the absorption traces at 778 nm which shows the formation of $Me_{10}Fc^{+}$.

Especially, the absorption trace at 778 nm shows two points at which the consumption of $Me_{10}Fc$ increases abruptly. The first point, marked as **1.**, shows the formation of $Me_{10}Fc^{+}$ due to oxygen contamination. When all oxygen is reduced, the slope of the curve decreases again and the formation of $Me_{10}Fc^{+}$ stagnates. Only the actual addition of dry oxygen in excess at point **2.** leads to the consumption of the remaining $Me_{10}Fc$. The main reaction is completed after 150 s. Based on these results, it can also be assumed that the $CoCp_2^{+}$ which forms during the chemical reduction of **24** does not initiate the reaction of interest, since the formation of $Me_{10}Fc^{+}$ depends only on the availability of oxygen. In addition, the recorded data suggest that the reduction occurs when the hydroperoxo dicopper(II) complex **27** is formed.

To gain further insights in this reaction the symmetric μ-hydroxo dicopper(II) complex **21** was used as a precursor for the ORR to test a step-by-step approach at lower temperatures. Therefore, the corresponding symmetric μ-1,2-peroxo dicopper(II) complex **20** was formed by reductive recycling reaction of **24** and subsequent exposure to dry oxygen in MeCN at –20 °C. The resulting UV/Vis spectra of these reactions are shown in Figure 74 as spectrum 1 and 2.

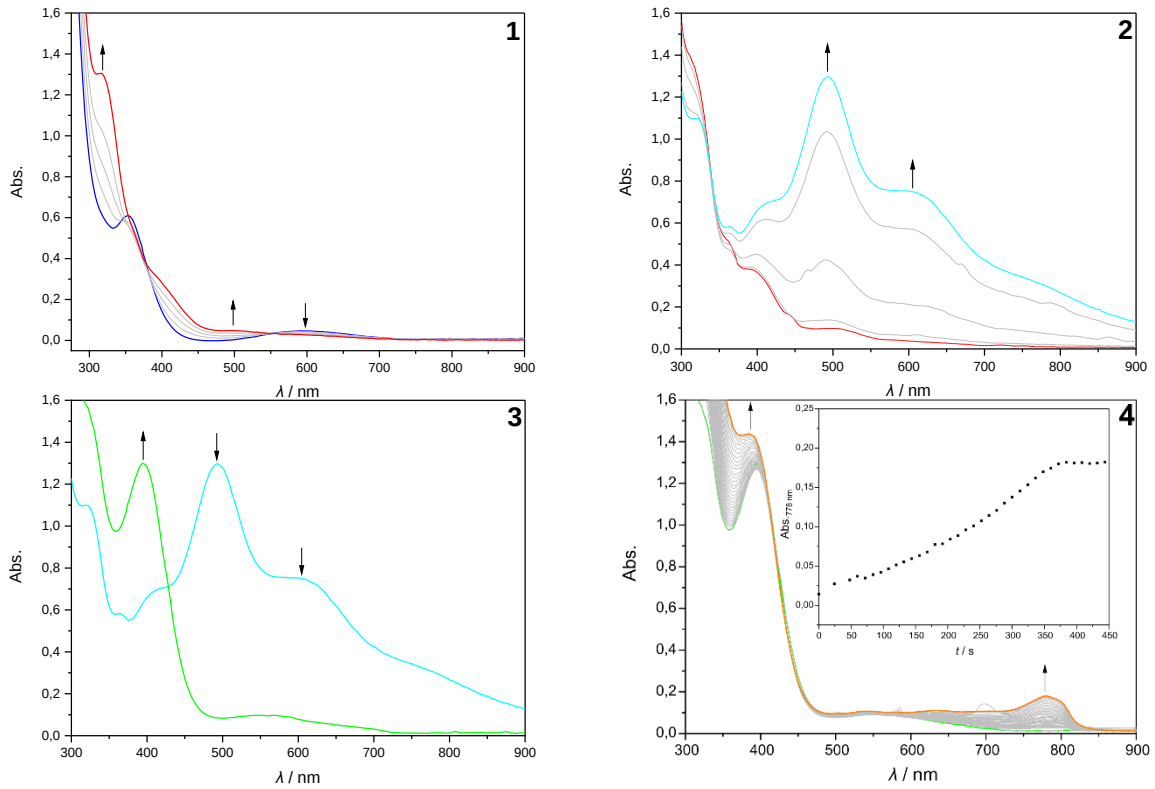

Figure 74: UV/vis spectra of a step-by-step approach for the oxygen reduction reaction starting from the symmetric μ-hydroxo dicopper(II) complex **21** (blue) in dry MeCN at 25 °C under inert conditions. 1: Chemical reduction with 2.0 eq. $CoCp_2$ led to the copper(I) complex **19** (red). 2: The peroxo dicopper(II) complex **20** was formed after addition of dry oxygen at –20 °C. 3: Addition of 150 eq. HLutOTf resulted in the hydroperoxo dicopper(II) complex **25** (green). 4: The orange spectrum formed after 20 eq. of$Me_{10}Fc$ was added. The inset shows the formation of the band at 778 nm over time.

The acid 2,6-lutidinium triflate was added immediately to the formed μ-1,2-peroxo dicopper(II) complex **20**, since this reactive species is decomposing under this reaction conditions. Subsequent addition of the reductant $Me_{10}Fc$ led to the desired reaction as shown in spectrum 4 of Figure 74. Similar to the non-symmetric congener, the emerging band at 778 nm indicates the successful conversion of $Me_{10}Fc$ to $Me_{10}Fc^+$. Moreover, it was determined that the added $Me_{10}Fc$ was completely converted to $Me_{10}Fc^+$. The reaction of interest is finished after 384 s. Interestingly, the reaction was not finished at this stage. Figure 75 shows that a consecutive reaction takes place. A new band is formed at 556 nm which decreases with time. This observation suggests that an unknown adduct must have formed. The decay of this species strongly indicates that it is probably a copper complex. However, the observed absorbance features cannot be assigned clearly to any of the copper complexes studied so far. Therefore, it is assumed that the product of the oxygen reduction reaction reacts or interacts with the dicopper complex. Analysis of the initial consumption of $Me_{10}Fc$ indicates that probably hydrogen peroxide is the product of the oxygen reduction reaction. However, hydrogen peroxide could not be detected with peroxide test strips, probably due to the low concentration of H_2O_2 in this experimental setup. Due to the excess of dioxygen and 2,6-lutidinium triflate in the reaction mixture, it is assumed that the hydroperoxo dicopper(II) complex **25** is probably present at the end of the reaction. A possible explanation for the appearance of the new band would be that **25** reacts or interacts with the resulting H_2O_2.

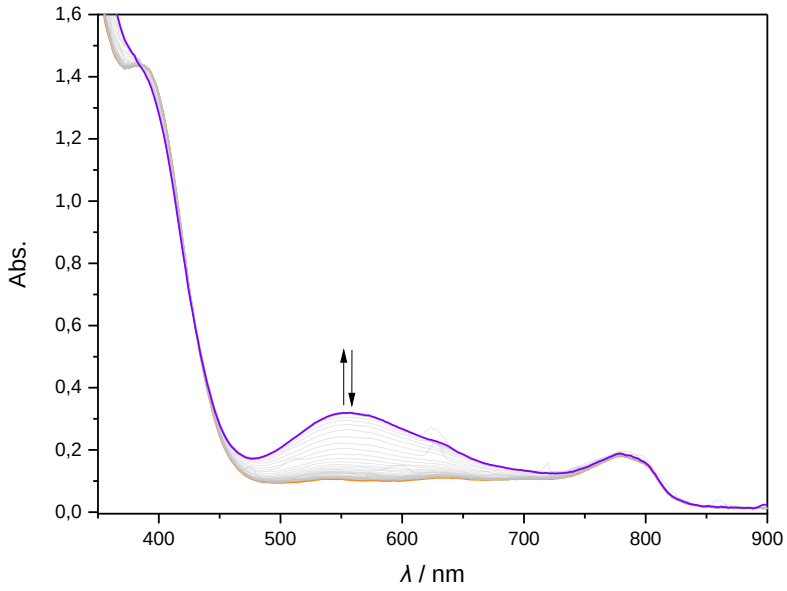

Figure 75: UV/vis spectrum of the formation of a new band at 556 nm in MeCN at –20 °C. Subsequently, the formed band bleaches over time.

The hypothesis was tested by using the same reaction setup, but decamethylferrocenium hexafluorophosphate ($Me_{10}FcPF_6$) was added instead of $Me_{10}Fc$. Therefore, the resulting UV/Vis spectrum should not feature a band at 558 nm, if the hydroperoxo dicopper(II) complex **25** reacts or interacts with the product of the ORR. Figure 76 shows the obtained UV/vis spectrum.

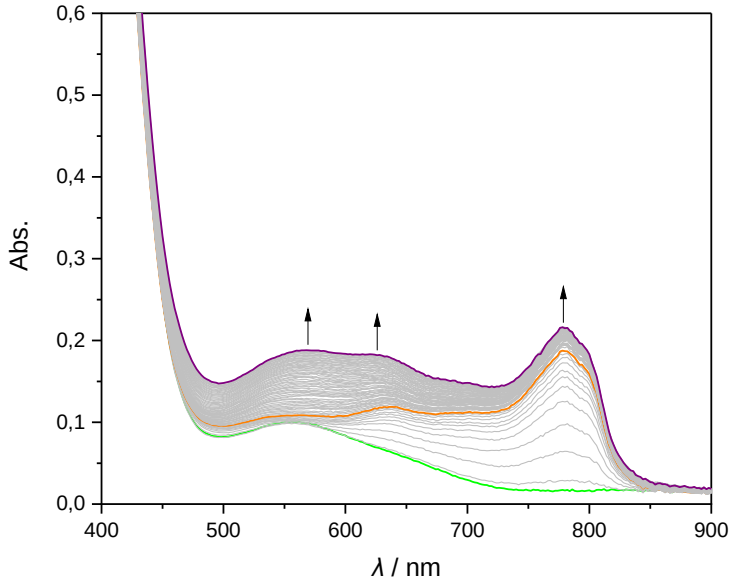

Figure 76: UV/vis spectrum of the addition of $Me_{10}FcPF_6$ to the *in-situ* formed hydroperoxo dicopper(II) complex **25** (green) led to the formation of the orange spectrum. Over time the violet spectrum with absorbance features at 569 nm, 626 nm and 778 nm formed.

Addition of $Me_{10}FcPF_6$ to the *in-situ* formed hydroperoxo dicopper(II) complex **25** results in the expected formation of the band at 778 nm (orange). Also, the band at 626 nm can be assigned to $Me_{10}FcPF_6$. However, a new band starts to rise at 569 nm. Even though, it is not the exact band at 556 nm from the previous experiment, these results indicate that is unlikely that the original band comes from the interaction or reaction of the ORR product with the hydroperoxo dicopper(II) complex **25**. Since the

observed unknown species is relatively unstable and decomposes rapidly, no further experiments could be performed to characterize this species.

In addition, it was investigated if the reduction can be performed in increments without losing the active species over time. Therefore, the hydroperoxo dicopper(II) complex **25** was formed again by protonation of the cupric peroxide **20**. The sequent addition of 30 eq. of $Me_{10}Fc$ in four portions with a short delay between each addition is depicted in the UV/vis spectrum in Figure 77.

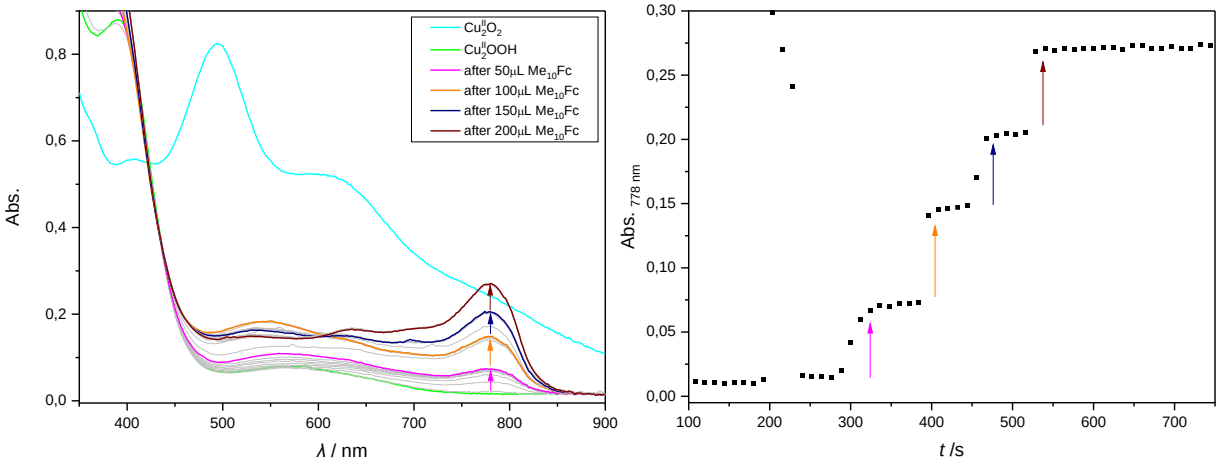

Figure 77: Left: UV/vis spectrum of the addition of four injections of $Me_{10}Fc$ to the *in-situ* formed hydroperoxo dicopper(II) complex **25** (green) led to the formation of typical $Me_{10}Fc^{+}$ spectrum. The characteristic spectrum of the symmetric peroxo dicopper(II) complex is show as reference in turquoise. Right: Formation of the band at 778 nm over time. The injections of $Me_{10}Fc$ are marked with color coded arrows.

The UV/vis spectrum shows the expected incremental increase of the band at 778 nm. This absorbance feature confirms that the added $Me_{10}Fc$ is oxidized to $Me_{10}Fc^{+}$. The absorption trace at 778 nm supports the fact that the reducing agent is converted completely to $Me_{10}Fc^{+}$, since the calculated absorbance values for complete oxidation are in good agreement with the observed values. This result suggests that the process can be repeated multiple times and it is possible that it might be a catalytic process. Interestingly, the recorded data shows again the formation of the band at around 550 nm after addition of 15 eq. of $Me_{10}Fc$. Subsequently, the decomposition of the corresponding species starts during the addition of the remaining reducing agent. A *pseudo*-isosbestic point forms at 607 nm for the decay. These observations confirm the ephemeral nature of the unknown species.

6.1.2 Oxygen reduction reaction with copper oxygen complexes based on the ligands II and III.

Furthermore, the ORR was tested for the closely related hydroperoxo dicopper(II) complex **IIc** This experiment allows to investigate the influence of the steric bulk at the TACN moieties on the ORR. Therefore, **25** was synthesized in the same manner as in the previous experiments to ensure comparability of results. The hydroxo dicopper(II) complex **IIe** was chemically reduced and dry oxygen was added in excess. Subsequently, 150 eq. of 2,6-lutidinium triflate were added and the hydroperoxo dicopper(II) complex **IIc** was obtained. Addition of 20 eq. of $Me_{10}Fc$ led to formation of the characteristic band at 778 nm. Figure 78 summarizes the resulting UV/vis spectra.

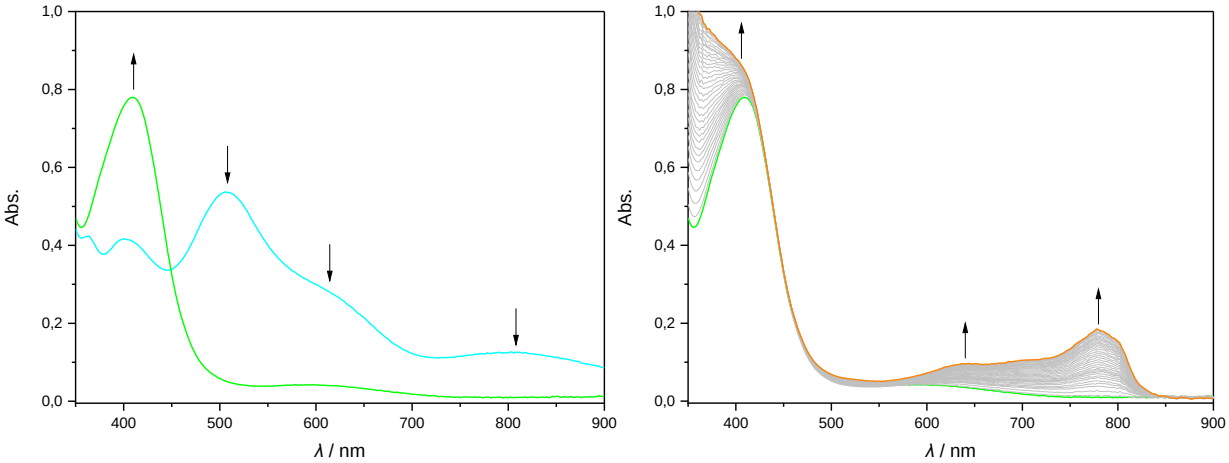

Figure 78: Left: UV/vis spectrum formation of the hydroperoxo dicopper(II) complex **IIc** (green) by the addition of 150 eq. of HLutOTf to the peroxo dicopper(II) complex **IIb** (turquoise) in MeCN at –20 °C. Right: Formation of the characteristic band at 778 nm after the addition of 20 eq. of $Me_{10}Fc$ (orange).

Due to the consumption of the reductant, it can be assumed that the reaction takes place. In contrast to the previous experiments, the formation of the band at 778 nm requires 543 s instead of 384 s under the same reaction conditions. Even this simple comparison shows that the deshielding of the bimetallic cleft by introduction of methyl residues leads to a faster conversion.

In the previous chapter, it was assumed that the redox couple $CoCp_2/CoCp_2^+$ of the chemical reduction is not involved in the actual ORR since the formation of $Me_{10}Fc^+$ depends only on the oxygen supply. The dinuclear complex based on *i*Pr_2TACN ligands can be used to verify this hypothesis since it is possible to crystallize the cupric peroxide **IIb** and **IIIb**. Therefore, a reductive synthesis of **IIb** or **IIIb** is not necessary if a cupric peroxide is directly used as starting material.

The crystalline peroxo dicopper(II) complex **IIIb** was dissolved in MeCN and cooled to –20 °C. Addition of 10 eq. of $Me_{10}Fc$ and 400 eq. of HLutOTf led to the formation of the expected band at 778 nm. In contrast to the other experiments, the formation of the band was very slow. Even though the reaction temperature was already higher than in the other experiments, the reaction temperature was increased during the experiments in increments to accelerate the reaction and reduce the measurement duration. Figure 79 shows the decisive UV/vis spectrum and the formation of the band at 778 nm over time.

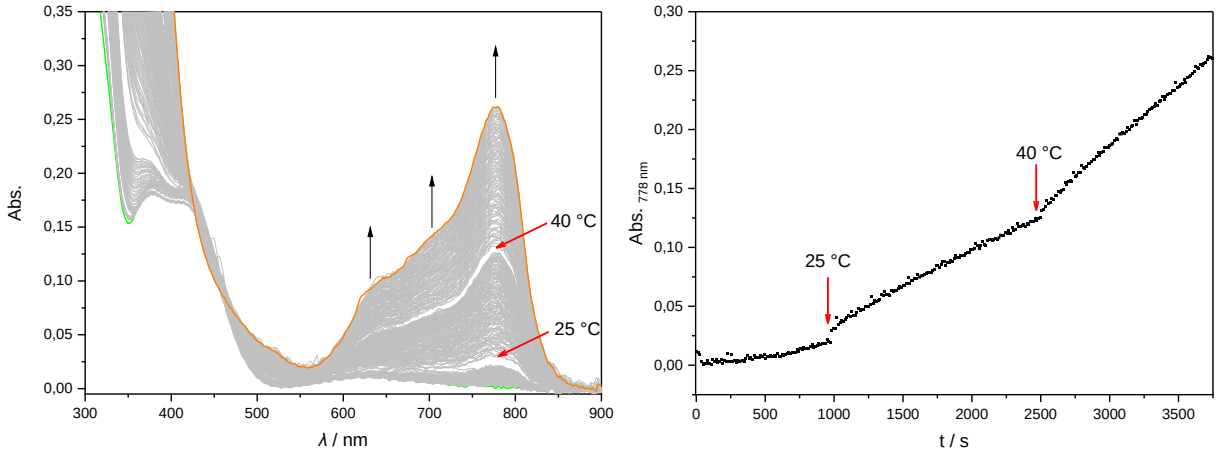

Figure 79: Left: UV/vis spectrum shows the typical formation of the band at 778 nm (orange) which can be assigned to $Me_{10}Fc^{+}$. Right: Formation of the band at 778 nm over time. The changes of the reaction temperatures are marked with red arrows.

The reaction temperature was increased from –20 °C to 25 °C and ultimately to 40 °C. With increased temperatures the reaction was faster, but a total of 3744 s was needed to deplete the 10 eq. of $Me_{10}Fc$. A longer reaction time was expected compared to the previous experiment, as earlier work suggests that **IIb** may be more likely to show increased reactivity than **IIIb**. This simple experiment indicates that the redox pair $CoCp_2/CoCp_2^{+}$ influences the ORR and might be involved in the reaction. It is likely that $CoCp_2/CoCp_2^{+}$ acts as a redox mediator.[204] This would explain the slower conversion This result suggest that a ORR reaction is also possible for **IIIb**.

6.2 Nucelophilic reactivity

Recent studies demonstrated that mononuclear superoxo copper complexes can act as a reactive nucleophiles and are deformylating reagents.[205,206] Scheme 53 shows a proposed reaction mechanism for the initial nucleophilic attack.[205] Similar results were found for a superoxo nickel(II) complex.[207]

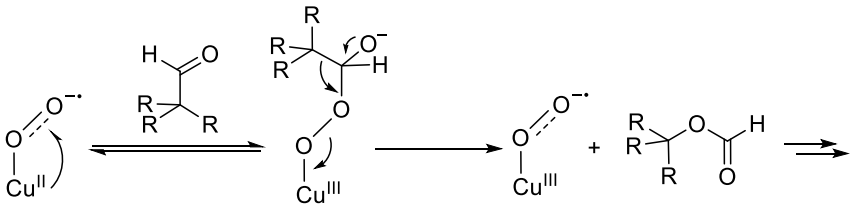

Scheme 53: Proposed reaction mechanism of the initial nucleophilic attack.[205]

In addition, an earlier study suggested that a mononuclear peroxo cobalt(III) complex can support a aldehyde deformylation.[208] A reaction mechanism was proposed for the deformylation of cyclohexanecarboxaldehyde (CCA) which is depicted in Scheme 54.[208,209] CCA is typically used for initial testing due to its α-H-atoms.

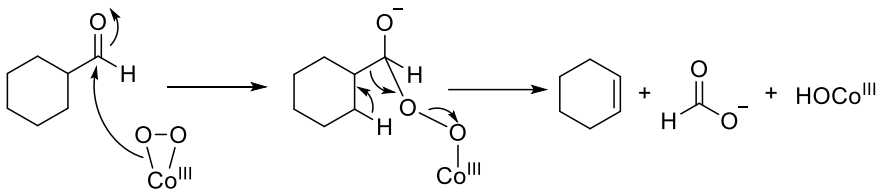

Scheme 54: Expected reaction mechanism of the aldehyde deformylation at a mononuclear peroxo cobalt(III) complex.[208,209]

Recently, a study demonstrated that not only mononuclear peroxo metal complexes are capable of deformylating aldehydes.[210] In this case a μ-oxo-μ-1,2-peroxo diferric complex was able to perform this nucleophilic reaction.[210]

These promising results of the mononuclear superoxo copper complexes and the peroxo metal complexes inspired the testing of this reactivities at the cupric superoxides and peroxides based on the Me_2TACN/pyrazolate ligands. For this purpose, the symmetric dinuclear complexes **20** and **26** were selected. The first experiments were performed with the symmetric μ-1,2-peroxo dicopper(II) complexes **20** in MeCN at –40 °. The complex was generated *in-situ* by chemical reduction of the μ-hydroxo complex dicopper(II) and addition of dry oxygen. Subsequently, 10 eq. dry CCA were added to the reaction mixture. The whole reaction was monitored by UV/vis spectroscopy and the respective UV/vis spectrum is shown in Figure 80.

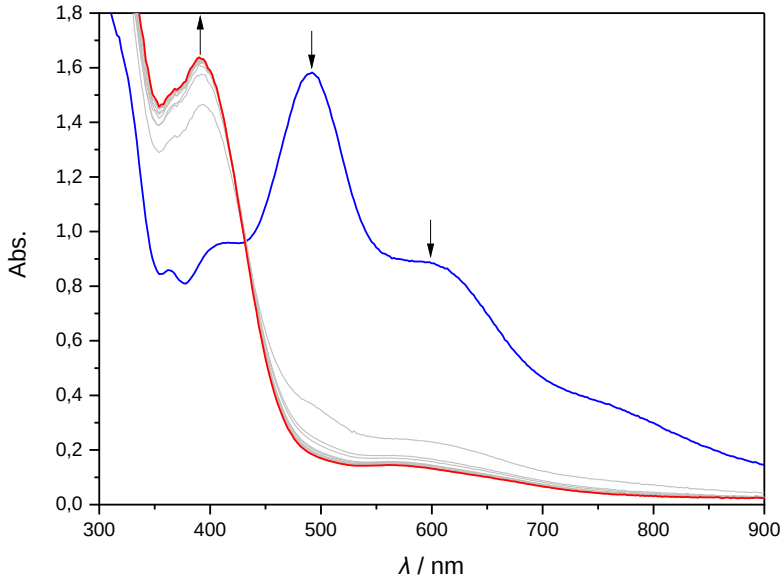

Figure 80: UV/vis spectrum of the addition of 10 eq. of CCA to the *in-situ* formed peroxo dicopper(II) complex **20** (blue) at –40 °C in MeCN.

The characteristic UV/vis bands of the peroxo dicopper(II) complex **20** bleach immediately after the addition of CCA. A distinctive band emerges at 392 m and a weak absorbance feature forms at 557 nm. These bands are reminiscent of the hydroperoxo dicopper(II) complex **25**. This indicates that an unexpected protonation of the peroxo dicopper(II) complex **20** occurred during the reaction.

For comparison, the experiments with the symmetric μ-1,2-superoxo dicopper(II) complexes **26** were performed. Therefore, the peroxo dicopper(II) complexes **20** was generated *in-situ* in EtCN. Subsequently, the one-electron oxidant $FcPF_6$ was added at –80 °C. The lower temperature was chosen to avoid the fast decay of the cupric superoxide. Directly after the injection of the oxidizing agent were 10 eq. of CCA added to the reaction mixture. The resulting UV/vis spectrum is shown in Figure 81.

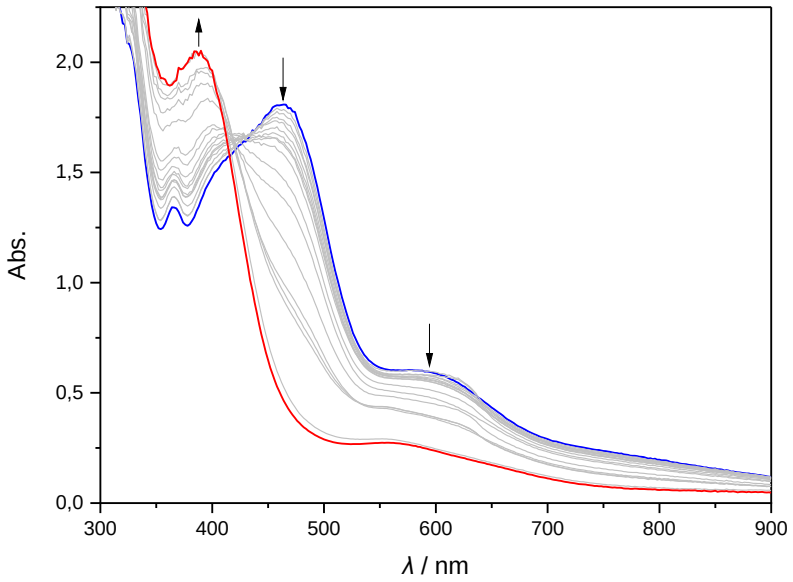

Figure 81: UV/vis spectrum of the addition of 1.2 eq of $FcPF_6$ and of 10 eq. of CCA to the *in-situ* formed peroxo dicopper(II) complex **20** (blue) at –80 °C in EtCN.

The UV/vis sprectrum shows that new absorbance features form at 387 nm and 564 nm. Similar to the previous experiments is the resulting spectrum reminiscent of the corresponding hydroperoxo dicopper (II) complex **25**. The observed bands are a slightly blue shifted in comparison to the expected bands of **25**. However, this spectrum was recorded at lower temperatures and in a different solvent as the comparison spectrum of the hydroperoxo dicopper (II) complex.

Analysis of the reaction mixtures by gas chromatography-mass spectrometry (GC-MS) revealed three fractions at different retention times. The EI-MS measurement showed that the reaction mixture consists of unreacted CCA (m/z = 112.09) and Fc (m/z = 186.01). In addition, a molecule with m/z = 138.13 was also found in the reaction mixture. Based on the mass spectrum, the molecule 1-(1-cyclohexen-1-yl)propanone was identified. The occurrence of this substance is attributed to an impurity of the starting material CCA. The expected product of these reactions, *i.e.* cyclohexene, was not found in reaction mixtures. Consequently, these results indicate that no aldehyde deformylation by a nucleophilic reaction could be detected. The formation of a hydroperoxo dicopper(II) complex **25** occurs probably due to formic acid which can be an impurity in CCA.

6.3 Summary and conclusion

In this chapter, results were presented and discussed for the reactivity studies. Initial experiments regarding the oxygen reduction reaction showed positive results.

For these experiments, the hydroperoxo dicopper(II) complexes **25** and **27** were prepared *in-situ* and the reductant decamethylferrocene was added. UV/vis experiments confirmed a fast and successful conversion of $Me_{10}Fc$ to $Me_{10}Fc^{+}$. In addition, it was shown that consumption $Me_{10}Fc$ depends only on the oxygen supply. Experiments using a step-by-step approach showed that probably hydrogen peroxide forms during the reaction. This approach revealed that an unknown copper oxygen adduct was formed after the reaction of interest. It was assumed that the product of the reaction would react with the hydroperoxo dicopper(II) complex **25**. However, it was shown that this species is also formed when the reaction is carried out with $Me_{10}FcPF_6$ instead of $Me_{10}Fc$. The oxygen reduction reaction was also investigated for the closely related hydroperoxo dicopper(II) complexes **IIc** and **IIIc**. It has been shown that the reaction is much slower when **IIc**. Since **IIIc** could be prepared from crystalline peroxo dicopper (II) complex **IIIb,** no reductive synthesis of **IIIc** was necessary. In particular, this experiment allowed us to investigate the possible influence of $CoCp_2/CoCp_2^{+}$. It was shown that the reaction proceeds significantly slower. From this it can be concluded that $CoCp_2/CoCp_2^{+}$ may act as a redox mediator.[204] Further research is needed to provide more evidence. For example, additional electrochemical studies with a rotating ring-disk electrode could support these results.

The experiments concerning the aldehyde deformylation were unsuccessful for the *in-situ* prepared peroxo dicopper(II) complex **20** and the superoxo dicopper(II) complexes **26**. In both cases, the formation of absorbance features was observed that are reminiscent of the corresponding hydroperoxo dicopper(II) complex **25**. GC-MS analysis of the resulting reaction mixture did not show the expected product cyclohexene. The formation of **25** was attributed to a formic acid contamination of CCA.

7 Closing remarks and Outlook

In this thesis, new bioinspired dinuclear complexes for the activation of dioxygen were explored. Novel TACN/pyrazolate ligand scaffolds $\mathbf{HL_{sym}}$ and $\mathbf{HL_{asym}}$ with reduced steric hindrance were introduced and successfully synthesized. In comparison, to the closely related and well-investigated symmetric and non-symmetric *i*Pr$_2$TACN/pyrazolate ligands the syntheses of the ligands presented in this work are more challenging to synthesize due to the formation of side products.[38,65,104,121] A synthesis route was established and optimized regarding temperature, reduction of side product formation and reaction time.

The novel symmetrical proligand $\mathbf{HL_{sym}}$ was used to form the dicopper(I) complex **19**. The direct synthesis was not possible. Nevertheless, an alternative synthetic route was introduced. The Cu^{I} species **19** was successfully synthesized by the chemical reduction of the hydroxo dicopper(II) complex **21**. The synthesis was monitored by UV/vis spectroscopy and confirmed the conversion to the desired product. This successful synthesis allowed the formation of the symmetric peroxo dicopper(II) complex **20**. The corresponding UV/vis spectrum indicate a μ-1,2-peroxo dicopper(II) complex structure. Additionally, resonance Raman spectroscopy of a frozen solution of **20** confirmed the successful formation.

The proligand $\mathbf{HL_{asym}}$ was used to gain access to the non-symmetric μ-hydroxo dicopper(II) complex **24**. Therefore, an extensive purification process was developed to produce crystalline material of **24**. Subsequent, ESI-mass spectrometry, UV/vis and IR spectroscopy confirmed the successful synthesis. A temperature-dependent magnetic susceptibility measurement with a SQUID magnetometer revealed the strongest antiferromagnetic coupling of all known μ-hydroxo dicopper(II) complexes based on TACN/pyrazolate compartmental ligands. Since the direct synthesis of the dicopper(I) complex **22** was not successful, the chemical reduction of μ-hydroxo dicopper(II) complex **24** was explored. The *in-situ* formed dicopper(I) complex **22** was used to synthesize the non-symmetric peroxo dicopper(II) complex **23**. In the UV/vis spectrum the characteristic bands of a μ-1,2-peroxo dicopper(II) complex were found. The obtained data for **23** fitted to the absorbance features of the known peroxo dicopper(II) complexes perfectly. Like all μ-1,2-peroxo dicopper(II) complexes which are based on a Me$_2$TACN/pyrazolate ligand scaffold, **22** showed a rapid decay. The decomposition is around four times slower than the decay of the symmetric cupric peroxide **20**. Further experiments revealed that the decomposition is a first-order reaction. The activation energy for the decomposition is with $E_A = 61.7\ \mathrm{kJ\cdot mol^{-1}} \pm 2.1\ \mathrm{kJ\cdot mol^{-1}}$ around 9.1 kJ·mol^{-1} higher than the E_A of the decomposition of symmetric derivative **20** to **21**. On the contrary, the decomposition of the symmetric peroxo dicopper(II) **20** is a second-order reaction.

Moreover, the hydroperoxo dicopper(II) complexes **25** and **27** of the novel Me$_2$TACN/pyrazolate were synthesized for the first time. Temperature-controlled UV/vis spectroscopy showed that the distinctive bands are shifted slightly to shorter wavelength compared to the known hydroperoxo dicopper(II) complexes based on *i*Pr$_2$TACN/pyrazolate.

The syntheses of the superoxo dicopper(II) complexes **26** and **28** were successful at lower temperatures (–40 °C). The recorded UV/vis data showed that the formed superoxo dicopper(II) complex **26** is probably converted rapidly into the corresponding hydroperoxo dicopper(II) complex after formation. This consecutive reaction could be explained by a hydrogen abstraction reaction, but the origin of the needed hydrogen atoms remained inconclusive. UV/vis measurements at even lower temperatures (–80 °C) showed the initial UV/vis spectrum of **26**. Recovery of the precursor peroxo dicopper(II) complex **20** was demonstrated by the addition of cobaltocene to **26**.

Additionally, the interaction of the cupric peroxides with Lewis acids were investigated. A novel lithium ion adduct was confirmed by UV/vis spectroscopy. In those experiments a drastic change of the characteristic bands was observed which suggested that a hydroperoxo dicopper(II) complex may have formed. Testing of the reverse reactions such as addition of an adequate base, demonstrated that the lithium adduct had formed. Furthermore, addition of a cryptand to the resulting reaction mixture showed that the peroxo dicopper(II) complex **20** was regained. The recorded UV/vis data indicated that a μ-1,1-O_2 unit might interact with the lithium ion.

Initial studies on the formation of calcium ion adducts with the peroxo dicopper(II) complexes **20** and **23** were conducted. The syntheses of these copper oxygen adducts from the corresponding hydroxo dicopper(II) complexes resulted in a complex system with numerous independent factors. Therefore, the calcium ion adducts of the cupric peroxides **IIb** and **IIIb** with increased steric hindrance were produced since these can be synthesized from crystalline dicopper(I) complexes **IIa** and **IIb**. Among others, UV/vis titrations experiments confirmed the formation of the calcium adducts.

Reactivity studies were also performed with the novel reactive oxygen adducts. Preliminary results regarding the oxygen reduction reaction are presented and discussed in this work. A series of experiments showed that the consumption of the added reductant for the ORR was depended on the oxygen supply. In addition, analysis of the initial oxygen consumption suggest that hydrogen peroxide is probably formed. However, the product could not be detected directly. Comparison experiments with the established hydroperoxo complexes indicated that $CoCp_2/CoCp_2^+$ act as a redox mediator in this reaction.

Detailed electrochemical studies with a rotating ring-disk electrode have to be performed in future studies to support and validate these promising results for the ORR.

This work has shown that Ca^{2+} ions can interact with peroxo dicopper(II) complexes. It would be of great interest to extend these studies to Mg^{2+} ions since magnesium cations are very important in biological process and are the second most abundant cation in cells.[211] In addition, the interactions of Na^+ and K^+ ions with the novel cupric peroxides with Na^+ and K^+ ions need to be elucidated.

Establishing a different reductant for the chemical reduction of the decomposition could also be beneficial in future research. It would be an improvement to find a suitable reducing agent that can be easily removed from the reaction solution after successful reduction. At the same time, it must also be able to ensure rapid conversion.

8 Experimental section

8.1 General Remarks and Procedures

8.1.1 Air and moisture sensitive compounds

All chemical reactions which were sensitive to oxygen or moisture, were carried out under an inert gas atmosphere (argon 5.0 or nitrogen 5.0) using Schlenk techniques or a glove box (MBRAUN LABmaster SP and MBRAUN UNIlab). The glove boxes were equipped with dioxygen and water sensors (H_2O- and O_2-levels always <0.1 ppm). Before usage, all laboratory glassware was dried oven overnight at 80 °C in an ove.

8.1.2 Solvents and other chemicals

Solvents were distilled, dried and degassed by purging with argon following standard procedures. If needed, the solvents were further degassed by four cycles of freeze-pump-thaw degassing and the water content was determined via KARL FISCHER titration[158]. The dried solvents acetonitrile, propionitrile and methanol were stored in the glove box over 3 Å molecular sieve. The sieve was activated prior to use at 400 °C in a muffle furnace for at least three hours. As the work on this thesis progressed, the classical procedures of drying of solvents was abandoned in favor of a safer method that uses activated 3 Å molecular sieve[212]. Dry diethyl ether was stored in a brown glass bottle to limit light exposure to avoid the formation of peroxides. Whenever possible MTBE was used instead of diethyl ether [213,214].

For the syntheses of the copper dioxygen complexes the oxygen gas (5.0) was dried over a column filled with phosphorus pentoxide prior to use. Additionally, the inert gas used at the Schlenk line was passed through a desiccant column and a CuO catalyst was used for deoxygenation.

$[Cu(MeCN)_4]ClO_4$ was synthesized according to the literature[159]. The pyrazole building block precursor 3,5-Bis(2-hydroxylethyl)-1*H*-pyrazole was synthesized by Andreas Schwarz according to the literature[144]. The Meyer group provided the chemicals HLutOTf and $FcPF_4$. The molecules **II**, **IIe**, **IIIa**, and **IIIe** were provided by Dr. Jerome Spyra[38]. All other chemicals which were used in this work, were purchased from commercial suppliers and used as received without any further purifications.

8.1.3 NMR Spectroscopy

All reported NMR-spectra were recorded on a BRUKER Avance 300 NMR spectrometer at room temperature. The chemical shifts (δ) are reported in parts-per -million (ppm) and are referenced to the residual proton signal of the used deuterated solvent ($CDCl_3$: δ = 7.26 ppm, DMSO-d_6: δ = 2.50 ppm). For ^{13}C-NMR spectra the carbon signal of the solvent was used as an internal standard ($CDCl_3$: δ = 77.16 ppm, DMSO-d_6: δ = 39.52 ppm). Traces of common impurities or contaminants were assigned according to the literature[215,216]. Signal multiplicities are abbreviated as s = singlet, d = duplet, t = triplet, q = quartet and m = multiplet. The respective coupling constants (*J*) are given in the unit

Hertz (Hz). The obtained NMR-Data was processed with MestReNova (version 14.2.0) by MESTRELAB RESEARCH.

8.1.4 IR Spectroscopy

Infrared data of the chemical compounds were recorded on a Cary 630 FTIR spectrometer with KBr windows manufactured by the company AGILENT. Solid samples were measured with an ATR module equipped with a swivel press and a diamond crystal. A DialPath accessory with a ZnSe window was used to measure liquids as a thin film. All infrared spectra were measured under inert conditions inside a MBRAUN UNIlab glove box. IR-spectra were recorded and analyzed using the software MicroLab FTIR by AGILENT. The following abbreviations were used to describe the relative intensity of the bands: w = weak, m = medium, s = strong.

8.1.5 ESI-MS

The electrospray ionisation mass spectra were measured by the service department Central Analytics - Mass Spectrometry of the Institute for Organic and Biomolecular Chemistry at the Georg-August-University Göttingen. They were recorded on a BRUKER DALTONICS micrOTOF (ESI-TOF-MS) and a maXis (ESI-QTOF-MS) from BRUKER DALTONICS. Unless stated otherwise, the used solvent was acetonitrile.

8.1.6 GC-MS

Gas chromatography-mass spectrometry was performed on a Trace (GC-MS) by THERMO FINNIGAN using electron ionization (EI) and a quadrupole mass analyzer at the Central Analytics - Mass Spectrometry department of the Institute for Organic and Biomolecular Chemistry at the Georg-August-University Göttingen.

8.1.7 UV/vis Spectroscopy

The UV/vis data were recorded using a Cary 60 UV/Vis spectrophotometer by AGILENT with a wavelength range of 190–1100 nm and a maximum scanning speed of 24000 nm/min. The spectrometer is additionally fitted with a CoolSpeK cryostat with a stirrer from the company UNISOKU to enable temperature-controlled measurement between −80 °C and +100 °C. Liquid nitrogen was used as coolant. All sample solutions were freshly prepared in a MBRAUN LABmaster SP glovebox with H_2O- and O_2-levels lower than 0.1 ppm and filled into a quartz cuvette (d = 1 cm) with a long bottleneck which was closed with a rubber septum. Also, all titrants were freshly prepared in the glovebox and filled into gas tight HAMILTION 1700 Series syringes with a dispensing volume between 50 to 100 µL depending on the measurement. The syringes were closed with rubber seals before they were taken out of the glovebox.

For the measurements where dry dioxygen was used, the oxygen gas was filled into a gas-tight syringe and injected via the rubber septum into the reaction mixture. If dry oxygen was used, it was always used in excess.

Before every measurement, the background was measured and subsequently subtracted from the measured data. Standard measuring temperature was −40 °C and the standard solvent was acetonitrile unless stated otherwise. The data was collected and analyzed with the Cary WinUV software from AGILENT. After every measurement cycle, the cryostat was heated to +100 °C for one hour to eliminate dew condensation.

8.1.8 Resonance Raman measurements

$^{16}O_2$ and $^{18}O_2$ labelled samples were prepared in NMR tubes equipped with a J. Young valve and were measured as frozen solutions. A Scientific LabRAM HR 800 spectrometer by HORIBA was used to record the resonance Raman spectra. A He:Ne-laser with an excitation wavelength of 633 nm or a diode-laser with an excitation wavelength of 457 nm was used depending on the sample. The spectrometer was equipped with an open-electrode CCD detector featuring a confocal pinhole with a user-controlled aperture. In addition, a free space optical microscope was used. A KONTI cryostat by CRYOVAC was used for the low temperature measurements. The obtained data was analyzed with the software HORIBA Scientific's LabSpec 5.

8.1.9 Magnetic measurements

For the measurement of the temperature dependent magnetic susceptibilities a QUANTUM-DESIGN MPMS-XL-5 SQUID magnetometer with a 5 T magnet was used. The solid crystalline sample was grinded into a fine powder and contained afterwards inside a gelatin capsule. The capusule was then placed in a non-magnetic sample holder. The obtained data were corrected for the diamagnetic contribution of the gelatin capsule. The recorded data was compared to a simulation of the experimental magnetic data using the program julX. This program uses a fitting procedure to the spin-Hamiltonian for Zeeman splitting and isotropic exchange coupling according to the equation[217]:

$$\hat{H} = -2J\hat{S}_1\hat{S}_2 + g\mu_B\vec{B}(\hat{S}_1 + \hat{S}_2)$$

The temperature-independent paramagnetism (TIP) and the paramagnetic impurities (PI) were considered and included into the calculation according to the following equation:

$$\chi_{calc} = (1 - \mathrm{PI})\chi + \mathrm{PI}\chi_{mono} + \mathrm{TIP}$$

8.1.10 XRD

Single crystal X-ray diffraction was performed to determine the molecular structure of the crystallized complexes. To this end, a STOE IPDS II diffractometer with an area detector (graphite monochromated Mo-Kα radiation (λ = 0.71073 Å) was used. XRD-Data were collected by using ω scans at 133 K. The molecular structure was solved by direct methods using the software packages SHELXS or SHELXT and subsequently refined on F^2 using all the available reflections with SHELXL-2014[218,219]. All atoms except for the hydrogen atoms were refined anisotropically. Hydrogen atoms were added via the HFIX command which placed them in the calculated position. Face-indexed absorption corrections were performed numerically using the program X-RED from STOE & CIE GMBH.

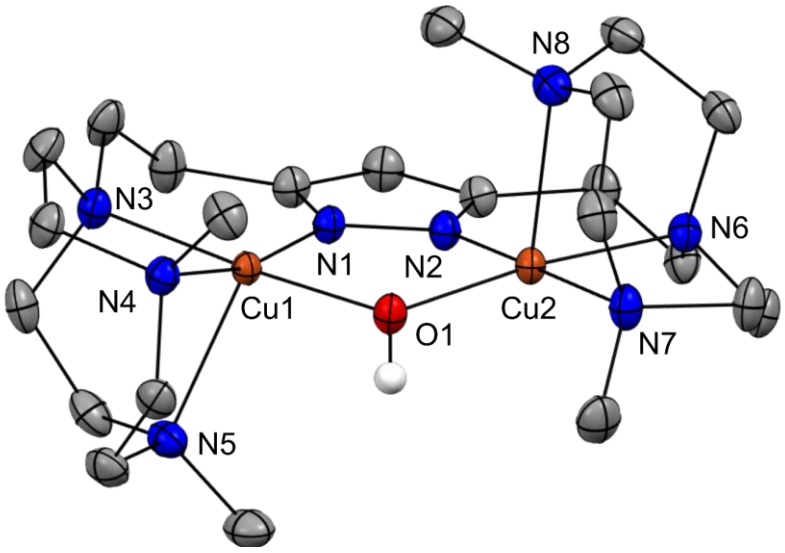

Figure 82: Molecular structure of the μ-hydroxo dicopper(II) complex **21** (thermal displacement ellipsoids given at 50 % probability). The two tetraphenylborate anions, propionitrile and the unnecessary hydrogen atoms are omitted for clarity. Selected Bond length [Å] and bond angles [°]: Cu(1)-O(1) 1.9473(10), Cu(1)-N(1) 1.9517(12), Cu(1)-N(3) 2.0539(12), Cu(1)-N(4) 2.0865(12), Cu(1)-N(5) 2.2334(13), Cu(2)-N(2) 1.9399(12), Cu(2)-O(1) 1.9505(10), Cu(2)-N(7) 2.0617(12), Cu(2)-N(6) 2.0710(12), Cu(2)-N(8) 2.2667(13), N(1)-Cu(1)-N(3) 93.00(5), O(1)-Cu(1)-N(4) 92.02(5), N(1)-Cu(1)-N(4) 166.95(5), N(3)-Cu(1)-N(4) 84.88(5), O(1)-Cu(1)-N(5) 99.42(5), N(1)-Cu(1)-N(5) 110.03(5), N(3)-Cu(1)-N(5) 84.46(5), N(4)-Cu(1)-N(5) 82.62(5), N(2)-Cu(2)-O(1) 89.61(5), N(2)-Cu(2)-N(7) 177.71(5), O(1)-Cu(2)-N(7) 91.86(5), N(2)-Cu(2)-N(6) 92.78(5), O(1)-Cu(2)-N(6) 173.93(5), N(7)-Cu(2)-N(6) 85.58(5), N(2)-Cu(2)-N(8) 97.77(5), O(1)-Cu(2)-N(8) 102.47(5), N(7)-Cu(2)-N(8) 83.63(5), N(6)-Cu(2)-N(8) 82.74(5), Cu(1)-O(1)-Cu(2) 117.95(5).

Table 16: Crystal data and structure refinement of **21**.

Compound	**21**
Empirical formula	$C_{74}H_9B_2Cu_2N_9O$
Formula weight [g/mol]	1271.25
Temperature [K]	133(2)
Wavelength [Å]	0.71073
Crystal system	Triclinic
Space group	P-1
Unit cell dimensions	a = 11.4020(3) Å α= 76.450(2)°
	b = 14.4362(4) Å β= 89.123(2)°
	c = 20.2492(6) Å γ = 87.519(2)°

Volume [Å^3]	3237.19(16)
Z	2
Density (calculated) [mg/m^3]	1.304
Absorption coefficient [mm^{-1}]	0.710
F(000)	1348
Crystal size [mm^3]	0.500 x 0.470 x 0.450
Theta range for data collection [°]	1.452 to 26.896
Index ranges	-14<=h<=14, -18<=k<=18, -25<=l<=25
Reflections collected	46583
Independent reflections	13748 [R(int) = 0.0260]
Completeness to theta = 25.242°	100.0 %
Absorption correction	Numerical
Max. and min. transmission	0.7993 and 0.6358
Refinement method	Full-matrix least-squares on F2
Data / restraints / parameters	13748 / 0 / 802
Goodness-of-fit on F^2	1.028
Final R indices [I>2sigma(I)]	R1 = 0.0298, wR2 = 0.0783
R indices (all data)	R1 = 0.0368, wR2 = 0.0819
Extinction coefficient	n/a
Largest diff. peak and hole	0.388 and -0.511 e.Å^{-3}

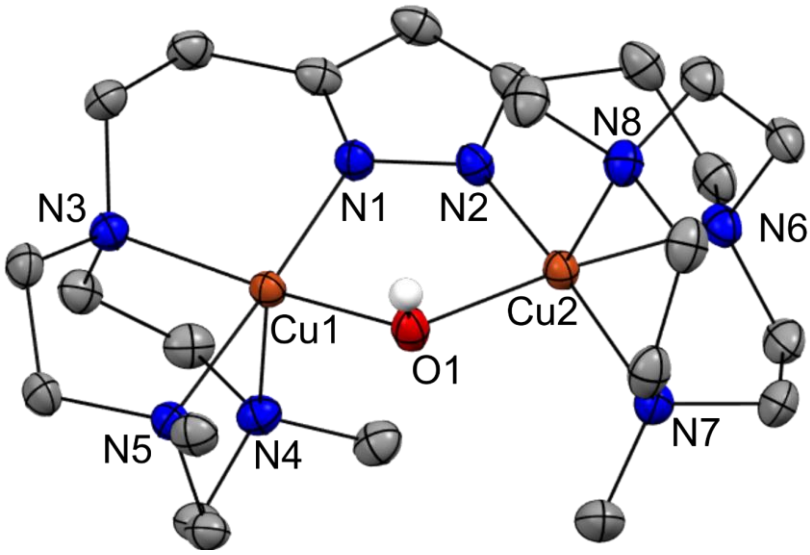

Figure 83: Molecular structure of the μ-hydroxo dicopper(II) complex **21b** (thermal displacement ellipsoids given at 50 % probability). The two perchlorate anions, water and the unnecessary hydrogen atoms are omitted for clarity. Selected Bond length [Å] and bond angles [°]: Cu(1)-O(1) 1.9398(13), Cu(1)-N(1) 1.9559(14), Cu(1)-N(3) 2.0579(14), Cu(1)-N(5) 2.0745(14), Cu(1)-N(4) 2.2668(15), Cu(2)-N(2) 1.9500(15), Cu(2)-O(1) 1.9503(12), Cu(2)-N(6) 2.0618(15), Cu(2)-N(7) 2.0749(15), Cu(2)-N(8) 2.2349(15), O(1)-Cu(1)-N(1) 88.57(6), O(1)-Cu(1)-N(3) 170.83(6), N(1)-Cu(1)-N(3) 92.19(6), O(1)-Cu(1)-N(5) 93.00(5), N(1)-Cu(1)-N(5) 177.54(6), N(3)-Cu(1)-N(5) 85.95(6), O(1)-Cu(1)-N(4) 106.11(6), N(1)-Cu(1)-N(4) 98.79(6), N(3)-Cu(1)-N(4) 82.81(6), N(5)-Cu(1)-N(4) 82.60(6), N(2)-Cu(2)-O(1) 89.00(6), N(2)-Cu(2)-N(6) 92.47(6), O(1)-Cu(2)-N(6) 173.30(6), N(2)-Cu(2)-N(7) 168.97(6), O(1)-Cu(2)-N(7) 92.00(6), N(6)-Cu(2)-N(7) 85.32(6), N(2)-Cu(2)-N(8) 107.74(6), O(1)-Cu(2)-N(8) 101.34(5), N(6)-Cu(2)-N(8) 84.45(6), N(7)-Cu(2)-N(8) 82.83(6), Cu(1)-O(1)-Cu(2) 118.55(6).

Table 17: Crystal data and structure refinement of **21b**.

Compound	**21b**
Empirical formula	$C_{23}H_{48}Cl_2Cu_2N_8O_{10}$
Formula weight [g/mol]	794.67
Temperature [K]	133(2)
Wavelength [Å]	0.71073
Crystal system	Triclinic
Space group	P-1
Unit cell dimensions	a = 8.9277(3) Å α= 70.966(3)°
	b = 11.7471(5) Å β= 78.170(3)°
	c = 16.7323(7) Å γ = 89.536(3)°
Volume [$Å^3$]	1620.34(12)
Z	2
Density (calculated) [mg/m^3]	1.629
Absorption coefficient [mm^{-1}]	1.542
F(000)	828
Crystal size [mm^3]	0.500 x 0.320 x 0.210
Theta range for data collection [°]	1.318 to 26.818
Index ranges	11<=h<=11, -14<=k<=14, -21<=l<=21
Reflections collected	22474
Independent reflections	6866 [R(int) = 0.0248]
Completeness to theta = 25.242°	99.9 %
Absorption correction	Numerical
Max. and min. transmission	0.7241 and 0.4550
Refinement method	Full-matrix least-squares on F^2
Data / restraints / parameters	6866 / 3 / 419
Goodness-of-fit on F^2	1.027
Final R indices [I>2sigma(I)]	R1 = 0.0256, wR2 = 0.0693
R indices (all data)	R1 = 0.0308, wR2 = 0.0716
Extinction coefficient	n/a
Largest diff. peak and hole	0.563 and -0.366 e.$Å^{-3}$

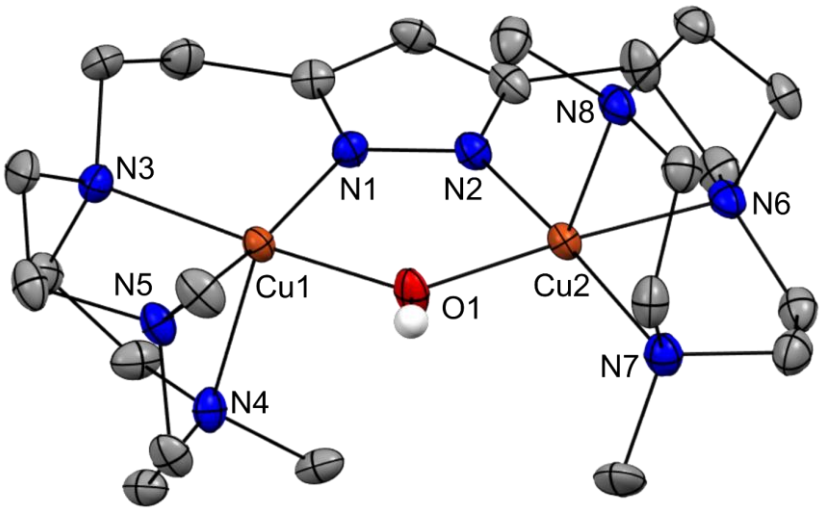

Figure 84: Molecular structure of the μ-hydroxo dicopper(II) complex **21c** (thermal displacement ellipsoids given at 50 % probability). The two perchlorate anions and the unnecessary hydrogen atoms are omitted for clarity. Selected Bond length [Å] and bond angles [°]: Cu(1)-O(1) 1.931(4), Cu(1)-N(1) 1.954(5), Cu(1)-N(3) 2.065(5), Cu(1)-N(5) 2.071(4), Cu(1)-N(4) 2.238(5), Cu(2)-O(1) 1.929(4), Cu(2)-N(2) 1.973(5), Cu(2)-N(6) 2.058(5), Cu(2)-N(7) 2.067(5), Cu(2)-N(8) 2.226(5), O(1)-Cu(1)-N(1) 86.88(18), O(1)-Cu(1)-N(3) 176.24(19), N(1)-Cu(1)-N(3) 92.92(19), O(1)-Cu(1)-N(5) 94.62(18), N(1)-Cu(1)-N(5) 172.5(2), N(3)-Cu(1)-N(5) 85.1(2), O(1)-Cu(1)-N(4) 100.53(18), N(1)-Cu(1)-N(4) 103.79(19), N(3)-Cu(1)-N(4) 83.17(18), N(5)-Cu(1)-N(4) 83.21(18), O(1)-Cu(2)-N(2) 87.05(18), O(1)-Cu(2)-N(6) 175.3(2), N(2)-Cu(2)-N(6) 92.92(19), O(1)-Cu(2)-N(7) 94.36(18), N(2)-Cu(2)-N(7) 171.7(2), N(6)-Cu(2)-N(7) 85.00(19), O(1)-Cu(2)-N(8) 100.57(19), N(2)-Cu(2)-N(8) 104.72(19), N(6)-Cu(2)-N(8) 84.00(18), N(7)-Cu(2)-N(8) 83.1(2), Cu(2)-O(1)-Cu(1) 123.7(2).

Table 18: Crystal data and structure refinement of **21c**.

Compound	**21c**
Empirical formula	$C_{23}H_{46}Cl_2Cu_2N_8O_9$
Formula weight [g/mol]	776.66
Temperature [K]	100(2)
Wavelength [Å]	0.71073
Crystal system	Monoclinic
Space group	Cc
Unit cell dimensions	a = 12.6309(6) Å α= 90°
	b = 11.5678(6) Å β= 101.205(2)°
	c = 22.1848(10) Å γ = 90°
Volume [$Å^3$]	3179.7(3)
Z	4
Density (calculated) [mg/m^3]	1.622
Absorption coefficient [mm^{-1}]	1.567
F(000)	1616
Crystal size [mm^3]	0.287 x 0.214 x 0.137
Theta range for data collection [°]	2.409 to 27.905
Index ranges	-16<=h<=16, -15<=k<=15, -29<=l<=29
Reflections collected	40029
Independent reflections	7596 [R(int) = 0.0366]
Completeness to theta = 25.242°	99.9 %
Absorption correction	Semi-empirical from equivalents

Max. and min. transmission	0.81 and 0.71
Refinement method	Full-matrix least-squares on F^2
Data / restraints / parameters	7596 / 3 / 405
Goodness-of-fit on F^2	1.209
Final R indices [I>2sigma(I)]	R1 = 0.0384, wR2 = 0.0841
R indices (all data)	R1 = 0.0407, wR2 = 0.0850
Extinction coefficient	0.400(16)
Largest diff. peak and hole	n/a

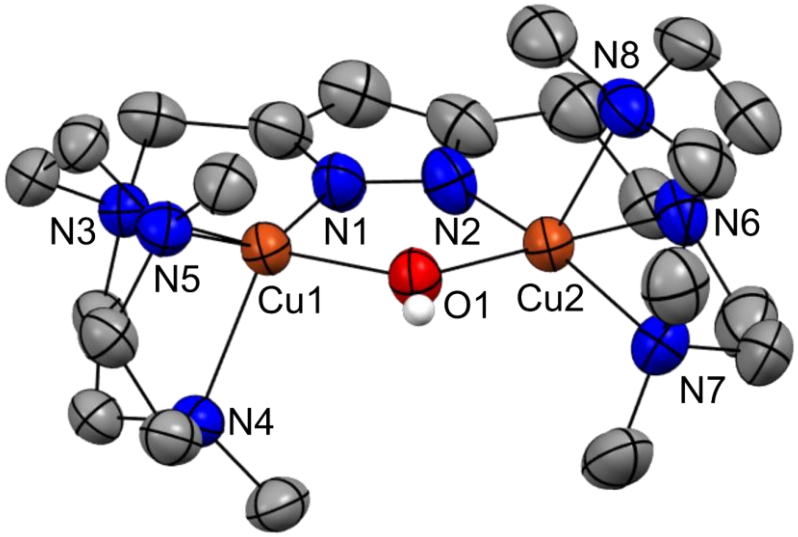

Figure 85: Molecular structure of the μ-hydroxo dicopper(II) complex **23** (thermal displacement ellipsoids given at 50 % probability). The two tetraphenylborate anions, acetonitrile, diethylether and the unnecessary hydrogen atoms are omitted for clarity. Selected Bond length [Å] and bond angles [°]: Cu(1)-N(1) 1.878(3), Cu(1)-O(1) 1.939(3), Cu(1)-N(5) 2.059(3), Cu(1)-N(3) 2.084(3), Cu(1)-N(4) 2.216(3), Cu(2)-N(2) 1.943(3), Cu(2)-O(1) 1.956(3), Cu(2)-N(7) 2.055(3), Cu(2)-N(6) 2.078(3), Cu(2)-N(8) 2.223(3), N(1)-Cu(1)-O(1) 85.99(12), N(1)-Cu(1)-N(5) 148.10(13), O(1)-Cu(1)-N(5) 106.24(11), N(1)-Cu(1)-N(3) 82.21(12), O(1)-Cu(1)-N(3) 167.83(11), N(5)-Cu(1)-N(3) 85.49(12), N(1)-Cu(1)-N(4) 123.26(14), O(1)-Cu(1)-N(4) 100.33(11), N(5)-Cu(1)-N(4) 84.18(12), N(3)-Cu(1)-N(4) 83.79(11), N(2)-Cu(2)-O(1) 87.61(12), N(2)-Cu(2)-N(7) 164.13(15), O(1)-Cu(2)-N(7) 97.99(12), N(2)-Cu(2)-N(6) 87.88(13), O(1)-Cu(2)-N(6) 174.21(12), N(7)-Cu(2)-N(6) 85.44(14), N(2)-Cu(2)-N(8) 110.24(14), O(1)-Cu(2)-N(8) 101.14(12), N(7)-Cu(2)-N(8) 83.35(14), N(6)-Cu(2)-N(8) 83.84(12), Cu(1)-O(1)-Cu(2) 121.01(13).

Table 19: Crystal data and structure refinement of **23**.

Compound	**23**
Empirical formula	$C_{78}H_{101}B_2Cu_2N_9O_{2.50}$
Formula weight [g/mol]	1353.37
Temperature [K]	133(2)
Wavelength [Å]	0.71073
Crystal system	Monoclinic
Space group	$P2_1/n$
Unit cell dimensions	a = 11.5479(2) Å a= 90°
	b = 46.7925(6) Å b= 91.0290(10)°
	c = 13.5743(2) Å g = 90°
Volume [$Å^3$]	7333.76(19)

Z	4
Density (calculated) [mg/m^3]	1.226
Absorption coefficient [mm^{-1}]	0.632
F(000)	2880
Crystal size [mm^3]	0.500 x 0.280 x 0.260
Theta range for data collection [°]	1.562 to 25.726
Index ranges	-14<=h<=12, -56<=k<=56, -16<=l<=16
Reflections collected	75964
Independent reflections	13842 [R(int) = 0.0356]
Completeness to theta = 25.242°	100.0 %
Absorption correction	Numerical
Max. and min. transmission	0.8615 and 0.6502
Refinement method	Full-matrix least-squares on F^2
Data / restraints / parameters	13842 / 8 / 877
Goodness-of-fit on F^2	1.024
Final R indices [I>2sigma(I)]	R1 = 0.0616, wR2 = 0.1716
R indices (all data)	R1 = 0.0775, wR2 = 0.1890
Extinction coefficient	n/a
Largest diff. peak and hole	1.186 and -0.554 e.Å^{-3}

8.2 Ligand Synthesis

The syntheses described in this chapter are based on literature known procedures and were modified as well improved either to maximise the yield and/or to improve the purity of the product. The synthesis of 1,4-Dimethyl-1,4,7-triazacyclononane is based on the works of WIEGHARDT *et al.*, TOLMAN *et al.* and ATKINS *et al.*[132,137,138]. The synthesis of the symmetric pyrazole building block is based on the work of AKITA *et al.*[144]. The synthesis of the non-symmetric pyrazole unit was based on the work of Silke Buchler and was optimized and refined together with Dr. Jerome Spyra[38,109]. Complex syntheses are inspired by the work of former PhD students and students of the Meyer working group and were adapted and improved[38,65,104,121,123,126,182]. Also, earlier version of some of the here shown syntheses can be found in the bachelor thesis of Tobias Weege and in the master thesis of the author[32,220].

8.2.1 Synthesis of 1,4-Dimethyl-1,4,7-triazacyclononane

8.2.1.1 Synthesis of *N*,*N*′,*N*″-tritosyldiethylenetriamine 3

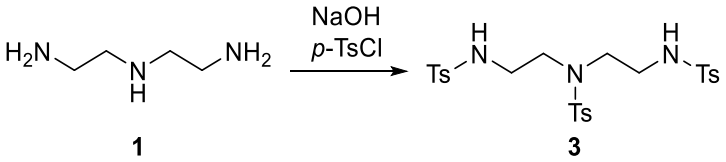

At 0 °C *p*-toluenesulfonyl chloride (300 g, 1.57 mol, 3.06 eq.) suspended in DCM (900 mL) was added dropwise to a mixture of diethylenetriamine (53.1 g, 55.3 mL, 515 mmol, 3.06 eq.) and sodium hydroxide (62.2 g, 1.55 mol, 3.02 eq.) in distilled water (400 mL). The reaction mixture was stirred overnight. The precipitated crude product was separated from the solvent, washed with distilled water (300 mL) and diethyl ether (100 mL). After recrystallization from acetonitrile, the product was washed with cold acetonitrile and dried in vacuum. The product *N*,*N*′,*N*″-tritosyldiethylenetriamine was obtained as a colorless solid (201 g, 357 mmol, 69 %).

^{1}H-NMR (300 MHz, DMSO-d_6): δ (ppm) = 7.68 – 7.62 (m, 6 H, Ar-H), 7.57 – 7.51 (m, 2 H, Ar-H), 7.43 – 7.33 (m, 6 H, Ar-H), 3.06 – 2.95 (m, 4 H, 3-CH_2, 5-CH_2), 2.86 – 2.74 (m, 4 H, 2-CH_2, 6-CH_2), 2.39 (s, 6 H, CH_3), 2.38 (s, 3 H, CH_3).

^{13}C-NMR (75 MHz, DMSO-d_6): δ (ppm) = 143.5 (C^q), 142.8 (C^q), 137.4 (C^q), 135.4 (C^q), 129.9 (C^{Ar}), 129.7 (C^{Ar}), 126.8 (C^{Ar}), 126.5 (C^{Ar}), 48.4 (C-3, C-5), 41.6 (C-2, C-6), 21.0 (CH_3).

8.2.1.2 Synthesis of *O*,*O′*-ditosylethylene glycol 4

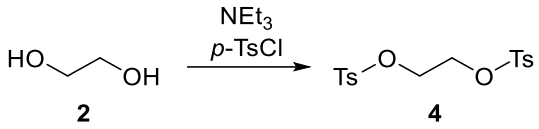

2 4

To a mixture of ethylene glycol (20.0 g, 18.0 mL, 322 mmol, 1.00 eq.) and triethylamine (75.0 g, 103 mL, 741 mmol, 2.30 eq.) in DCM (60 mL) a suspension of *p*-toluenesulfonyl chloride (135 g, 709 mmol, 2.20 eq.) in DCM (300 mL) was added dropwise at 0 °C. The reaction mixture was stirred overnight. Subsequently, DCM (500 mL) and distilled water (450 mL) were added. The organic phase was separated, the aqueous phase was extracted with DCM (3 × 135 mL) and the combined organic phases were dried over magnesium sulfate. After removing the organic solvent under vacuum, the crude solid product was recrystallized from DCM. The product could be collected as a colorless crystalline solid (94.5 g, 255 mmol, 79 %) after filtration and drying in vacuum.

^{1}H-NMR (300 MHz, $CDCl_3$): δ (ppm) = 7.76 – 7.69 (m, 4 H, Ar-H), 7.37 – 7.29 (m, 4 H, Ar-H), 4.18 (s, 4 H, 1-CH_2, 2-CH_2), 2.45 (s, 6 H, CH_3).

^{13}C-NMR (75 MHz, $CDCl_3$): δ (ppm) = 145.4 (C^q), 132.5 (C^q), 130.1 (C^{Ar}), 128.1 (C^{Ar}), 66.8 (C-1, C-2), 21.8 (CH_3).

8.2.1.3 Synthesis of *N*,*N′*,*N″*-tritosyl-1,4,7-triazacyclononane 5

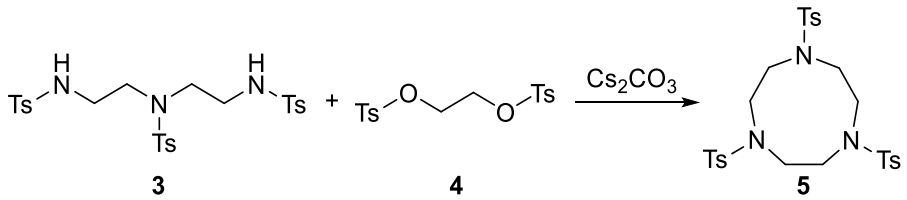

3 4 5

A mixture of *N*,*N′*,*N″*-tritosyldiethylenetriamine (90.0 g, 159 mmol, 1.00 eq.) and caesium carbonate (114 g, 350 mmol, 2.20 eq.) in DMF (940 mL) was stirred for 1.5 h at room temperature. *O*,*O′*-ditosylethylene glycol (59.3 g, 159 mmol, 1.00 eq.) in DMF (350 mL) was added dropwise to the suspension and subsequent the reaction mixture was stirred for two days at room temperature. Distilled water (3.50 L) was added and the reaction mixture was stirred for 1 h. The precipitated solid was collected, added to a 1:1 mixture of distilled water (1.10 L) and DMF (1.10 L) and stirred overnight. Filtration, washing of the crude solid product with ethanol (350 mL) and drying the solid in vacuum for three days gave the product as a clean colorless solid (86.7 g, 147 mmol, 92 %).

^{1}H-NMR (300 MHz, $CDCl_3$): δ (ppm) = 7.73 – 7.66 (m, 6 H, Ar-H), 7.34 – 7.29 (m, 6 H, Ar-H), 3.42 (s, 12 H, CH_2), 2.43 (s, 9 H, CH_3)

^{13}C-NMR (75 MHz, $CDCl_3$): δ (ppm) = 144.0 (C^q), 134.8 (C^q), 130.0 (C^{Ar}), 127.7 (C^{Ar}), 52.0 (CH_2), 21.6 (CH_3).

8.2.1.4 Synthesis of 1-(*p*-tosyl)-1,4,7-triazacyclononane 6

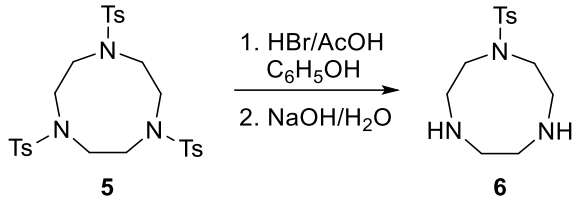

5 **6**

Hydrobromic acid in acetic acid (33 %, 550 mL) were added to *N*,*N*′,*N*″-tritosyl-1,4,7-triazacyclononane (53.0 g, 89.6 mmol, 1.00 eq.) and phenol (63.2 g, 672 mmol, 7.50 eq.). The resulting mixture was slowly heated to 70 °C and stirred vigorously for two days. Caution: Large amounts of gaseous hydrobromic acid evolved during the heating of this reaction mixture. To cope with the resulting gas three gas-washing bottles were used. The first one was empty, the second was filled with an aqueous concentrated sodium bicarbonate solution and the last one contained a saturated sodium thiosulfate solution. Additionally, it is recommended to start the reaction with a positive inert gas pressure to avoid water from backfilling into the reaction flask during cooling of the reaction[136,138]. The resulting orange precipitate was separated and washed with diethyl ether (4 × 300 mL). Subsequently the solid was dissolved in an aqueous sodium hydroxide solution (1 M, 400 mL) and chloroform (200 mL) was added. The organic phase was separated, the aqueous phase was extracted with chloroform (3 × 135 mL) and the combined organic phases were dried over magnesium sulfate. After the solvent was removed and drying under vacuum, the product was obtained as a colorless solid (19.3 g, 68.1 mmol, 76 %). The product is not stable but can be stored for 2 days at −26 °C under argon.

^{1}H-NMR (300 MHz, $CDCl_3$): δ (ppm) = 7.70 – 7.65 (m, 2 H, Ar-H), 7.32 – 7.27 (m, 2 H, Ar-H), 3.21 – 3.14 (m, 4 H, 2-CH_2, 9-CH_2), 3.10 – 3.04 (m, 4 H, 3-CH_2, 8-CH_2), 2.88 (s, 4 H, 5-CH_2, 6-CH_2), 2.41 (s, 3 H, CH_3), 1.75 (s, 2 H, NH).

^{13}C-NMR (75 MHz, $CDCl_3$): δ (ppm) = 143.3 (C^{q}), 135.8 (C^{q}), 129.8 (C^{Ar}), 127.4 (C^{Ar}), 54.1 (C-5, C-6), 49.8 (C-2, C-6), 49.8 (C-2, C-9), 49.7 (C-3, C-8), 21.6 (CH_3).

8.2.1.5 Synthesis of 4,7-dimethyl-1-(*p*-tosyl)-1,4,7-triazacyclononane 7

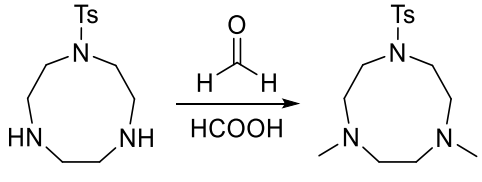

6 **7**

At 0 °C formaldehyde (32.0 mL, 36.5 %) was added dropwise to a stirring suspension of 1-(*p*-tosyl)-1,4,7-triazacyclononane (10.5 g, 37.1 mmol, 1.00 eq.) in distilled water (9.0 mL). Following this formic acid (32.0 mL) was added dropwise and the reaction mixture was heated under reflux for 24 h. After

cooling of the reaction mixture hydrochloric acid (23 mL, 33 %) was added and all volatile components were removed under vacuum with a liquid nitrogen cooled cold trap. Aqueous sodium hydroxide solution (3 M) was added slowly to the residue until the pH = 11 was reached and afterwards the solution was extracted with chloroform (3 × 80 mL). The combined organic phases were dried over magnesium sulfate and the solvent was removed in vacuum. Drying of the resulting oil at 1×10^{-3} bar with heating to 50 °C yielded the pure product as a yellow solid (10.5 g, 33.7 mmol, 91 %). The product is very stable and can be stored at room temperature.

^{1}H-NMR (300 MHz, $CDCl_3$): δ (ppm) = 7.69 – 7.62 (m, 2 H, Ar-H), 7.32 – 7.26 (m, 2 H, Ar-H), 3.27 – 3.21 (m, 4 H, 2-CH_2, 9-CH_2), 2.93 – 2.86 (m, 4 H, 3-CH_2, 8-CH_2), 2.68 (s, 4 H, 5-CH_2, 6-CH_2), 2.41 (s, 3 H, CH_3), 2.39 (s, 6 H, CH_3).

^{13}C-NMR (75 MHz, $CDCl_3$): δ (ppm) = 143.2 (C^q), 136.1 (C^q), 129.7 (C^{Ar}), 127.3 (C^{Ar}), 57.6 (C-5, C-6), 57.2 (C-2, C-9), 51.4 (C-3, C-8), 46.4 (CH_3), 21.6 (CH_3).

8.2.1.6 Synthesis of 1,4-dimethyl-1,4,7-triazacyclononane 8

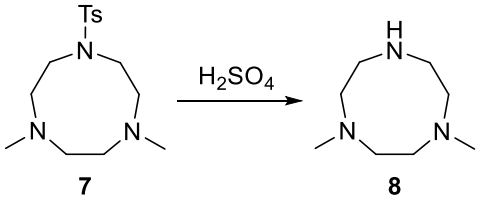

7 **8**

4,7-dimethyl-1-(*p*-tosyl)-1,4,7-triazacyclononane (8.00 g, 25.7 mmol, 1.00 eq.) was dissolved in concentrated sulfuric acid (80 mL) and the reaction mixture was heated under reflux for 24 h. The acidic mixture was cooled to 0 °C and the pH was carefully adjusted to 12 starting with an aqueous sodium hydroxide solution (1 M) and ending with an aqueous sodium hydroxide solution (5 M). The aqueous solution was extracted with chloroform (4 × 100 mL), the organic phases were combined and dried with magnesium sulfate. Under vacuum the solvent was removed and a brown oil formed. Purification with a bulb-to-bulb distillation at 50 °C using a liquid nitrogen cooled cold trap as the receiving flask yielded the desired compound as a colorless viscous oil (2.75 g, 17.5 mmol, 68 %). The product cannot be stored for long time. Even under argon at −26 °C decomposition occurs but the compound can be purified again with a second bulb-to-bulb distillation. The decomposition product can be separated as a yellow and highly viscous oil.

^{1}H-NMR (300 MHz, $CDCl_3$): δ (ppm) = 2.96 (s(br), 1 H, NH), 2.63 – 2.57 (m, 4 H, 2-CH_2, 9-CH_2), 2.50 – 2.43 (m, 8 H, 3-CH_2, 8-CH_2, 5-CH_2, 6-CH_2), 2.34 (s, 6 H, CH_3).

^{13}C-NMR (75 MHz, $CDCl_3$): δ (ppm) = 54.7 (C-5, C-6), 53.29 (C-3, C-8), 46.6 (C-2, C-9), 45.6 (CH_3).

MS (ESI^+, MeCN): m/z = 158.2 $[M+H]^+$, 127.1 $[M+H–2CH_3]^+$, 101.1 $[M+H–2CH_3–C_2H_4]^+$.

8.2.2 Synthesis of the pyrazole units

8.2.2.1 Synthesis of 3,5-Bis(2-chloroethyl)-1*H*-pyrazole hydrochloride 14

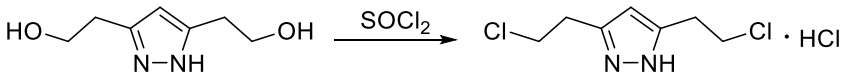

13 **14**

At 0 °C thionyl chloride (50 mL) was added dropwise to 3,5-Bis(2-hydroxyethyl)-1*H*-pyrazole (3.70 g, 23.7 mmol, 1.00 eq.) and subsequently the resulting reaction mixture was stirred for 1 h at 60 °C. The excess of thionyl chloride was removed and recycled with help of a cold trap. The resulting yellow oil was taken up in ethanol (20 mL) and overlayed with diethyl ether (40 mL). Slow diffusion crystallization at −26 °C overnight led to a colorless compound. This compound was washed with diethyl ether (3 × 25 mL) and dried under oil-pump vacuum. The formed product was a colorless solid (3.51 g, 15.4 mmol, 65 %).

^{1}H-NMR (300 MHz, DMSO-d_6): δ (ppm) = 6.35 (s, 1 H, Pz-H), 3.88 (t, $^{3}J_{HH}$ = 6.8 Hz, 4 H, CH_2Cl), 3.09 (t, $^{3}J_{HH}$ = 6.7 Hz, 4 H, CH_2).

^{13}C-NMR (75 MHz, DMSO-d_6): δ (ppm) = 144.8 (3,5-C^{pz}), 104.4 (4-C^{pz}), 43.1 (CH_2Cl), 29.3 (CH_2).

8.2.2.2 Synthesis of 3,5-Bis(2-chloroethyl)-1-(tetrahydro-2*H*-pyran-2-yl)-pyrazole 15

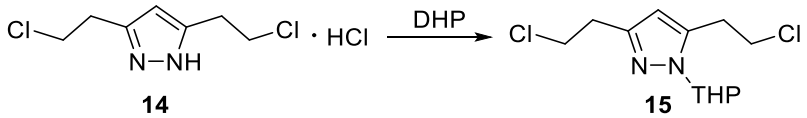

14 **15**

3,5-Bis(2-chlorethyl)-1*H*-pyrazole hydrochloride (3.50 g, 18.1 mmol, 1.00 eq.) was dissolved in DCM (80 mL) and 3,4-Dihydro-2*H*-pyran (5.49 g, 5,09 mL, 65.3 mmol, 3.60 eq.) was added dropwise to the solution. The reaction mixture was stirred for 24 h and subsequently a solution of sodium bicarbonate (16.8 g) in deionized water (300 mL) was added. After the extraction of the aqueous phase with DCM (2 × 125 mL), the organic phases were combined and dried over magnesium sulfate. Under reduced pressure the solvent was removed, the resulting oil was suspended in hexane (8 mL) and diethyl ether was added dropwise until the solution became clear. The desired colorless solid product (3,71 g, 13.4 mmol, 74 %) was obtained after crystallization at −26 °C and drying under vacuum.

^{1}H-NMR (300 MHz, DMSO-d_6): δ (ppm) = 6.16 (s, 1 H, Pz-H),5.34 (dd, $^{3}J_{HH}$ = 9.7 Hz, 2.5 Hz, 1 H, CH_2), 3.90 - 3.68 (m, 6 H, $CH_2^{3`}$, $CH_2Cl$), 3.14 (t, $^{3}J_{HH}$ = 7.1 Hz, 2 H, $CH_2$), 2.94 (t, $^{3}J_{HH}$ = 7.1 Hz, 2 H, $CH_2$), 2.33 – 2.16 (m, 1 H, $CH_2^{6`}$), 2.03 – 1.90 (m, 1 H, $CH_2^{6`}$), 1.87 – 1.33 (m, 4 H, $CH_2^{4`}$, $CH_2^{5`}$).

8.2.2.3 Synthesis of 5-(2-hydroxyethyl)-3-(hydroxymethyl)-1*H*-pyrazole 17

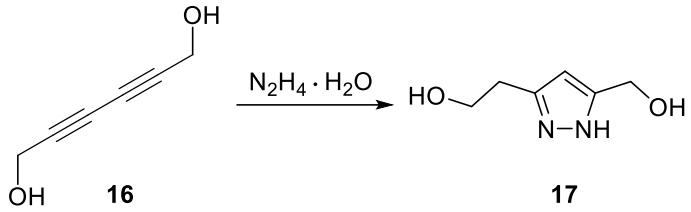

2,4-Hexadiyne-1,6-diol (2.50 g, 22.7 mmol, 1.00 eq.) and hydrazine monohydrate (3.41 g, 3,30 mL, 68,1 mmol, 3.00 eq.) were dissolved in ethanol (125 mL) and the reaction mixture was heated under reflux overnight. After the reaction mixture cooled down to room temperature the excess hydrazine monohydrate and the solvent were removed under rotary vane pump vacuum and with the help of a liquid nitrogen cooled cold trap. Ethanolic hydrochloric acid (6 M, 10 mL) and diethyl ether (100 mL) were added to the viscous residue and the resulting mixture was stirred overnight. The solvent was decanted and the product (2.52 g, 17.7 mmol, 78 %), a highly viscous brown oil, was dried under vacuum at the Schlenk line. (With regard to the above mentioned please note that the successful synthesis of this product is highly dependent on the purity of the reagent 2,4-hexadiyne-1,6-diol.)

^{1}H-NMR (300 MHz, $CDCl_3$): δ (ppm) = 6.44 (s, 1 H, Pyr-H), 4.57 (s, 2 H, CH_2Cl), 3.68 (t, J = 6.4 Hz, CH_2Cl), 2.83 (t, J = 6.4 Hz, CH_2).

8.2.2.4 Synthesis of 5-(2-chloroethyl)-3-(chloromethyl)-1*H*-pyrazole hydrochloride 18

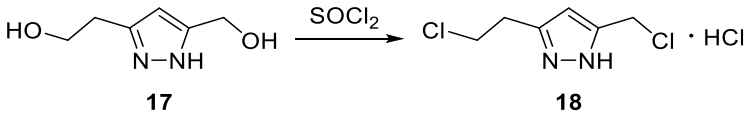

At 0 °C thionyl chloride (80 mL) was added dropwise to 5-(2-hydroxyethyl)-3-(hydroxymethyl)-1*H*-pyrazole (2.50 g, 17,6 mmol, 1.00 eq.) and the resulting reaction mixture was stirred for 2 h at 60 °C. The excess thionyl chloride was removed and recycled with help of a liquid nitrogen cooled cold trap. The resulting brown oil was stirred in an excess of diethyl ether (100 mL) for one day. Subsequently the solvent was decanted and the purification process was repeated two times. The resulting solid was dried under vacuum and the product was obtained as a colorless solid (2,01 g, 9.32 mmol, 53 %).

^{1}H-NMR (300 MHz, $CDCl_3$): δ (ppm) = 6.22 (s, 1 H, Pyr-H), 4.67 (s, 2 H, CH_2Cl), 3.84 (t, J = 6.9 Hz, 2 H, CH_2Cl), 3.03 (t, J = 6.9 Hz, 2 H, Pyr-CH_2).

8.2.3 Synthesis of the ligand scaffolds

8.2.3.1 Synthesis of HL_{sym} with 3,5-Bis(2-chloroethyl)-1*H*-pyrazole hydrochloride

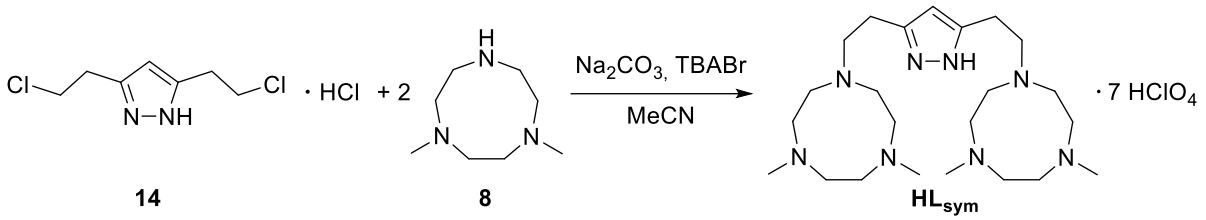

To the stirring suspension of 3,5-Bis(2-chloroethyl)-1*H*-pyrazole hydrochloride (2.50 g, 10.9 mmol, 1.00 eq.), tetrabutylammonium bromide (1.40 g, 4.35 mmol, 0.40 eq.) and sodium carbonate (13.28 g, 125 mmol, 11.5 eq.) in acetonitrile (200 mL) was added 1,4-dimethyl-1,4,7-triazacyclononane (3.77 g, 24.0 mmol, 2.20 eq.). The reaction mixture was heated immediately to 100 °C and stirred for 24 h. Once the reaction mixture cooled down, the excess of sodium carbonate was filtered off and a yellow liquid was obtained. The solvent was removed and the remaining yellow oil was taken up in DCM (150 mL), washed with sodium hydroxide (1 M, 100 mL) and the aqueous phase was extracted with DCM (3 × 75 mL). The organic phases were dried over magnesium sulfate and the solvent was removed under reduced pressure. Afterwards the resulting yellow viscous oil was dried under vacuum overnight. Then the oil was dissolved in DME (22 ml) and concentrated perchloric acid was added dropwise until the emerging colorless precipitate started to dissolve again. An orange rubbery solid formed as a 1:1 mixture of ethanol (75 mL) and diethyl ether (75 mL) was added to the reaction mixture. After viscously stirring for 1 h at room temperature the yellow solvent mixture was decanted, ethanol (100 mL) was added and an off-white solid started to formed after stirring for 2 d. The solvent was decanted and the process of adding ethanol (100 mL) and stirring for 1 – 2 d was repeated until no orange solid was left in the flask. Subsequently the solvent was carefully decanted, diethyl ether (100 mL) was added and the mixture was stirred for 1 d. After removing of the solvent, the product and drying under vacuum was obtained as an off-white solid (4.59 g, 40.3 mmol, 37 %).

MS (ESI^+, MeCN): *m*/*z* = 535.2 $[M+HClO_4+H]^+$, 435.3 $[M+H]^+$, 218.1 $[M+2H]^{2+}$.

8.2.3.2 Synthesis of HL_{sym} with 3,5-Bis(2-chloroethyl)-1-(tetrahydro-2*H*-pyran-2-yl)-pyrazole

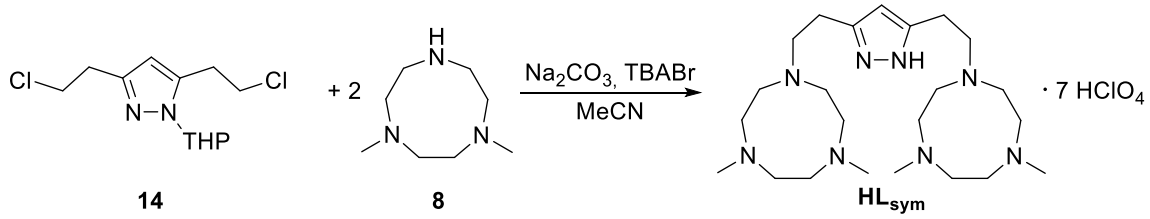

3,5-Bis(2-chloroethyl)-1-(tetrahydro-2*H*-pyran-2-yl)-pyrazole (1.98 g, 7.14 mmol, 1.00 eq.), tetrabutylammonium bromide (0.85 g, 2.64 mmol, 0.37 eq.) and sodium carbonate (8.56 g, 80.7 mmol, 11.3 eq.) were suspended in dry acetonitrile (140 mL). 1,4-dimethyl-1,4,7-triazacyclononane (2.36 g,

15.0 mmol, 2.10 eq.) was added dropwise before the reaction mixture was heated under reflux at 100 °C for 24 h. After filtration the solvent was removed, the residue was taken up in ethanolic hydrochloric acid (6 M, 20 mL). and stirred for 2 h. The reaction mixture was extracted with chloroform (4 × 100 mL) and the combined organic phases were dried over magnesium sulfate. After the solvent was removed under reduced pressure, the residue is taken up in DME (20 mL). Concentrated perchloric acid was added dropwise to the solution until the forming colorless precipitate dissolved again. A 1:1 mixture of ethanol (60 mL) and diethyl ether (60 mL) was added and the mixture was stirred for 1 h. The resulting yellow liquid phase was discarded, ethanol (200 mL) was added to the formed brown solid and stirred vigorously for 1 d. At this stage a solid started to form as a colorless powder in the reaction mixture. The solvent was decanted carefully, substituted by diethyl ether (200 mL) and stirred again vigorously for 2 d. The process of decanting diethyl ether, adding of diethyl ether and stirring for 2 d was repeated until the brown solid was gone and the only the colorless powder was left. After removing the solvent, the colorless product (3.50 g, 3.07 mmol, 43 %) was isolated and dried under vacuum.

MS (ESI$^+$, MeCN): *m*/*z* = 535.2 [M+HClO$_4$+H]$^+$, 435.3 [M+H]$^+$, 218.1 [M+2H]$^{2+}$.

8.2.3.3 Synthesis of HL$_{asym}$ with 5-(2-chloroethyl)-3-(chloromethyl)-1*H*-pyrazole hydrochloride

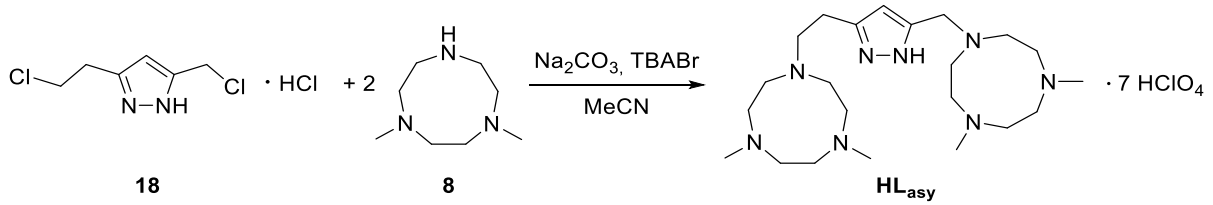

18 **8** **HL$_{asy}$**

1,4-dimethyl-1,4,7-triazacyclononane (1.56 g, 9.90 mmol. 2.20 eq.) was added dropwise to a stirring suspension of 5-(2-chloroethyl)-3-(chloromethyl)-1*H*-pyrazole hydrochloride (0.97 g, 4.50 mmol, 1.00 eq.), tetrabutylammonium bromide (0.54 g, 1.67 mmol, 0.37 eq.) and sodium carbonate (5.39 g, 50.9 mmol, 11.3 eq.) in dry acetonitrile (120 mL). Subsequently the reaction mixture was stirred at 90 °C for 24 h. The reaction mixture was filtered and the solvent was removed under vacuum. The residue was dissolved in DCM (25 mL), washed with a sodium hydroxide solution (1 M, 20 mL) and the aqueous phase was extracted with DCM (3 × 80 mL). Then the combined organic phases were dried over magnesium sulfate and the solvent was removed under vacuum. After drying the residue overnight at the Schlenk line DME (10 mL) was added and concentrated perchloric acid was added dropwise to the solution until the forming colorless precipitate started to dissolve again. To the orange solution a 1:1 mixture of ethanol (20 mL) and diethyl ether (20 mL) was added. A brown solid formed and the mixture was stirred vigorously for 1 h at room temperature. The formed yellow solution was discarded and replaced by ethanol (50 mL) After stirring the reaction mixture for 24 h, the process of discarding and replacing of the solvent was repeated three times with diethyl ether (3 × 90 mL). During this cleaning process the colorless solid product formed. The product (2.07 g, 1.85 mmol, 41 %) was separated and dried under reduced pressure over night.

MS (ESI$^+$, MeCN): *m*/*z* = 521.4 [M+HClO$_4$+H]$^+$, 421.4 [M+H]$^+$, 211.2 [M+2H]$^{2+}$.

8.3 Synthesis of the copper complexes

8.3.1 Synthesis of dicopper(I) complexes

8.3.1.1 Synthesis of the symmetric dicopper(I) complex 19

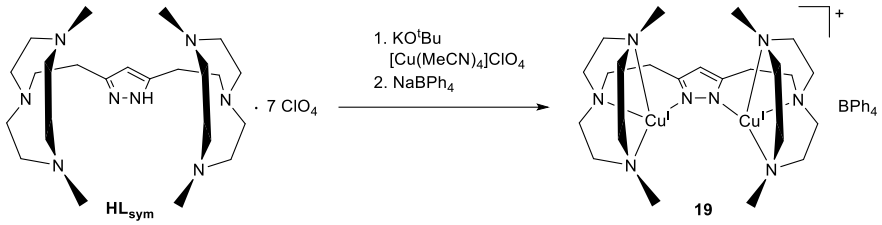

HL$_{sym}$ (148 mg, 130 µmol, 1.00 eq.) was suspended in dry methanol (2.00 mL) under anaerobic conditions. A solution of KO^{t}Bu (119 mg, 1.06 mmol, 8.15 eq.) in dry methanol (1.00 mL) was added and the orange-colored reaction mixture was stirred for 20 min at room temperature. The Cu^I-source, in form of [Cu(MeCN$_4$)]ClO$_4$ (85.2 mg, 260 µmol, 2.00 eq.), was dissolved in dry methanol (1.00 mL), added to the reaction and the reaction mixture was stirred for 30 min. Addition of a solution of NaBPh$_4$ (66.8 mg, 195 µmol, 1.50 eq.) in dry methanol (1.00 mL) led to a colorless precipitate. Filtration of the suspension with a syringe equipped with three layers of Whatman filters gave the desired complex. The filtered solid residue was dried under vacuum for 10 min and dry acetone (2.00 mL) was added. The suspension was stirred for 5 min and subsequently filtered through three layers of Whatman filter. The pale-yellow solution was tried to crystallize with slow vapor diffusion of diethyl ether at −26 °C.

8.3.1.2 Synthesis the non-symmetric dicopper(I) complex 22

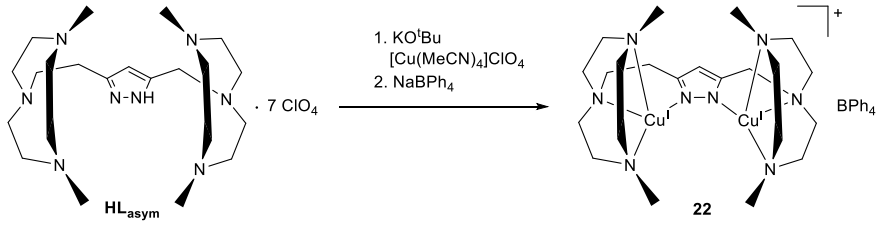

HL$_{asym}$ (109 mg, 97.0 µmol, 1.00 eq.) and KO^{t}Bu (88.7 mg, 790 µmol, 8.15 eq.) were dissolved in dry methanol (2.50 mL). The suspension was stirred for 10 min at room temperature and a solution of [Cu(MeCN)$_4$]ClO$_4$ (63.5 mg, 194 µmol, 2.00 eq.) in dry methanol (1.00 mL) was added. Subsequently, the yellow mixture was stirred for 40 min. Addition of NaBPh$_4$ (49.8 mg, 145 µmol, 1.50 eq.) in dry methanol (1.50 mL) gave a colorless precipitate. The solid was collected via filtration, dried under vacuum for 10 min and was dissolved in as little as necessary acetone. Slow diffusion of ether into the concentrated solution at room temperature gave no single crystals.

8.3.1.3 Synthesis of the dicopper(I) complex IIa

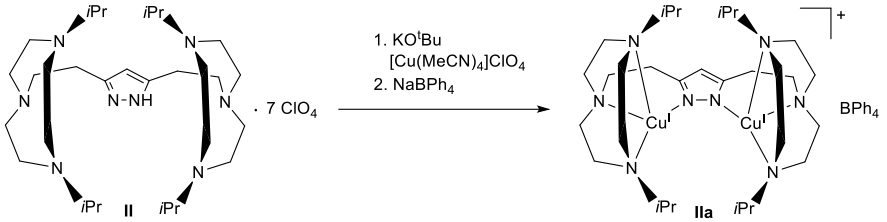

Dicopper(I) complex **IIa** was obtained by a refined synthesis of the literature known syntheses[38,65,182]. $HL_{i\mathrm{Pr}}^{\mathrm{sym}}$ (250 mg, 202 µmol, 1.00 eq.) and KO^{t}Bu (185 mg, 1.64 mmol, 8.15 eq.) were dissolved in dry methanol (3.00 mL) under anaerobic conditions. After stirring the reaction mixture for 10 min, the suspension was filtered with help of a syringe equipped with a Whatman filter. To the stirring yellow filtrate was added a solution of $[Cu(MeCN)_4]ClO_4$ (132 mg, 404 µmol, 2.00 eq.) in dry methanol (1.00 mL) and the mixture was stirred for 20 min. Addition of $NaBPh_4$ (104 mg, 303 µmol, 1.50 eq.) dissolved in methanol (1.50 mL) resulted in precipitation of the product as a colorless solid. The product was collected via filtration and dried under vacuum in the glove box. Subsequently the solid was dissolved in as little as possible dry acetone. The desired product was obtained after 14 d by slow diffusion of dry diethyl ether into the concentrated solution. After collecting the solid and washing it with dry cold diethyl ether, the product was obtained as off-white crystals (154 mg,116 µmol, 57 %).

8.3.2 Synthesis of the *µ*-hydroxo dicopper(II) complexes

8.3.2.1 Synthesis of the symmetric *µ*-hydroxo dicopper(II) complex 21

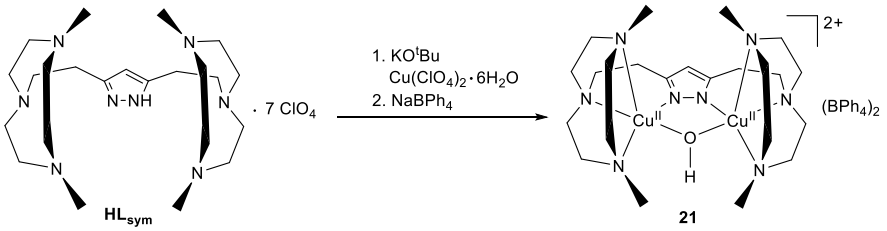

Ligand **HL$_{sym}$** (250 mg, 220 µmol, 1.00 eq.) was suspended in methanol (3.50 mL) and a solution of KO^{t}Bu (177 mg, 1.58 mmol, 7.15 eq.) in methanol (1.50 mL) was added to the stirring suspension. After 15 min the resulting colorless precipitate was removed via filtration with a Whatman filter from the reaction mixture and $Cu(ClO_4)_2 \cdot 6\,H_2O$ (163 mg, 0.44 mmol, 2.00 eq.) in methanol (1.00 mL) was added dropwise to the clear and pale-yellow solution. A dark blue solution started to form immediately and was stirred for 20 min. Addition of a solution of $NaBPh_4$ (113 mg, 0.33 mmol, 1.50 eq.) in methanol (1.00 mL) gave a blue precipitate which was separated from the solution. Subsequently acetone was added dropwise to the precipitate until a clear and very concentrated blue solution was formed. Slow diffusion of diethyl ether into the solution at room temperature led to the formation of a colorless precipitate which was discarded. The solvent was removed under reduced pressure and the residue was dissolved in propionitrile (1.40 mL). The process of slow diethyl ether diffusion was repeated at −26 °C.

Amorphous blue $[L^{sym}Cu_2(\mu\text{-}OH)](BPh_4)_2$ formed after four days and was separated from the mixture. The formed blue precipitate was dissolved again in propionitrile and diethyl ether diffusion at −26 °C yielded the product as blue crystals (91.1 mg, 75.0 µmol, 34 %) which were suitable for a single crystal diffraction experiment.

IR (ATR): $\tilde{\nu}/cm^{-1}$ = 570 m, 610 s, 703 s, 732 s, 842 m, 907 w, 999 m, 1058 m, 1135 w, 1286 m, 1331 m, 1423 m, 1462 m, 1577 m, 3052 w, 3627 w.

MS (ESI^+, MeCN): *m*/*z* = 895.4 $[M+BPh_4]^+$, 689.2 $[M+CF_3CO_2]^+$, 288.1 $[M]^{2+}$.

UV/vis (MeCN): λ_{max}/nm (ε/L mol^{-1} cm^{-1}) = 353 (3300), 595 (280)

8.3.2.2 Synthesis of the symmetric μ-hydroxo dicopper(II) complex 21b/21c with sodium acetate/sodium formate

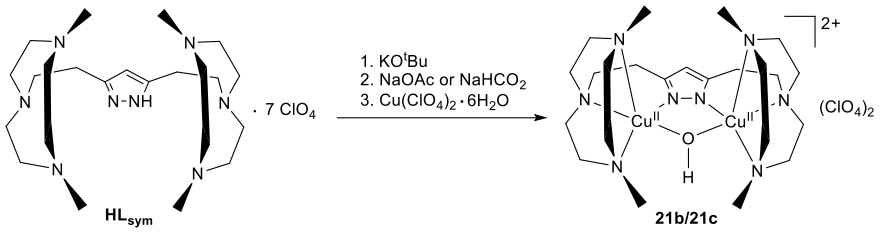

To the ligand **HL_{sym}** (232 mg, 205 µmol, 1.00 eq.) and KO^tBu (164 mg, 1.46 mmol, 7.15 eq.) were added methanol (3.50 mL) and the resulting suspension was put in the ultra-sonic bath for 10 min. After filtration of the suspension a solution of sodium acetate (33.6 mg, 409 µmol, 2.00 eq.) or sodium formate (27.8 mg, 409 µmol, 2.00 eq.) in methanol was added. Afterwards, a solution of $Cu(ClO_4)_2 \cdot 6\ H_2O$ (152 mg, 409 µmol, 2.00 eq.) in methanol (1.00 mL) was added and a turbid blue solution formed. Subsequently few drops of water were added carefully until the solution became clear. (At this point it is important to notice that an excess of water will inhibit crystallization of the product and only a blue oil will be formed during crystallization). Crystalline $[L_{sym}Cu_2(\mu\text{-}OH)](ClO_4)_2$ was obtained by slow diffusion of diethyl ether into the reaction mixture at room temperature and aerobic conditions. The supernatant fluid was removed, the solid was washed with cold diethyl ether and dried under reduced pressure. The product (117 mg, 96.1 µmol, 47 % using sodium acetate as an additive / 102 mg, 83.9 µmol, 41 % with sodium formate) was yielded as blue crystals.

MS (ESI^+, MeCN): *m*/*z* = 895.4 $[M+HClO_4+H]^+$, 288.1 $[M]^{2+}$.

UV/vis (MeCN): λ_{max}/nm (ε/L mol^{-1} cm^{-1}) = 353 (3300), 595 (280).

8.3.2.3 Synthesis of the non-symmetric *μ*-hydroxo dicopper(II) complex 24

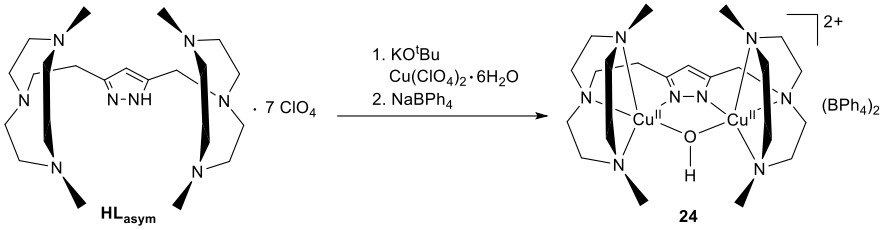

Ligand system **HL$_{asym}$** (517 mg, 460 µmol, 1.00 eq.) and KO^{t}Bu (369 mg, 3.29 mmol, 7.15 eq.) were dissolved in methanol (5.50 mL). A solution of $Cu(ClO_4)_2 \cdot 6\,H_2O$ (341 mg, 920 µmol, 2.00 eq.) in methanol (2.50 mL) was added and was stirred overnight at room temperature. Addition of a solution of $NaBPh_4$ (331 mg, 966 mmol, 2.10 eq.) in methanol (2.00 mL) led to the precipitation of a dark green solid which subsequently was dissolved in propionitrile (5.00 mL). Once again, the green colored and turbid reaction mixture was filtered with a Whatman filter and two drops of deionized water was added. Slow diethyl ether diffusion to the clear green filtrate at room temperature yielded the desired product (293 mg, 244 µmol, 53 %) as green single crystals.

IR (ATR): $\tilde{\nu}/cm^{-1}$ = 571 w, 611 s, 703 s, 732 s, 801 w, 995 m, 1068 m, 1093 m, 1260 m, 1362 w, 1424 m, 1460 m, 1579 m, 1697 m, 2128 w, 2982 w, 3054 w, 3590 w.

MS (ESI$^+$, EtCN): *m*/*z* = 883.4 $[M+BPh_4]^+$, 281.1 $[M]^{2+}$.

UV/Vis (MeCN): λ_{max}/nm (ε/L mol^{-1} cm^{-1}) = 364 (3500), 616 (210).

8.3.2.4 Synthesis of non-symmetric *μ*-hydroxo dicopper(II) complex 24b with with sodium formate

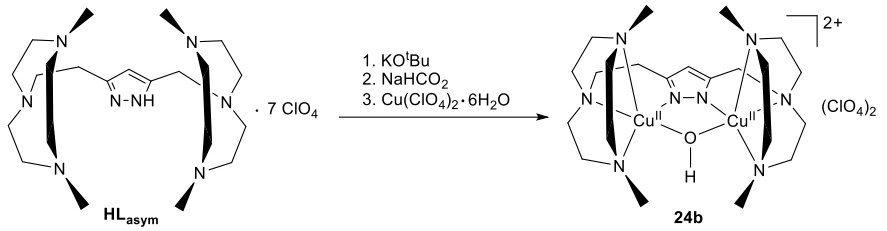

HL$_{asym}$ (204 mg, 182 µmol, 1.00 eq.) and KO^{t}Bu (146 mg, 1.30 mmol, 7.15 eq.) were dissolved in methanol (4.00 mL) and stirred for 1 h at room temperature. A solution of sodium formate (24.7 mg, 363 µmol, 2.00 eq.) was added. $Cu(ClO_4)_2 \cdot 6\,H_2O$ (135 mg, 363 µmol, 2.00 eq.) dissolved in methanol (2.00 mL) was added dropwise to the stirring reaction mixtures and the resulting green and turbid solution was stirred for 20 min. Subsequently six drops of distilled water were added and the reaction mixture was filtered through three layers of Whatman filter. Slow vapour diffusion of diethyl ether to the clear green solution yielded crystalline material after ten days (39.5 mg, 50.8 µmol, 28 %).

UV/Vis (MeCN): λ_{max}/nm (ε/L mol^{-1} cm^{-1}) = 364 (3500), 616 (210).

9 Appendix

MS-ESI Isotopic patterns of the symmetric *μ*-hydroxo dicopper(II) complex 21 before purification

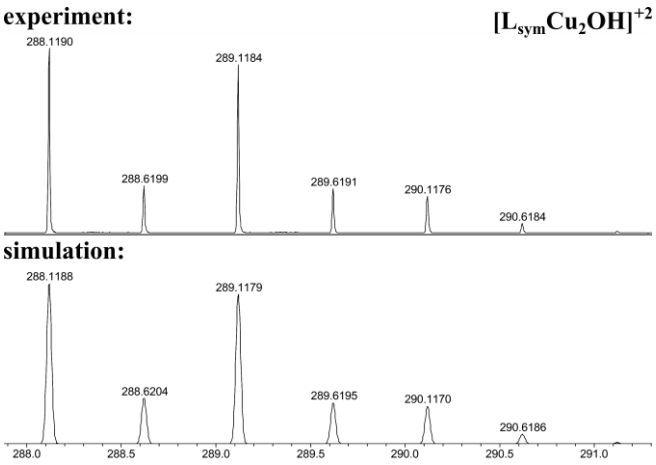

Figure 86: Comparison of the isotopic pattern of **21** ($[L_{sym}Cu_2OH]^{2+}$) with the corresponding simulation.

MS-ESI Isotopic patterns of the symmetric *μ*-hydroxo dicopper(II) complex 21

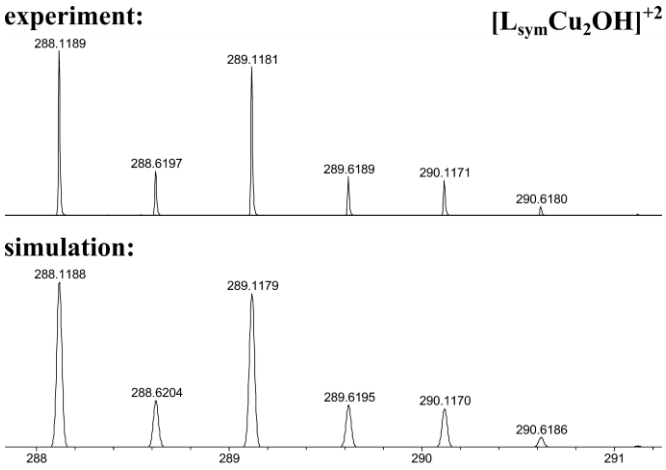

Figure 87: Comparison of the isotopic pattern of **21** ($[L_{sym}Cu_2OH]^{2+}$) with the corresponding simulation.

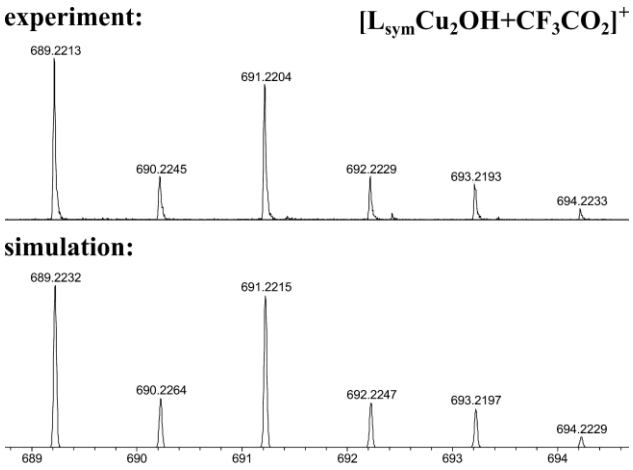

Figure 88: Comparison of the isotopic pattern of **21** ([$L_{sym}Cu_2OH+CF_3CO_2]^+$)with the corresponding simulation.

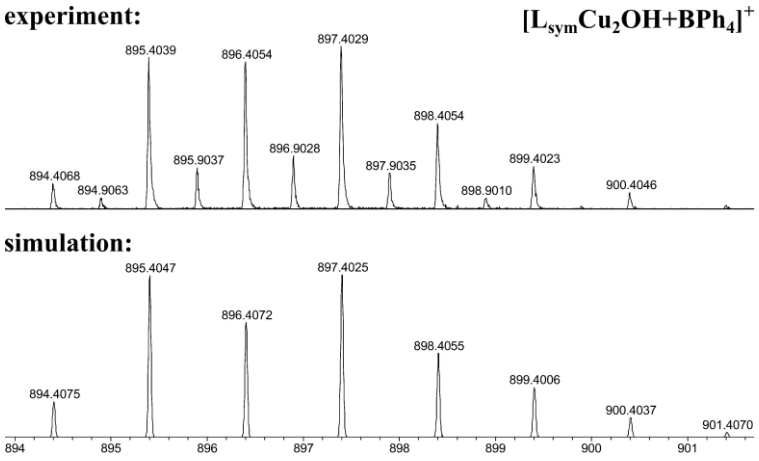

Figure 89: Comparison of the isotopic pattern of **21** ([$L_{sym}Cu_2OH+BPh_4]^+$)with the corresponding simulation.

Decomposition of the symmetric μ-1,2-peroxo dicopper(II) complex 20

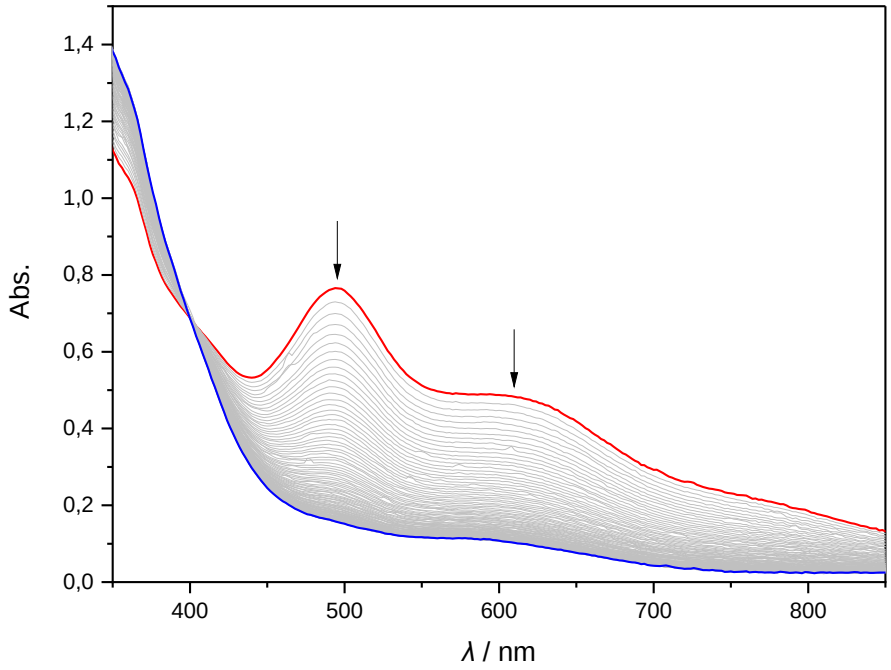

Figure 90: UV/vis absorbance spectra of the decomposition of the μ-1,2-peroxo dicopper(II) complex **20** (red) to the μ-hydroxo dicopper(II) complex **21** (blue) in dry MeCN at 10 °C. The spectrum features an isosbestic point at 400 nm.

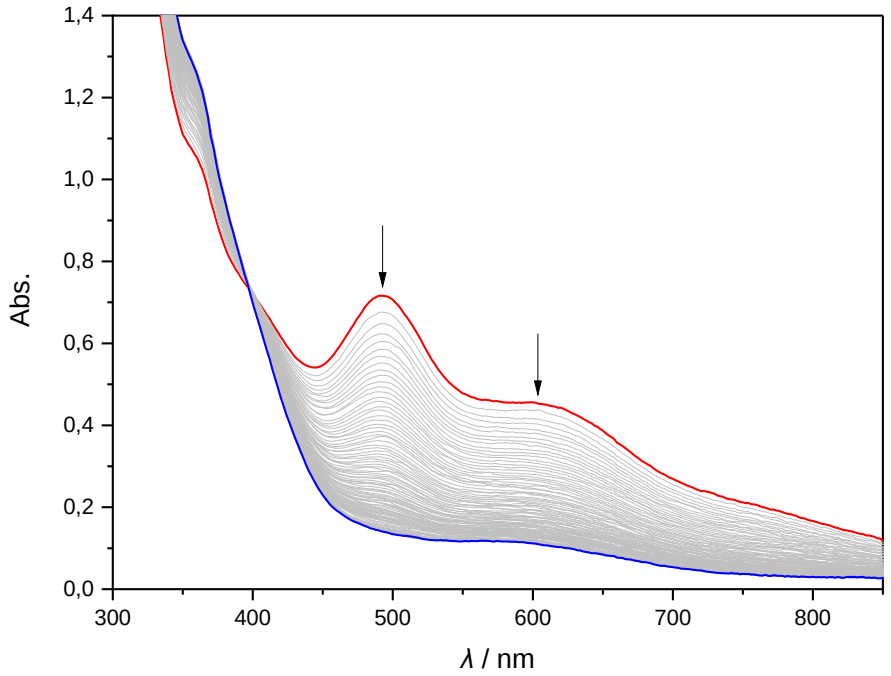

Figure 91: UV/vis absorbance spectra of the decomposition of the μ-1,2-peroxo dicopper(II) complex **20** (red) to the μ-hydroxo dicopper(II) complex **21** (blue) in dry MeCN at 0 °C. The spectrum features an isosbestic point at 400 nm.

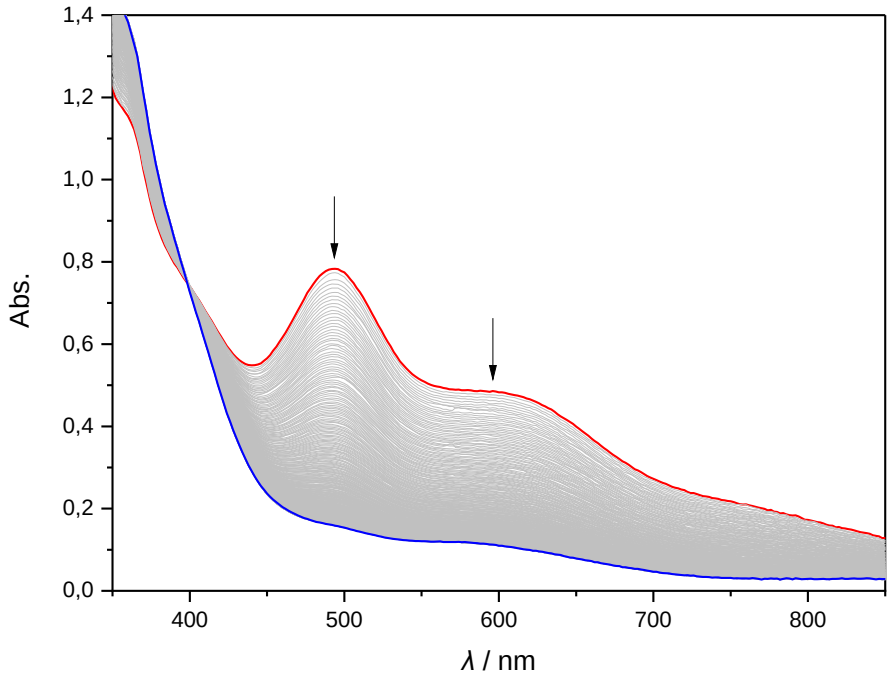

Figure 92: UV/vis absorbance spectra of the decomposition of the μ-1,2-peroxo dicopper(II) complex **20** (red) to the μ-hydroxo dicopper(II) complex **21** (blue) in dry MeCN at –10 °C. The spectrum features an isosbestic point at 400 nm.

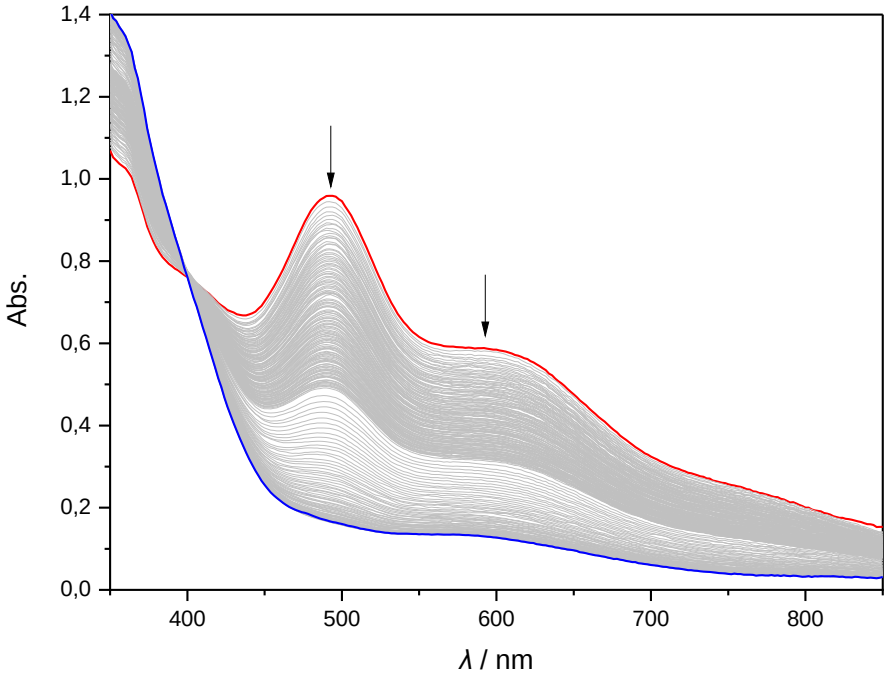

Figure 93: UV/vis absorbance spectra of the decomposition of the μ-1,2-peroxo dicopper(II) complex **20** (red) to the μ-hydroxo dicopper(II) complex **21** (blue) in dry MeCN at –20 °C. The spectrum features a *pseudo*-isosbestic point at 400 nm.

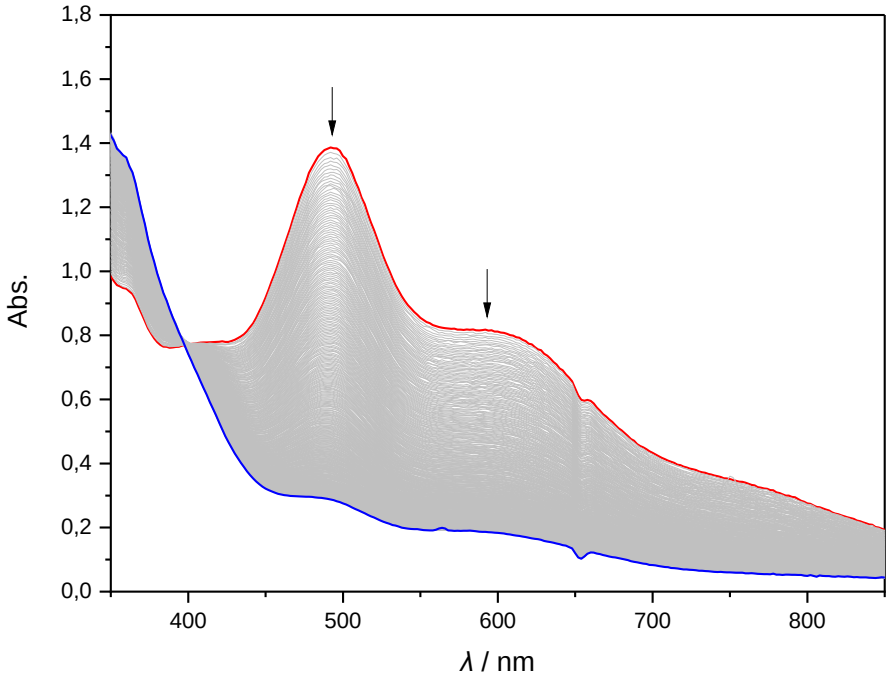

Figure 94: UV/vis absorbance spectra of the decomposition of the μ-1,2-peroxo dicopper(II) complex **20** (red) to the μ-hydroxo dicopper(II) complex **21** (blue) in dry MeCN at –30 °C. The spectrum features a *pseudo*-isosbestic point at 400 nm.

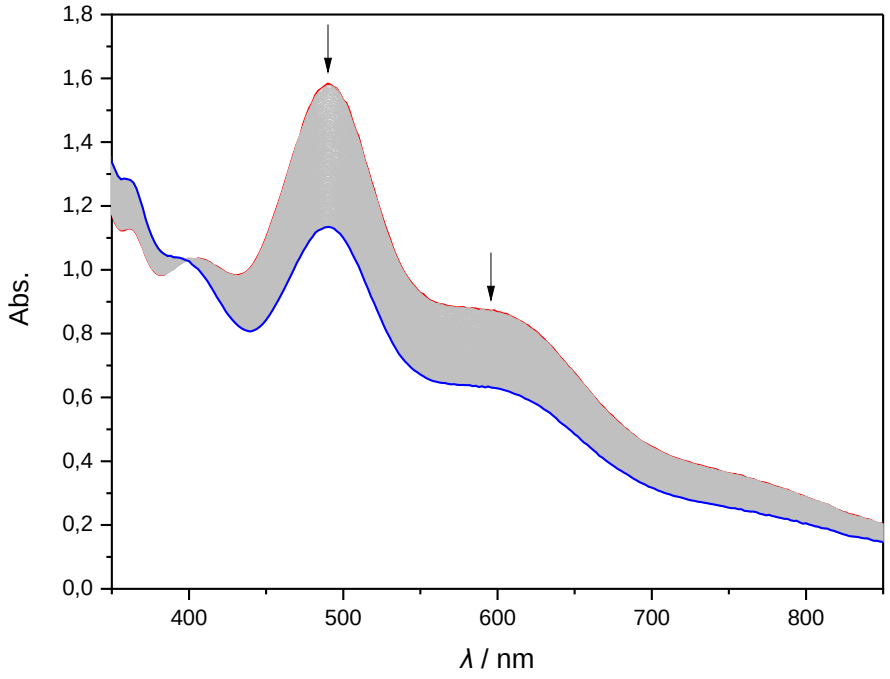

Figure 95: UV/vis absorbance spectra of the decomposition of the μ-1,2-peroxo dicopper(II) complex **20** (red) to the μ-hydroxo dicopper(II) complex **21** (blue) in dry MeCN at –40 °C. The spectrum features an isosbestic point at 400 nm.

MS-ESI Isotopic patterns of the non-symmetric *μ*-hydroxo dicopper(II) complex 24

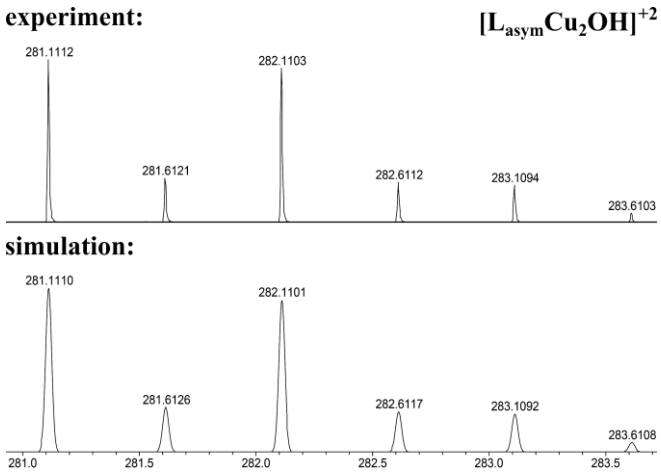

Figure 96: Comparison of the isotopic pattern of **24** ($[L_{asym}Cu_2OH]^{2+}$) with the corresponding simulation.

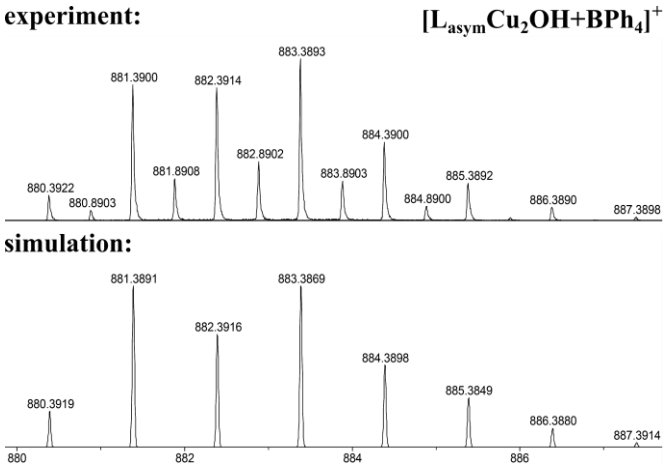

Figure 97: Comparison of the isotopic pattern of **24** ($[L_{asym}Cu_2OH+BPh_4]^{+}$)with the corresponding simulation.

Resonance Raman Spectrum of the non-symmetric *μ*-1,2-peroxo dicopper(II) complex 23

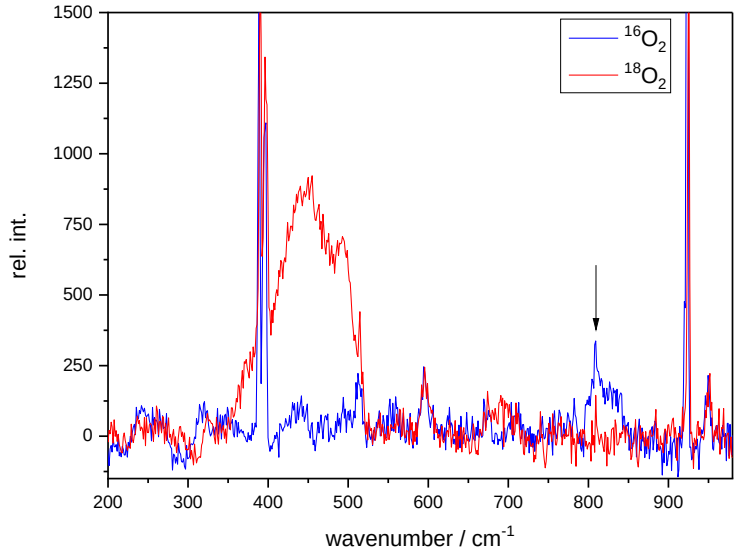

Figure 98: rR spectra for $^{16}O_2$ and $^{18}O_2$ labelled non-symmetric peroxo dicopper(II) complexes **23** in frozen MeCN solution (λ_{ex} = 633 nm).

Decomposition of the non-symmetric *μ*-1,2-peroxo dicopper(II) complex 23

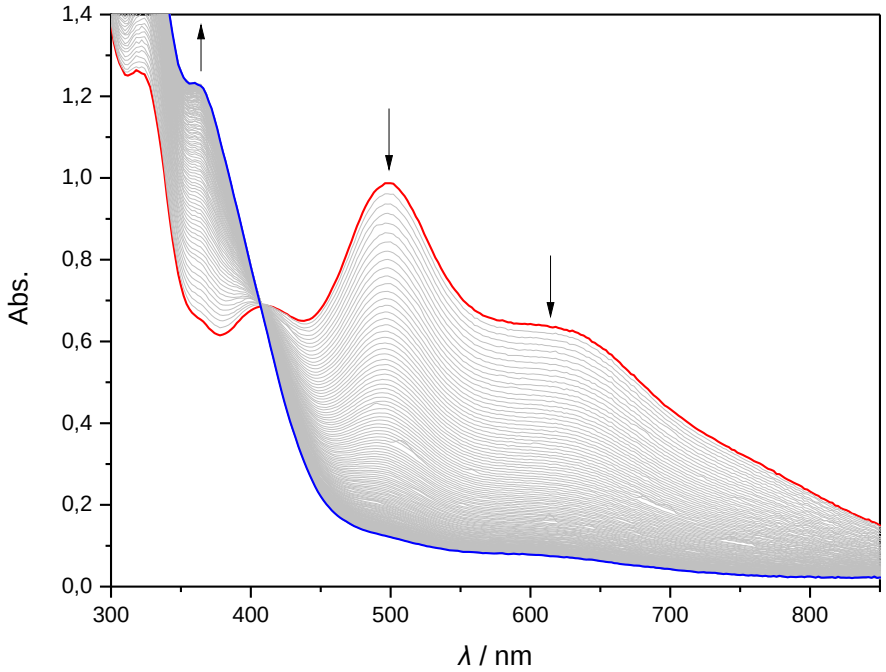

Figure 99: UV/vis absorbance spectra of the decomposition of the *μ*-1,2-peroxo dicopper(II) complex **23** (red) to the *μ*-hydroxo dicopper(II) complex **24** (blue) in dry MeCN at 35 °C. The spectrum features a *pseudo*-isosbestic point at 407 nm.

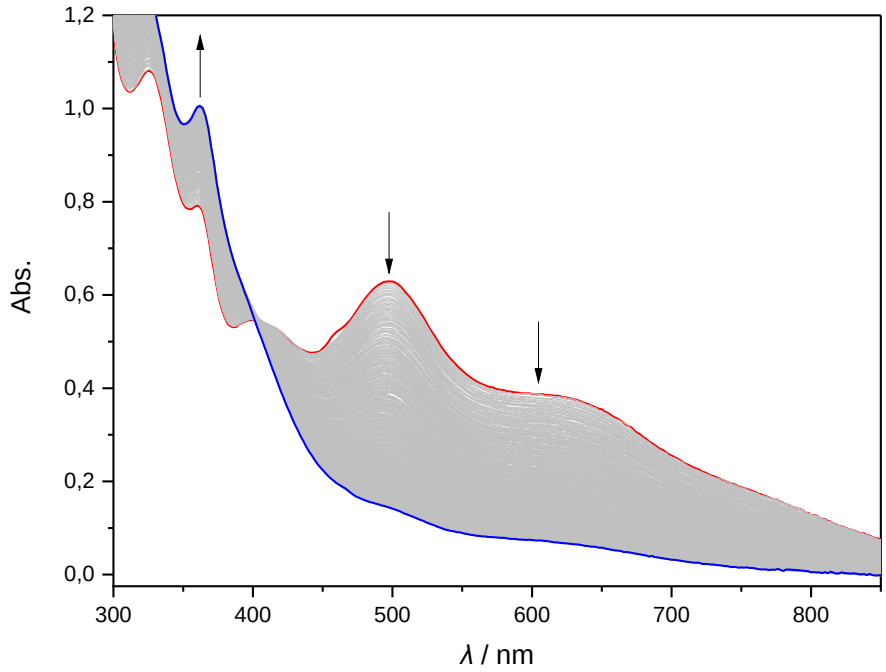

Figure 100: UV/vis absorbance spectra of the decomposition of the μ-1,2-peroxo dicopper(II) complex **23** (red) to the μ-hydroxo dicopper(II) complex **24** (blue) in dry MeCN at 25 °C. The spectrum features a *pseudo*-isosbestic point at 404 nm.

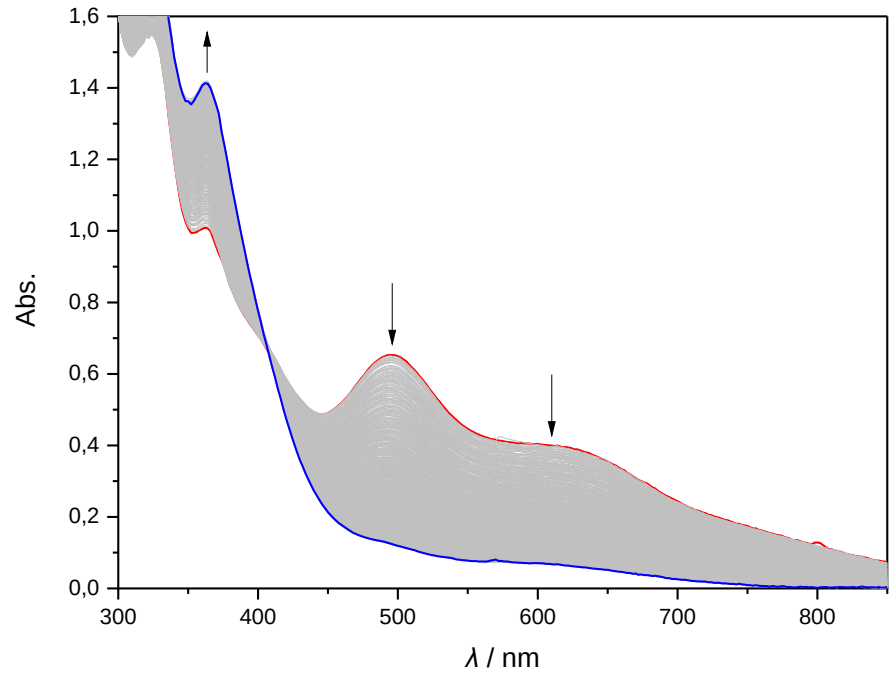

Figure 101: UV/vis absorbance spectra of the decomposition of the μ-1,2-peroxo dicopper(II) complex **23** (red) to the μ-hydroxo dicopper(II) complex **24** (blue) in dry MeCN at 15 °C. The spectrum features a *pseudo*-isosbestic point at 407 nm.

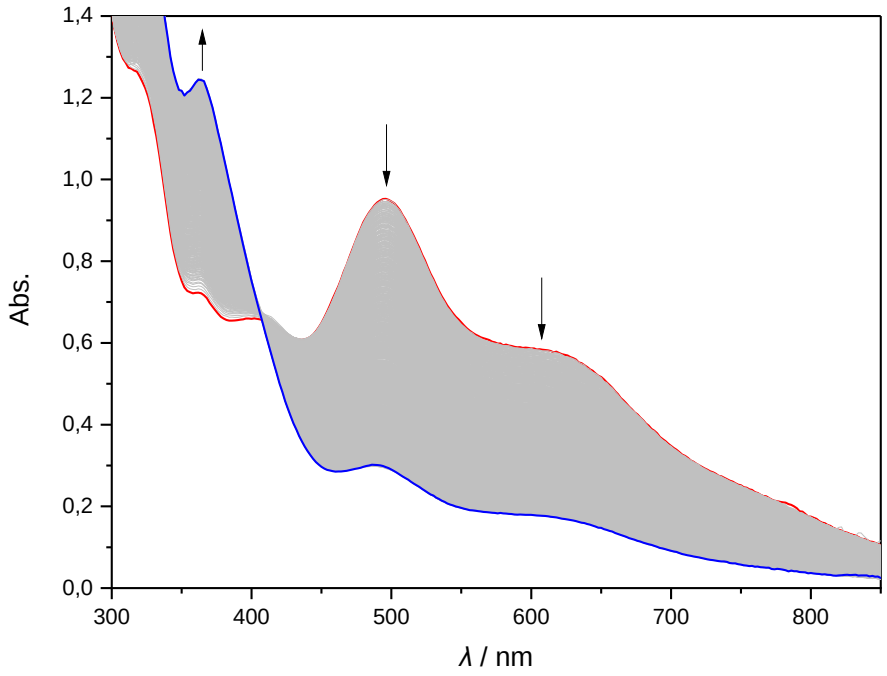

Figure 102: UV/vis absorbance spectra of the decomposition of the μ-1,2-peroxo dicopper(II) complex **23** (red) to the μ-hydroxo dicopper(II) complex **24** (blue) in dry MeCN at 5 °C. The spectrum features a *pseudo*-isosbestic point at 407 nm.

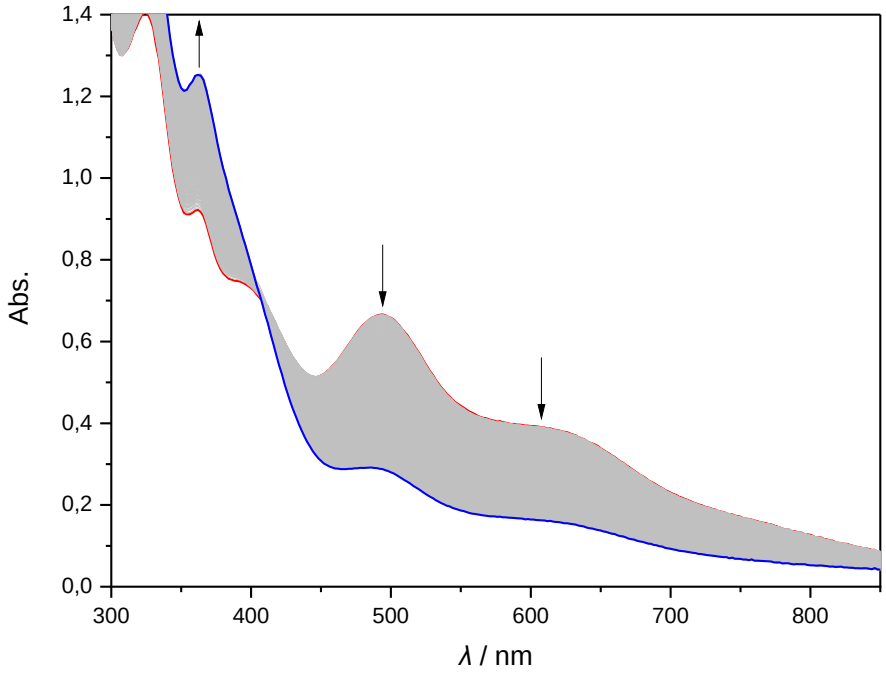

Figure 103: UV/vis absorbance spectra of the decomposition of the μ-1,2-peroxo dicopper(II) complex **23** (red) to the μ-hydroxo dicopper(II) complex **24** (blue) in dry MeCN at –5 °C. The spectrum features a peudo-isosbestic point at 407 nm.

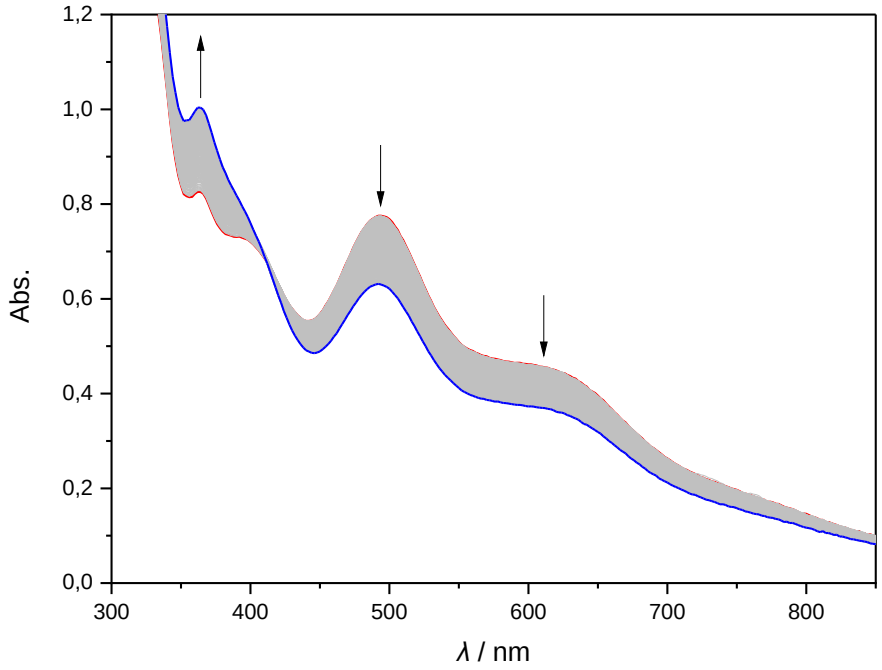

Figure 104: UV/vis absorbance spectra of the decomposition of the μ-1,2-peroxo dicopper(II) complex **23** (red) to the μ-hydroxo dicopper(II) complex **24** (blue) in dry MeCN at –15 °C. The spectrum features a *pseudo*-isosbestic point at 409 nm.

10 Abbreviations

Ac	acetate
bpp	bis(pyridyl)pyrazolate
BQPA	bis(2-pyridylmethyl)(2-quinolylmethyl)amine
CCA	cyclohexanecarboxaldehyde
d	doublet
DFT	density functional theory
ATR	attenuated total reflection
Cp	cyclopentadienyl
Cp*	pentamethylcyclopentadienyl
d	diameter (UV/vis) or days (syntheses)
DBU	1,8-Diazabicyclo[5.4.0]undec-7-ene
DCM	dichloromethane
DHP	3,4-Dihydro-2*H*-pyran
DME	1,2-dimethoxyethane
DMF	dimethylformamide
DMSO	dimethyl sulfoxide
e.g.	exempli gratia = for example
EI	electron ionization
eq.	equivalents
ESI	electrospray ionization
et al.	and others (lat.: et alii/et aliae)
EtCN	propionitrile
Et_2O	diethyl ether
EtOH	ethanol
Fc	ferrocene
FTIR	Fourier-transform infrared
GC	gas chromatography
h	hours
HLutOTf	2,6-Lutidinium triflate
Hz	hertz
i.e.	id est; here: that is
in-situ	here: in the reaction mixture
*i*Pr	isopropyl
iPr_3TACN	1,4,7-triisopropyl-1,4,7-triazacylcononane

IR	infrared
J	coupling constant
Lut	2,6-Lutidine
LMCT	ligand-metal charge transfer
m	multiplet (NMR), medium (IR)
Me	methyl
MeCN	acetonitrile
MeOH	methanol
MeL66	3,5-bis{bis-[2-(1-methyl-1H-benzimidazol-2-yl)-ethyl]-
MS	mass spectrometry
MTBE	Methyl *tert*-butyl ether
m/*z*	mass-to-charge ratio
NaOAc	Sodium acetate
NMR	nuclear magnetic resonance
OTf	Triflate anion
PCET	Proton-induced electron transfer
Ph	phenyl
pMMO	particulate methane monooxygenase
ppm	parts-per-million
q	quartet
QTOF	quadrupole-time-of-flight
R	residue
rR	resonance raman spectroscopy
RT	room temperature
s	singlet (NMR), strong (IR)
SQUID	superconducting quantum interference device
t	triplet
TACN	1,4,7-Triazacyclononane
TBABr	Tetrabutylammoniumbromid
TEMPO	(2,2,6,6,-Tetramethylpiperidin-1-yl)oxyl
TFE	2,2,2-trifluoroethanol
THF	tetrahydrofuran
THP	tetrahydropyran
TP^{iPr}	hydrotris(3,5-diisopropylpyrazolyl)borate anion
trpy	terpyridine

TMPA	tris(2-pyridylmethyl)amine
TOF	time-of-flight
Ts	tosyl
UV/vis	ultraviolet-visible spectroscopy
vs.	versus
w	weak (IR)
XRD	X-ray diffraction
XYLOH	2,6-bis((bis[2-(2-pyridyl)ethyl]amine)methyl)phenol
18-crown-6	1,4,7,10,13,16-hexaoxacyclooctadecane

11 References

[1] P. R. Shukla, J. Skea, E. C. Buendia, V. Masson-Delmotte, H.-O. Pörtner, D. C. Roberts, P. Zhai, R. Slade, S. Connors, R. van Diemen, M. Ferrat, E. Haughey, S. Luz, S. Neogi, M. Pathak, J. Petzold, J. P. Pereira, P. Vyas, E. Huntley, K. Kissick, M. Belkacemi, J. Malley, *Climate Change and Land: An IPCC Special Report on Climate Change, Desertification, Land Degradation, Sustainable Land Management, Food Security, and Greenhouse Gas Fluxes in Terrestrial Ecosystems*, **2019**.

[2] R. A. Himes, K. D. Karlin, *Proc. Natl. Acad. Sci.* **2009**, *106*, 18877–18878.

[3] R. A. Himes, K. Barnese, K. D. Karlin, *Angew. Chem. Int. Ed.* **2010**, *49*, 6714–6716.

[4] S. J. Blanksby, G. B. Ellison, *Acc. Chem. Res.* **2003**, *36*, 255–263.

[5] P. S. Casey, T. McAllister, K. Foger, *Ind. Eng. Chem. Res.* **1994**, *33*, 1120–1125.

[6] H. D. Gesser, N. R. Hunter, C. B. Prakash, *Chem. Rev.* **1985**, *85*, 235–244.

[7] A. A. Latimer, A. Kakekhani, A. R. Kulkarni, J. K. Nørskov, *ACS Catal.* **2018**, *8*, 6894–6907.

[8] M. Ravi, M. Ranocchiari, J. A. van Bokhoven, *Angew. Chem. Int. Ed.* **2017**, *56*, 16464–16483.

[9] J. Y. Lee, K. D. Karlin, *Curr. Opin. Chem. Biol.* **2015**, *25*, 184–193.

[10] V. C. C. Wang, S. Maji, P. P. Y. Chen, H. K. Lee, S. S. F. Yu, S. I. Chan, *Chem. Rev.* **2017**, *117*, 8574–8621.

[11] R. Balasubramanian, A. C. Rosenzweig, *Acc. Chem. Res.* **2007**, *40*, 573–580.

[12] M. H. Sazinsky, S. J. Lippard, in *Sustain. Life Planet Earth Met. Mastering Dioxygen Other Chewy Gases*, Springer International Publishing, **2015**, pp. 205–256.

[13] C. W. Koo, A. C. Rosenzweig, *Chem. Soc. Rev.* **2021**, *50*, 3424–3436.

[14] C. W. Koo, F. J. Tucci, Y. He, A. C. Rosenzweig, *Science* **2022**, *375*, 1287–1291.

[15] S. C. Bete, L. K. May, P. Woite, M. Roemelt, M. Otte, *Angew. Chem. Int. Ed.* **2022**, *61*, DOI 10.1002/anie.202206120.

[16] S. Sanchez, A. L. Demain, *Org. Process Res. Dev.* **2011**, *15*, 224–230.

[17] W. Kaim, B. Schwederski, *Bioanorganische Chemie: Zur Funktion Chemischer Elemente in Lebensprozessen*, B.G. Teubner Verlag, Wiesbaden, **2004**.

[18] K. J. Waldron, J. C. Rutherford, D. Ford, N. J. Robinson, *Nature* **2009**, *460*, 823–30.

[19] L. Que, W. B. Tolman, *Nature* **2008**, *455*, 333–340.

[20] E. I. Solomon, D. E. Heppner, E. M. Johnston, J. W. Ginsbach, J. Cirera, M. Qayyum, M. T. Kieber-Emmons, C. H. Kjaergaard, R. G. Hadt, L. Tian, *Chem. Rev.* **2014**, *114*, 3659–3853.

[21] J. Y. Lee, K. D. Karlin, *Curr. Opin. Chem. Biol.* **2015**, *25*, 184–193.

[22] C. E. Elwell, N. L. Gagnon, B. D. Neisen, D. Dhar, A. D. Spaeth, G. M. Yee, W. B. Tolman, *Chem. Rev.* **2017**, *117*, 2059–2107.

[23] I. A. Koval, P. Gamez, C. Belle, K. Selmeczi, J. Reedijk, *Chem. Soc. Rev.* **2006**, *35*, 814.

[24] E. I. Solomon, U. M. Sundaram, T. E. Machonkin, *Chem. Rev.* **1996**, *96*, 2563–2606.

[25] S. Iwata, C. Ostermeier, B. Ludwig, H. Michel, *Nature* **1995**, *376*, 660–669.

[26] T. Tsukihara, H. Aoyama, E. Yamashita, T. Tomizaki, H. Yamaguchi, K. Shinzawa-Itoh, R. Nakashima, R. Yaono, S. Yoshikawa, *Science* **1996**, *272*, 1136–1144.

[27] T. K. Das, C. Pecoraro, F. L. Tomson, R. B. Gennis, D. L. Rousseau, *Biochemistry* **1998**, *37*, 14471–14476.

[28] B. G. Malmstroem, *Chem. Rev.* **1990**, *90*, 1247–1260.

[29] C. Cambillau, K. Brown, M. Tegoni, M. Prudêncio, A. S. Pereira, S. Besson, J. J. Moura, I. Moura, *Nat. Struct. Biol.* **2000**, *7*, 191–195.

[30] M. Prudêncio, A. S. Pereira, P. Tavares, S. Besson, I. Cabrito, K. Brown, B. Samyn, B. Devreese, J. Van Beeumen, F. Rusnak, G. Fauque, J. J. G. Moura, M. Tegoni, C. Cambillau, I. Moura, *Biochemistry* **2000**, *39*, 3899–3907.

[31] M. Pascaly, I. Jolk, B. Krebs, *Chemie unserer Zeit* **1999**, *33*, 334–341.

[32] M. Dzemski, Neue Pyrazolat-Kompatimentliganden Für Bioinspirierte Dinukleare Kupferkomplexe, Master thesis, Georg-August-Universtät Göttingen, **2017**.

[33] J. P. Klinman, *Chem. Rev.* **1996**, *96*, 2541–2562.

[34] J. A. Guckert, M. D. Lowery, E. I. Solomon, *J. Am. Chem. Soc.* **1995**, *117*, 2817–2844.

[35] E. I. Solomon, M. J. Baldwin, M. D. Lowery, *Chem. Rev.* **1992**, *92*, 521–542.

[36] H. B. Gray, B. G. Malmström, R. J. P. Williams, *J. Biol. Inorg. Chem.* **2000**, *5*, 551–559.

[37] P. M. Colman, H. C. Freeman, J. M. Guss, M. Murata, V. A. Norris, J. A. M. Ramshaw, M. P. Venkatappa, *Nature* **1978**, *272*, 319–324.

[38] C.-J. Spyra, Bioinspired Dinuclear Copper Complexes for Small Molecule Activation, Dissertation, Georg-August-Universtät Göttingen, **2021**.

[39] E. I. Solomon, R. G. Hadt, *Coord. Chem. Rev.* **2011**, *255*, 774–789.

[40] H. J. Wijma, I. MacPherson, O. Farver, E. I. Tocheva, I. Pecht, M. P. Verbeet, M. E. P. Murphy, G. W. Canters, *J. Am. Chem. Soc.* **2007**, *129*, 519–525.

[41] R. J. P. Williams, *Inorg. Chim. Acta Rev.* **1971**, *5*, 137–155.

[42] J. Mccracken, J. Peisach, S. Pember, S. J. Benkovic, J. J. Villafranca, R. J. Miller, *J. Am. Chem. Soc.* **1988**, *110*, 1069–1074.

[43] H. Nakata, T. Yamauchi, H. Fujisawa, *J. Biol. Chem.* **1979**, *254*, 1829–1833.

[44] J. A. Tainer, E. D. Getzoff, J. S. Richardson, D. C. Richardson, *Nature* **1983**, *306*, 284–287.

[45] J. S. Valentine, D. L. Wertz, T. J. Lyons, L.-L. Liou, J. J. Goto, E. B. Gralla, *Curr. Opin. Chem. Biol.* **1998**, *2*, 253–262.

[46] N. Ito, S. E. V. Phillips, C. Stevens, Z. B. Ogel, M. J. McPherson, J. N. Keen, K. D. S. Yadav, P. F. Knowles, *Nature* **1991**, *350*, 87–90.

[47] J. A. Halfen, V. G. Young, W. B. Tolman, *Angew. Chem.* **1996**, *108*, 1832–1835.

[48] D. Yin, S. Urresti, M. Lafond, E. M. Johnston, F. Derikvand, L. Ciano, J.-G. Berrin, B. Henrissat, P. H. Walton, G. J. Davies, H. Brumer, *Nat. Commun.* **2015**, *6*, 10197.

[49] J. W. Whittaker, *Chem. Rev.* **2003**, *103*, 2347–2364.

[50] H. Decker, T. Schweikardt, F. Tuczek, *Angew. Chem. Int. Ed.* **2006**, *45*, 4546–4550.

[51] T. Klabunde, C. Eicken, J. C. Sacchettini, B. Krebs, *Nat. Struct. Biol.* **1998**, *5*, 1084–1090.

[52] A. Rompel, H. Fischer, D. Meiwes, K. Büldt-Karentzopoulos, R. Dillinger, F. Tuczek, H. Witzel, B. Krebs, *J. Biol. Inorg. Chem.* **1999**, *4*, 56–63.

[53] C. Eicken, F. Zippel, K. Büldt-Karentzopoulos, B. Krebs, *FEBS Lett.* **1998**, *436*, 293–299.

[54] M. E. Cuff, K. I. Miller, K. E. van Holde, W. A. Hendrickson, *J. Mol. Biol.* **1998**, *278*, 855–870.

[55] K. E. van Holde, K. I. Miller, H. Decker, *J. Biol. Chem.* **2001**, *276*, 15563–15566.

[56] J. A. Lukin, C. Ho, *Chem. Rev.* **2004**, *104*, 1219–1230.

[57] R. E. Stenkamp, *Chem. Rev.* **1994**, *94*, 715–726.

[58] J. Markl, *Chemie unserer Zeit* **1996**, *30*, 6–18.

[59] M. Metz, E. I. Solomon, *J. Am. Chem. Soc.* **2001**, *123*, 4938–4950.

[60] E. I. Solomon, R. Sarangi, J. S. Woertink, A. J. Augustine, J. Yoon, S. Ghosh, *Acc. Chem. Res.* **2007**, *40*, 581–591.

[61] J. E. Pate, R. W. Cruse, K. D. Karlin, E. I. Solomon, *J. Am. Chem. Soc.* **1987**, *109*, 2624–2630.

[62] E. I. Solomon, *Inorg. Chem.* **2016**, *55*, 6364–6375.

[63] E. I. Solomon, P. Chen, M. Metz, S.-K. Lee, A. E. Palmer, *Angew. Chem- Int. Ed.* **2001**, *40*, 4570–4590.

[64] N. Kindermann, E. Bill, S. Dechert, S. Demeshko, E. J. Reijerse, F. Meyer, *Angew. Chem. Int. Ed.* **2015**, *54*, 1738–1743.

[65] N. Kindermann, Diiron and Dicopper Complexes with Pyrazolate/Tacn Hybrid Ligands for Small Molecule Activation, Dissertation, Georg-August-Universität Göttingen, **2015**.

[66] K. E. Dalle, T. Gruene, S. Dechert, S. Demeshko, F. Meyer, *J. Am. Chem. Soc.* **2014**, *136*, 7428–7434.

[67] M. Merkx, D. A. Kopp, M. H. Sazinsky, J. L. Blazyk, J. Müller, S. J. Lippard, *Angew. Chem. Int. Ed.* **2001**, *40*, 2782–2807.

[68] P. Nordlund, H. Eklund, *J. Mol. Biol.* **1993**, *232*, 123–164.

[69] Y. Matoba, T. Kumagai, A. Yamamoto, H. Yoshitsu, M. Sugiyama, *J. Biol. Chem.* **2006**, *281*, 8981–8990.

[70] M. M. Benning, S.-B. Hong, F. M. Raushel, H. M. Holden, *J. Biol. Chem.* **2000**, *275*, 30556–30560.

[71] K. Kappaun, A. R. Piovesan, C. R. Carlini, R. Ligabue-Braun, *J. Adv. Res.* **2018**, *13*, 3–17.

[72] A. L. Gavrilova, B. Bosnich, *Chem. Rev.* **2004**, *104*, 349–384.

[73] Z. Tyeklar, R. R. Jacobson, N. Wei, N. N. Murthy, J. Zubieta, K. D. Karlin, *J. Am. Chem. Soc.* **1993**, *115*, 2677–2689.

[74] N. Kitajima, K. Fujisawa, C. Fujimoto, Y. Moro-oka, S. Hashimoto, T. Kitagawa, K. Toriumi, K. Tatsumi, A. Nakamura, *J. Am. Chem. Soc.* **1992**, *114*, 1277–1291.

[75] M. T. Kieber-Emmons, J. W. Ginsbach, P. K. Wick, H. R. Lucas, M. E. Helton, B. Lucchese, M. Suzuki, A. D. Zuberbühler, K. D. Karlin, E. I. Solomon, *Angew. Chem. Int. Ed.* **2014**, *53*, 4935–4939.

[76] S. Palavicini, A. Granata, E. Monzani, L. Casella, *J. Am. Chem. Soc.* **2005**, *127*, 18031–18036.

[77] J. A. Halfen, S. Mahapatra, E. C. Wilkinson, S. Kaderli, V. G. Young, L. Que, A. D. Zuberbuhler, W. B. Tolman, *Science (80-.).* **1996**, *271*, 1397–1400.

[78] J. Lücken, T. Auth, S. I. Mozzi, F. Meyer, *Inorg. Chem.* **2020**, *59*, 14347–14354.

[79] D. Das, Y.-M. Lee, K. Ohkubo, W. Nam, K. D. Karlin, S. Fukuzumi, *J. Am. Chem. Soc.* **2013**, *135*, 4018–4026.

[80] S. Fukuzumi, L. Tahsini, Y. Lee, K. Ohkubo, W. Nam, K. D. Karlin, *J. Am. Chem. Soc.* **2012**, *134*, 7025–7035.

[81] R. R. Jacobson, Z. Tyeklar, A. Farooq, K. D. Karlin, S. Liu, J. Zubieta, *J. Am. Chem. Soc.* **1988**, *110*, 3690–3692.

[82] K. D. Karlin, R. W. Cruse, Y. Gultneh, *J. Chem. Soc., Chem. Commun.* **1987**, 599–600.

[83] N. Wei, N. N. Murthy, Q. Chen, J. Zubieta, K. D. Karlin, *Inorg. Chem.* **1994**, *33*, 1953–1965.

[84] L. M. Mirica, X. Ottenwaelder, T. D. P. Stack, *Chem. Rev.* **2004**, *104*, 1013–1046.

[85] N. Kitajima, K. Fujisawa, Y. Moro-oka, K. Toriumi, *J. Am. Chem. Soc.* **1989**, *111*, 8975–8976.

[86] K. D. Karlin, J. C. Hayes, S. Juen, J. P. Hutchinson, J. Zubieta, *Inorg. Chem.* **1982**, *21*, 4106–4108.

[87] E. I. Solomon, F. Tuczek, D. E. Root, C. A. Brown, *Chem. Rev.* **1994**, *94*, 827–856.

[88] J. A. Larrabee, T. G. Spiro, *J. Am. Chem. Soc.* **1980**, *102*, 4217–4223.

[89] T. B. Freedman, J. S. Loehr, T. M. Loehr, *J. Am. Chem. Soc.* **1976**, *98*, 2809–2815.

[90] T. J. Thamann, J. S. Loehr, T. M. Loehr, *J. Am. Chem. Soc.* **1977**, *99*, 4187–4189.

[91] N. P. Vargo, J. B. Harland, B. W. Musselman, N. Lehnert, M. Z. Ertem, J. R. Robinson, *Angew. Chem. Int. Ed.* **2021**, *60*, 19836–19842.

[92] K. Magnus, H. Ton-That, *J. Inorg. Biochem.* **1992**, *47*, 20.

[93] K. E. Dalle, F. Meyer, *Eur. J. Inorg. Chem.* **2015**, *2015*, 3391–3405.

[94] A. N. Desnoyer, A. Nicolay, P. Rios, M. S. Ziegler, T. D. Tilley, *Acc. Chem. Res.* **2020**, *53*, 1944–1956.

[95] S. Ferrer, J. G. Haasnoot, J. Reedijk, E. Müller, M. Biagini Cingi, M. Lanfranchi, A. M. Manotti Lanfredi, J. Ribas, *Inorg. Chem.* **2000**, *39*, 1859–1867.

[96] X. C. Zhang, Y. H. Chen, B. Liu, *Bull. Korean Chem. Soc.* **2008**, *29*, 511–514.

[97] J. G. Haasnoot, *Coord. Chem. Rev.* **2000**, *200–202*, 131–185.

[98] J. Klingele, S. Dechert, F. Meyer, *Coord. Chem. Rev.* **2009**, *253*, 2698–2741.

[99] G. La Monica, G. A. Ardizzoia, in *Prog. Inorg. Chem.*, **2007**, pp. 151–238.

[100] K. B. Wiberg, *Angew. Chem. Int. Ed. English* **1986**, *25*, 312–322.

[101] A. Prokofieva, A. I. Prikhod, E. A. Enyedy, E. Farkas, W. Maringgele, S. Demeshko, S. Dechert, F. Meyer, *Inorg. Chem.* **2007**, *46*, 4298–4307.

[102] S. Benini, W. R. Rypniewski, K. S. Wilson, S. Miletti, S. Ciurli, S. Mangani, *Structure* **1999**, *7*, 205–216.

[103] S. M. Fabiane, M. K. Sohi, T. Wan, D. J. Payne, J. H. Bateson, T. Mitchell, B. J. Sutton, *Biochemistry* **1998**, *37*, 12404–12411.

[104] K. Dalle, Bioinspired Activation of Oxygen with Pyrazole-Supported Dinuclear Copper Complexes, Dissertation, Georg-August-Universität Göttingen, **2014**.

[105] K. E. Dalle, S. Dechert, F. Meyer, *Z. Anorg. Allg. Chem.* **2015**, *641*, 2181–2189.

[106] D. Piñero, P. Baran, R. Boca, R. Herchel, M. Klein, R. G. Raptis, F. Renz, Y. Sanakis, *Inorg.*

Chem. **2007**, *46*, 10981–10989.

[107] F. Meyer, *Eur. J. Inorg. Chem.* **2006**, *2006*, 3789–3800.

[108] J. B. H. Strautmann, S. Dammers, T. Limpke, J. Parthier, T. P. Zimmermann, S. Walleck, G. Heinze-Brückner, A. Stammler, H. Bögge, T. Glaser, *Dalt. Trans.* **2016**, *45*, 3340–3361.

[109] S. Buchler, F. Meyer, E. Kaifer, H. Pritzkow, *Inorg. Chim. Acta* **2002**, *337*, 371–386.

[110] K. E. Dalle, T. Gruene, S. Dechert, S. Demeshko, F. Meyer, *J. Am. Chem. Soc.* **2014**, *136*, 7428–7434.

[111] A. Brinkmeier, K. E. Dalle, L. D'Amore, R. A. Schulz, S. Dechert, S. Demeshko, M. Swart, F. Meyer, *J. Am. Chem. Soc.* **2021**, *143*, 17751–17760.

[112] T. Lohmiller, C. Spyra, S. Dechert, S. Demeshko, E. Bill, A. Schnegg, F. Meyer, *JACS Au* **2022**, *2*, 1134–1143.

[113] J. Ackermann, F. Meyer, E. Kaifer, H. Pritzkow, *Chem. - A Eur. J.* **2002**, *8*, 247–258.

[114] D. E. Fenton, *Chem. Soc. Rev.* **1999**, *28*, 159–168.

[115] K. Wieghardt, *Pure Appl. Chem.* **1988**, *60*, 509–516.

[116] R. Bhula, P. Osvath, D. C. Weatherburn, *Coord. Chem. Rev.* **1988**, *91*, 89–213.

[117] D. K. Cabbiness, D. W. Margerum, *J. Am. Chem. Soc.* **1969**, *91*, 6540–6541.

[118] A. E. Martell, R. D. Hancock, R. J. Motekaitis, *Coord. Chem. Rev.* **1994**, *133*, 39–65.

[119] R. D. Hancock, A. E. Martell, *Comments Inorg. Chem.* **1988**, *6*, 237–284.

[120] J. I. van der Vlugt, *Eur. J. Inorg. Chem.* **2012**, *2012*, 363–375.

[121] A. Brinkmeier, Bimetallic Copper Complexes for Bioinspired Dioxygen Activation and Catalytic Water Oxidation, Dissertation, Georg-August-Universtät Göttingen, **2017**.

[122] A. Brinkmeier, R. A. Schulz, M. Buchhorn, C.-J. Spyra, S. Dechert, S. Demeshko, V. Krewald, F. Meyer, *J. Am. Chem. Soc.* **2021**, *143*, 10361–10366.

[123] J. Lücken, Transformations of Energy-Related Small Molecules at Dinuclear Complexes, Dissertation, Georg-August-Universtät Göttingen, **2020**.

[124] N. Kindermann, S. Dechert, S. Demeshko, F. Meyer, *J. Am. Chem. Soc.* **2015**, *137*, 8002–8005.

[125] N. Kindermann, C.-J. Günes, S. Dechert, F. Meyer, *J. Am. Chem. Soc.* **2017**, *139*, 9831–9834.

[126] A. Kochanke, Kupferkomplexe Mit Pyrazol/TACN-Hybridliganden Für Die Biomimetische Aktivierung Kleiner Moleküle, Master thesis, Georg-August-Universtät Göttingen, **2016**.

[127] M. A. Winnik, *Chem. Rev.* **1981**, *81*, 491–524.

[128] V. Martí-Centelles, M. D. Pandey, M. I. Burguete, S. V. Luis, *Chem. Rev.* **2015**, *115*, 8736–

8834.

[129] K. E. Krakowiak, J. S. Bradshaw, D. J. Zamecka-Krakowiak, *Chem. Rev.* **1989**, *89*, 929–972.

[130] R. N. Greene, *Tetrahedron Lett.* **1972**, *13*, 1793–1796.

[131] H. Stetter, E. Roos, *Chem. Ber.* **1954**, *87*, 566–571.

[132] J. E. Richman, T. J. Atkins, *J. Am. Chem. Soc.* **1974**, *96*, 2268–2270.

[133] F. Chavez, A. D. Sherry, *J. Org. Chem.* **1989**, *54*, 2990–2992.

[134] C. Galli, *Org. Prep. Proced. Int.* **1992**, *24*, 285–307.

[135] B. L. Shaw, *J. Am. Chem. Soc.* **1975**, *97*, 3856–3857.

[136] D. A. Valyaev, S. Clair, L. Patrone, M. Abel, L. Porte, O. Chuzel, J.-L. Parrain, *Chem. Sci.* **2013**, *4*, 2815–2821.

[137] C. Flassbeck, K. Wieghardt, *Z. Anorg. Allg. Chem.* **1992**, *608*, 60–68.

[138] J. A. Halfen, W. B. Tolman, K. Weighardt, *Inorg. Synth.* **1998**, *32*, 75–81.

[139] R. B. Leng, *Chem. Eng. Prog.* **2004**, *100*, 37–44.

[140] P. Désogère, Y. Rousselin, S. Poty, C. Bernhard, C. Goze, F. Boschetti, F. Denat, *European J. Org. Chem.* **2014**, *2014*, 7831–7838.

[141] G. Gros, J. Hasserodt, *European J. Org. Chem.* **2015**, *2015*, 183–87.

[142] A. Thangavel, M. Wieliczko, J. Bacsa, C. C. Scarborough, *Inorg. Chem.* **2013**, *52*, 13282–13287.

[143] C. J. Coghlan, E. M. Campi, W. R. Jackson, M. T. W. Hearn, *Green Chem.* **2016**, *18*, 5477–5484.

[144] A. Gondoh, T. Koike, M. Akita, *Inorganica Chim. Acta* **2011**, *374*, 489–498.

[145] F. Bendrath, V. Specowius, D. Michalik, P. Langer, *Tetrahedron* **2012**, *68*, 6456–6462.

[146] S. Reim, D. Michalik, K. Weisz, Z. Xiao, P. Langer, *Org. Biomol. Chem.* **2008**, *6*, 3079–3084.

[147] M. Veronelli, N. Kindermann, S. Dechert, S. Meyer, F. Meyer, *Inorg. Chem.* **2014**, *53*, 2333–2341.

[148] L. Wang, X. Yu, X. Feng, M. Bao, *J. Org. Chem.* **2013**, *78*, 1693–1698.

[149] A. V. Gulevich, A. S. Dudnik, N. Chernyak, V. Gevorgyan, *Chem. Rev.* **2013**, *113*, 3084–3213.

[150] W. W. Paudler, A. G. Zeiler, *J. Org. Chem.* **1969**, *34*, 999–1001.

[151] S. Buchler, Präorgnisierte Zweikernkomplexe Neuer Pyrazolat-Kompartimentliganden, Dissertation, Ruprecht-Karls-Universität Heidelberg, **2002**.

[152] J. Ackermann, Biomimetische Oxidationsreaktionen Mit Zweikernigen

Kupferpyrazolatkomplexen, Dissertation, Georg-August-Universität Göttingen, **2003**.

[153] T. Nizami, R. Hua, *Molecules* **2014**, *19*, 13788–13802.

[154] Q. Zheng, R. Hua, Y. Wan, *Appl. Organomet. Chem.* **2009**, *24*, 314–316.

[155] M. Seeba, Bioinspired Dinuclear Copper Complexes for Catalytic Oxidation of Phenolic Substrates, Dissertation, Georg-August-Universität Göttingen, **2017**.

[156] M. Seeba, Bioinspirierte Dinukleare Kupferkomplexe Zur Phenoloxidation, Master thesis, Georg-August-Universität Göttingen, **2012**.

[157] L. A. Muse, *J. Chem. Educ.* **1972**, *49*, 465–467.

[158] K. Fischer, *Angew. Chem.* **1935**, *48*, 394–396.

[159] H.-C. Liang, K. D. Karlin, R. Dyson, S. Kaderli, B. Jung, A. D. Zuberbühler, *Inorg. Chem.* **2000**, *39*, 5884–5894.

[160] N. G. Connelly, W. E. Geiger, *Chem. Rev.* **1996**, *96*, 877–910.

[161] M. Winkler, Dinukleare Kupfer-Sauerstoffkomplexe Auf Basis Eines Asymmetrischen Ligandensystem, Bachelor thesis, Georg-August-Universität Göttingen, **2019**.

[162] H. A. Jahn, E. Teller, *Proc. R. Soc. London. Ser. A - Math. Phys. Sci.* **1937**, *161*, 220–235.

[163] A. W. Addison, T. N. Rao, J. Reedijk, J. Van Rijn, G. C. Verschoor, *J. Chem. Soc. Dalt. Trans.* **1984**, 1349–1356.

[164] A. G. Blackman, E. B. Schenk, R. E. Jelley, E. H. Krenske, L. R. Gahan, *Dalt. Trans.* **2020**, *49*, 14798–14806.

[165] A. Kumar Singh, J. I. van der Vlugt, S. Demeshko, S. Dechert, F. Meyer, *Eur. J. Inorg. Chem.* **2009**, *2009*, 3431–3439.

[166] V. H. Crawford, H. W. Richardson, J. R. Wasson, D. J. Hodgson, W. E. Hatfield, *Inorg. Chem.* **1976**, *15*, 2107–2110.

[167] E. Ruiz, P. Alemany, S. Alvarez, J. Cano, *Inorg. Chem.* **1997**, *36*, 3683–3688.

[168] E. Ruiz, P. Alemany, S. Alvarez, J. Cano, *J. Am. Chem. Soc.* **1997**, *119*, 1297–1303.

[169] W. E. Geiger, *J. Am. Chem. Soc.* **1974**, *96*, 2632–2634.

[170] G. E. Herberich, W. Klein, U. Kölle, D. Spiliotis, *Chem. Ber.* **1992**, *125*, 1589–1595.

[171] M. J. Henson, M. A. Vance, C. X. Zhang, H.-C. Liang, K. D. Karlin, E. I. Solomon, *J. Am. Chem. Soc.* **2003**, *125*, 5186–5192.

[172] P. W. Atkins, J. de Paula, *Physikalische Chemie*, Wiley-VCH Verlag GmbH & Co. KGaA, Weinheim, Germany, **2006**.

[173] L. Sooväli, E.-I. Rõõm, A. Kütt, I. Kaljurand, I. Leito, *Accredit. Qual. Assur.* **2006**, *11*, 246–255.

[174] M. Weitzer, S. Schindler, G. Brehm, S. Schneider, E. Hörmann, B. Jung, S. Kaderli, A. D. Zuberbühler, *Inorg. Chem.* **2003**, *42*, 1800–1806.

[175] I. Garcia-Bosch, A. Company, J. R. Frisch, M. Torrent-Sucarrat, M. Cardellach, I. Gamba, M. Güell, L. Casella, L. Que, X. Ribas, J. M. Luis, M. Costas, *Angew. Chem. Int. Ed.* **2010**, *49*, 2406–2409.

[176] C. Würtele, F. W. Heinemann, S. Schindler, *J. Coord. Chem.* **2010**, *63*, 2629–2641.

[177] H. R. Lucas, L. Li, A. A. N. Sarjeant, M. A. Vance, E. I. Solomon, K. D. Karlin, *J. Am. Chem. Soc.* **2009**, *131*, 3230–3245.

[178] U. M. Sundaram, H. H. Zhang, B. Hedman, K. O. Hodgson, E. I. Solomon, *J. Am. Chem. Soc.* **1997**, *119*, 12525–12540.

[179] H. Komori, Y. Higuchi, *J. Biochem.* **2015**, *158*, 293–298.

[180] E. I. Solomon, A. J. Augustine, J. Yoon, *Dalt. Trans.* **2008**, *9226*, 3921.

[181] W. Shin, U. M. Sundaram, J. L. Cole, H. H. Zhang, B. Hedman, K. O. Hodgson, E. I. Solomon, *J. Am. Chem. Soc.* **1996**, *118*, 3202–3215.

[182] C. J. Günes, Ein Reaktiver Dikupfer(II)-Superoxo-Komplex Für Wasserstoffatom-Abstraktionsreaktionen, Master thesis, Georg-August-Universität Göttingen, **2016**.

[183] J. Mangue, C. Gondre, J. Pécaut, C. Duboc, S. Ménage, S. Torelli, *Chem. Commun.* **2020**, *56*, 9636–9639.

[184] S. Kakuda, C. J. Rolle, K. Ohkubo, M. A. Siegler, K. D. Karlin, S. Fukuzumi, *J. Am. Chem. Soc.* **2015**, *137*, 3330–3337.

[185] J. Yano, V. Yachandra, *Chem. Rev.* **2014**, *114*, 4175–4205.

[186] C. Zhang, *Sci. China Life Sci.* **2015**, *58*, 816–817.

[187] M. Suga, F. Akita, K. Hirata, G. Ueno, H. Murakami, Y. Nakajima, T. Shimizu, K. Yamashita, M. Yamamoto, H. Ago, J.-R. Shen, *Nature* **2015**, *517*, 99–103.

[188] B. Gerey, E. Gouré, J. Fortage, J. Pécaut, M.-N. Collomb, *Coord. Chem. Rev.* **2016**, *319*, 1–24.

[189] S. Fukuzumi, K. Ohkubo, Y.-M. Lee, W. Nam, *Chem. - A Eur. J.* **2015**, *21*, 17548–17559.

[190] G. T. Babcock, M. Wikström, *Nature* **1992**, *356*, 301–309.

[191] V. R. I. Kaila, M. I. Verkhovsky, M. Wikström, *Chem. Rev.* **2010**, *110*, 7062–7081.

[192] S. Fukuzumi, S. Mandal, K. Mase, K. Ohkubo, H. Park, J. Benet-Buchholz, W. Nam, A. Llobet, *J. Am. Chem. Soc.* **2012**, *134*, 9906–9909.

[193] C. W. Machan, *ACS Catal.* **2020**, *10*, 2640–2655.

[194] S. Dey, B. Mondal, S. Chatterjee, A. Rana, S. Amanullah, A. Dey, *Nat. Rev. Chem.* **2017**, *1*, 0098.

[195] R. Borup, J. Meyers, B. Pivovar, Y. S. Kim, R. Mukundan, N. Garland, D. Myers, M. Wilson, F. Garzon, D. Wood, P. Zelenay, K. More, K. Stroh, T. Zawodzinski, J. Boncella, J. E. McGrath, M. Inaba, K. Miyatake, M. Hori, K. Ota, Z. Ogumi, S. Miyata, A. Nishikata, Z. Siroma, Y. Uchimoto, K. Yasuda, K. Kimijima, N. Iwashita, *Chem. Rev.* **2007**, *107*, 3904–3951.

[196] I. Willner, Y.-M. Yan, B. Willner, R. Tel-Vered, *Fuel Cells* **2009**, *9*, 7–24.

[197] Y. Zhao, G. Yu, F. Wang, P. Wei, J. Liu, *Chem. – A Eur. J.* **2019**, *25*, 3726–3739.

[198] H. Oh, S. Choi, J. Y. Kim, H. S. Ahn, S. Hong, *Chem. Commun.* **2019**, *55*, 12659–12662.

[199] K. M. Kadish, L. Frémond, J. Shen, P. Chen, K. Ohkubo, S. Fukuzumi, M. El Ojaimi, C. P. Gros, J. M. Barbe, R. Guilard, *Inorg. Chem.* **2009**, *48*, 2571–2582.

[200] J. P. Collman, S. Ghosh, A. Dey, R. A. Decréau, Y. Yang, *J. Am. Chem. Soc.* **2009**, *131*, 5034–5035.

[201] S. Fukuzumi, Y.-M. Lee, W. Nam, *ChemCatChem* **2018**, *10*, 9–28.

[202] D. A. Quist, M. A. Ehudin, A. W. Schaefer, G. L. Schneider, E. I. Solomon, K. D. Karlin, *J. Am. Chem. Soc.* **2019**, *141*, 12682–12696.

[203] J. Mangue, C. Gondre, J. Pécaut, C. Duboc, S. Ménage, S. Torelli, *Chem. Commun.* **2020**, *56*, 9636–9639.

[204] M. L. Pegis, C. F. Wise, D. J. Martin, J. M. Mayer, *Chem. Rev.* **2018**, *118*, 2340–2391.

[205] P. Pirovano, A. M. Magherusan, C. McGlynn, A. Ure, A. Lynes, A. R. McDonald, *Angew. Chem. Int. Ed.* **2014**, *53*, 5946–5950.

[206] W. D. Bailey, N. L. Gagnon, C. E. Elwell, A. C. Cramblitt, C. J. Bouchey, W. B. Tolman, *Inorg. Chem.* **2019**, *58*, 4706–4711.

[207] C. Panda, A. Chandra, T. Corona, E. Andris, B. Pandey, S. Garai, N. Lindenmaier, S. Künstner, E. R. Farquhar, J. Roithová, G. Rajaraman, M. Driess, K. Ray, *Angew. Chem. Int. Ed.* **2018**, *57*, 14883–14887.

[208] Q. Zhang, A. Bell-Taylor, F. M. Bronston, J. D. Gorden, C. R. Goldsmith, *Inorg. Chem.* **2017**, *56*, 773–782.

[209] J. Cho, R. Sarangi, W. Nam, *Acc. Chem. Res.* **2012**, *45*, 1321–1330.

[210] B. Kripli, M. Szávuly, F. V. Csendes, J. Kaizer, *Dalt. Trans.* **2020**, *49*, 1742–1746.

[211] Y. Funato, H. Miki, *J. Biochem.* **2019**, *165*, 219–225.

[212] D. B. G. Williams, M. Lawton, *J. Org. Chem.* **2010**, *75*, 8351–8354.

[213] D. E. Clark, *Chem. Health Saf.* **2001**, *8*, 12–22.

[214] R. J. Kelly, *Chem. Health Saf.* **1996**, *3*, 28–36.

[215] G. R. Fulmer, A. J. M. Miller, N. H. Sherden, H. E. Gottlieb, A. Nudelman, B. M. Stoltz, J. E. Bercaw, K. I. Goldberg, *Organometallics* **2010**, *29*, 2176–2179.

[216] H. E. Gottlieb, V. Kotlyar, A. Nudelman, *J. Org. Chem.* **1997**, *62*, 7512–7515.

[217] Eckhard Bill, *JulX*, Max-Planck-Institute For Chemical Energy Conversion, Mühlheim an Der Ruhr, **2008**.

[218] G. M. Sheldrick, *Acta Crystallogr. Sect. A Found. Crystallogr.* **2015**, *71*, 3–8.

[219] G. M. Sheldrick, *Acta Crystallogr. Sect. C Struct. Chem.* **2015**, *71*, 3–8.

[220] T. Weege, New Bioinspired Dinuclear Copper Complexes for the Activation of Oxygen, Bachelor thesis, Georg-August-Universtät Göttingen, **2019**.

12 Overview of ligands and dicopper complexes

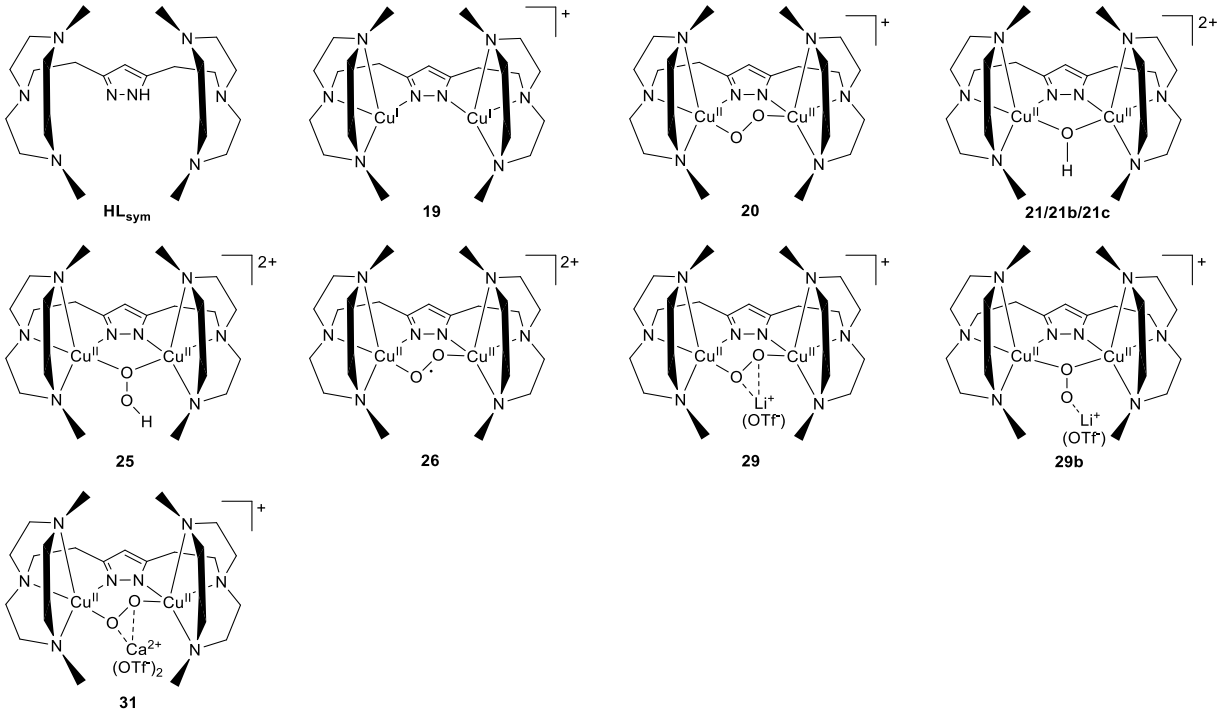

Figure 105: Overview of the dicopper complex based on ligand scaffold **HL$_{sym}$.**

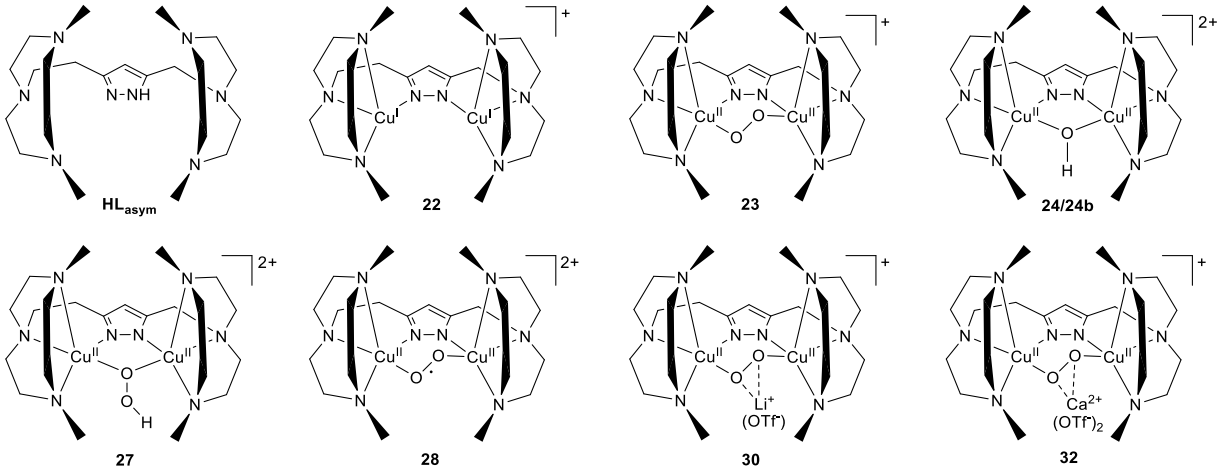

Figure 106: Overview of the dicopper complex based on ligand scaffold **HL$_{asym}$.**

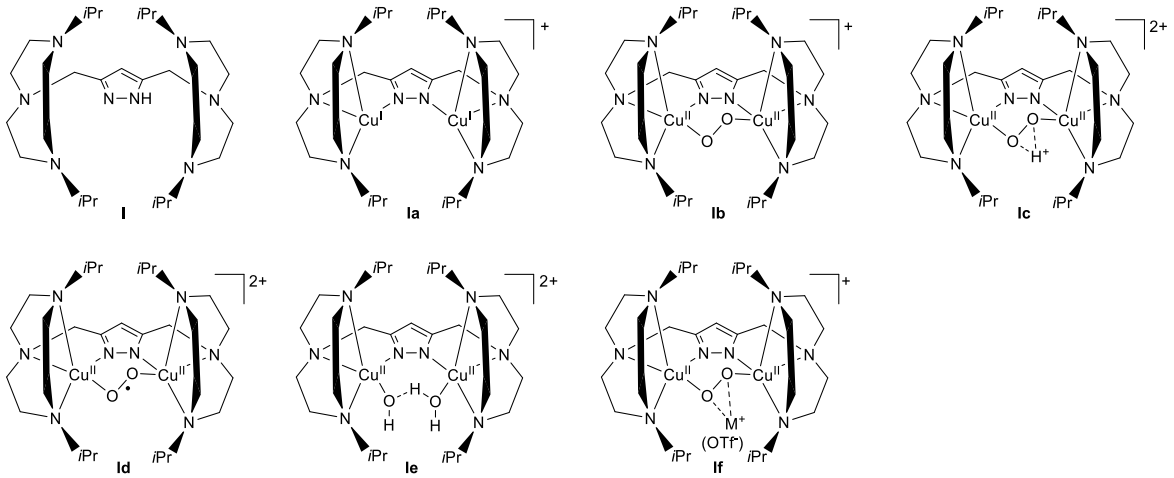

Figure 107: Overview of the dicopper complex based on ligand scaffold **I** established by DALLE and BRINKMEIER.[104,110,111,121,122]

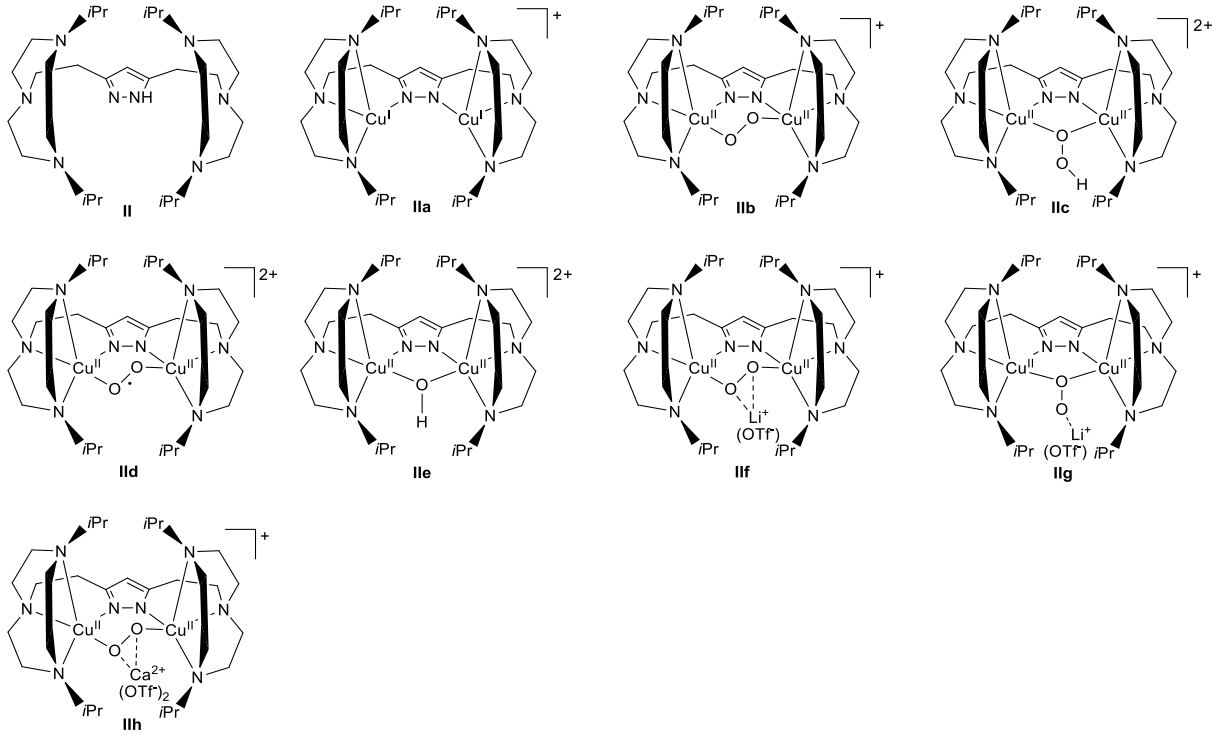

Figure 108: Overview of the dicopper complex based on ligand scaffold **II** mainly established by KINDERMANN.[64,65,124,125]

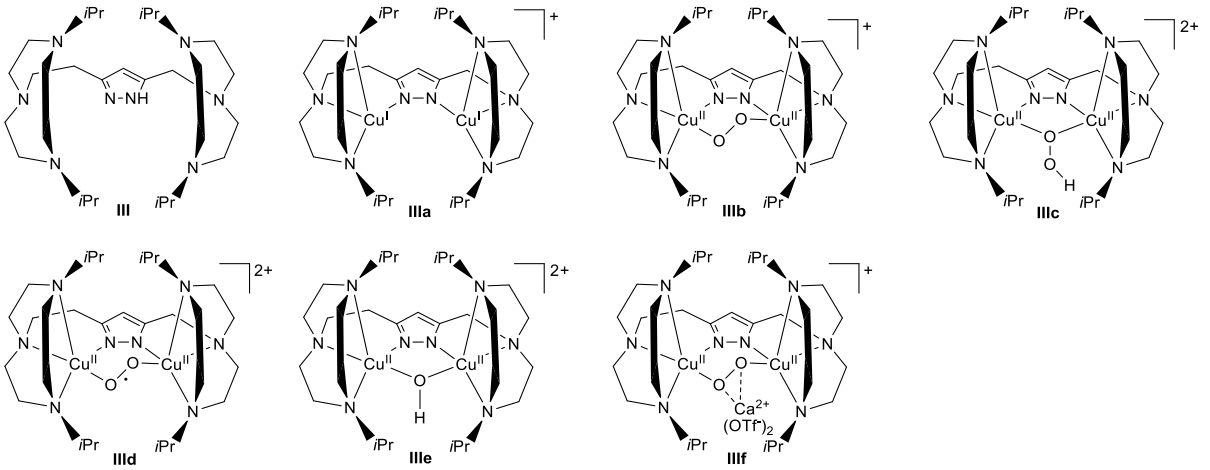

Figure 109: Overview of the dicopper complex based on ligand scaffold **III** mainly established by SPYRA.[38,112]

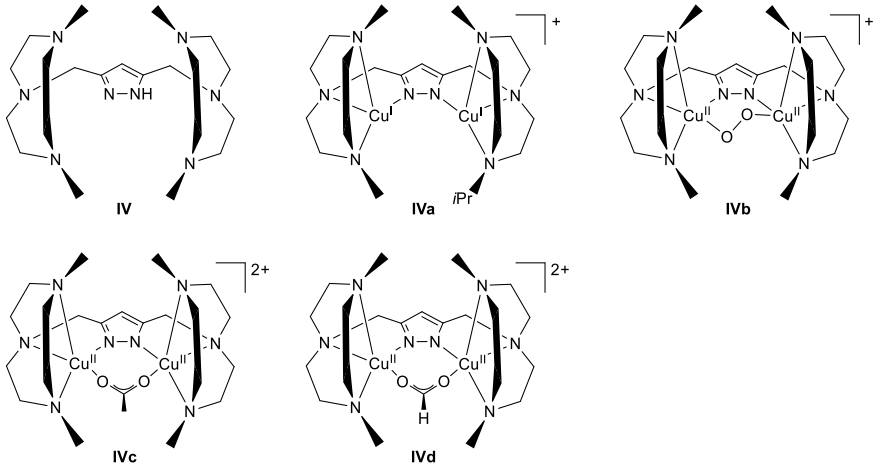

Figure 110: Overview of the dicopper complex based on ligand scaffold **IV** established by BRINKMEIER and LÜCKEN.[78,121,123]

13 Acknowledgments

First and foremost, I want to thank Prof. Dr. Franc Meyer for giving me the opportunity to pursue this research project, the guidance, the scientific freedom he granted me and his endless optimism.

Further I would like to thank Prof. Dr. Inke Siewert for co-supervising this work, constructive comments and insightful discussions regarding this work.

I want to thank Dr. Sebastian Dechert for performing all the XRD and Raman measurements of this work, the scientific discussions and the lunch breaks. I also want to thank Dr. Serhiy Demeshko for the preparation and conduction of the SQUID measurements.

I thank the NMR department for keeping the NMR machines in good shape, the Zentral Analytik – Massenspektrometrie of the IOBC for the measurements, Andreas Schwarz for providing chemicals and starting materials, Britta Müller, Dr. Claudia Stückl and the Dean's office of the Faculty of Chemistry for taking care of all administrative matters and the workshops for their technical support.

I want to thank Pierre Pascal Kachel and Tobias Weege for their experimental work during their Bachelor thesis. It was a joy to work with you and I had a great time supervising your Bachelor theses. I also like to thank Marius Deuker for his work during his research internship.

Special thanks to my lab mate Jerome Spyra for the great time and the support during the ups and downs of lab work. I would also like to thank the "Magic Blue Team" consisting of Roland Alexander Schulz, Thomas Kothe and Jerome Spyra for the local fame and glory.

I want to acknowledge and express my gratitude to all my co-workers who helped in conducting my research. I am very grateful and your support and efforts are very much appreciated. Especially, I like to thank to Anna Kölpin, Alexander Brinkmeier, Guillermo Duran-Solares, Hendrik Stevens, Jana Lücken, Massimiliano Morganti and Mike Schütze.

I want to thank my family and friends for their affection and support during the last years. Finally, I like to thank Sonja for her love and her endless support. Without your support and motivation, this work would not have been possible.